Self-assembled Perylene Bisimide Dimers and their Interaction with Double-stranded DNA

Dissertation zur Erlangung
des naturwissenschaftlichen Doktorgrades
Julius-Maximilians-Universität Würzburg

vorgelegt von
Jana Gershberg
aus Frunse

Würzburg 2016

Eingereicht bei der Fakultät für Chemie und Pharmazie am

____

Gutachter der schriftlichen Arbeit:
1. Gutachter: Prof. Dr. Frank Würthner
2. Gutachter: Prof. Dr. Jürgen Seibel

Prüfer des öffentlichen Promotionskolloquiums
1. Prüfer: Prof. Dr. Frank Würthner
2. Prüfer: Prof. Dr. Jürgen Seibel
3. Prüfer: Prof. Dr. Ingo Fischer

Datum des öffentlichen Promotionskolloquiums
28.07.2016

Doktorurkunde ausgehändigt am ______________

Für meine Familie

Danksagung

Mein besonderer Dank gilt Prof. Dr. Frank Würthner für die Chance an interessanten Forschungsthemen arbeiten zu dürfen, für die zahlreichen Hilfestellungen und die wertvollen Diskussionen und Ratschläge. Des Weiteren möchte ich mich für die zahlreichen Möglichkeiten zum wissenschaftlichen und internationalen Austausch von Forschungsergebnissen bedanken. Die besonders guten Arbeitsbedingungen und das entgegengebrachte Vertrauen in meine selbstständige Arbeit haben sehr zu meiner wissenschaftlichen und persönlichen Entwicklung beigetragen.

Dr. Ivo Piantanida und Dr. Marijana Radić Stojković danke ich für die sehr gute Zusammenarbeit und den wissenschaftlichen Austausch, aus dem die gemeinsame Veröffentlichung hervorging. Die zahlreichen Besuche, sowohl meinerseits in Zagreb als auch die Besuche von Ivo und Marijana in Würzburg, haben entschieden zu den Ergebnissen dieser Arbeit beigetragen. Weiterhin bedanke ich mich für den schönen Empfang in Zagreb und die angenehme Gesellschaft bei den freizeitlichen Unternehmungen.

Ich danke Herrn Dr. Chantu Saha-Möller für die professionelle Unterstützung und Überarbeitungen der Manuskripte als auch das Korrekturlesen dieser Arbeit.

Herrn Dr. Matthias Grüne und Frau Elfriede Ruckdeschel danke ich für die Messungen von NMR Spektren und die Hilfsbereitschaft bei Rückfragen. Herrn Dr. Michael Büchner, Herrn Fritz Dadrich und Frau Antje Hautzinger danke ich für die Aufnahme der Massenspektren. Bei Frau Liselotte Michels und Frau Sabine Timmroth bedanke ich mich für die Durchführung der CHN Elementaranalysen am Institut für Anorganische Chemie. Bei Frau Christiana Toussaint bedanke ich mich für die Hilfe bei allen organisatorischen Fragen.

Ich bedanke mich bei Frau Dr. Franziska Fennel für die Unterstützung bei der gemeinsamen Veröffentlichung und die vielen hilfreichen Diskussionen.

Bei Dr. Matthias Stolte bedanke ich mich herzlich für die Geduld und für die zahlreichen Hilfestellungen bei physikalischen und spektroskopischen Fragestellungen und das Korrekturlesen der Arbeit.

Ich danke für die synthetische Unterstützung dem Laboranten Johannes Thein, den Masterstudentinnen Kerstin Müller und Claudia Kupper, dem Bachelorstudenten Daniel Fersch und der Auszubildenden Carolin Christ.

Ich danke dem gesamten AK Würthner für die schöne Zeit während der Doktorarbeit und die vielen lustigen Stammtischabende. Insbesondre danke ich M. Sc. Annike Weißenstein und Dr. Sabin Suraru für den schönen und amüsanten Laboralltag. Außerdem danke ich Annike und M. Sc. Valentin Kunz für das Korrekturlesen der Arbeit.

Ich denke meiner Familie und Freunden für die Unterstützung und den immerwährenden Halt während der gesamten Zeit.

List of Abbreviations

A	Adenine
AFM	Atomic force microscopy
Ala	Alanine
BTA	Benzene-1,2,3-tricarboxamide
C	Cytosine
CD	Circular dichroism
DIPEA	*N*,*N*-Diisopropylethylamine
DMF	Dimethylformamide
DMSO	Dimethyl sulfoxide
DNA	Deoxyribonucleic acid
DOSY	Diffusion-Ordered NMR Spectroscopy
ESI	Electrospray ionization
eqn	Equation
G	Guanine
Gly	Glycine
GPC	Gel permeation chromatography
FT-IR	Fourier transform infrared spectroscopy
HATU	*O*-(7-azabenzotriazol-1-yl)-*N*,*N*,*N*’,*N*’-tetramethyluronium hexafluorophosphate
HOBt	Hydroxybenzotriazole
HOPG	Highly oriented pyrolytic graphite
HOMO	Highest occupied molecular orbital
HPLC	High-performance liquid chromatography
ICD	Induced circular dichroism
ITC	Isothermal titration calorimetry
LAH	Lithium aluminium hydride
LD	Linear dichroism
LUMO	Lowest unoccupied molecular orbital
MALDI	Matrix-assisted laser desorption/ionization
MES	2-(*N*-morpholino)ethanesulfonic acid
m.p.	Melting point
MS	Mass spectrometry
NEt_3	Triethylamine

NMR	Nuclear magnetic resonance
PBA	Perylene tetracarboxylic bisanhydride
PBI	Perylene-3,4:9,10-bis(dicarboximide) (often mentioned as perylene-3,4:9,10-tetracarboxylic acid bisimide or perylene bisimide)
PDB	Protein data bank
Phe	Phenylalanine
RNA	Ribonucleic acid
ROESY	Rotating-frame nuclear Overhauser effect NMR
RT	Room temperature
T	Thymine
*t*Boc	*tert*-butyloxycarbonyl
TFA	Trifluoroacetic acid
THF	Tetrahydrofuran
UV/Vis	Ultraviolet/Visible
VPO	Vapor pressure osmometry

Table of Contents

Aim of the thesis

“Self-assembly” is a widely spread term emphasizing the association of components into ordered structures without human interference which can be expanded on nature and technology.[1] The parallels to nature are undisputed since the self-assembly is present in living organisms on different scales inspiring the imitation in artificial non-living systems.[2] This field of research attracted scientists of various disciplines for many decades for many reasons. Researches are animated to apply the concept in designing materials and related functions to create new technologies. This made the understanding of the self-assembly processes a greatly developing research field for chemists, biologist and physicists.[3] Each discipline tackles the problem or rather its solution from different points of view. Learning from nature, biologist study organized patterns in cells or tissues. Chemists synthesize or fabricate self-assembled compositions and physicists explore already arranged systems.[1] The entirety of these approaches will provide a comprehensive picture of the self-assembly event.

Regarding chemical methods, self-assembly is an important part of supramolecular chemistry which deals with molecular assemblies though intermolecular bonds as defined by J.M. Lehn.[4] Terms like non-covalent interactions or ‘host-guest’ chemistry originally defining supramolecular chemistry were largely expanded in the last decades, thus, molecular devices and machines, molecular recognition and ‘self-processes’ enriched this chemistry research area.[4b] However, the molecular self-assembly is still associated with non-covalent interactions of molecules which might be van der Waals, electrostatic, hydrophobic or π-π-interactions, as well as hydrogen or coordination bonds and many others. Other than defining the driving forces of the arrangement, classifications and concepts were introduced to categorize the self-assembly to keep an overview on the occurring self-organization pathways. Classes like strict or irreversible self-assembly, precursor modification followed by self-assembly, self-assembly with postmodification, assisted or directed self-assembly and self-assembly with intermittent processing covered the main possible events. However, each case has to be carefully evaluated because of the overlapping properties of the classes.[5]

As already mentioned, the desire to explore the self-assembly process is mainly inspired by nature. Self-assembly of proteins, pairing of DNA or building up of membranes and tissues are some of the interesting proceedings in living organisms making worth to enhance the knowledge of their causes and effects. Although, these biological processes involve many complex individual steps which are understood in many cases, they are difficult to mimic. Therefore, the self-assembly is investigated on smaller and thereby simpler artificial systems. However, the manipulation of the self-assembly processes, such as the size of a particular aggregate of artificial molecules, is a notable challenge. Often, the size of aggregates is randomly distributed following the isodesmic aggregation behavior,[6] whereby, the self-assembly of biological systems often proceed through the cooperative pathway which is more or less an all or nothing process.[2, 7] The task to imitate this aggregation pathway has already been successfully mastered for many artificial systems.[8] However, the control of the size of aggregates on a certain level is a tough mission which requires precise conditions and structure-property considerations.[9]

Chromophores bearing large aromatic π-surfaces are attractive candidates to study their self-assembly behavior due to the formation of intermolecular π-π-contacts. For instance, porphyrins, phthalocyanines or perylenes are supposed to be appropriate dyes to fulfill the requirements, particularly because their electronic and photophysical properties make them appealing for applications.[10] Perylene bisimide (PBI) dyes gained much attention because of their thermal and photophysical stability as well as their promising application in organic electronics.[11] Thus, many diverse structural variations of the PBI dyes have been achieved and utilized in different research fields.[12] Herein, the most interesting property of these dyes is the self-assembly behavior of bay-unsubstituted chromophores as they are known to display a planar aromatic core which leads to the formation of columnar stacks though the strong π-π-interactions.[13] Beside the structural composition, factors like solvent, concentration and temperature may confine the size of a particular stack.[14] To find the right compromise between the structural and conditional possibilities and desired functionalities pose definitely a challenge.

The aim of the thesis is to rationally design PBI dyes where the aggregate size can be controlled by the right choice of conditions. For this purpose, a bay-unsubstituted PBI building block was equipped with amide functions capable to form hydrogen bonds (red dashed lines in Figure 1). Beside π-π-interactions, hydrogen bonds should contribute to the self-assembly as an additional driving force that should direct the H-type self-assembly to the dimeric species (see Figure 1). Furthermore, the variation of the external environment has to guide the self-assembly of these dimers to larger stacks of even numbered size through the anti-cooperative aggregation pathway. Finally, the interactions of the excitonically coupled PBI dimers with DNA/RNA are elucidated.

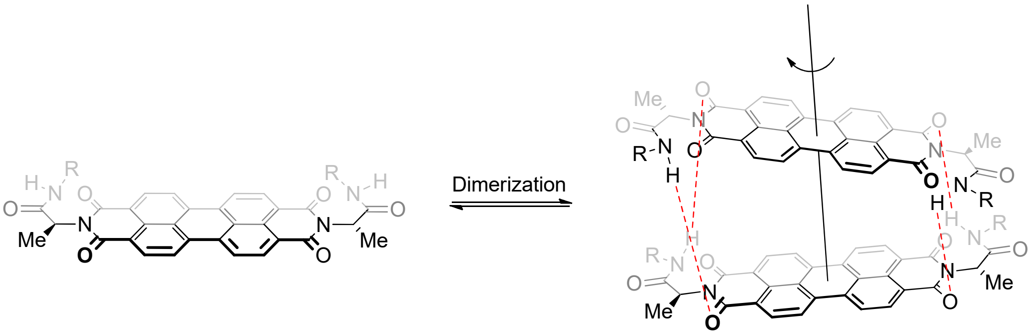

Figure 1: Schematic representation of the dimerization process of a PBI dye functionalized with amide groups in the imide positions. Red dashed lines illustrate the hydrogen bond contacts in the dimeric stack.

Chapter 1 gives an overview on interactions of small molecules with DNA. For this purpose, DNA as a supramolecular building block and its functions are described in detail. The main binding modes occurring upon binding of ligands to DNA and their determination by spectroscopic methods are illustrated. At the end, the literature examples of self-assembled π-systems interacting with DNA are presented.

Chapter 2 is focused on the determination of the binding parameters of self-assembled systems in the thermodynamically equilibrated state. The most important binding models are mathematically derived and examples from literature for each aggregation mode are listed. In the end of this chapter, some of the experimental issues und possibilities to control the self-assembly are demonstrated.

In **Chapter 3**, the dimerization processes of PBI dyes bearing L-alanine functions in the imide position which are connected to different solubilizing side chains are presented. The control of the aggregate size was realized by a delicate interplay of structural features of the PBI building block and the choice of solvent. The dimerization process was followed mainly by UV/Vis and NMR spectroscopy accompanied by some supplementary techniques.

The further growth of the mentioned dimers in the anti-cooperative fashion is described in **Chapter 4**. The formation of even-numbered aggregates has been achieved by the variation of solvents. Additionally, a newly developed K_2-K model has been derived which process the obtained absorption data with much more accuracy than the conventionally used K_2-K model.

Chapter 5 presents the synthesis of a series of water soluble PBI dyes functionalized with amino acids and cationic side chains. Afterwards, the self-assembly behavior of these dyes and their interaction with DNA and RNA was elaborated using thermal denaturation, fluorimetric titration and circular dichroism experiments. The measurement provided the evidence for the formation of stable complexes of the PBI dyes and the applied polynucleotides. The strength of interaction is dependent on the number of positive charges, the chiral centers of the PBI dyes as well as the secondary structure of DNA/RNA. Based on the obtained data, it was concluded that the PBIs form excitonically coupled dimers in the grooves of DNA/RNA.

Finally, **Chapters 6** and **7** conclude the thesis with summaries in English and German.

Chapter 1
Interactions of π-conjugated molecular building blocks with DNA

Abstract: This chapter provides a short introduction on features and functions of DNA as a supramolecular building block and its interactions with small π-conjugated molecules and π-stacked nanosystems. The most important binding modes such as electrostatic interaction, intercalation and groove binding are described in more detail. The spectroscopic techniques such as UV/Vis absorption, fluorescence and circular dichroism which are most important for this thesis are illustrated for general cases of interactions. Finally, examples of molecules were chosen to demonstrate the interactions of aggregated π-systems with DNA.

1.1 Introduction

The deoxyribonucleic acid (DNA) is the source of the genetic information which is responsible for all biological processes and development of cellular forms of life.[15] The gene expression contains the transcription step, in which DNA sequences are copied into ribonucleic acid (RNA), and translation process, in which these RNAs are decoded for protein synthesis. These cellular regulations have included several molecular recognition events, mainly by proteins, which are necessary for the frictionless transfer of genetic information. The recognition of DNA on the molecular level became interesting in the scientific world since the binding of guest molecules may influence significantly the function of DNA as well as the binding molecule leading, for instance, to modulation of biological processes.[16] The modifications of DNA behavior open a great field in development of chemotherapeutical agents[17] as well as in bioimaging[18] and sensing research areas.

The application of recognition processes requires its understanding on the molecular level which includes the knowledge of the interacting molecules and responsible forces. Several requirements for the guest molecules have to be fulfilled such as high selectivity and large association constants.[16] Some of the important classes of molecules and their interaction with DNA will be discussed in the following sections.

As important as the rational design of the suitable guest molecules, is the understanding of the DNA molecule and its change of functions upon binding of a guest molecule. The biomolecular building block DNA is a complex molecule providing several binding sides for small molecules leading to different interaction modes like major and minor groove binding, intercalation and sugar-phosphate backbone binding, often called external or electrostatic interactions.[16, 19] Other recognition types are covalent binding and metal-coordination which won't be discussed in this literature survey. In the following sections, the most important binding modes and examples of DNA dye interactions will be discussed. The interactions of guest molecules with RNA are not the focus of this chapter but would be mentioned for comparison.

1.2 DNA as supramolecular building block

The natural DNA is a linear polymer with directional chains which compose of nucleotides consisting of purine (adenine (A) and guanine (G)) and pyrimidine (cytosine (C) and thymine (T)) bases, a sugar moiety (deoxyribose) and a negatively charged phosphate backbone (see Figure

2).[15] To facilitate the information exchange in the scientific world, often abbreviations for nucleotide sequences are used. For instance, poly (dA-dT)$_2$ is a polynucleotide of alternating adenine and thymine bases in a double-stranded DNA. These abbreviations will be used in the following chapters where necessary.

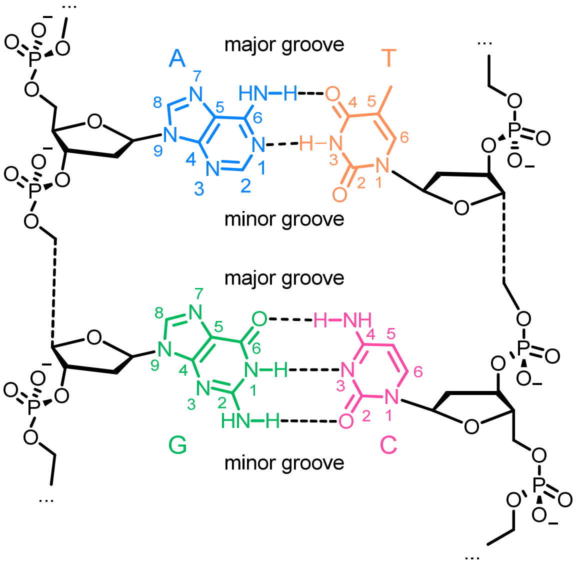

Figure 2: By Watson and Crick proposed hydrogen bonded base pair patterns (A-T and G-C) pointing into major and minor grooves. The bases are linked by glycoside bonds to the negatively charged phosphate backbone.[15]

Since Watson and Crick, the structure of double-stranded (ds) B-DNA is generally known.[20] Other double-helical forms such as the left-handed Z-DNA and the right-handed shorter and fatter A-DNA are present in biological systems as well.[19a] The three dimensional structure of the B-DNA is a right-handed double helix from complementary antiparallel arranged nucleic acids connected by hydrogen bonds (see Figure 3). The nucleic bases are arranged almost perpendicular to the helical axis and stack by π-π-interactions in a parallel fashion upon each other with an interplanar distance of 3.5 Å. The linear distance between the bases is around 0.34 nm and the helical structure repeats every 3.4 nm which means one turn comprises ten bases. The entire diameter of the helix is 2 nm. The stability of the helix is provided by hydrogen bonds (Watson-Crick hydrogen bond recognition), π-π-stacking between the bases and the hydrophobic effect.

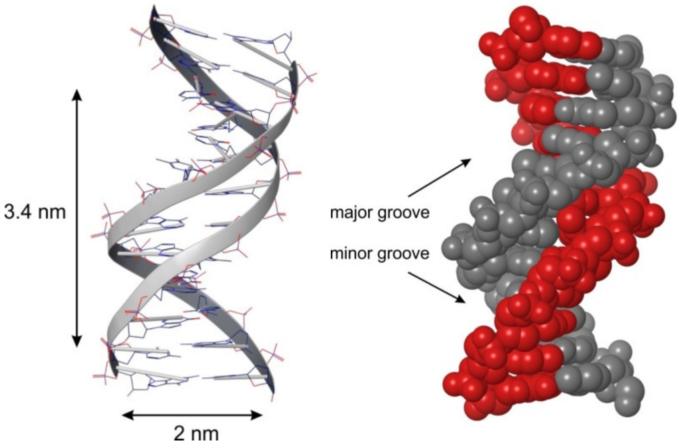

Figure 3: The crystal structure of the synthetic DNA dodecamer d(CpGpCpGpApApTpTpCpGpCpG) as representative example of DNA double helical structure.[21]

The hydrophobic bases are located in the core of the helix to avoid the contact to the aqueous environment. The bases approach each other by weak van der Waals forces, thus the hydrogen bonds can be formed. The large stabilization of the double helix results as a sum of all these forces. The base pairs are connected to diametrically opposed glycoside bonds, this connection leads to formation of wells in the double helix called minor and major groove. In the B-structure, the major groove is of 1.2 nm width and 0.85 nm depth. In contrast to the major groove, the minor groove is of 0.6 nm width and 0.75 nm depth. The donor- and acceptor atoms in the grooves allow potential interactions by hydrogen bonds with guest molecules. In the physiological media, these interactions arise mainly from reversible, non-covalent interactions with proteins. These structural features allow binding of molecules to DNA to change properties of both, the guest and host molecule. Molecular recognition of DNA by small molecules can occur in several ways like major and minor groove binding, intercalation and external electrostatic binding. These most important interactions will be described in the following sections.

Molecular and supramolecular chirality of DNA can be of significant importance in the recognition of DNA by chiral molecules. Therefore, stereochemical response can explain the mode of interaction which allows differentiation between enantiomers giving specific enantioselectivity.[22] The mechanisms of the binding events can be studied by different techniques. The important one for this work is circular dichroism, which will be discussed in detail in section 1.4.4.

1.3 Binding modes

The biomacromolecules DNA provide several binding sites for guest molecules, for instance proteins in the biological environment. The main binding motifs which are involved in the interaction of small molecules with DNA are external binding, groove binding (to major and minor groove) and intercalation (see Figure 4 for schematic representation). [16, 19b, 19c]

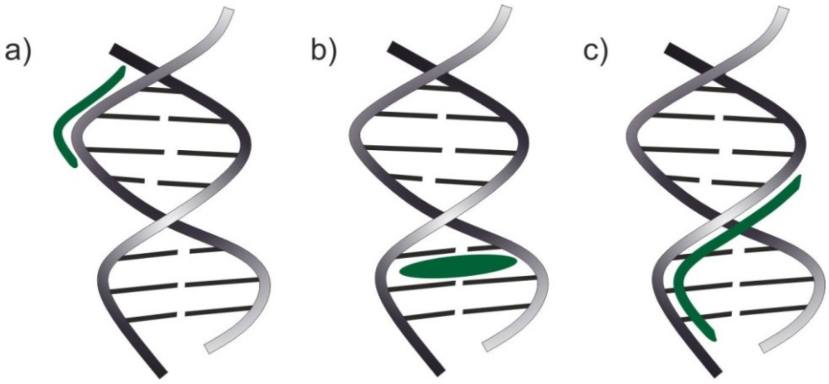

Figure 4: Schematic representation of the main binding modes to (ds)-DNA. a) External electrostatic binding to the phosphate backbone. b) Intercalation of a guest molecule. c) Groove binding of a guest molecule. The scheme is based on a review of Ihmels and Otto.[16] (Reproduced and adopted with permission from Springer, Copyright (2016)).

The external binding originates in most cases from electrostatic interactions between positively charged guest and negatively charged phosphates of DNA. Intercalation requires a planar aromatic molecule which interacts with base pairs by π-π-stacking. In contrast to that, binding of molecules in the grooves of DNA is usually based on hydrogen bonds of the ligand to the functional groups of the DNA, van der Waals and hydrophobic interactions. However, in the synthetic design of small molecules all possible interactions have to be considered, since, more than one binding mode can be involved in the binding event.

1.3.1 Electrostatic interactions

Electrostatic interactions (see Figure 4a) between ligand molecules and DNA often occur concomitant with other binding mechanisms like intercalation and groove binding.[19a] However, in the physiological environment, the DNA double helix is stabilized by cations, for instance metal ions, which form a counterionic shell around the negative charge density on the nucleic acids. This phenomenon was already described in 1970s as counterion condensation.[23] The condensation has the purpose to neutralize the overall negative charge of DNA. The interaction of binding molecules with DNA leads to a release of the condensed ions which has a positive entropical contribution to the binding free energy and a significant influence on the binding affinity of cationic ligands. Thus, positively charged molecules, such as proteins, which bind by a binding mode other than the external binding additionally benefit from electrostatic interaction resulting in increased binding strength. But this also means that the melting temperature, which will be explained in section 1.4.1, and the binding constants are strongly dependent on the salt concentration in the applied media.[23c] Electrostatic interactions are often non-specific and may be difficult to follow spectroscopically. Nevertheless, there are examples of molecules which are known to interact with DNA by electrostatic interactions. For instance, polyamines like spermine and spermidine bind to DNA by electrostatic interactions (see Figure 5 for structure of natural polyamines).[24] These polyamines exhibit several functions in the cellular environment like DNA packaging into chromatin as well as neutralization of charges in histones. [25]

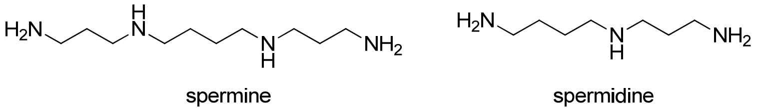

Figure 5: Structure of the natural polyamines spermine and spermidine.

1.3.2 Intercalation

Insertion of planar aromatic polycyclic molecules[26] between the base pairs is termed intercalation (see Figure 4b for schematic representation and Figure 6 for structural examples).[27] Classical intercalators are often inserted with their whole aromatic core between the base pairs (for instance ethidium bromide[28], see Figure 6). Molecules with additional bulky side chains or interacting units located in the grooves of DNA are threading intercalators[29] (for instance nogalamycin,[30] Figure 6). Further examples are naphthalene diimide derivatives, which are known to intercalate and interact with the major grooves of DNA by positively charged side chains[31] as well as several metal intercalators which can interact by both coordination to functional groups of DNA and intercalation of the aromatic ligands attached to the metal core .[32]

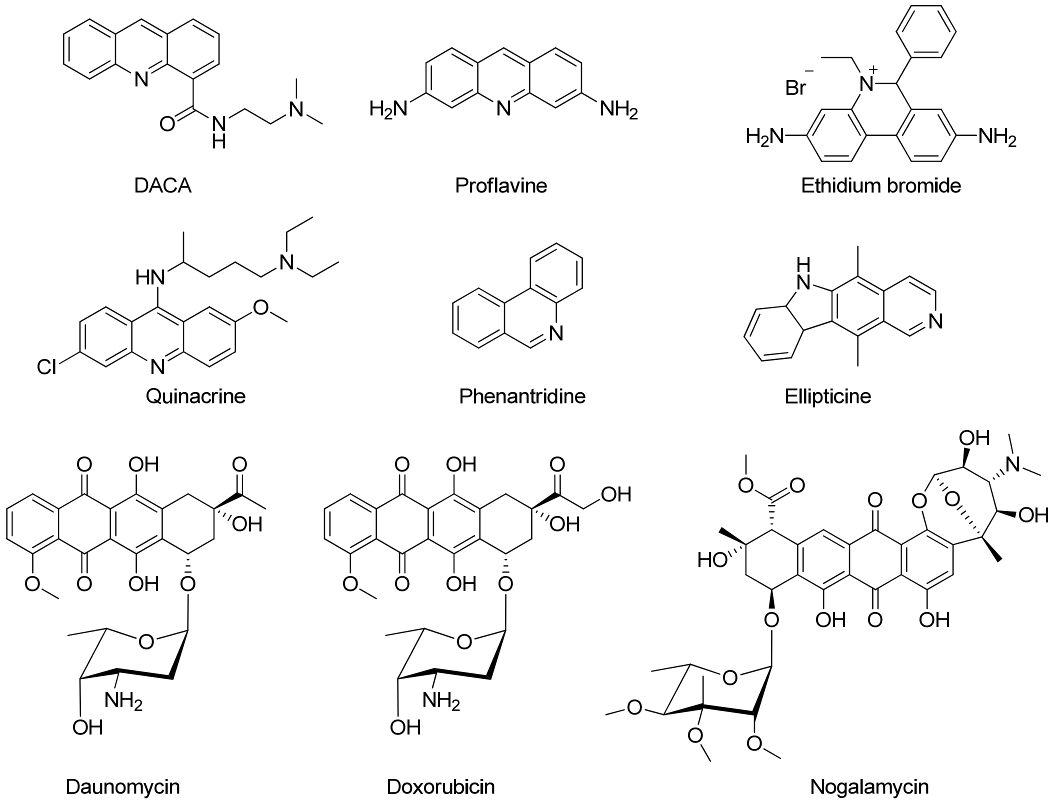

Figure 6: Examples for intercalating molecules.[26]

An important driving force for successful intercalation is the transfer of a hydrophobic ligand molecule from aqueous media into the hydrophobic site of DNA in which π-π-stacking interactions can take place.[33] Additionally, the hydration shell around the ligand is dissolved resulting in an entropically favorable release of surrounding water molecules of the ligand. Intercalation of ligand molecules results in significant conformational changes of the DNA double helix. The base pairs have to separate by 3.4 Å to provide a large enough cavity for insertion of the incoming molecule. Often, the intercalating molecules have positive charges in the side chains or the aromatic core which could contribute to binding by electrostatic interactions with negatively charged DNA backbone. In addition, the lengthening and unwinding of the helix increase the distance between phosphates leading to a decrease of the charge density along the double helix which has an additional positive entropic impact.[34]

Furthermore, favorable interactions between the frontier orbitals, the lowest unoccupied molecular orbital (LUMO) of the intercalating molecule and the highest occupied molecular orbital (HOMO) of the adjacent purine bases seem to stabilize the intercalation complex shown in studies of complexes of phenanthridinium cations (for instance, ethidium bromide, see Figure 6) and DNA.[28] Bathochromic shifts in the absorption spectra of the intercalation complexes originate from these orbital interactions (see section 1.2.1).

Molecules can be incorporated by their long axis parallel or perpendicular to the binding pocket between the base pairs which often results in different spectroscopic responses, especially in circular dichroism spectra which will be discussed later in this chapter. For instance, the antitumor anthracycline derivative nogalamycin (Figure 6) is intercalated perpendicular to the helix axis, as illustrated in the crystal structure in Figure 7, left. The nogalamycin sugar substituents are located in both grooves of the DNA in which hydrogen bonds are formed for stabilization.[35] In contrast to nogalamycin, the antitumor agent *N*-(2-(dimethylamino)ethyl)acridine-4-carboxamide[36] (DACA, Figure 7, middle) and the natural anticancer plant product ellipticine[37] (Figure 7, right) are intercalated in a parallel fashion into DNA. The side chain of DACA molecules is facing the groove causing stabilization by the formed hydrogen bonds which is not the case for ellipticine although the pyridine nitrogen is pointing to the groove of the DNA (see crystal structures of the complexes in Figure 7).

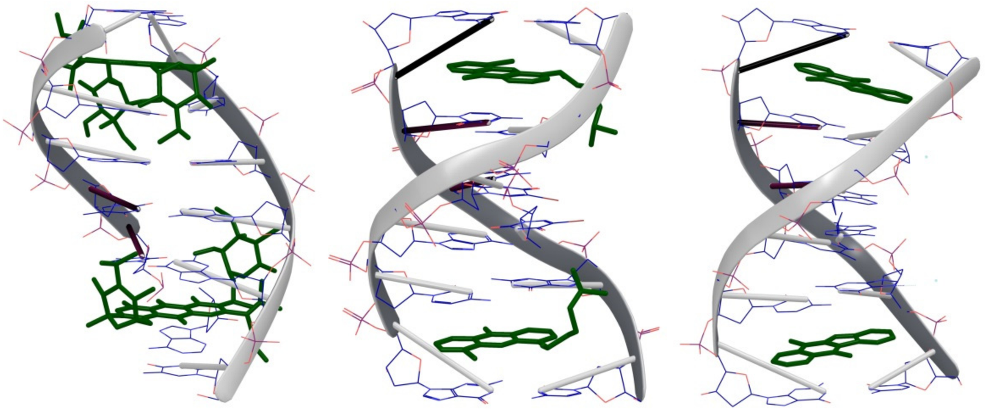

Figure 7: Crystal structures of three molecules intercalation into DNA. Nogalamycin[35] (left, PDB access code 182D), *N*-(2-(dimethylamino)ethyl)acridine-4-carboxamide[36] (DACA, middle, PDB access code 367D) and ellipticine[37] (right, PDB access code 1Z3F). All images were drawn with MacroModel.

It is important to note that the binding constants of intercalation (10^4 to 10^6 M^{-1}) are in general significantly lower than those of groove binding (10^5 to 10^9 M^{-1}) which can be influenced by multiple binding modes or additional intercalating motives. After the intercalation of one ligand molecule, no second insertion of a second molecule in close vicinity takes place which is called ‘neighbor exclusion principle’.[38] This phenomenon is of importance in the design of bis-, tris- and tetraintercalators because the connecting spacer chain has to be of appropriate length to ensure multiple intercalations. Further information concerning multiple intercalators can be found in the corresponding literature.[16]

1.3.3 Groove Binding

Binding molecules can be distinguished whether they bind into the major or the minor groove of the DNA double helix. Proteins of α-helical form are known to interact primarily with the major groove of DNA via hydrogen bonding, hydrophobic and van der Waals interactions. Mainly because, the major groove provides required shape and space variations and great amount of donor and acceptor groups for the formation of hydrogen bonds. Amino acids involved in the major groove binding are often arginine, histidine, lysine, serine, asparagine, glutamine and glutamate. But, it is not easy to predict which side chains of the amino acids interact with which base because hydrogen bonds can be formed between two stacked base pairs or even through bridging water molecules between the protein surface and DNA groove.[39] For this reason, the design of synthetic proteins for groove binding is challenging.[19a] Another examples for major groove binders are oligonucleotides, which form Hoogsteen and reversed Hoogsteen hydrogen bonds[40] in the groove of DNA leading to the formation of triplex DNA which is only possible for double-stranded DNA with purine base (A or G) rich regions. Oligonucleotides are not selective groove binders but there are examples for oligonucleotide analogues which were used in clinical experiments.[41]

Major and minor grooves differ not only in their size, but also in the electrostatic potential, hydrogen bonding motifs, steric demand and hydration. Synthetic molecules, in contrast to proteins and oligonucleotides, bind preferentially into the minor groove, mainly due to their size. Of significant importance is the chemical structure of minor groove binders. Most of them consist of aromatic rings which are connected by rotational bonds allowing the molecule to bend in an optimal crescent shape for fitting perfectly into the groove (see Figure 8 for examples).[42]

To avoid the sterical hindrance because of the 2-aminoguanine moiety, many molecules bind preferentially into minor grooves with AT-rich areas compared to GC including grooves and exhibit selectivity for B- over the A-form of DNA and RNA.[43] However, some groove binders are known in the literature which preferentially bind to GC base pairs rich regions.[44] Although hydrogen bonding and hydrophobic interactions are important driving forces for binding, groove binders often possess additional cationic units interacting with the negative charges of the DNA backbone which contribute largely to the binding strength.

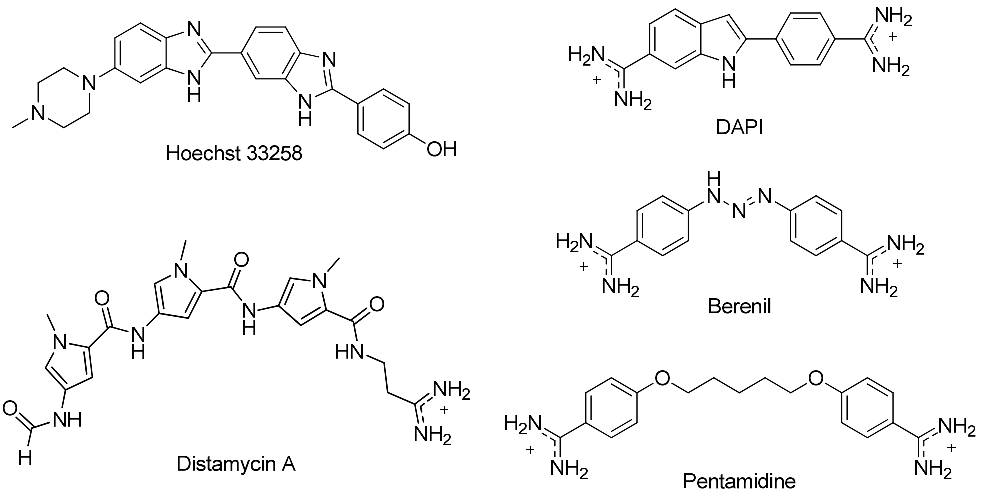

Figure 8: Examples for groove binding molecules.[19a]

Moreover, the unfavorable hydration displacement is compensated by Van der Waals and hydrophobic interactions.[45] Generally, the interactions of inserted molecules in the grooves do not cause a pronounced conformational change of the double helix as it is the case for intercalated molecules.

Similar to the intercalating molecules, groove binders like the natural distamycin, the synthetic diarylamidines (4',6-diamidino-2-phenylindole (DAPI), berenil, pentamidine) and bis-benzimidazoles (such as Hoechst 33258) often have an important clinical application (Figure 8).[42b, 46] DAPI was previously used as an anti-parasitic agent, but nowadays a more common application is as fluorescent staining molecule for DNA because of its easy transport into the cell. It binds readily to AT-rich regions of the minor groove because of the larger space originating from the absence of the guanine NH_2 group. The phenyl and the indole rings lie parallel to the groove walls and expand across the base pair sequences such as ATT. The nitrogen of the indole ring forms a forked hydrogen bond to the O2 (see Figure 2) of the two thymine bases. Additionally, the positively charged amidine groups at the end of DAPI molecule establish hydrogen bonds to the adenine N2 (Figure 2), thus, these electrostatic interactions contribute positively to the binding strength of DAPI to DNA (Figure 9, left).[47] Another prominent groove binder is

Hoechst 33258 (Figure 9, right). The molecule, which is widely used as a staining agent, readily enters the cell and binds strongly to the minor groove of DNA with AT-rich areas. The NH groups of the benzimidazoles form bridging hydrogen bonds between adenine and thymine. By the crescent structure of the molecule, it is able to span over four to five base pairs.[48]

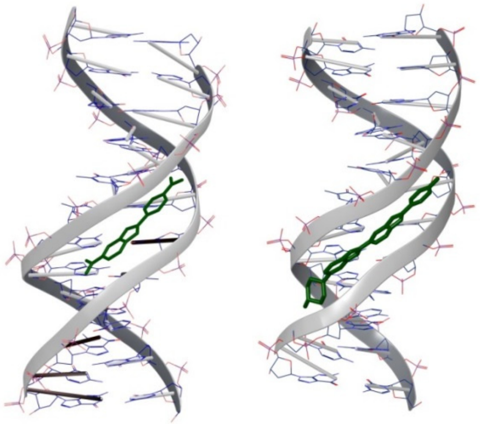

Figure 9: Crystal structure of 4',6-diamidino-2-phenylindole[47] (left, (DAPI), PDB access code 1D30) and Hoechst 33258[48] (right, PDB access code 8BNA).[48] All images were drawn with MacroModel.

1.4 Determination of interaction

The right choice of the method or at least a combination of methods is essential for the determination of the interaction of a small molecule with DNA. Moreover, the binding modes have to be distinguishable by the applied technique. Although, X-ray diffraction analysis provides the most convincing information on the type of interaction, it is challenging to grow required single crystals of DNA molecules containing a bound ligand. It is to note that an ensemble of techniques is necessary to evaluate the kind of interaction between the ligand and DNA.[49] Here, the focus lies on optical methods used for the determination of the interactions of small molecules with DNA. Other methods like footprinting,[44, 50] large number of assays[51], electrochemical methods (for instance cyclic voltammetry),[52] calorimetry,[53] dialysis,[54] atomic force microscopy,[55] just to name some of them, are described extensively in the literature. UV/Vis and florescence spectroscopy as well as circular dichroism are the most important optical methods and therefore will be described in details in the following sections.

1.4.1 UV/Vis absorption spectroscopy

Ultraviolet-visible (UV/Vis) absorption spectroscopy is probably the most simple but, nevertheless, a very useful technique to obtain information on the stability of DNA/ligand complexes as well as the mode of interaction. The UV/Vis absorption spectrum of DNA displays a broad band in the range of 200 to 300 nm with a maximum at 253 – 270 nm and an extinction coefficient of 6000 – 9000 M^{-1} cm^{-1} per base which allows the determination of the concentration of DNA as concentration of bases by measuring the absorbance.[56] This absorption originates from complex electronic transitions in the purine and pyrimidine moieties.[57] Changes of the environment like pH or ionic strength variations can result in changes on the position and intensity of the DNA absorption which has to be considered in the investigations of the ligand binding. To evaluate if interactions of a molecule with DNA take place, monitoring of the melting temperature can be used where the fact is exploited that the single stands (ss) of the DNA have higher absorbance than the double strand (ds) of the same DNA molecule. This observation is attributed to the hypochromic effect (decrease of the absorbance) which occurs by the stacking of the base pairs in the double strand.[58] The separation of DNA into single strands can be achieved by treating it with denaturing agents or by the gradual increase of temperature. The simultaneous record of the absorbance with increasing temperature the characteristic melting temperature (T_m) of the applied DNA can be detected which is defined as the temperature value corresponding to the transformation of 50% of the double strands into single strands. This value depends on the sequence, pH and the ionic strength in the solution as well as the origin of the DNA. The point of inflection in the absorbance/temperature plot at the absorption wavelength of DNA (260 nm) corresponds to the transition of 50% of the ds-DNA into ss-DNA (see Figure 10, left).

The melting temperature value of DNA/ligand complex is shifted to higher temperature in comparison to the value of the free DNA molecule if stabilizing interaction takes place which provides the first indication whether interactions of ligand with DNA are present.[59]

Additionally, the interactions of a ligand with DNA are studied by the comparison of the absorption spectrum of the free ligand with the one of DNA/ligand complex which shows a visible shift of the maximum (see Figure 10, right). In the case of intercalation, usually hypochromic (decrease of band intensity) and bathochromic (shift to longer wavelengths) effects occur upon binding which is attributed to the π-π interactions between the aromatic chromophore and base pairs of DNA. Upon the interaction, the π electrons of the ligand and the ones of the DNA bases are combined which decreases the energetic level of the π-π* electron transition leading to the bathochromic shift. [52b, 56, 60]

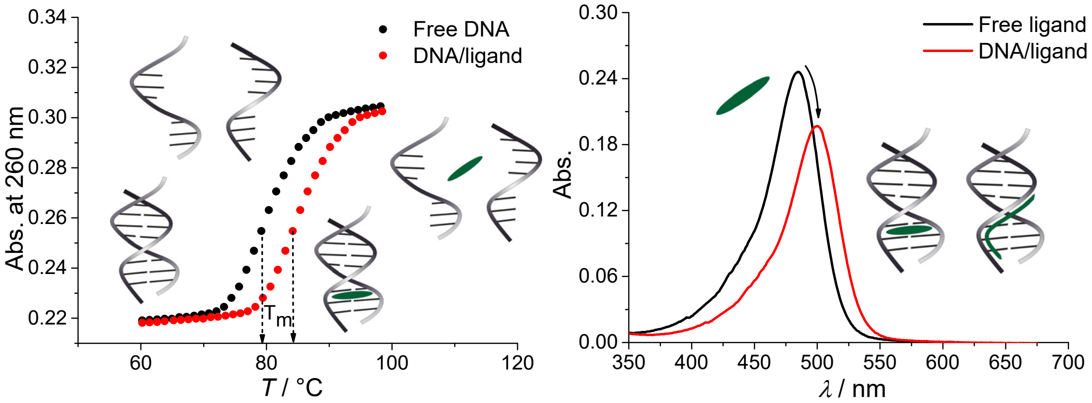

Figure 10: Representative illustration of the thermal denaturation curves with the corresponding melting temperatures (T_m) of free DNA and DNA ligand complex for the case of intercalation (left, Figure adopted from previous report[17a], (Reproduced and adopted with permission from Elsevier, Copyright (2016)). Expected UV/Vis absorption spectra of free ligand and DNA/ligand complex upon intercalation or groove binding. [61] (Reproduced and adopted with permission from Taylor & Francis, Copyright (2016)).

Additionally, the hydrophobic environment in the binding pocket of DNA can lead to the red shift of the absorbance of the ligand. In contrast to groove binding which results in similar or weaker observations in the UV/Vis absorption spectrum as in the case of intercalation, external binding sometimes leads to a hypsochromic shift.[61] Furthermore, a hyperchromic effect in the absorption region of DNA (increase of absorbance) can be observed upon external binding which is correlated to conformational and structural changes of DNA after the DNA/ligand complex formation. This phenomenon corresponds to the interaction of charged molecules with the negative phosphate backbone of DNA resulting in a contraction and overall disruption of the secondary structure of the helix.[62]

Binding constants for the DNA-ligand association process were determined using several models, the most used being Scatchard,[63] or its McGhee and von Hippel formalism,[38] or Benesi and Hildebrand.[64] These models use different assumptions and simplifications but are sufficiently applicable depending on the considered system. The derivation, variations and progressions of the available models are described in details in the literature and are not part of this work.[65]

1.4.2 Viscosity measurements

UV/Vis absorption measurements and other optical methods may not provide sufficient indication on the binding mode of a small molecule with DNA. Hydrodynamic methods such as viscosity measurements represent a technique for the study of interaction because it is sensitive to changes of the DNA molecule length in solution. The intercalative binding mode of a ligand molecule to DNA provokes a lengthening of the DNA helix since the income of a binding molecule causes a separation of the base pairs in order to accommodate the molecule which results in an increase of the DNA viscosity. In contrast to intercalation, electrostatic interaction induces aggregation of DNA molecules which leads to a decreased viscosity due to reduction of the freedom of motion of DNA. The same is observed for groove binding since this binding mode causes a bent or loop of the helix which reduces the length of the helix.[31, 66]

In the viscosity measurement the flow time of the sample solutions is determined after thermal equilibrium is reached. The relative viscosity is calculated by the equation $\eta \sim (t - t_0)/t$, where t and t_0 are the flow times of the sample solution and pure solvent, respectively. Commonly, the data are expressed as $(\eta/\eta_0)^{1/3}$ against DNA/ligand ratio, where η_0 is the viscosity of pure DNA and η the one of DNA/ligand complex.[52c] The obtained results can be confirmed by control experiments in which known intercalators such as ethidium bromide are measured for comparison.[67] Viscosity measurements are often combined with optical or microscopic techniques to receive a comprehensive understanding of the binding mode.[55, 68]

1.4.3 Fluorescence spectroscopy

Nucleotides are at room temperature almost non-fluorescent, nevertheless, fluorescence spectroscopy is a useful method to explore DNA/ligand interactions for fluorescent ligands providing important information on the binding mode and constants as well as orientation and localization of the ligand within the DNA.[57] While the latter is studied by fluorescence anisotropy and fluorescence resonance energy transfer (FRET),[59] additional information regarding the position of the binding molecule can be obtained from quenching experiments. The fluorescence quenching can have reasons like molecular rearrangements, energy transfer, and complex formation or excited state reactions and is described by the Stern-Volmer equation.[69] The quenching experiments with known quenchers, such as halide ions, provide useful information about the binding of a ligand to DNA. The groove binders are stronger affected by quenchers than intercalators due to hindered accessibility of the ligand by the quencher and protective repulsion of the phosphate backbone with the negatively charged quenching molecule. Owning to these reasons, the intercalating molecules exhibit lower Stern-Volmer quenching constant (K_{SV}).[59]

However, the simple prediction of the emission properties of the DNA-ligand complex is difficult to make. The observed signals have to be interpreted depending on the observed system.

1.4.4 Circular and linear dichroism

Measurement of differential absorption of right- and left-handed circularly polarized light is defined as circular dichroism (CD) spectroscopy. It provides important information on the orientation of the binding molecule within the DNA. In addition, conformational changes upon binding of small molecules to DNA can be assessed by the changes of the obtained signals. Achiral molecules do not exhibit any CD signal. However, upon binding to DNA induced CD (ICD) signals can occur, giving hints for the alignment of the bound molecule within DNA. This is a significant advantage compared to the UV/Vis absorption experiments which display signals of all kind of species, whether bound or unbound. Additionally, the binding of a ligand to DNA can provoke conformational changes of the double helix. Thus, the characteristic signals of DNA in the UV region can be approached for further information of the binding mode and strength.

For intercalation, a general model was developed which predicts the orientation of the binding molecule relative to the fixed axis of DNA in which all sites have equal presumption toward binding.[70] The sign of a ICD signal is a product of two terms in which the first term is solely dependent on the properties of the polynucleotide alone, hence, it is not supposed to change and was empirically found to be negative for DNA. The second term is a function of the orientation of the adduct transition relative to the polynucleotide structure. The schematic illustration of an intercalated molecule between the base pairs is shown in Figure 11.

The xyZ is the coordinate system of the polynucleotide. The Z axis is the direction of the helix and the base pairs are located on the plane perpendicular to this axis. The x axis lies along the sector connecting the two ribose units and y axis is perpendicular to it. The intercalated molecule is placed on the plane parallel to that of the base pairs. The position of the ligand is given by the angle φ. The moment of the ligand can change along the directions X and Y which induce CD signals of different signs. This means that the signals are negative in X direction and positive in Y direction by taking into account the negative signal for DNA (see Figure 12a).[70]

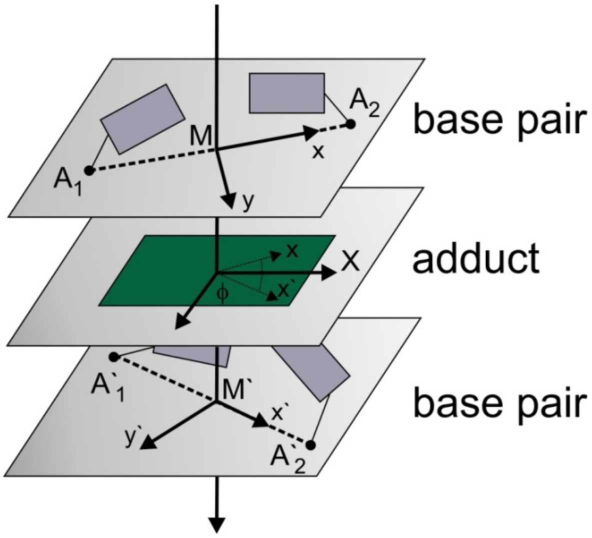

Figure 11: Definition of the coordination system of an intercalation polynucleotide/ligand complex. xyZ and XYZ are the axis of the base pairs and ligand, respectively, with A_1 and A_2 as ribose units and M as their midpoint. The scheme is based on a report from Schipper *et al.* (Reproduced and adopted with permission from Elsevier, Copyright (2016)). [70]

This model is just an approximate approach to explain the occurring ICD signals but can offer information on the orientation of the binding molecule. At this point, it should be noted that exciton coupling of self-stacked dyes in close vicinity would give both positive and negative signals.[61] The changes of the ICD signals of the polynucleotides in the UV region are sometimes evaluated as indications for particular interaction mode. This analysis of the signals is often difficult to correlate to DNA signals because the intercalating molecule often shows transitions in the same absorption region. Thus, the interpretation of the ICD signals in the DNA absorption region can only be qualitative.[61]

In the case of groove binding, the position of the bound molecule can not be easily assessed as described above. The position between the DNA helix and the transition moment of the ligand is characterized by the distance of the moment from the helix and the angle between the distance and the helix axis. The direction of the transition moment is limited by two angles, the one between the transition moment and the helix axis and the other between the projection of the transition moment on the plane perpendicular to the helix axis and the distance vector. Moreover, the induced CD signals can depend on the binding pocket. Often, the bound molecule in the groove own higher degree of freedom than the intercalated ligand which increases the number of possible positions and orientations of the ligand in the groove. Furthermore, in contrast to intercalation where ICD signals are much lower than 10 $\Delta\varepsilon/M^{-1}$ cm^{-1}, for groove binding the values are often higher and of positive sign, probably because groove binders have contacts to larger part of the DNA (see Figure 12b).[61]

In contrast to CD, linear dichroism (LD) uses light polarized parallel and perpendicular to the macroscopic orientation axis. By this method, the angle between the transition dipole moment of the complex and polynucleotide helix axis can be determined. The long polynucleotides are oriented by a flow or an electric field, which orient the bound molecule as well and lead to specific LD signals.[71]

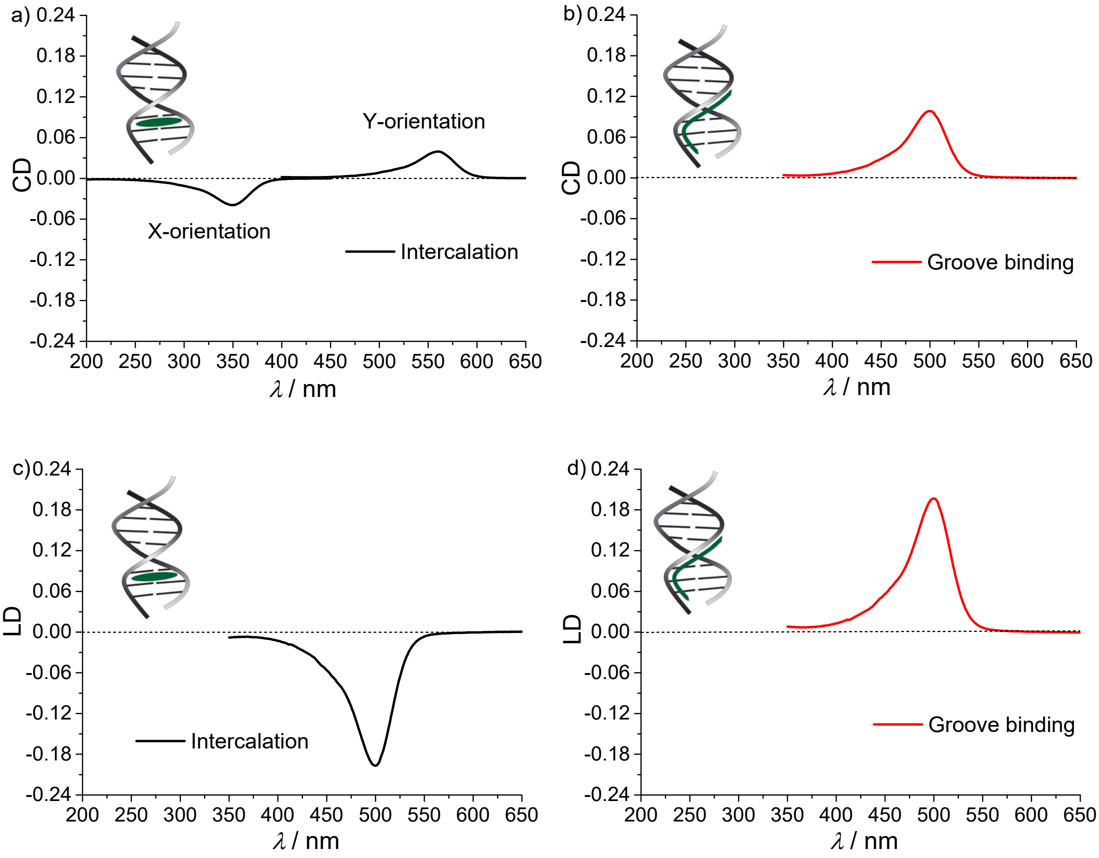

Figure 12: Schematic presentation of the expected CD and LD signals for the intercalation and groove binding of small molecule to DNA. The scheme is based on a review of Biver (Reproduced and adopted with permission from Taylor & Francis, Copyright (2016).)[61]

The orientation of the ligand relative to the helix axis is translated into LD signals, which means a 90° angle is indicative for an intercalative binding mode. Due to the fact that achiral molecules do not show any LD signals and the signals of the polynucleotides are displayed in the UV region, the observed LD signals in the chromophore absorption region are indicative for the particular binding mode. Furthermore, DNA of B-type conformation shows negative LD signals. Correspondingly, the negative long wavelength band of the interacting ligand, which is slightly bathochromically shifted, is typical for intercalation (see Figure 12c). [71]

For the determination of the orientation of a groove binding molecule within the DNA by using LD spectroscopy, the polarization axis of the dye has to be known. Often, groove binders with elongated aromatic systems have transitions dipoles which are polarized along the long axis, thus, they lie along the groove. Typically, this leads to LD signals of positive sign (see Figure 12d). Similar to intercalation, the LD signals reflect those of absorption and are slightly red shifted in comparison to the free ligand.[61]

The spectroscopic features of externally bound molecules are less informative. The LD and CD spectra give no rise to significant changes upon electrostatic binding of a ligand when no structural or conformational changes of the polynucleotide occur. Therefore, this mode of binding won't be discussed in detail.

When ligand molecules are bound as dimers to DNA the absorption spectra are generally different compared to monomers resulting in exciton coupling between the dyes. The LD and CD exciton spectra may provide information about the orientation of such dimers. If the dimer is chiral, which is the case when they are formed in the chiral DNA molecule, the CD spectrum shows a typical bisignate CD signal (one positive and one negative CD band). Therefore, different parameters, for instance, magnitude of CD and interaction energy can be calculated. And, LD can also be used for determination of angles between the helix axis and the two transition moments.[71]

1.5 Interaction of supramolecular nanosystems with DNA

The above mentioned examples of molecules which interact with DNA by intercalation or groove binding mostly form complexes by insertion of a single molecule. Supramolecular nanosystems which are based on aggregates in solution may interact with the biomacromolecule as well. Here, DNA may act as a template and change evident spectroscopic properties of the interacting ligands. On the other hand, the function of the DNA molecule may change as well. In the following sections, some examples are presented for ligand molecules interacting with DNA as aggregated molecules in the groove of the DNA.

1.5.1 Distamycin A and polyamides

One of the molecules interacting as a supramolecular complex with DNA is the pyrrole-amidine antibiotic distamycin A (see Figure 8). This drug binds preferably to AT-rich minor grooves of DNA rather than GC-rich sequences. The X-ray crystal structure of the 1:1 complex of distamycin/DNA revealed a tight binding of the crescent molecule to the minor groove.[72] Later, NMR studies of the interactions of distamycin with DNA possessed that the ligand binds as an antiparallel dimer into the minor groove.[73] The 2D NMR studies confirmed that at ratios about 2 equiv., the binding of two ligand molecules is preferred over the 1:1 complex. Additionally, molecular modelling indicated that the minor groove has to expand for the accommodation of the dimeric distamycin A. The responsible forces for this complex formation could be identified as electrostatic interactions as well as hydrogen bonding between the ligands and DNA. Moreover, the ligand-ligand and ligand-DNA stacking interactions have a significant contribution to the complex stabilization. In the late 90ties the single crystal structure of the 2:1 complex of distamycin and DNA octamer $d(GTATATAC)_2$ was published which illustrates well the stacked dimer in the minor groove (see Figure 13).[74]

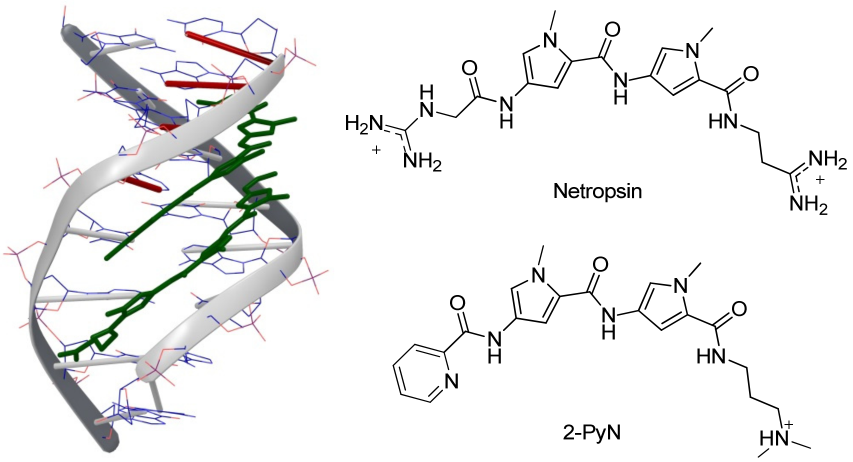

Figure 13: Crystal structure of distamycin A and $d(GTATATAC)_2$ complex (left, PDB 378D).[74] Structures of Netropsin and pyridine-2-carboxamide-netropsin (2-PyN, right). The image of DNA/distamycin A complex was drawn with MacroModel.

Analogues to the natural products distamycin A and netropsin (for structure see Figure 13) which have different aromatic rings connected by peptide bonds are known to bind specifically to the minor groove. A replacement of the pyrrole ring, for instance by 1-methylimidazole or pyridine, change the recognition properties of the binding molecule. The polypeptide pyridine-2-carboxamide-netropsin (2-PyN, see Figure 13) binds specifically the five base pair sequence TGTCA by forming an antiparallel dimer in the minor groove of the ds-DNA. Additionally, the affinity and the binding constants could be enhanced by covalent linkage of two 2-PyN molecules by the introduction of alkyl spacers.[75] Moreover, the introduction of a modified pyrrole ring, for instance 1-methyl-3-hydroxy-pyrole, in various position of the ligand molecule resulted in consequent structural recognition of TA instead of AT sequences. The specific recognition of TA base pairs could be attributed to distinct hydrogen bonds between the base pairs and the dimeric binding molecule.[76]

Many other polypeptide molecules, which contain various heterocyclic aromatic rings like indoles, furans or benzimidazoles showed binding to minor groove of ds-DNA by insertion of dimers into the binding pocket. GC base pair recognition is rare, however, was also observable.[77]

1.5.2 Cyanine dyes

Cyanine dyes contain typically two nitrogen-containing heterocycles and are connected by a polymethine bridge of different length which specifies the absorption and emission properties of the dyes. The various structural features allow the application of these chromophores as intercalators[78] as well as groove binders.[79] Moreover, several cyanine dyes are known to change their binding mode depending on the sequences of the applied DNA molecules.[80]

More interesting for this thesis is the interaction of π-stacked cyanine dye aggregates with DNA. For this purpose, cyanine dyes are appropriate molecules as they tend to aggregate in aqueous solution because of their hydrophobic and polarizable character. In the UV/Vis titration experiments of dicarbocyanine dye DiSC$_2$(5) (see Figure 14a for the structure) and poly(dA-dT)$_2$ the formation of H-type aggregates of the cyanine dyes templated by the polynucleotide was observed (see Figure 14b).[81] The binding of aggregates in the minor groove of DNA is driven by van der Waals interactions and the hydrophobic effect. Interestingly, homopolynucleotide of AT bases and the alternating GC polynucleotide didn’t template the aggregate formation. In contrast, replacing of the guanine base by inosine (I) even promoted the aggregate formation of DiSC$_2$(5) in the minor groove of IC base pair sequences. These observations were attributed to different reasons. The AT homopolynucleotide favors the binding of monomeric molecules rather than dimers due to the particularly narrow minor groove. The steric hindrance of the amino group of guanine obviously prevents the favorable van der Waals interactions between the binding molecules in the groove of GC rich sequences. This steric demand is evidently not present in IC rich grooves which favors the binding of DiSC$_2$(5) aggregates. Comparative experiments with AT polynucleotides of various lengths revealed that DiSC$_2$(5) binds as a face to face dimer to 5 AT base pairs (AT-5) which was illustrated by molecular modelling studies (see Figure 14c for schematic illustration). Furthermore, when the length of the polynucleotide is twice as long (AT-10), DiSC$_2$(5) forms two dimers aligned in an end to end fashion in the minor groove (see Figure 14c). CD experiments exhibited splitting of the CD signal of DiSC$_2$(5) in the presence of AT-5 and poly(dA-dT)$_2$ resulting in a pronounced Cotton effect due to the electronically coupled dyes which were bound in a right-handed conformation in the minor groove of DNA (see Figure 14c and Figure 14d).

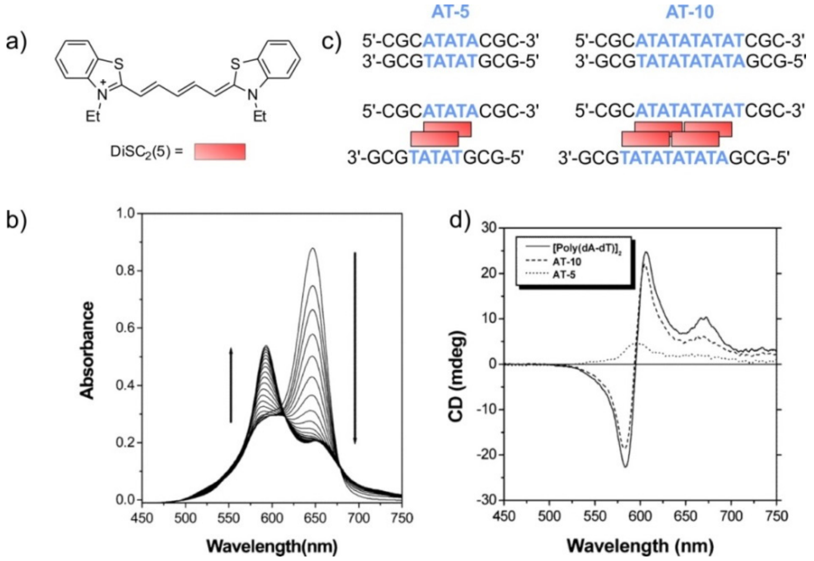

Figure 14: a) Structure of 3,3'-diethyldithiacarbodicyanine (DiSC$_2$(5)). b) Changes of UV/Vis absorption spectra of DiSC$_2$(5) upon addition of poly(dA-dT)$_2$ in an aqueous solution. Arrows indicate spectral changes upon increasing DNA concentration. c) Schematic illustration of the DNA-templated assembly of DiSC$_2$(5) dimers in AT-rich sequences. Binding sites are shown in blue. d) CD spectra of DiSC$_2$(5) in the presence of poly(dA-dT)$_2$ and polynucleotides containing 5 (AT-5) and 10 AT (AT-10) base pairs.[82] (Reproduced and adopted with permission from American Chemical Society Copyright (2016)).

In contrast, binding of a single DiSC$_2$(5) dimer to AT-5 provoked only a weak positive CD signal. These dimeric aggregates of DiSC$_2$(5) have to be of defined structure with quite rigid conformation because the UV/Vis absorption spectra of the bound dimers revealed a narrow transition band compared to the aggregates formed in aqueous solution. In an aggregate of indefinite size with random structure a broadening of the absorption band would be visible. Furthermore, the binding of DiSC$_2$(5) dimers is cooperative which means binding of the second dimer is favored leading to beneficial van der Waals interactions which was confirmed by additional CD experiments. The binding of the second dimer is enabled by the widening of the minor groove for the first dimer molecule facilitating the interactions of the two dimers.[82]

Structural variations of the heterocyclic rings as well as the length of the polymethine chain change the binding affinity of the dimer aggregates to DNA. Cyanine dyes with shorter polymethine chain were preferentially bound than those with longer chains because the twisting of the polymethine chain, which is needed for the groove binding, is prevented the longer the chain becomes. Additionally, the cyanine dyes with more hydrophobic heterocycles form dimers more effectively in the groove of DNA. The introduction of positively charged groups or sterical hindrance can induce the formation of J-aggregates of cyanine dyes in the binding pocket of DNA which opens additional application possibilities for cyanine aggregates.[83]

1.5.3 Perylene bisimide dyes

Beside the cyanine dyes, other dyes with extended aromatic π-systems, for instance perylene bisimide (PBI) dyes, were applied to target DNA. Mostly, PBI dyes were either covalently bound to DNA[84] or their interaction with G-quadruplexes was studied.[85] The reports of non-covalent binding of PBI dyes to ds-DNA are rare. Nevertheless, two examples will be presented in which, in particular, groove binding of PBI dyes is explored.

Several PBI dyes appended with polyamine chains of different length and number of positive charges were investigated on their interaction with ds-DNA and G-quadruplexes in a comparative manner.[86] Techniques like UV/Vis absorption and CD spectroscopy as well as various FRET based assays were used to determine the interaction of the dyes with the two DNA structures. The interaction of PBI dyes POL-3, POL-4 and POL-8 with DNA were analyzed by UV/Vis and CD titration experiments as they showed highest selectivity in comparison to the other applied PBI dyes (see Figure 15). The absorption spectra of the dyes alone in the MES/KCl buffer solution exhibit broad signatures which are characteristic for PBI dyes in aqueous media. Upon addition of ds-DNA or G-quadruplex DNA to each of the PBI molecules a bathochromic shift and a vibronic structure of mostly monomeric chromophore was observed.

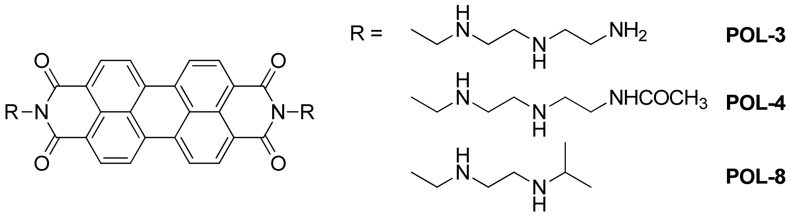

Figure 15: Structures of the PBI derivatives POL-3, POL-4 and POL-8.[86]

The absence of isosbestic points indicates a complex equilibrium situation which includes more than two species existing in solution. Further information was provided by CD spectroscopy which showed differences in the signal features depending on the applied DNA structure (see Figure 16). The CD signals of all applied PBI molecules displayed positive CD signals after the addition of G-quadruplex solution Figure 16a). Furthermore, the shape of the signals was similar to those of UV/Vis absorption spectra which was interpreted as strong coupling of the dyes with the terminal G-quartet of the G-quadruplex DNA. The CD signals of POL-4 were of weaker intensity compared to POL-3 and POL-8 which pointed to lower binding constant of POL-4 toward G-quadruplexes. In contrast to the results obtained for the interaction of PBI dyes and G-quadruplexes, the CD signals of PBI molecules showed bisignate Cotton effects after the addition of ds-DNA (see Figure 16b). These CD spectroscopic features suggest that the dyes are arranged as excitonically coupled aggregates in the groove of DNA. The arrangements of PBI dyes on the top of G-quadruplex as well as in the groove of ds-DNA are illustrated in the molecular models in Figure 16c. In the complex of POL-3 with G-quadruplex DNA, the PBI molecule interacts by π-π-stacking with the G-quartet. The stoichiometry of the complex is 1:1 or 2:1 in which the monomeric PBI molecule is located on the terminal G-quartets of the G-quadruplex DNA which reflects the obtained CD signals (see Figure 16c, C). The side chains of the PBI molecules point into the groove of the G-quadruplex DNA and form hydrogen bonds to the phosphate groups. In this particular study, the strength of the interaction is probably dependent of the number of positive charges in the side chains of the PBI molecules. But, structural and conformational differences of G-quadruplexes have to be considered for further investigations as well.

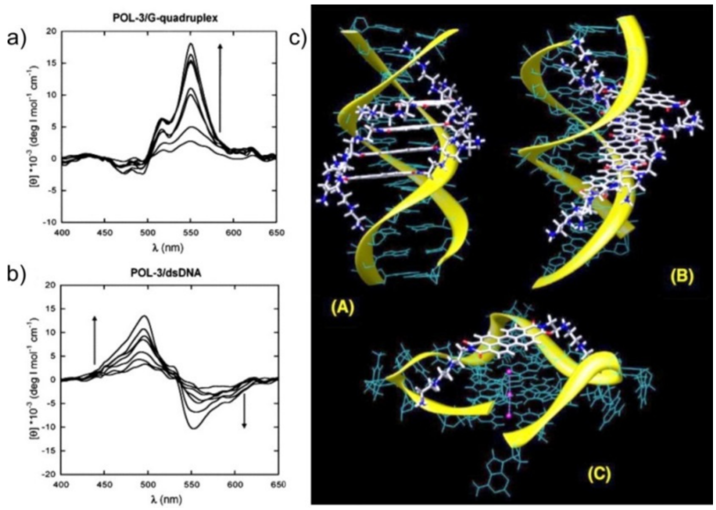

Figure 16: CD spectra of POL-3 (c = 2 x 10^{-5} M) in the presence of G-quadruplex DNA (a) and ds-DNA (b) at increasing DNA/POL-3 molar ratio (r = 0.5, 1, 2, 4, 8, 12, 15, and 20) in MES/KCl buffer. c) Representative models of POL-3 with ds-DNA (A and B) and G-quadruplex DNA (C).[86] (Reproduced and adopted with permission from Elsevier, Copyright (2016)).

The model for the complex of the POL-3 and ds-DNA represents the excitonically coupled PBI molecules (at least two) in the major groove of the DNA helix which agrees with the obtained bisignate CD signals (see Figure 16c, A and B). The authors suggest that the interaction of the PBI molecules with ds-DNA is rather weak because the charged side chains do not have many contacts to the phosphate groups in the grooves.

Because the focus of the given studies was on G-quartet binding, groove binding was treated quite superficial. A more comprehensive study on the interaction of PBI molecules with DNA trough groove binding was provided by Würthner, Piantanida and coworkers.[87] They synthesized two enantiomeric PBI molecules **L-5** and **D-5** which were functionalized with L- and D-alanine and connected to spermine chains through amide bonds (see Figure 17).

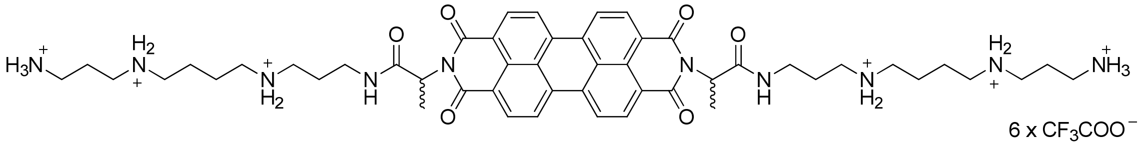

L-5 or **D-5**

Figure 17: Structures of PBIs **L-5** and **D-5**.

The self-assembly properties of the chiral PBI dyes in aqueous solution were strongly dependent on the concentration. In the concentration-dependent UV/Vis absorption studies a transition from monomeric to aggregated species was displayed. The aggregation behavior was attributed to the formation of dimers and subsequent growth to extended aggregates upon increasing concentration which has already been observed for similar spermine functionalized PBI dyes before.[88] But it has been noted that the dimerization is more favored than the formation of larger aggregates due to the repulsion of positively charged spermine chains and sterical hindrance of the methyl groups of the amino acids. Additionally, the CD spectroscopic studies revealed strong bisignate CD signals for the concentrated solutions of the PBI molecules confirming the presence of the helical π-stacks with *P*- and *M*-configuration, respectively. An important feature for the study of the interaction with DNA, the PBI dyes were CD silent at low concentration supporting the fact that the molecules are in the monomeric form and do not induce any CD signal. Moreover, the aggregate growth could be initiated by the addition of aqueous NaCl solution and simultaneous increase of ionic strength simulating the physiological conditions.

For the study of the interactions of the enantiomeric PBI pair with DNA, long synthetic polynucleotides (poly(dA-dT)$_2$, poly(dG-dC)$_2$, poly dA-poly dT and poly A-poly U) were used to avoid the binding of the dyes at the end of the double strands and to ensure structural and conformation variations of the DNA sequences. Thermal denaturation experiments showed clear stabilization effect of the ds-polynucleotides caused by the formation of PBI/polynucleotide complexes associated with large ΔT values already at the low PBI/polynucleotide ratio r of 0.05 even though biphasic curves were observed in some cases. Furthermore, large binding constants (log K_s) between 9.4 and 9.8 were determined by fluorescence spectroscopic titration experiments accompanied with complete fluorescence intensity quenching of PBIs upon the addition the ds-polynucleotides (see Figure 18, left). The intensity decrease was attributed either to the formation of PBI H-type aggregates, non-emissive PBI/DNA or PBI aggregate/DNA complexes. Besides that, the analysis of the binding events according to the Scatchard equation[63] a saturation of the binding sites at a PBI/polynucleotide phosphate ratio r of about 0.1 was determined which comprise ten polynucleotides as a PBI binding pocket.

Deeper insights into the binding mode of the PBI molecules to DNA were provided by CD spectroscopic studies. At similar PBI/polynucleotide ratios applied in the CD titration experiments, different CD signatures in the absorption region of the PBI dyes were observed depending on the kind of polynucleotide (Figure 18, right). Intercalation binding mode was excluded by viscometry measurements, thus, the observed bisignate CD signals, respectively for the L- and D-enantiomer, for poly(dA-dT)$_2$, poly dA-poly dT and poly A-poly U were assigned to excitonically coupled PBI dimers bound in the minor groove of DNA (Figure 18a-c, right).

The growth to extended PBI aggregates is limited by the size of the minor groove as well as the interaction of the positively charged spermine chains with the negative phosphate backbone. The slightly different shapes of the CD signals of the respective enantiomers were attributed to variations of the arrangement of the PBI dimers in the groove. An exceptionally different CD pattern was found for the GC polynucleotide expressed in no mirror-image correlation of the signals (Figure 18d, right). In the long wavelength region positive signals occurred for both enantiomers, whereas at short wavelengths a negative signal for the D- and no signal at all for the L-enantiomer was observed. These observations were explained by the hindrance of the accommodation for the L-enantiomeric PBI dimer caused by the steric impact of the guanine base which obviously doesn't play a role for the insertion of the D-enantiomeric PBI dimer. Alternatively, the embedding of a single **L-5** molecule in the groove of poly(dG-dC)2 may be possible.

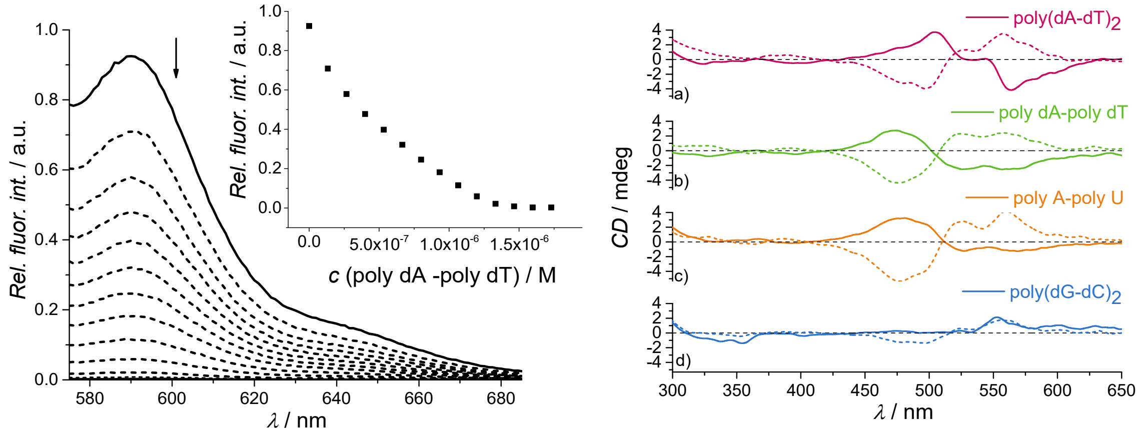

Figure 18: Left: Changes of fluorescence spectrum of **D-5** ($c = 5 \times 10^{-7}$ M) upon addition of poly dA-poly dT at pH 7.0, buffer sodium cacodylate, $I = 0.05$ M. Arrow indicate spectral changes with increasing concentration of poly dA-poly dT. Inset: Dependence of fluorescence intensity at $\lambda_{max} = 590$ nm on the amount of poly dA-poly dT. Right: CD spectra of **L-5** and **D-5** upon interaction with a) poly(dA-dT)$_2$, b) poly dA-poly dT, c) poly A-poly U and d) poly(dG-dC)$_2$ at pH 7.0 in sodium cacodylate buffer, $I = 0.05$ M; polynucleotide concentration: 4×10^{-5} M; r [c (PBI)]/[c (polynucleotide)] = 0.15; L-configured PBI (solid line), D-configured PBI (dashed line).[87] (Reproduced and adopted with permission from Royal Society of Chemistry, Copyright (2016)).

In summary, the spectroscopic studies of **L-5** and **D-5** showed that the steric demand in the amino acids of the PBI dyes and the chiral center plays a significant role for the molecular recognition of polynucleotides. Both dyes form excitonically coupled dimers in the minor groove of DNA and major groove of RNA forced by hydrophobic interactions and hydrogen bonding, thus, the polynucleotides act as templates for a particular aggregate size of PBI dyes.

Chapter 2

Determination of binding constants of self-assembled supramolecular structures

Abstract: In this chapter, the most common aggregation models for dimerization (monomer-dimer equilibrium) and growth into oligomers (isodesmic) are derived to describe composition of supramolecular species in thermodynamic equilibrium. Additionally, the experimentally observable values obtained by UV/Vis and NMR spectroscopy are elucidated by means of the aggregation models. Afterwards, the conventional K_2-K model is presented that has been utilized to describe cooperative supramolecular polymerization. For each type of aggregation behavior, examples are illustrated. Finally, issues arising from the accomplishment of experiments as well as approaches to control the aggregation behavior are presented.

2.1 Introduction

The self-assembly of molecules is an essential pathway in nature to obtain large structures with complex functions. The protein self-association[89] or the creation of multicomponent architectures like the tobacco mosaic virus[90] are guided by the concatenation of building blocks leading to the formation of assembled supramolecular structures. The understanding of the self-assembly processes directed researches into the application of this knowledge in various artificial systems. Thus, self-organisation protocols are utilized in in surfactant chemistry,[91] preparation of electronic devices[92] or in biomedicine[93]. The physical understanding[8, 94] and mathematical description [6, 95] of the aggregate formation provided insights into structure-property relationships needed to achieve particular self-assembled patterns. Assuming the presence of thermodynamically equilibrated aggregates, several aggregation models were developed which describe the experimental observations. The following sections will focus on the description of aggregation processes under thermodynamic conditions which presume an equilibrium between the monomeric and the noncyclic aggregated state (for self-association involving cyclic aggregates, see the review of Hunter and Anderson[96]). The common mathematical models, such as monomer-dimer model, isodesmic model as well as the nucleation-elongation model describe the self-assembly in a simple way which is often sufficient to describe the distribution of the species for the given concentrations and temperatures. By taking into account kinetic phenomena, the self-assembly behavior gets complicated, hence, further mathematical models are need.[97] Additionally, experimental limitations like insolubility or confined concentration range often hamper a proper mathematical evaluation of the self-assembly process. These drawbacks will be highlighted at the end of this chapter.

2.2 Monomer-dimer model

The simplest situation can be described as an equilibrium between the monomeric species and the smallest possible aggregate, the dimer aggregate.[95a] Considering the equilibrium between monomer (M) and dimer (D) in solution as $M + M \rightleftharpoons M_2$ the equilibrium (dimerization) constant K_2 can be expressed as:[98]

$$K_2 = [M_2\,]/\,[M]^2 = c_\mathrm{D}\,/c_M^2 \qquad (1)$$

In this expression, $[M] = c_{\mathrm{M}}$ is the concentration of the monomers and $[M_2] = c_{\mathrm{D}}$ the concentration of the dimers aggregate.

Using the eqn (1), the mass balance equation eqn (2) can be derived as:

$$c = c_{\mathrm{M}} + 2c_{\mathrm{D}} = c_{\mathrm{M}} + 2K_2c_{\mathrm{M}}^2 = c_{\mathrm{M}}(1 + 2K_2c_{\mathrm{M}}) \, , \tag{2}$$

where c is the total concentration of molecules. The fraction of monomers α_{M} eqn (3) can be derived using eqn (2) as follows:

$$\alpha_{\mathrm{M}} = \frac{c_{\mathrm{M}}}{c} = \frac{c_{\mathrm{M}}}{c_{\mathrm{M}}+2c_{\mathrm{D}}} = \frac{1}{1+2K_2c_{\mathrm{M}}} \, . \tag{3}$$

Using the expression eqn (3) of $\alpha_{\mathrm{M}} = c_{\mathrm{M}}/c$ and the division of eqn (2) by c yields the equation (4).

$$1 = \frac{c_{\mathrm{M}}(1+2K_2c_{\mathrm{M}})}{c} = \frac{c_{\mathrm{M}}}{c} + \frac{2K_2c_{\mathrm{M}}^2}{c} = \alpha_{\mathrm{M}} + \alpha_{\mathrm{M}}(2K_2c_{\mathrm{M}}) = \alpha_{\mathrm{M}}(1 + 2K_2c_{\mathrm{M}}) \, . \tag{4}$$

By taking into account $c_{\mathrm{M}} = \alpha_{\mathrm{M}}c$, a quadratic expression can be derived (5) by the rearrangement of the equation (4),

$$0 = \alpha_{\mathrm{M}}(1 + 2K_2c_{\mathrm{M}}) - 1 = \alpha_{\mathrm{M}}(1 + 2K_2c\alpha_{\mathrm{M}}) - 1 = 2K_2c\alpha_{\mathrm{M}}^2 + \alpha_{\mathrm{M}} + 1 \, , \tag{5}$$

which has only one physically meaningful solution, eqn (6).

$$\alpha_{\mathrm{M}} = \frac{\sqrt{8K_2c+1}-1}{4K_2c} \, . \tag{6}$$

The equation (6) can be connected to changes of physical properties of a chromophore, for instance NMR shifts or UV/Vis absorption spectra. For this purpose, the fraction of the dimer aggregates (general description as α_{A}) is defined as $\alpha_{\mathrm{A}} = 1 - \alpha_{\mathrm{M}}$. For a general situation, the physical property of the monomer is denoted as Z_{M} and that of the dimer as Z_{A}. This provides the equation (7).

$$Z = Z_{\mathrm{M}}\alpha_{\mathrm{M}} + Z_{\mathrm{A}}\alpha_{\mathrm{A}} = Z_{\mathrm{M}}\alpha_{\mathrm{M}} + Z_{\mathrm{A}}(1 - \alpha_{\mathrm{M}}) \, . \tag{7}$$

Here, Z is the overall physically observed property. Generally, the physical properties of both monomer and dimer are unknown. Thus, the equation (7) is transformed into (8) by using (6).

$$Z = Z_{\mathrm{M}}\left(\frac{\sqrt{8K_2c+1}-1}{4K_2c}\right) + Z_{\mathrm{A}}\left(\frac{4K_2c+1-\sqrt{8K_2c+1}}{4K_2c}\right) \, . \tag{8}$$

The subtraction of Z_M and rearrangement of this expression leads to equation (9).

$$Z - Z_\mathrm{M} = (Z_\mathrm{A} - Z_\mathrm{M})\left(\frac{4K_2c+1-\sqrt{8K_2c+1}}{4K_2c}\right). \tag{9}$$

Using the mass balance (2), the equation (10) can be formulated as a quadratic form,

$$0 = 2K_2c_\mathrm{M}^2 + c_\mathrm{M} - c\ , \tag{10}$$

which has only one physically meaningful solution:

$$c_\mathrm{M} = \frac{\sqrt{8K_2c+1}-1}{4K_2}. \tag{11}$$

Additionally, the mole fraction of the dimer aggregate can be written as:

$$\alpha_A = \frac{4K_2c+1-\sqrt{8K_2c+1}}{4K_2c} \tag{12}$$

The changes of physical properties upon dimerization which depend on the absolute concentration are obtained using the concentration of the dimer aggregate $c_\mathrm{D} = \alpha_\mathrm{A}c/2$:

$$Z = Z_\mathrm{M}c_\mathrm{M} + Z_\mathrm{A}c_\mathrm{D} = c\left(Z_\mathrm{M}\alpha_\mathrm{M} + Z_\mathrm{A}\left(\frac{\alpha_\mathrm{A}}{2}\right)\right) = c\left(Z_\mathrm{M}\alpha_\mathrm{M} + Z_\mathrm{A}\left(\frac{1-\alpha_\mathrm{M}}{2}\right)\right). \tag{13}$$

By the subtraction of cZ_M and rearrangement the equation (13) can be written as:

$$Z - cZ_\mathrm{M} = c\left((2Z_\mathrm{M} + Z_\mathrm{A})\left(\frac{1-\alpha_\mathrm{M}}{2}\right)\right). \tag{14}$$

The multiplication by c through $(1-\alpha_\mathrm{M})/2$ and applying of (6) give (15):

$$Z - cZ_\mathrm{M} = (2Z_\mathrm{M} + Z_\mathrm{A})\left(\frac{4K_2c+1-\sqrt{8K_2c+1}}{8K_2c}\right). \tag{15}$$

The same approach can be used to derive the equations using the dependence on α_M. There are several methods to investigate the dimerization process. ^{1}H NMR or UV/Vis dilution studies are the most common ones for chromophores. Beside the experimental issues like limited solubility, both methods can be applied in confined concentration ranges (10^{-4} to 10^{-1} for NMR and 10^{-7} to 10^{-2} for UV/Vis). The derived equations (6) and (15) of the monomer-dimer model can be applied to concentration-dependent changes of e.g. the chemical shifts or extinction coefficients. For concentration-dependent ^{1}H NMR studies, the resonance signals of the dimer are defined as

δ_A and that of the monomer as δ_M. By applying these definitions to the above derived equations expressions (16) and (17) are obtained for conditions of fast equilibrium (i. e. complex formation and dissociation is fast on the NMR time scal.

$$\delta - \delta_M = (\delta_A - \delta_M)\left(\frac{4K_2c+1-\sqrt{8K_2c+1}}{4K_2c}\right). \tag{16}$$

$$\delta - \delta_A = (\delta_M - \delta_A)\left(\frac{\sqrt{8K_2c+1}-1}{4K_2c}\right) \quad . \tag{17}$$

Similarly, the changes of the apparent extinction coefficients $\bar{\varepsilon}$upon dilution are transformed into the equations (18) and (19) which contain the extinction ε_A for the dimer aggregate and ε_M for the monomer:

$$\bar{\varepsilon} - \varepsilon_M = (\varepsilon_A - \varepsilon_M)\left(\frac{4K_2c+1-\sqrt{8K_2c+1}}{4K_2c}\right); \tag{18}$$

$$\bar{\varepsilon} - \varepsilon_A = (\varepsilon_M - \varepsilon_A)\left(\frac{\sqrt{8K_2c+1}-1}{4K_2c}\right). \tag{19}$$

The aggregation behavior of many chromophores has been described by the monomer-dimer model.[99] The self-assembly behavior was suggested to be limited mainly by the sterical demand of substituents or electrostatic interactions of the dye molecules. Noteworthy, often, there seems to be no rational consideration to create a dimeric aggregate rather than the obtained results are justified by particular molecular features. This observation can be explained by the fact that the trapping of the aggregate size is essentially difficult. There are several examples of dye molecules, for instance perylene bisimides (PBI), which were particularly designed to form only the dimer aggregate. These examples are discussed in introduction of Chapter 3.[14, 100] Additionally, the comprehensive investigation of the dimerization process of PBIs **5-9** is presented in the main part of Chapter 3.

2.3 Isodesmic model

The self-assembly of extended aggregates (beyond the dimer) can be ideally evaluated by means of the isodesmic model (equal *K* model).[95a] This simple model is only valid under the assumption of linear, noncyclic aggregates whereby all binding constants (*K*) of each aggregation step are equal. Because each π-system or dye has two π-faces, it is not surprising that many aggregation processes of these molecules have been evaluated by this model. The non-covalent binding event can be written as:[98]

$$M + M \overset{K_2}{\rightleftharpoons} M_2 \ ,$$

$$M_2 + M \overset{K_3}{\rightleftharpoons} M_3 \,,$$

$$M_{\mathrm{n-1}} + M \overset{K_n}{\rightleftharpoons} M_{\mathrm{n}} \,,$$

$$K = K_2 = K_3 = K_4 = \ldots = K_n \,. \tag{20}$$

The binding constant of the *n*th binding process is accordingly defined as:

$$K_{\mathrm{n}} = \frac{[M_{\mathrm{n}}]}{[M_{\mathrm{n-1}}][M]} = \frac{c_{\mathrm{n}}}{c_{\mathrm{n-1}}c_{\mathrm{M}}} = \frac{c_{\mathrm{n}}}{K_{\mathrm{n-1}}c_{\mathrm{n-2}}c_{\mathrm{M}}^2} = \cdots = \frac{c_{\mathrm{n}}}{(K_2K_3K_4K_5 \ldots K_{\mathrm{n-1}})c_{\mathrm{M}}^n} \,. \tag{21}$$

The mass balance for the aggregating molecule is written as follows.

$$c = c_{\mathrm{M}} + 2K_2c_{\mathrm{M}}^2 + 3K_2K_3c_{\mathrm{M}}^3 + 4K_2K_3K_4c_{\mathrm{M}}^4 + \cdots \,. \tag{22}$$

Rearranging of the equation and using the fact of equal binding constant gives:

$$c = c_{\mathrm{M}}(1 + 2Kc_{\mathrm{M}} + 3K^2c_{\mathrm{M}}^2 + 4K^3c_{\mathrm{M}}^3 + \cdots) \,. \tag{23}$$

Considering the Taylor series expansion $1 + 2x + 3x^2 + \cdots + nx^{n-1} = \frac{1}{(1-x)^2}$for $0 < x < 1$ the equation (24) is obtained.

$$Kc = \frac{Kc_{\mathrm{M}}}{(1-Kc_{\mathrm{M}})^2} \,. \tag{24}$$

Using the definition of molar fraction of monomers α_{M} (3) which now can be formulated as $\alpha_{\mathrm{M}} = Kc_{\mathrm{M}}/Kc$, the equation (24) can be transformed into (25).

$$\alpha_{\mathrm{M}} = (1 - Kc_{\mathrm{M}})^2 = (1 - \alpha_{\mathrm{M}}Kc)^2 \,. \tag{25}$$

The multiplication of the bracket terms gives the quadratic expression which has only one physically meaningful solution (26).

$$\alpha_{\mathrm{M}} = \frac{2Kc+1-\sqrt{4Kc+1}}{2K^2c^2} \tag{26}$$

Accordingly, the molar fraction of the extended aggregate is expressed as:

$$\alpha_{\mathrm{A}} = 1 - \frac{2Kc+1-\sqrt{4Kc+1}}{2K^2c^2}\,. \tag{27}$$

The application of the derived isodesmic model on the concentration-dependent ^{1}H NMR or UV/Vis absorption studies lead to the similar set of equations as those determined from the monomer-dimer model.

$$\delta - \delta_{\mathrm{A}} = (\delta_{\mathrm{M}} - \delta_{\mathrm{A}})\left(\frac{2Kc+1-\sqrt{4Kc+1}}{2K^2c^2}\right); \tag{28}$$

$$\bar{\varepsilon} - \varepsilon_{\mathrm{A}} = (\varepsilon_{\mathrm{M}} - \varepsilon_{\mathrm{A}})\left(\frac{2Kc+1-\sqrt{4Kc+1}}{2K^2c^2}\right). \tag{29}$$

Simple bay-unsubstituted perylene bisimide dyes are known to aggregate in organic solvents trough π-π-interactions leading to the formation of infinite columnar aggregates. PBI dyes **1** and **2** which bear solubilizing tridodecyloxyphenyl and tridodecylphenyl groups, respectively, in the imide positions (Figure 19a), show significant changes in the UV/Vis absorption spectra upon concentration change. Upon aggregation, a transition from the well resolved vibronic absorption bands of the monomeric species to the hypsochromically shifted band of decreased intensity were observed in different solvents which indicates the formation of H-type aggregates (see Figure 19b for a representative example of PBI **1** in toluene).[13, 101a, 101b]

Nonlinear least-squares analysis of the degree of aggregation obtained by means of eqn (30) reveals a good agreement with the isodesmic model eqn (29) (see Figure 19c). Noteworthy, the fit of the data to the monomer-dimer model does not show a good match, shown as dashed black line for comparison in Figure 19.

$$\alpha_A = \frac{\bar{\varepsilon}-\varepsilon_M}{\varepsilon_A-\varepsilon_M} \tag{30}$$

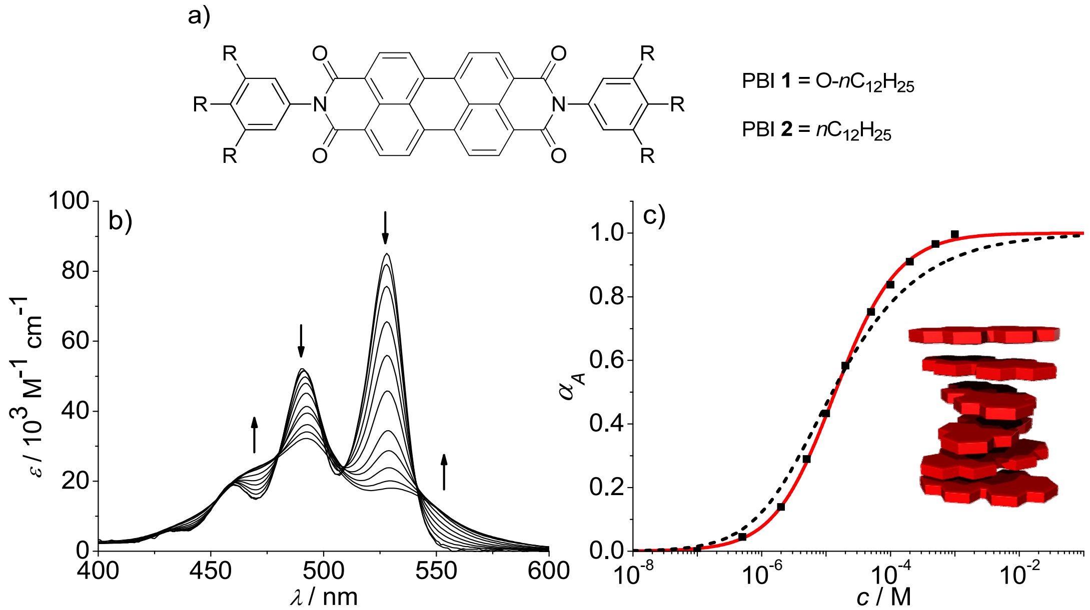

Figure 19: a) Structures of PBI dyes **1** and **2**. b) Concentration-dependent UV/Vis absorption spectra of PBI **1** in toluene ($c = 1.0 \times 10^{-7} - 1.0 \times 10^{-3}$ M). Arrows indicate the spectral changes upon increasing concentration. c) Analysis of the concentration-dependent data according to the isodesmic (red line) and dimer (dashed black line) aggregation models ($R^2 = 0.999$). Inset: The proposed illustration of the structure for this columnar aggregate. [12-13, 101] (Reproduced and adopted with permission from Royal Society of Chemistry, Copyright (2016)).

For PBI **1** in toluene, the aggregation constant K of 4.5×10^4 M^{-1} was determined. Moreover, comprehensive aggregation studies in other organic solvents showed aggregation through π-π-stacking via the isodesmic pathway. [13, 101] Here, the binding constants decreased from the non-polar solvents like methylcyclohexane ($K = 1.5 \times 10^7$ M^{-1}) to the polar solvents such as tetrahydrofuran ($K = 5.4 \times 10^4$ M^{-1}). In solvents of intermediate polarity but high polarizability (chloroform, dichloromethane), the aggregation ability was exceptionally low ($K = 2.6 \times 10^2$ M^{-1} and 1.6×10^3 M^{-1}, respectively). Interestingly, the alkylphenyl-substituted analogue PBI **2** which was extensively studies by various methods such as NMR, UV/Vis spectroscopy and vapor pressure osmometry (VPO) showed significant lower aggregation propensity in comparison to PBI **1**.[13, 101b] This observation was attributed to the charge transfer interactions between the electron poor PBI core and electron rich trialkoxyphenyl substituents of neighboring dyes in the aggregate of PBI **1**.

2.4 K_2-K model

It has been realized by careful studies over a large concentration range that the isodesmic model often doesn't fulfil the requirements for the description of the self-assembly of many supramolecular polymerizations.[8, 96] The experimentally observed formation of a nucleus, characterized by a critical concentration, at which the extended aggregates with larger stability were formed, was not captured by this simple mathematical description of the aggregation process. In order to develop an appropriate aggregation model the isodesmic model was modified by assuming that the binding constant of the initial nucleation process differs significantly from the one of the elongation process. [6, 95] In this work, only the nucleation to a dimer nucleus is relevant, therefore, for the general nucleation-elongation model the reader is referred to the appropriate literature.[102] Considering the nucleus s of 2, the same equilibria are obtained as described in section 2.3 for the isodesmic growth.

By defining the cooperativity factor of $\sigma = K_2/K$, the binding constant is written as:

$$K = K_2/\sigma = K_3 = K_4 = \ldots = K_n \,. \tag{31}$$

Taking into account the equilibrium (21) and the definition of the cooperativity factor σ the mass balance (23) can be rearranged into (32):

$$c = c_\mathrm{M}(1 + 2\sigma K c_\mathrm{M} + 3\sigma K^2 c_\mathrm{M}^2 + \cdots) = c_\mathrm{M}(1 + \sigma(2Kc_\mathrm{M} + 3K^2 c_\mathrm{M}^2 + \cdots) \,. \tag{32}$$

Multiplication by K and application of the Taylor series expansion lead to the equation (33):

$$Kc = Kc_\mathrm{M}(1-\sigma) + \frac{K\sigma c_\mathrm{M}}{(1-Kc_\mathrm{M})^2} \,. \tag{33}$$

The transformation into the molar fraction of monomers α_M gives the expression:

$$\alpha_\mathrm{M} = \frac{(1-Kc_M)^2}{(1-Kc_\mathrm{M}(2-Kc_\mathrm{M})(1-\sigma)} = \frac{(1-\alpha_\mathrm{M}Kc)^2}{(1-\alpha_\mathrm{M}Kc(2-\alpha_\mathrm{M}Kc)(1-\sigma)} \,. \tag{34}$$

The multiplication and rearrangement of (34) gives:

$$\alpha_\mathrm{M}^3 K^2 c^2 (\sigma - 1) + \alpha_\mathrm{M}^2 Kc(Kc - 2(\sigma - 1) - \alpha_\mathrm{M}(2Kc + 1) - 1) = 0 \,. \tag{35}$$

The solutions of this cubic equation may include complex numbers. Thus, the relevant solution can be obtained by certain algorithms in different software packages. However, the calculation of

Kc as a function of Kc_M can be easily performed for particular σ values by using the equation (36):

$$Kc = (1-\sigma)Kc_M + \frac{\sigma Kc_M}{(1-Kc_M)^2}\,. \tag{36}$$

Finally, the α_A is determined from the obtained values by using (37) which can be plotted against the corresponding Kc values which is illustrated in Figure 20.

$$\alpha_A = 1-\alpha_M = 1-\frac{Kc_M}{Kc} \tag{37}$$

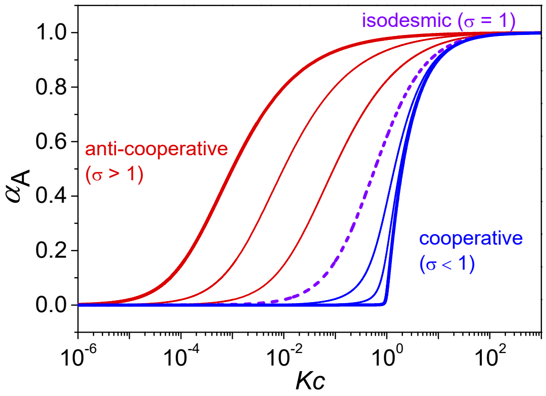

Figure 20: Schematic illustration of various K_2-K aggregation processes. Plot of the fraction of aggregated molecules α_A as a function of the normalized concentration Kc with different σ values according to eqn (36) and (37). For the curves from left to right $\sigma = 10^3$, 10^2, 10 (red curves), 1 (violet dashed curve) , 10^{-1}, 10^{-2}, and 10^{-4} (blue curves) were applied.[6] (Reproduced and adopted with permission from Royal Society of Chemistry, Copyright (2016)).

Based on the above mentioned definition of the cooperativity factor σ, three main cases can be distinguished. For $\sigma = 1$, both the nucleation K_2 and the aggregation constant K are equal which is represented by the isodesmic model (violet dashed line in Figure 20). The cooperative growth is characterized by $\sigma < 1$ (blue curves in Figure 20). Here, the dimerization process proceeds till a critical concentration of K^{-1} is reached at which a sharp increase of α_A occurs that correspond to an instantaneous formation of extended aggregates. In the anti-cooperative aggregation process the formation of the dimer is much more favored than further aggregation ($\sigma > 1$, red lines in Figure 20).

For a long time, the self-assembly of PBI dyes was described by using mostly the isodesmic model which seems to be an appropriate choice for simple PBI structures (see Section 2.3 for an example). However, the explanation of the aggregation behavior of hydrogen bonded PBI dyes **3a-e** (Figure 21) fails by simply using the isodesmic model.[103]

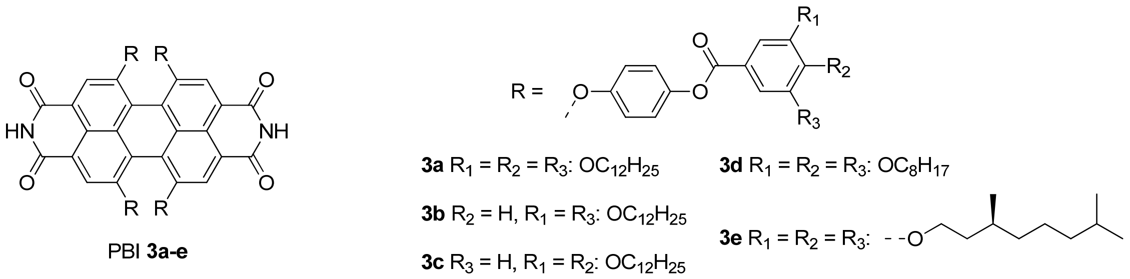

Figure 21: Structures of the PBI dyes **3a-e**.

For instance, the tetra-bay-substituted PBI dye **3e** self-assembles by forming J-type aggregates in methylcyclohexane characterized by the bathochromically shifted band upon an increase of the concentration (Figure 22a). The sterically demanding bay-substituents provoke a twist of the PBI core which prohibits the formation of columnar long aggregates. The additional emergence of intermolecular hydrogen bonds results in the formation of helical double string fibers which was confirmed by several spectroscopic techniques (see the schematic illustration in Figure 22b).

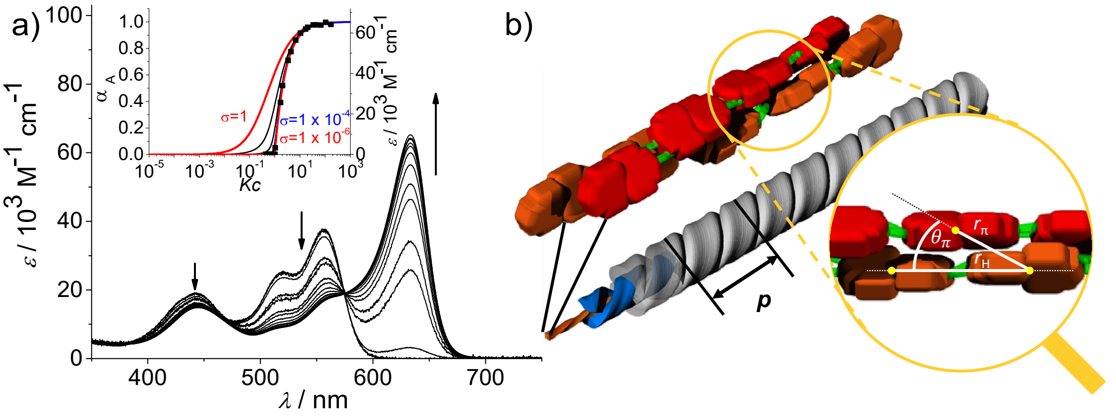

Figure 22: a) Concentration-dependent UV/Vis absorption spectra of the chiral PBI **3e** ($c = 7.3 \times 10^{-5} – 1.9 \times 10^{-7}$ M) in methylcyclohexane. Arrows indicate the spectral changes upon increasing concentration Inset: Analysis of the concentration-dependent data at 633 nm according to the K_2-K model (lines from left to right: $\sigma = 1$, 0.1, 0.01, 0.001, 0.0001 and 0.000001). b) Schematic illustration of the packing of PBI **3a-e** into the slipped J-type aggregates. The red blocks represent the PBI core and green lines are the hydrogen bonds.[103] (Reproduced and adopted with permission from American Chemical Society, Copyright (2016)).

The analysis of the aggregation behavior of **3e** by means of the K_2-K model by applying a manual fitting procedure resulted in a good fit for a cooperativity factor σ of about 10^{-6}. The dimerization constant K_2 of 13 ± 11 M^{-1} and an aggregation constant K of 2.3×10^6 $M^{-1} \pm 0.1 \times 10^6$ M^{-1} confirm the highly cooperative aggregation process which originates from the favorable interplay of π-π-interactions and hydrogen bonding.

Both the isodesmic and K_2-K model provide the possibility to determine the number-average DP_N and the weight-averaged degree of polymerization DP_W which show the average size of an aggregate or rather the number of molecules in a particular aggregate. For the mathematical derivation of these values the reader is referred to the corresponding literature. [6, 95]

Up to now, just the concentration-dependent measurements were taken into consideration to elaborate the self-assembly behavior. Due to the often occurred experimental limitations of these experiments, temperature-dependent measurements became prevalent owing to the accessibility of large data sets. Therefore, models were developed which treat the temperature-dependent changes in NMR or UV/Vis spectroscopical experiments accompanied by the aggregation phenomenon. The corresponding mathematical derivation can be found in the literature.[104]

2.5 Experimental issues

Researchers are often confronted with three main difficulties during the investigations of the self-assembly processes of supramolecular structures: experimental execution, mathematical description and combination of both. Concerning the experiments, the investigation of the self-assembly processes require specific experimental conditions to follow the growth process. Both NMR and UV/Vis spectroscopy are limited by the applicable concentration range. However, for the determination of reasonable binding constant values and confirmation of a particular model a concentration range of at least two orders of magnitude is necessary. In situations where more than two species are equilibrated the range has even to be expanded.[6] To fulfill these experimental requirements, the studied system has to be soluble over a wide concentration range and an experimental technique is needed that is sensitive over the whole concentration range.

In contrast to the cooperative and isodesmic growth of supramolecular structures, very few examples are known in the case of the anti-cooperative aggregation.[105] The anti-cooperative case seems to be difficult to monitor experimentally because the formation of large aggregates require high concentrations which is often not accessible. Additionally, the whole transition from the monomeric to the aggregated state with the nucleus in between has to be spectroscopically resolved which is also difficult to achieve. An example of an anti-cooperative aggregation process which was extensively studied and mathematically evaluated by a newly developed model is presented in Chapter 4.

Even if the experiments were successful, the mathematical description of the aggregation process might be difficult to elaborate. A good fit between the data and model doesn't mean automatically that this particular model is the best one to describe the aggregation behavior of the studied system. A mathematic model containing many unknown parameter provides generally better fits than the one with less free parameters. This fact might be acceptable if the obtained values do physically and chemically (e.g. no negative binding constants, meaningless extinction coefficients or ^{1}H NMR changes) make sense.[98]

Recently, the issue of the indistinguishability of the monomer-dimer and the isodesmic model was addressed in the literature.[106] Regarding the equations (18) and (28) or (19) and (29), respectively, both became identical under the condition of $2K_2 = K$, which indicates the indistinguishability of these two models. Therefore, the authors derive the mathematical origin of this phenomenon which is not addressed here but can be found in the corresponding literature. [106] More important are the qualitative statements made by the authors. Often the choice of a particular model is justified by the applicable concentration range. In the low concentration regime the monomer-dimer model is selected by the investigator and the isodesmic model in the high concentration regime. The mathematical derivation of the models revealed that the indistinguishability is valid for any concentration which makes this justification incorrect. Obviously, it is important to determine the aggregate size by using several techniques beside NMR and UV/Vis spectroscopy thus the limitation to a dimer can be legitimated. Nevertheless, the authors propose to base the choice of particular model on structural consideration and chemical intuition rather than on the applied concentration range. The experimental indistinguishability of the monomer-dimer and the isodesmic model is addressed in Chapter 3. The condition of $2K_2 = K$ could not be reproduced for the described experimental data. In our cases the conditions of $K_2 = K$ seems to be valid. However, the reason for the similar fitting curves for the monomer-dimer and isodesmic model could not be identified.

2.6 Control of the self-assembly pathway

Inspired by the efficient control mechanisms in nature, researchers developed several strategies to direct the self-assembly pathway. Generally, there are two possibilities to enable the desired route, namely external and internal stimuli. The aggregation process of supramolecular systems is externally promoted by the solvents, concentration and temperature. Internally, the rational design of molecular structure is the crucial feature. Of course, interplay of all factors can be decisive which kind of aggregate is formed. The external control mechanisms were already addressed a few times, and hence, the molecular features will be discussed in the following section.

As recognized earlier, the self-assembly via the isodesmic pathway mostly required solely π-π-interactions.[94e] Very recently, Fernández and coworkers reviewed strategies for self-assembly through the cooperative pathway.[8] A notable feature of the (anti-)cooperative self-assembled system is the interplay of several responsible forces. The influence of supplementary factors like hydrogen bonding, metal-metal, metal-ligand, and dipole-dipole interactions or other weak forces direct the self-assembly into (anti-)cooperative direction. Below, the focus lies on the impact of hydrogen bonding, *i. e.* for other contributions the reader is referred to corresponding literature.[8]

There are several molecule classes involving hydrogen bond motives which self-assemble in cooperative fashion. On the other side, the same kind of molecules show isodesmic self-assembly by avoiding the hydrogen bonded functional groups. The converse argument could be that the anti-cooperative self-assembly of similar molecules should be possible as well. This might be achieved by changing the hydrogen bond motive or rather the position of those functional groups within the respective molecule (see Chapter 4).

The isodesmic and cooperative self-assembly of perylene bisimide dyes was exemplified in previous sections. Other prominent classes of π-systems aggregating through both isodesmic and cooperative path are for instance benzene-1,2,3-tricarboxamides (BTAs), oligo(*p*-phenylene vinylene)s (OPVs) or oligo(phenylene ethynylene)s (OPEs). The contrary self-assembly of these molecules and other dyes was comparatively described in the review of Kulkarni *et. al*.[94e]

For instance, the self-assembly behavior of the BTA molecules **1a,b** and **2** was extensively studied by the Meijer group. By using temperature-dependent CD and UV/Vis spectroscopy, they elucidated the cooperative aggregation behavior of the chiral BTA **1a** and the achiral BTA **1b** (see Figure 23 and Figure 24a).[104b] While the chiral derivative show preferential right-handed helicity in the H-type columnar stack the achiral analogue aggregates into helical stack without distinct direction of the helix. However, the self-assembly was described by the nucleation-elongation model proposing the cooperativity factors σ of $10^{-4} - 10^{-6}$ for both. Beside π-π-interactions, the driving forces for the supramolecular polymerization were attributed to the intermolecular triple hydrogen bonding between the amide functions.

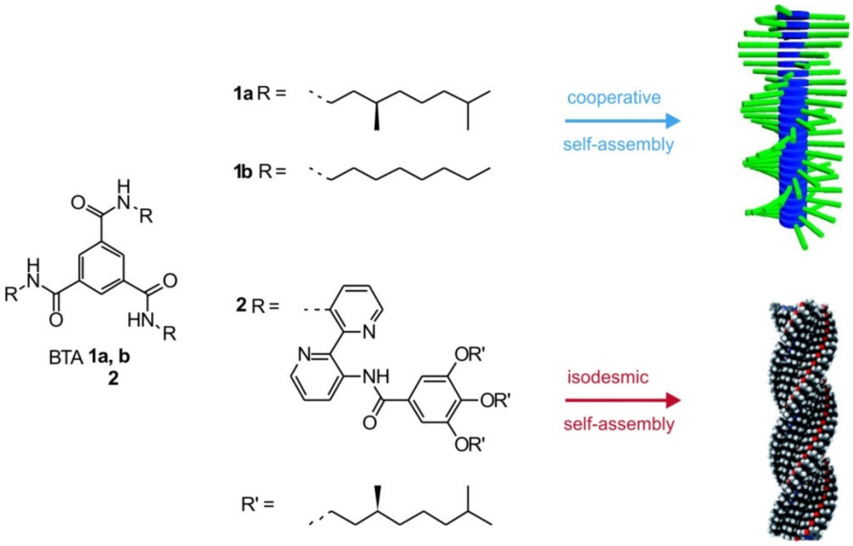

Figure 23: Structures of BTA **1a,b** and **2** and the arrangement of them in the supramolecular stack through the cooperative and isodesmic aggregation pathway.[104b, 107] (Figures reproduced and adopted with permission from American Chemical Society and Royal Society of Chemistry, Copyright (2016)).

In contrast to BTAs **1a** and **b**, BTA **2** functionalized with 3,3'-bis(acylamino)-2,2'-bipyridine groups shows completely different aggregation behavior. Indeed, BTA **2** forms helical structures in the nonpolar solvent methylcyclohexane but the self-assembly has been described by the isodesmic model which was verified by temperature-dependent UV/Vis absorption studies (see Figure 23 and Figure 24b). Furthermore, X-ray and quantum chemical calculations predicate no formation of intermolecular hydrogen bonds. On the contrary, six intramolecular hydrogen bonds between the amide NH and nitrogen of the pyridine groups are present in the molecule leading to growth of the helical stack only determined by π-π-interactions. The variation between the self-assembly pathways of the BTA molecules originates obviously from the different hydrogen bonding connectivity. The comparison of structural features of other classes of molecules exposed similar observations.[94e] Based on previously reported literature,[95b, 108] Kulkarni *et al.* concluded that dipole-dipole interactions and electrostatic interactions in the direction of growth lead to cooperative self-assembly. Through the intermolecular directional hydrogen bonds in a complex long-range dipole-dipole interactions can lead to the formation of large stacks in a cooperative fashion. In contrast, the presence of solely π-π-interaction, hydrophobic and van der Waals interaction without any electronic impact cause most likely isodesmic self-assembly.

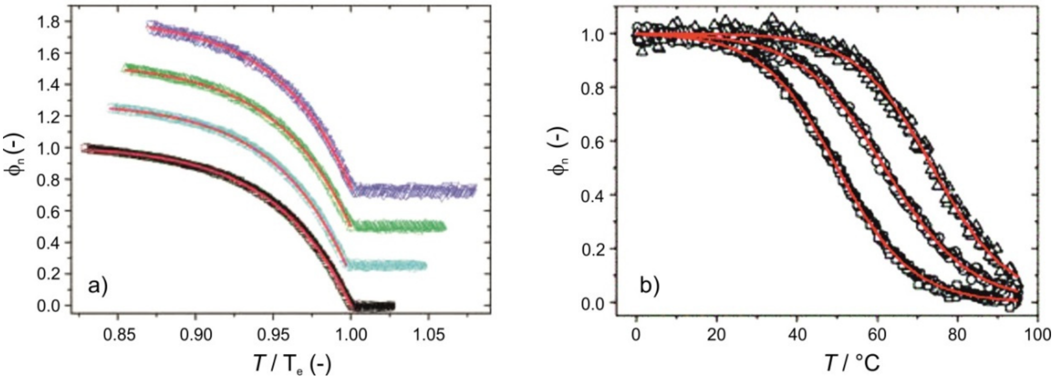

Figure 24: a) The degree of aggregation ϕ_n with fitted elongation regime (red line) as function of temperature for BTA **1a** in heptane at different concentrations (1.2 x 10^{-5} M (blue open triangle pointing down) to 3.8 x 10^{-5} M (black open square)). The curves are shown with a 0.25 offset for each next concentration and as a function of the normalized temperature T/T_e (T_e as the elongation temperature).[104b]. b) The degree of aggregation ϕ_n as a function of temperature for different concentrations of BTA **2** (1.0 x 10^{-5} M (squares) to 3.5 x 10^{-4} M (triangles)) in methylcyclohexane with corresponding fit based on the sigmoidal function.[107] (Reproduced and adopted with permission from American Chemical Society and Royal Society of Chemistry, Copyright (2016))

They proved this concept by means of computational studies using molecules which aggregation behavior has already been elucidated experimentally. The optimization of a tetrameric stack of BTAs **3** and **4** using the BLYP/DZVP/B97D/CC-PVDZ level of theory and calculation of total self-consistent field electron density captured on to isosurfaces of molecular potential was performed (see Figure 25). BTA **3** exhibits a large dipole moment of 36 D and, in contrast, BTA **4** show very low dipole moment of 1.5 D. These results confirm the assumption made by the authors that directional intermolecular hydrogen bonds in BTA **3** lead to cooperative self-assembly and the lack of them to isodesmic growth.

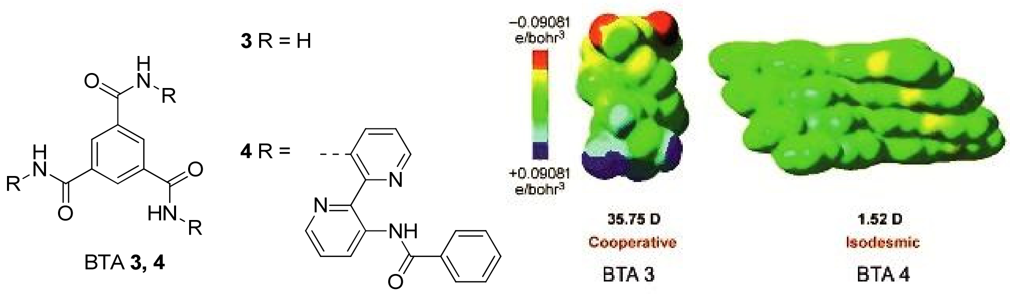

Figure 25: Structures of BTAs **3** and **4**. Electrostatic potential isosurfaces plotted on electronic density isosurfaces of 4×10^{-4} e bohr^{-3} for the tetramer of BTA **3** and **4**, along with the dipole moment in the stack direction as obtained from the BLYP/DZVP/B97D/CC-PVDZ level of theory. [94e] (Reproduced and adopted with permission from John Wiley and Sons, Copyright (2016))

Considering these results, a parallel may be drawn between cooperative and anti-cooperative self-assembly. The necessity of an additional driving force other than π-π-interaction has already been ascertained for the anti-cooperativity. The directional intermolecular hydrogen bonds are obviously necessary but they have to be located on the nucleus, such as a dimer, disfavoring further growth. As postulated, this might be achieved by rational structural design of molecules. One if the approaches to achieve that will be presented in the following chapters.

Chapter 3

Self-assembly of amide-functionalized perylene bisimide dyes into dimer aggregates*

Abstract: A series of homochiral perylene bisimide (PBI) dyes (**5**-**8**) functionalized at the imide positions with amide groups, that are derived from L-alanine, are investigated in terms of their self-assembly properties. Structural variation of the PBIs was made by changing the peripheral substituents at the amide nitrogen atoms. PBI **5** bearing peripheral 3,5-bis(dodecyloxy)benzyl substituents was chosen as a prime example and its aggregation properties were thoroughly studied by a combination of different methods. Concentration-dependent ^{1}H NMR and UV/Vis studies of this amide-functionalized homochiral PBI showed exclusive formation of dimers in chloroform. The π-π-interactions and hydrogen bonds were indicated as responsible forces for limiting the aggregate size to dimers. Molecular modeling revealed a bracket like structure of PBI **5** dimer aggregate that complies well with the obtained spectroscopic results. The involvement of hydrogen bonds in the dimer aggregate was confirmed by IR spectroscopy. 2D NMR techniques such as diffusion ordered (DOSY) NMR and rotating-frame nuclear Overhauser effect (ROESY), vapor pressure osmometry (VPO) and isothermal calorimetry (ITC) experiments confirmed finally the size of the PBI **5** aggregate as a dimer. The self-assembly properties of PBI derivatives **6**-**8** were studied by concentration-dependent UV/Vis spectroscopy and NMR techniques. These PBIs show similar aggregation behavior as the prime example **5** since they also form dimer aggregates in chloroform. The dimerization constants (K_2) of this series of PBIs are discussed in a comparative manner revealing that the dimerization property of these PBIs is dependent on the nature of the amide substituents.

---

*A part of this chapter was published by Jana Gershberg, Franziska Fennel, Thomas H. Rehm, Stefan Lochbrunner, Frank Würthner, *Chem. Sci.* **2016**, *7,* 1729-1737. Reproduced and adopted with permission from The Royal Society of Chemistry. Copyright (2016).

3.1 Introduction

The organization of supramolecular systems by π-π-interactions[109] and hydrogen bonds is a key feature in many biomolecular structures such as DNA and proteins.[110] The application of this principal to artificial nanosystems has accordingly gained much interest.[111] Indeed, supramolecular structures created by such intermolecular forces has been successfully applied in electronic devices such as organic field-effect transistors and solar cells.[11b, 92, 112] Perylene bisimide (PBI) dyes are promising candidates for the elucidation of self-assembly behavior of π-aromatic systems because their structural diversity allows a multifunctional utilization in solvents of different polarities and broad ranges of concentration and temperature.[101c] Bay-unsubstituted PBIs with functionalities in the imide positions are known to form columnar aggregates driven by π-π-interactions.[13] However, realization of aggregates of particular size is challenging due to the presence of randomly dispersed aggregate mixtures in solution. Investigations towards structure-functional property relationships of PBI dyes were enabled by designing covalently bound PBI dimers, trimers or oligomeric systems. [113] However, much less examples are known to date in which a particular aggregate size was trapped at a certain stage by non-covalent forces.

Würthner and coworkers introduced an unsymmetric PBI molecule, which contained imide substituents with significant sterical demand such as 2,5-di-*tert*-butylphenyl and benzyl groups.[14] The self-assembly properties of this PBI were studied by means of concentration-dependent NMR and UV/Vis spectroscopy in a solvent mixture of chloroform/methylcyclohexane (1:5) displaying a discrete dimer formation. The bulky substituents prevent the growth of extended aggregates because of restricted access of the π-surfaces at one side of the PBI core. Hence, a preferred head-to-tail dimer stack composed of two PBI molecules with rotational displacement of 30° was formed, which was confirmed by ROESY NMR in combination with molecular modeling. The restriction of the aggregate size of this particular PBI molecule was achieved by the contribution of the sterical constraints as well as particular selection of the solvent composition.

Recently, the same group reported examples of PBI dyes which form dimeric aggregate structures by metal complexation or by templating the self-assembly through the interaction with DNA. In the first case, selective binding of Ba^{2+} to the crown ether substituents in the bay-positions of the PBI molecules was exploited to accomplish the dimer formation. The formation of the sandwich type dimer aggregate quenches the monomer emission which can be applied as a "turn-off" sensor.[100a] In the case of DNA-templated PBI self-assembly, the aggregate size is limited to the width of the binding pocket in the minor groove of the double-stranded DNA. The evaluation of the spectroscopic data pointed at a selective recognition of certain base pair sequences depending on the chirality, steric impact and the number of positive charges in the side chains of the PBI dyes.[114]

In 2002, Schenning and Meijer *et al.* reported a bay-unsubstituted homochiral PBI molecule containing terminal carbamate groups at the imide positions.[100b] UV/Vis and CD spectroscopic experiments of this carbamate-functionalized PBI showed the formation of aggregates in toluene, chloroform and tetrachloroethane, whereas the monomeric species prevailed in THF. Apart from the obvious π-π-interactions, intermolecular hydrogen bonding from the carbamate NH-group to the carbonyl oxygen of the imide substituents made responsible for the aggregate formation as revealed by IR spectroscopy. The authors proposed a dimeric structure for the PBI aggregate on the basis of MALDI measurements. However, further in-depth investigations to confirm the proposed dimeric structure were not provided.

As evident from the above discussion only very few examples of PBI molecules are known which aggregate into discrete dimers. Thus, we synthesized new PBI molecules possessing functionalities that should favor dimer formation. Several aspects in the molecular design of the new PBIs were taken into account. The introduced didodecyloxybenzyl or didodecylbenzyl groups in the periphery of the new PBIs **5** and **6** should provide the necessary solubility in organic solvents, whereas the oligo(ethylene glycol) side chains in benzyl group of PBI **7** should facilitate studies in aqueous media which might be of interest for future studies. The branched alkyl side chains at amide nitrogen atoms of PBI **8** enable to evaluate the impact of the phenyl group on the aggregation behavior. Finally, the amide functions ascertain the formation of hydrogen bonds for all newly synthesized PBI dyes. The expectation was that the specific interplay of π-π-interactions and hydrogen bonds would restrict the size of the aggregate to the dimeric structures. For comparison and completeness, the reference compound PBI **9** having an unbranched alkyl chain, which was previously synthesized and analyzed by Thomas H. Rehm, was included in the following investigations.[115]

The amide-functionalized homochiral PBI **5** bearing dodecyloxy chains in the periphery was extensively studied as a prime example by several spectroscopic methods. The concentration-dependent UV/Vis and NMR spectroscopic studies in chloroform confirmed that no extended aggregates of PBI **5** beside dimers are formed. Structural evidence for a bracket-like dimer structure of PBI **5** was provided by 2D NMR and molecular modeling. Further complementary studies such as vapor pressure osmometry (VPO) and isothermal calorimetry (ITC) experiments corroborated the exclusive presence of dimers in solution. Due to the similar structural features of PBIs **6**, **7** and **8** the investigations of their aggregation behavior were confined to concentration-dependent UV/Vis and NMR studies. These PBIs also form dimer aggregates in chloroform.

3.2 Results and discussion

3.2.1 Molecular design and synthesis

Our molecular design of PBIs **5-8** is based on the functionalization of PBI scaffold at imide positions with hydrogen bonding amide groups derived from a homochiral amino acid and respective benzyl or alkyl amines bearing solubilizing terminal substituents (Scheme 1).

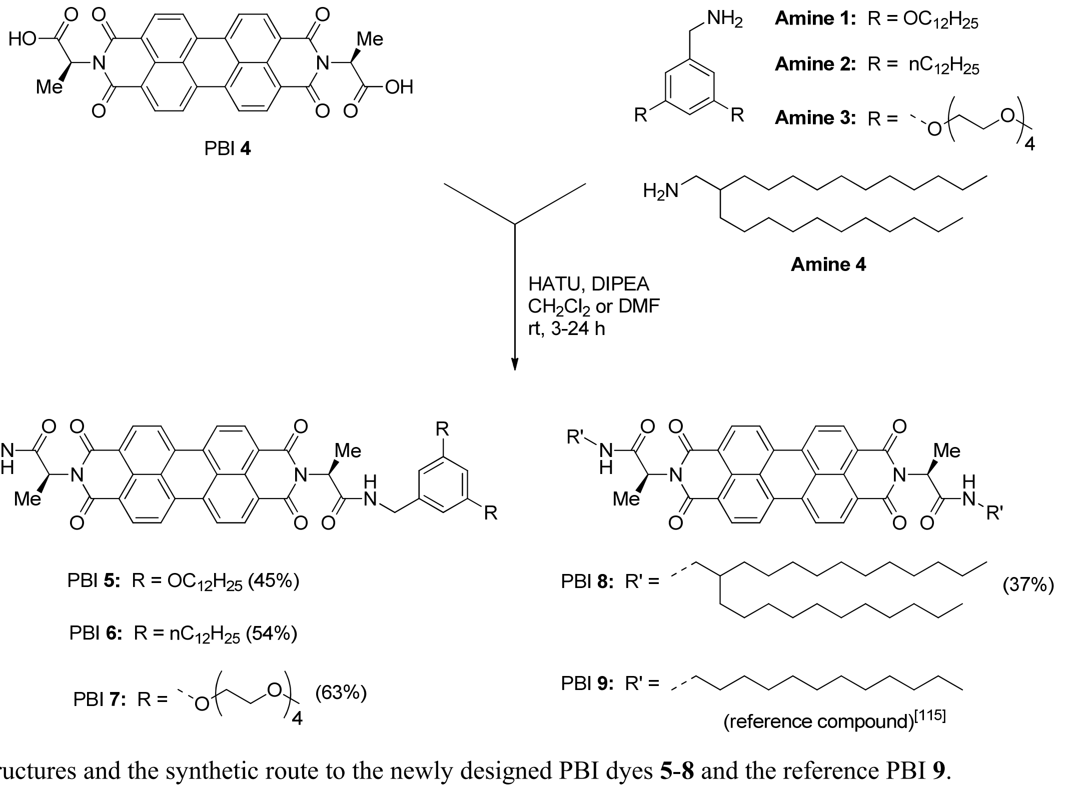

Scheme 1: Structures and the synthetic route to the newly designed PBI dyes **5-8** and the reference PBI **9**.

In contrast to previously investigated PBI organogelators,[116] in which the amide groups tethered to the PBI supported a cooperative fibre growth by hydrogen bonds, in the present design a reversed connectivity of the amide group is applied. According to molecular modeling (vide infra), this design should support the formation of hydrogen-bonded dimers by intermolecular interactions between the amide NH and the PBI carbonyl groups instead of cooperative supramolecular fibre growth. On the basis of the abovementioned concept, we have designed the homochiral PBIs **5**-**8** with appended L-alanine at the imide positions and bearing dialkoxybenzyl amide substituents, and synthesized these PBI dyes according to the route displayed in Scheme 1. The L-alanine functionalized symmetrical PBI **4**, which was used as a precursor for all PBIs, and benzyl amine **1** used for PBI **5** were prepared according to literature procedures.[14, 117] The peptide coupling reaction of amino acid functionalized PBI **4** with amine **1** in the presence of the activation reagents *N*,*N*-diisopropylethylamine (DIPEA) and *O*-(7-azabenzotriazol-1-yl)-*N*,*N*,*N*',*N*'-tetramethyluronium hexafluorophosphate (HATU) afforded the desired PBI building block **5** in 45% yield. The syntheses of the homochiral PBIs **6**, **7** and **8** were based on the similar peptide coupling approach of PBI **4** with the corresponding amines **2**, **3** and **4** (Scheme 1). The syntheses of the later amines are accomplished as follows.

The benzyl amine **2** was synthesized according to the procedure reported in the Bachelor thesis of Annika Bothe (Scheme 2).[118] Compound **3** was synthesized by a Sonogashira cross-coupling reaction of the commercially available 3,5-dibromobenzonitrile (**1**) and 1-dodecyne (**2**) in 88% yield. The reduction of the nitrile group in **3** by LAH afforded the compound **4** in 93% yield. Afterwards, the second reduction by Pd/C and H_2 gave the desired amine **2** with the yield of 91%.

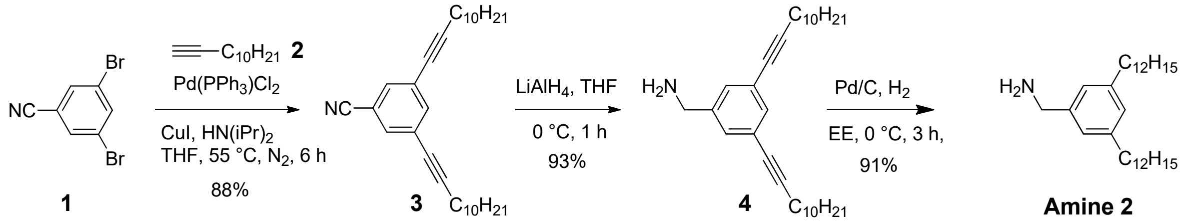

Scheme 2: Synthetic route to the benzyl amine **2**.

The oligo(ethylene glycol) functionalized benzyl amine **3** was synthesized according to the procedures previously applied for similar molecules (Scheme 3).[119] In the first step, tetra(ethylene glycol) monomethyl ether (**5**) was tosylated and subsequently reacted with 3,5-dihydroxybezoate (**7**). The obtained ester **8** was reduced by LAH to the corresponding alcohol **9**, the latter was brominated by the Appel reaction (CBr_4/PPh_3) to the bromide **10**. The treatment of this bromide with sodium azide afforded the azide **11**, which was reduced with LAH to the desired amine **3** with a yield of 67% in the final step.

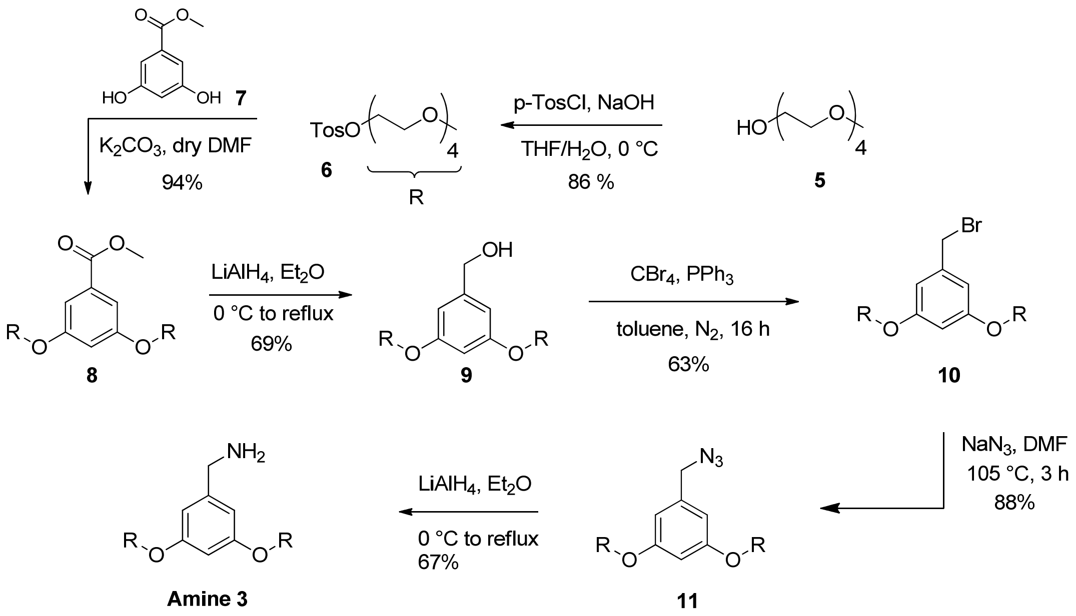

Scheme 3: Synthetic route to the benzyl amine **3**.

The synthesis of the branched alkyl amine **4** was accomplished in five steps according to the route shown in Scheme 4. The reduction of the commercially available trocosan-12-one (**12**) with LAH to trocosan-12-ol (**13**) and subsequent mesylation to compound **14** were performed according to literature.[120] The reaction of compound **14** with LiBr afforded bromide **15**, the latter was subsequently converted to nitrile **16** in yield 87% by using sodium cyanide. In the final step, the reduction of **16** with LAH gave the desired alkyl amine **4** in quantitative yield.

The peptide coupling reaction of PBI **4** precursor with the amines **2**, **3** and **4** in the presence of DIPEA and HATU afforded the desired PBIs **6**, **7** and **8**, respectively, in 37-63% yields. These new PBIs were characterized by ^{1}H NMR, high-resolution mass spectroscopy and, where possible, with elemental analysis or ^{13}C NMR. The detailed synthesis procedures and product characterization are reported in Experimental Section.

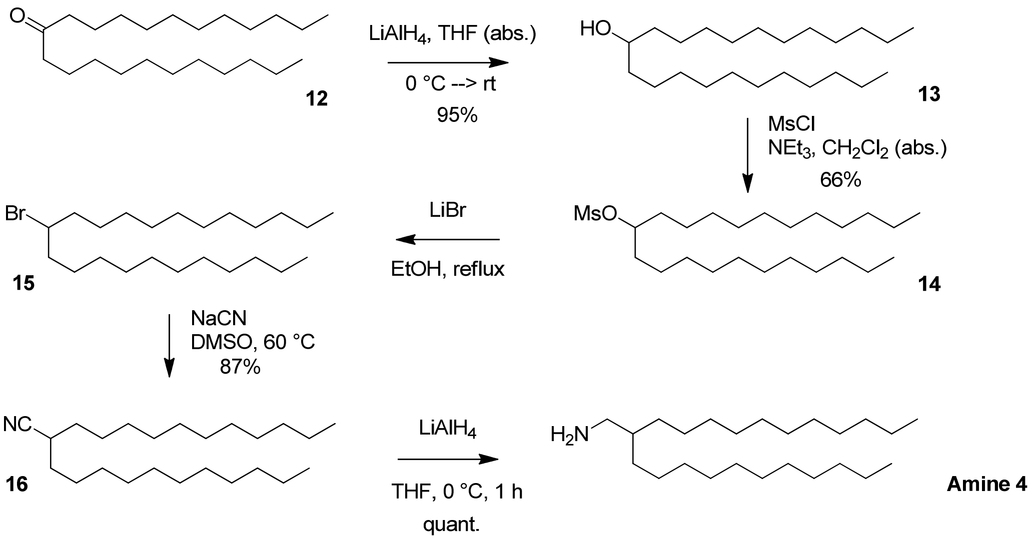

Scheme 4: Synthetic route to the branched alkyl amine **4**.

3.2.2 Concentration-dependent ^{1}H NMR studies of PBI 5

NMR spectroscopy is a powerful technique to follow the formation of supramolecular structures qualitatively and quantitatively as well. Thus, we have first studied the self-assembly of PBI **5** by concentration-dependent ^{1}H NMR spectroscopy in chloroform. Upon increasing the concentration of **5** from 6.5 x 10^{-6} M to 1.3 x 10^{-2} M, the signal (a broad singlet) of the perylene protons (H1) experiences a significant upfield shift from 8.7 to 7.7 ppm, indicating π-π-interactions between the PBI dyes (Figure 26).[14, 121] In contrast, the signal of the amide NH proton (partially overlapped by the solvent signal) undergoes a downfield shift upon increasing the concentration, pointing at the formation of hydrogen bonds.[122] The chemical shifts of the remaining more peripheral protons experience comparatively smaller changes ($\Delta\delta < 0.2$ ppm) upon concentration change (Figure 26). For instance, protons H5/5' and H7 in the terminal group show a small downfield shift at higher concentration which is suggestive of very weak C-H···O hydrogen bonding to the carbonyl oxygen atom, while the small upfield shift of H2 and H6 protons may relate to an aromatic shielding effect by the neighbouring PBI dye upon π-π-stacking. At higher concentration (1.3 x 10^{-2} M), the hydrogen bonding of the amide groups provoked a splitting of the diastereotopic protons H4 and H4' into two well separated signals (Figure 26).

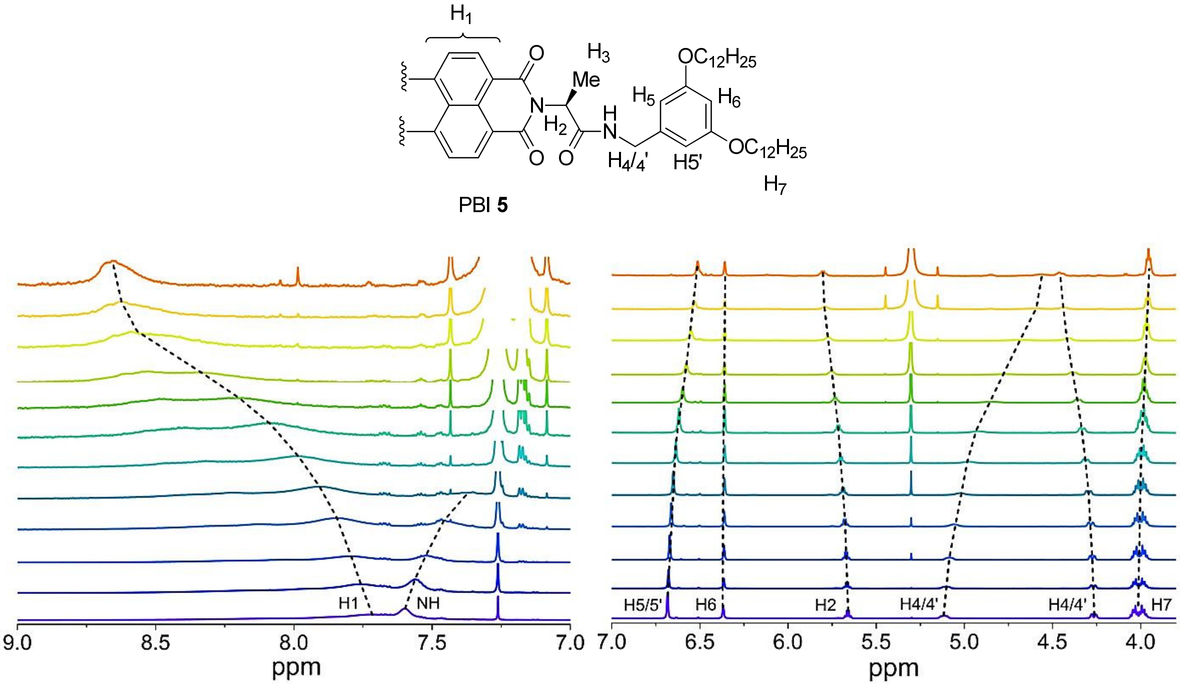

Figure 26: Structure of one half of the symmetric PBI **5** with the significant protons numbered and changes of the chemical shifts of PBI **5** protons H1 and NH (left) and H2, H4/4', H5/5', H6, and H7 (right) in concentration-dependent ^{1}H NMR spectra in CDCl3 at 298 K (1.3 x 10^{-2} M (bottom) – 6.5 x 10^{-6} M (top)).

The sharp signals observed in ^{1}H NMR spectra of PBI **5** over the measured concentration range suggest the formation of a π-stack of discrete size. Nonlinear least-squares analysis of the changes of the proton resonance signals shows a good fit to the monomer-dimer model (for representative examples see Figure 27).

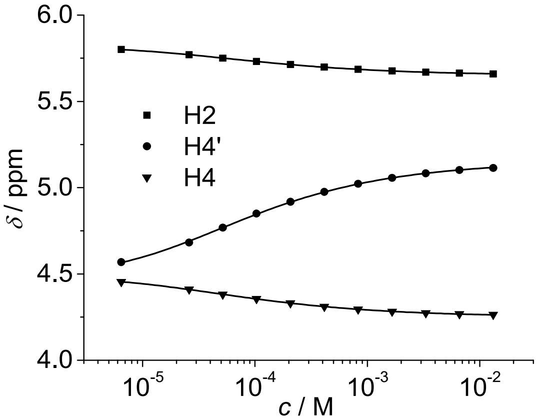

Figure 27: Fitting of the concentration-dependent chemical shift (δ) changes of protons H2 and H4/4' to the dimer model by means of nonlinear least-squares analysis as representative examples (correlation coefficient $R^2 = 0.999$).

Details on the fitting procedure are given in the Experimental Section. By the fitting of the chemical shift changes of each proton a dimerization constant K_2 in the range of about 1.2 x 10^4 M^{-1} could be obtained (Table 1). This high dimerization constant indicates an almost complete dimer formation of PBI **5** in chloroform at the highest considered concentration (1.3 x 10^{-2} M). Indeed, at this concentration, a degree of aggregation α_A above 93% was found (Table 1).

Table 1 Dimerization constants (K_2) and degrees of aggregation (α_A) obtained in the considered concentration range (6.5 x 10^{-6} – 1.3 x 10^{-2} M) from the best fitting of the chemical shift changes of the protons of PBI **5** in chloroform.

Protons	**H1**	**H2**	**H3**	**H4**	**H4'**	**H5/5'**
K_2 / 10^4 M^{-1}	1.0 ± 0.08	1.1 ± 0.04	1.0 ± 0.08	1.3 ± 0.06	1.4 ± 0.05	1.2 ± 0.03
α_A[a]	1 – 98%	11 – 95%	11 – 93%	13 – 94%	14 – 94%	12 – 95%

[a] α_A values at the lowest concentration of 6.5 x 10^{-6} M and the highest concentration of 1.3 x 10^{-2} M

Compared with the binding constants of simple PBIs in chloroform, e.g. < 20 M^{-1} for PBI **2** (Scheme 5),[13] the dimerization constant for PBI **5** is very high ($K_2 \approx 10^4$ M^{-1} in chloroform, Table 1), which suggests a favorable interplay of π-π-interactions and hydrogen bonds in dimer formation of PBI **5**.[13]

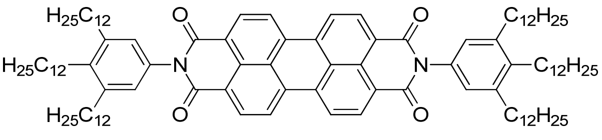

PBI **2**

Scheme 5: Structure of PBI **2** that showed isodesmic self-assembly in chloroform.[13, 101a, 101b, 123]

3.2.3 Evaluation of structure and size of PBI 5 aggregates

The structure and size of PBI **5** aggregates in solution have been explored by several spectroscopic techniques. PBI **5** has amide functional groups, which are potentially able to form intermolecular hydrogen bonds. The feasible hydrogen bond acceptors are carbonyl oxygens either of the imide or amide functional groups of another PBI molecule. As IR spectroscopy is a useful tool to distinguish between hydrogen bonded and free NH stretching vibrations of amide groups, spectra of PBI **5** were recorded at the concentration of 1.3 x 10^{-2} M and 4.1 x 10^{-4} M in chloroform (Figure 28).

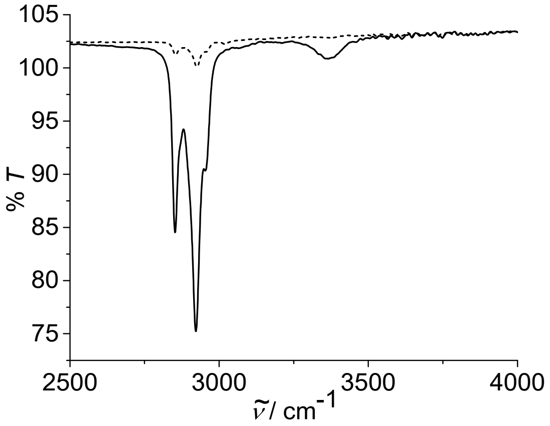

Figure 28: FT-IR spectra of PBI **5** at the concentrations of 1.3 x 10^{-2} M (solid line) and 4.1 x 10^{-4} M (dotted line) in chloroform at 293 K.

As displayed in Figure 28, in the extended region of the spectrum of the concentrated solution (solid line) two sets of signals could be observed. The set of two prominent signals at 2853 and 2922 cm^{-1} could be assigned to the CH stretching vibrations, while the small broad band at 3370 cm^{-1} to the hydrogen bonded NH stretching vibration. The stretching vibrations of free NH groups, which usually appear in the region between 3500 and 3600 cm^{-1},[100b] could not be detected, implying that all NH groups are involved in hydrogen bonds. At the lower concentration of 4.1 x 10^{-4} M, only weak bands are observed because of the instrumental limitations. However, no stretching vibrations of free NH groups could be observed at this concentration.

Since diffusion ordered (DOSY) NMR spectroscopy provides information on aggregate size, DOSY spectra of PBI **5** were measured in chloroform at a concentration of 1.3 x 10^{-2} M. The hydrodynamic radius of PBI **5** was then determined from the diffusion coefficient (D) according to the Stokes-Einstein equation:

$$D = \frac{k_B T}{6\pi\eta R} \tag{38}$$

with k_B as the Boltzmann constant, T as temperature, η as the viscosity of the solvent and R as the hydrodynamic radius.

The analysis of the DOSY spectrum of PBI **5** revealed a high value for the translational diffusion coefficient D of 2.96 10^{-10} m^2 s^{-1} in chloroform (Figure 29), pointing at the existence of small aggregates. According to the Stokes-Einstein equation a hydrodynamic diameter of 2.6 nm for PBI **5** dimers in chloroform was calculated. By measuring the distance between the most distant atoms in the *OPLS2001** (MacroModel) geometry optimized dimer structure (bearing methoxy instead of dodecyloxy substituents), an averaged size of the PBI **5** dimer of 1.8 nm was identified (see Figure 32). Taking into account the length of the alkoxy chains of ca. 1 nm, this size is in good agreement with that obtained from the DOSY NMR experiments.

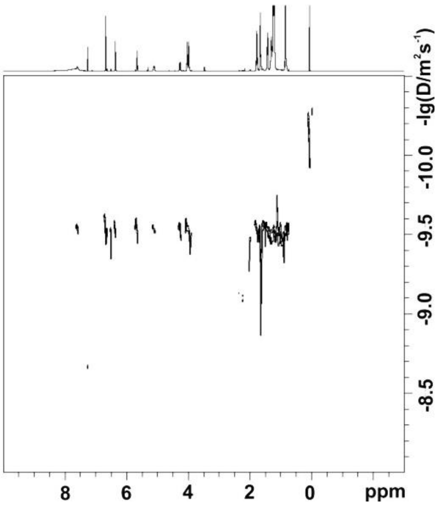

Figure 29: DOSY NMR spectrum (600 MHz, 293 K) of PBI **5** at $c = 1.3 \times 10^{-2}$ M in chloroform. The diffusion coefficients D [m^2 s^{-1}] are plotted in a logarithmic scale against the chemical shift δ [ppm].

As next, vapor pressure osmometry (VPO) measurements were performed since this method provides the possibility to measure the total osmolality of fluids and to calculate the molecular mass of compounds in aqueous and organic solutions. The solutions containing solutes have lower vapor pressure than the pure solvent which leads to a vapor pressure difference, and thus to a temperature difference (ΔT) during the measurement. This ΔT is proportional to the number of particles or number of moles dissolved in the solution. By this method concentrations or the molecular mass can be determined. For the determination of the mass, benzil was used as a standard. For the calibration, we measured voltages at a constant temperature of 303 K which are divided by the concentration (molalities) and plotted against the molality of the calibrant (see Figure 30, left). The linear regression leads to the calibration constant K_{cal} as the y-value at $c = 0$. The values for PBI **5** are plotted correspondingly to the calibration measurements. The c / g kg^{-1} value was obtained by dividing the initial weight of PBI **5** with the weight of the solvent (Figure 30, right).

The extrapolation provides K_{meas} value. The molecular weight (M) is then determined by the equation 39a. By dividing the obtained value M of 2955.6 g/mol with the molecular weight of PBI, the number of molecules (N) in the aggregate can be determined (eqn 39b). For PBI **5**, $N = 2$ is obtained by this method. This result corroborates the hydrodynamic diameter of PBI **5** dimer determined by DOSY measurements. It is to note that the latter method is often not very reliable because the DOSY technique is constructed for spherical molecules that may not be present in the case of the PBI dimer.

$$M = {}^{K_{cal}}/_{K_{meas}} = 2955.6\,{}^{g}/_{mol} \tag{39a}$$

$$N = {}^{M}/_{M_{PBI\,\mathbf{5}}} = 2.04 \tag{39b}$$

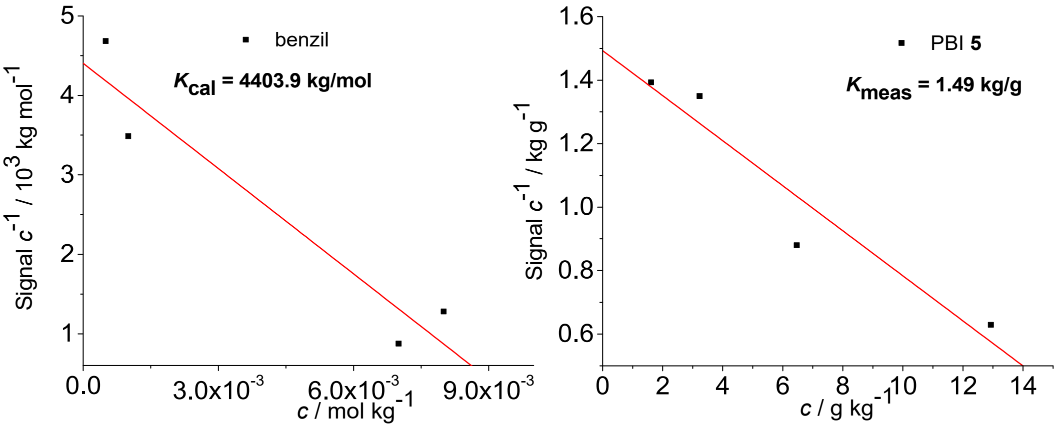

Figure 30: VPO measurements of benzil (calibration curve, left) and PBI **5** in chloroform at 303 K (1.3 x 10^{-2} to 1.7 x 10^{-3} M, right). The K values are interpolated y-values at x = 0.

To further substantiate the formation of dimers and to get structural information, we performed rotating-frame nuclear Overhauser effect (ROESY) NMR experiments with a sample of PBI **5** in chloroform at the highest concentration (1.3 x 10^{-2} M) applied for the ^{1}H NMR studies (Figure 31). If dimers were formed, cross-coupling between the protons of two PBI molecules in close vicinity should be noticed. Indeed, three weak signals are observed in the ROESY NMR spectrum for the intermolecular cross-coupling of protons H2 and H5/5', H2 and NH, and H3 and H5/5' (marked with red circles in the spectrum) which are attributed to intermolecular couplings. These results also corroborate the formation of dimers which can be well illustrated by the molecular model.

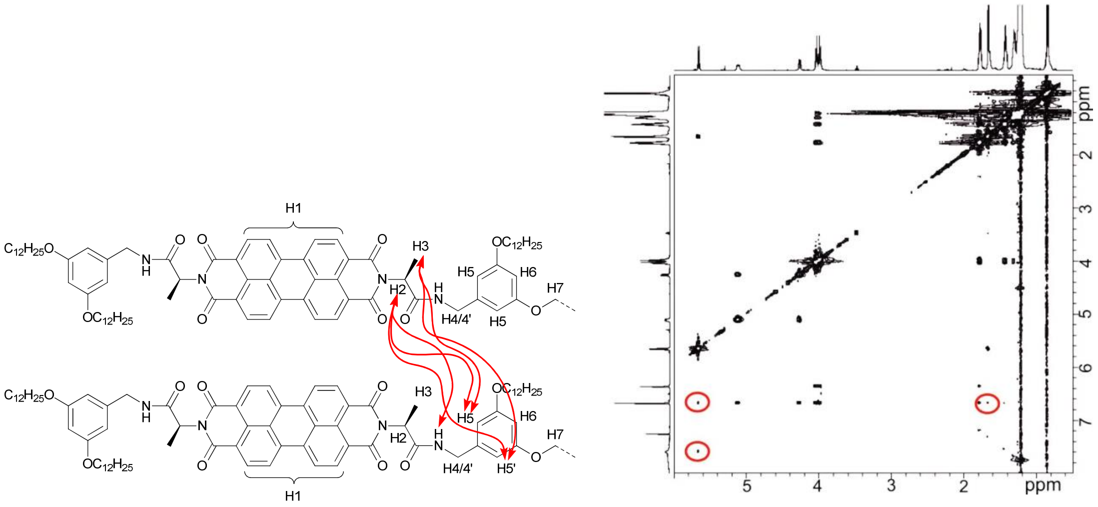

Figure 31: Significant part of the ROESY NMR spectrum (600 MHz, 298 K) of PBI **5** at $c = 1.3 \times 10^{-2}$ M in chloroform. ROESY correlations between the protons of two PBI **5** molecules are indicated with red arrows (left).

As mentioned before, geometry-optimized dimer structure of PBI **5** was modelled by *OPLS2001** (MacroModel). The analysis of the dimer structure (Figure 32) shows that the two PBI molecules with an interplanar distance of 3.3 Å, twist angle of 40° and slip angle of 83° form a bracket-like structure, in which the phenyl residues of the individual molecules clasp the counter molecule.

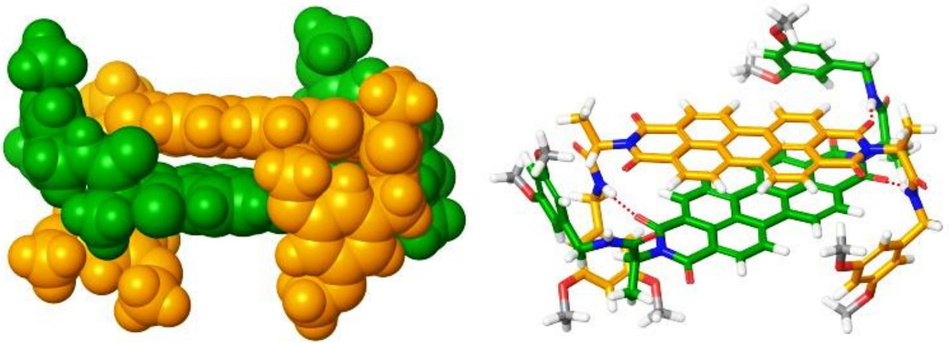

Figure 32: *OPLS2001** (MacroModel) geometry-optimized structure of self-assembled PBI **5** dimer with dodecyloxy chains replaced by methoxy groups.

The hydrogen bond contacts have already been verified by IR spectroscopy. However, the structural model shows that the bonds are formed between NH protons and carbonyl oxygen atoms of the other PBI molecule (illustrated by the dashed red lines), and not between the amide groups of the molecules (like in fiber formation) leading to the tightly bound dimer structure. According to the modelled dimer structure, the distances between the cross-coupled protons are close to the

5 Å limit for ROESY experiments. The rigid dimer structure obtained from the molecular modeling illustrates well that the phenyl rings and their long alkoxy chains shield the PBI cores, thus further π-π-stacking into larger aggregates becomes unlikely. Self-assembly into larger aggregates is even disfavored by sterical effects.

3.2.4 UV/Vis spectroscopic and isothermal calorimetric studies of PBI 5 self-assembly

Further studies on self-assembly of PBI **5** were performed by the commonly used concentration-dependent UV/Vis spectroscopy. Due to the good solubility of PBI **5** in chloroform, absorption studies could be performed over a wide concentration range from 1.6 x 10^{-6} to 1.3 x 10^{-2} M. At low concentrations, the spectra show a well-resolved vibronic structure with the 0-0, 0-1 and 0-2 transitions of the monomeric PBI molecule with the three most intensive bands at 528, 491 and 460 nm (Figure 33).

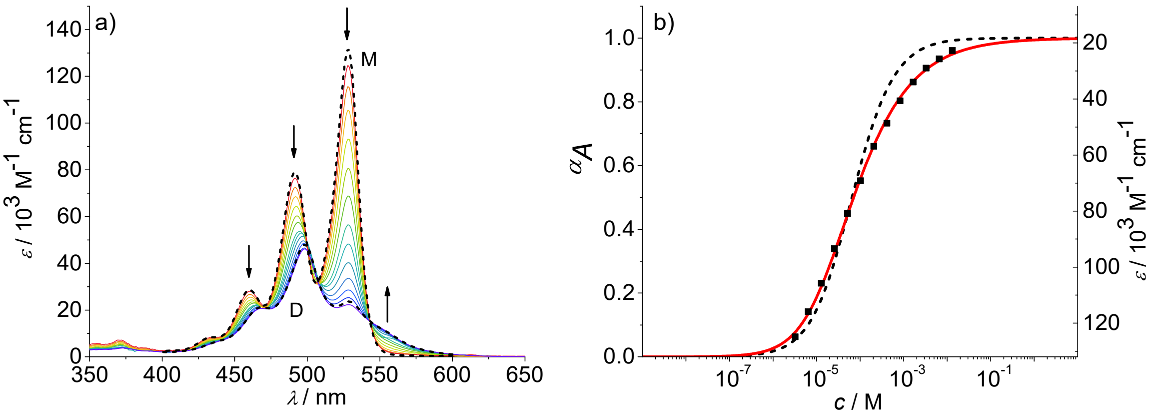

Figure 33: a) Concentration-dependent UV/Vis absorption spectra of PBI **5** in chloroform (c = 1.6 x 10^{-6} – 1.3 x 10^{-2} M) at 293 K. The dotted lines are the calculated monomer (M) and dimer (D) spectra from available data in terms of the dimer model. Arrows indicate the spectral changes upon increasing concentration. b) Analysis of the concentration-dependent data at 528 nm according to the dimer (red line) and isodesmic (black dashed line) aggregation models ($R^2 = 0.999$ for dimer fit). Left and right axes display the degree of aggregation and extinction, respectively, for a direct comparison.

The ratio of $A^{0\rightarrow0}/A^{0\rightarrow1}$ at the lowest concentration (1.6 x 10^{-6} M) is larger than 1.6, which is a characteristic spectral feature of monomeric bay-unsubstituted PBI dyes in solution.[124] Upon increasing the concentration, a transformation to a broadened spectrum with a significantly lower extinction coefficient at 498 nm occurs. The hypsochromic shift of the absorption maximum of 30 nm indicates a predominant H-type excitonic coupling, which was observed for many other bay-unsubstituted PBI dyes.[99d, 101a, 101b] Over the whole concentration range two clear isosbestic points at 543 and 507 nm are evident, indicating an aggregation equilibrium between two species. Nonlinear least-squares analysis of the concentration-dependent extinction coefficients at 529 nm using the monomer-dimer model (eqn (40)) reveals a good fit (see Figure 33b and Experimental Section).

$$\bar{\varepsilon}_{A^{0-0}} = \left((\varepsilon_{A^{0-0}})_{max} - (\varepsilon_{A^{0-0}})_{min}\right)\frac{\sqrt{8K_2c+1}-1}{4K_2c} + (\varepsilon_{A^{0-0}})_{min} \ , \tag{40}$$

where $(\varepsilon_{A^{0-0}})_{\mathrm{max}}$ and $(\varepsilon_{A^{0-0}})_{\mathrm{min}}$ are the maximum and minimum extinction coefficients as calculated by this analysis for the extinction of the monomer and dimer, respectively, and $\bar{\varepsilon}_{A^{0-0}}$ is the respective concentration-dependent extinction. With the obtained values for $(\varepsilon_{A^{0-0}})_{\mathrm{max}}$ and $(\varepsilon_{A^{0-0}})_{\mathrm{min}}$ the degree of aggregation α_A was calculated according to eqn (41).

$$\alpha_A = \frac{\bar{\varepsilon}_{A^{0-0}} - (\varepsilon_{A^{0-0}})_{max}}{(\varepsilon_{A^{0-0}})_{min} - (\varepsilon_{A^{0-0}})_{max}} \tag{41}$$

It is to note that the calculation of α_A as denoted in eqn (41) is only possible if just two distinct species exist. These species have to be distinguishable by clearly different extinction coefficients at a given wavelength.

By the nonlinear least-squares analysis of the apparent experimental extinction coefficients $\bar{\varepsilon}_{A^{0-0}}$ a dimerization constant K_2 of 1.41 x 10^4 M^{-1} ± 3.2 x 10^2 M^{-1} and a degree of dimerization α_A from 6% to 96% were calculated in the considered concentration regime between 1.6 x 10^{-6} and 1.3 x 10^{-2} M, indicating an almost complete transition from monomers to the dimer aggregate of PBI **5**. These results are in excellent agreement with those of ^{1}H NMR studies discussed before. Additionally, the calculated absorption spectra of monomer and dimer match very well with the respective experimental spectra (Figure 33a, black dashed lines).

To obtain some thermodynamic parameters for the dimerization process of PBI **5**, isothermal calorimetry (ITC) dilution experiments were performed (Figure 34, left). Dilution ITC experiments were performed by sequential injections of a concentrated solution of PBI **5** (7.5 x 10^{-3} M) into the stirred calorimeter cell which contained at the beginning pure chloroform (1.43 mL). An injection sequence of 127 x 1.5 μL in 2 min intervals was used. The positive heat flow signals during the dilution of the concentrated solution of PBI **5** indicate that the dissociation is an endothermic process meaning, on the other hand, that the association/aggregation of the PBI molecules is an exothermic process. The data were analyzed using MicroCal Origin and fitted to the dimer dissociation model (Figure 34, right). These experiments revealed an enthalpy ($\Delta H°$) value of 36.5 kJ mol^{-1} ± 1.5 kJ mol^{-1} for the dimer dissociation process. Accordingly, the exothermic dimerization of PBI **5** is, as expected for hydrogen-bonding and π-π-stacking, an enthalpically favoured process. It is to note that the dimerization constant ($\approx 10^4$ M^{-1}) obtained from ITC experiments agrees well with the value determined from UV/Vis experiments.

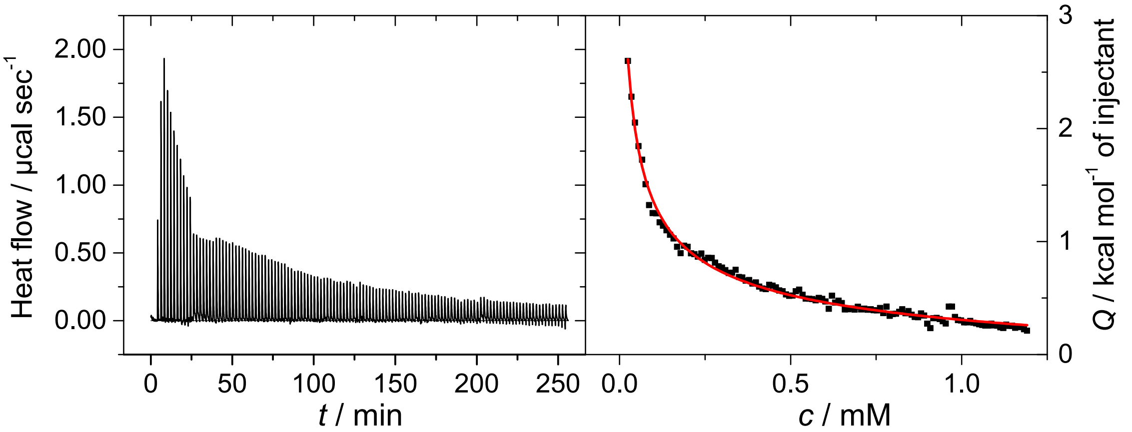

Figure 34: Calorimetric data for the dissociation process of the PBI **5** in chloroform. Left: Raw data for injection of PBI **5** with an injection concentration of 7.5 x 10^{-3} M into chloroform at 293 K (end concentration of PBI **5** in the cell is 1.1 x 10^{-3} M). Right: Integrated injection heats and fit (red line) to the dimer dissociation model with $K_{diss} = 0.0968 \pm 0.011$ mM ($K_{ass} = 1/K_{diss} = 1.0 \times 10^4$ M^{-1}) and (36.5 ± 1.5) kJ mol^{-1}.

3.2.5 Concentration-dependent UV/Vis studies of PBIs 6-9 in chloroform

The comprehensive investigations of the aggregation behavior of PBI **5** undoubtedly confirmed the formation of dimer aggregates in the particular solvent chloroform. The other PBIs **6**, **7**, **8** in this series and the reference compound **9** contain the same PBI scaffold functionalized with amide group derived from the amino acid L-alanine as the prime example PBI **5**. This structural feature is obviously responsible for the formation of discrete aggregate size due to π-π-stacking and hydrogen bonding, the latter is enabled by the amide groups. Keeping this in mind, it can be assumed that the PBIs **6-9** self-assemble in the same fashion as PBI **5** under similar conditions. However, differences in the binding strength can be expected owing to the different substituents in the periphery of the PBI dyes. This aspect has already been addressed in the literature for more simple PBI chromophores.[13] To confirm this anticipation, the PBI dyes **6-9** were subjected to concentration-dependent UV/Vis studies in chloroform.

The concentration-dependent UV/Vis studies of PBI **6** were performed in the concentration range of 6.4 x 10^{-6} – 1.2 x 10^{-2} M in chloroform (Figure 35a). Similar to the absorption studies of PBI **5** in chloroform, the spectra display a characteristic vibronic structure of the monomeric PBI dye at the concentration of 6.4 x 10^{-6} M. The 0-0, 0-1 and 0-2 transitions at 528, 491 and 460 nm exhibit slightly lower extinctions than those of PBI **5**. Upon increasing concentration to 1.2 x 10^{-2} M, the spectra experience a hypochromic and hypsochromic shift to 496 nm, indicating the formation of the H-type aggregates. The numerous isosbestic points at 541, 510 and 477 nm characterize the aggregation equilibrium between two species in solution.

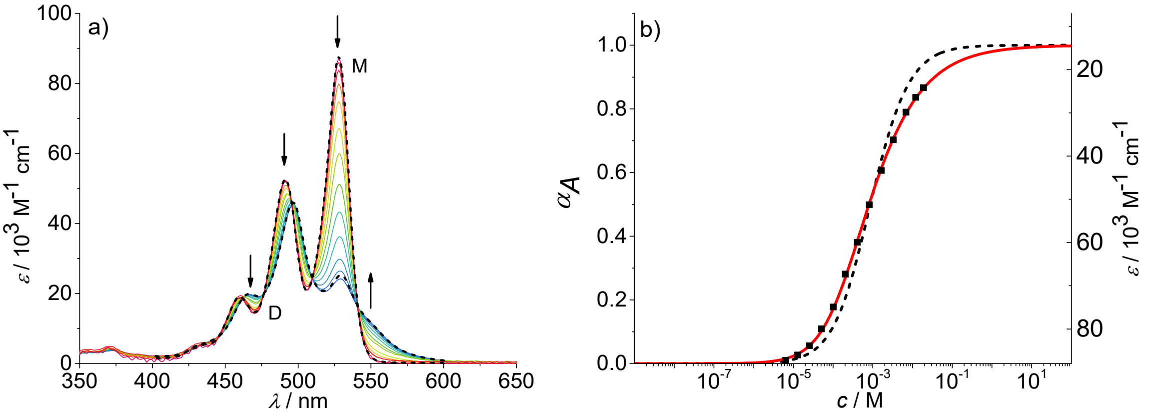

Figure 35: a) Concentration-dependent UV/Vis absorption spectra of PBI **6** in chloroform (c = 6.4 x 10^{-6} – 1.2 x 10^{-2} M) at 293 K. The dotted lines are the calculated monomer (M) and dimer (D) spectra from available data in terms of the dimer model. Arrows indicate the spectral changes upon increasing concentration. b) Analysis of the concentration-dependent data at 528 nm according to the dimer (red line) and isodesmic (black dashed line) aggregation models ($R^2 = 0.999$ for dimer fit). Left and right axes display the degree of aggregation and extinction, respectively, for a direct comparison.

The nonlinear least-squares analysis by means of the dimer model (see eqn (40) and (41) and Experimental Section) at the monomer absorption of 528 nm reveals a good fit to the model with a dimerization constant K_2 of 1.3 x 10^3 M^{-1} ± 40 M^{-1} (see Figure 35b). Moreover, the calculated absorption spectra of monomer and dimer (Figure 35a, black dashed lines) match very well with the corresponding experimental spectra.

The K_2 value of **6** is one order of magnitude lower than the one determined for PBI **5**. Additionally, the degree of aggregation α_A could only reach a maximum of 87% at the highest concentration applied. Unfortunately, higher concentration could not be achieved because of the high optical density of the solution and instrumental limitations. The aggregation tendency of PBI **6** is obviously lower than that of PBI **5**. Taking into account that the only difference between this two dyes is the absence of oxygen atoms in the dodecyl side chains of PBI **6**, it has to be considered that the oxygen contribute significantly to the aggregation strength. This effect has already been observed for more simple pair of PBIs **1** and **2**, even though the aggregation model is different for these PBIs.[13] The aggregation constant K of 2.6 x 10^2 M^{-1} of PBI **1** in chloroform is also one order of magnitude higher than that of PBI **2** (< 20 M^{-1}). This observation was attributed to charge-transfer interactions between the electron-poor PBI scaffold and electron-rich trialkoxyphenyl substituents of PBI **1**. This is most likely also the case for PBI **5**.

Next, the absorption properties of PBI **7**, which is equipped with ethylene glycol chains at the phenyl substituents, were investigated. For this purpose, the UV/Vis spectra in the concentration range of 6.9 x 10^{-6} – 1.2 x 10^{-2} M were recorded in chloroform (Figure 36a).

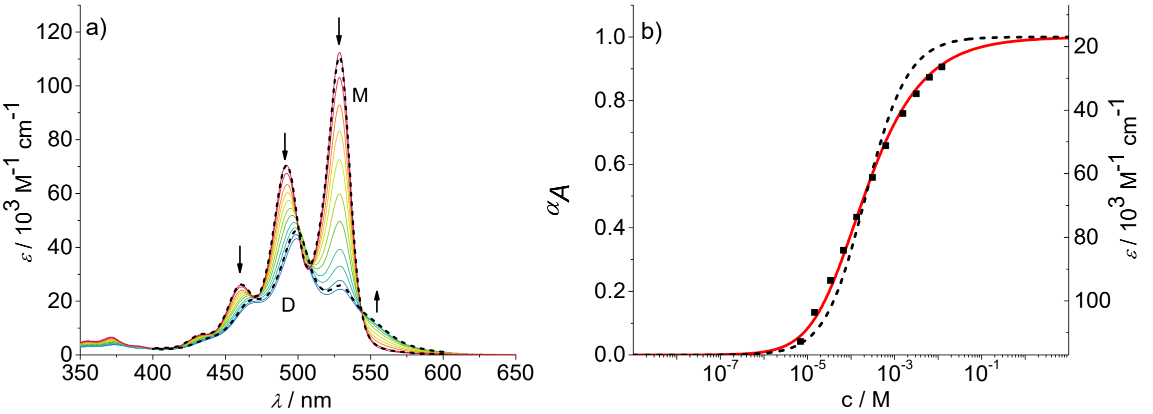

Figure 36: a) Concentration-dependent UV/Vis absorption spectra of PBI **7** in chloroform (c = 6.9 x 10^{-6} – 1.2 x 10^{-2} M) at 293 K. The dotted lines are the calculated monomer (M) and dimer (D) spectra from available data in terms of the dimer model. Arrows indicate the spectral changes upon increasing concentration. b) Analysis of the concentration-dependent data at 529 nm according to the dimer (red line) and isodesmic (black dashed line) aggregation models (R^2 = 0.998). Left and right axes display the degree of aggregation and extinction, respectively, for a direct comparison.

For PBI **7**, at low concentrations three absorption maxima at 529, 492 and 461 nm displaying extinction coefficients that are in the same range as those of **5** and **6** were observed revealing the presence of the monomeric dye. The increase of concentration leads to the formation of the H-type aggregate with the absorption maximum at 499 nm which is accompanied by a hypochromic shift of the absorption. The occurrence of two isosbestic points at 509 and 543 nm indicates an equilibrium between two species allowing similar analysis of the absorption data as in the previous cases (Figure 36b). Also for PBI **7**, the data could be fitted by the monomer-dimer model, leading to a dimerization constant K_2 of 6.0 x 10^3 M^{-1} ± 224 M^{-1}. Other than for PBI **6,** an almost complete transition from the monomer to the dimer could be reached in the applied concentration range substantiated by the aggregation degree α_A of 93%. Thus, both K_2 and α_A values lie between those of PBI **5** and **6**. As mentioned before, similar trend has already been observed for other PBI dyes equipped which similar side chains.[13]

Considering the aggregation behavior of PBI **1**, **2** and other simple PBI dyes, it can be assumed that the self-assembly tendency should be reduced in the absence of phenyl rings in peripheral substituents of the PBI dyes. Thus for the purpose of completeness, PBI dye **8** and the reference compound **9**[115] that contain branched and straight alkyl chains, respectively, in the periphery of the PBI scaffold are added to this study. The UV/Vis absorption spectra of PBI **9** have already been recorded by T. Rehm.[115] However, to acquire more detailed information, the measurements were repeated for broader concentration range with smaller concentration steps. UV/Vis absorption spectra of **8** and **9** were recorded in chloroform in the concentration range of 1.4 x 10^{-5} – 3.0 x 10^{-2} M and 4.7 x 10^{-6} – 1.9 x 10^{-2} M, respectively (Figure 37a and Figure 38a). For both dyes, at the respective lowest concentration, the transition maxima are located at 527, 490 and 459 nm with similar extinction coefficients. With increasing concentration, the formation of H-type aggregates with a hypsochromically shifted absorption maxima to 494 nm was observed. However, the spectra obviously keep the sharp vibronic structure at the respective highest concentration, implying that no complete transition to the aggregated species has been passed. It can be assumed that by further increase of the concentration the broad and less structured spectra might be obtained. But, the high optical density and the related instrumental limitations confine further investigations. Nevertheless, the analysis of the absorption data at the monomer absorption of 527 nm by means of the monomer-dimer model revealed a good fit for both PBIs **8** and **9** (Figure 37b and Figure 38b).

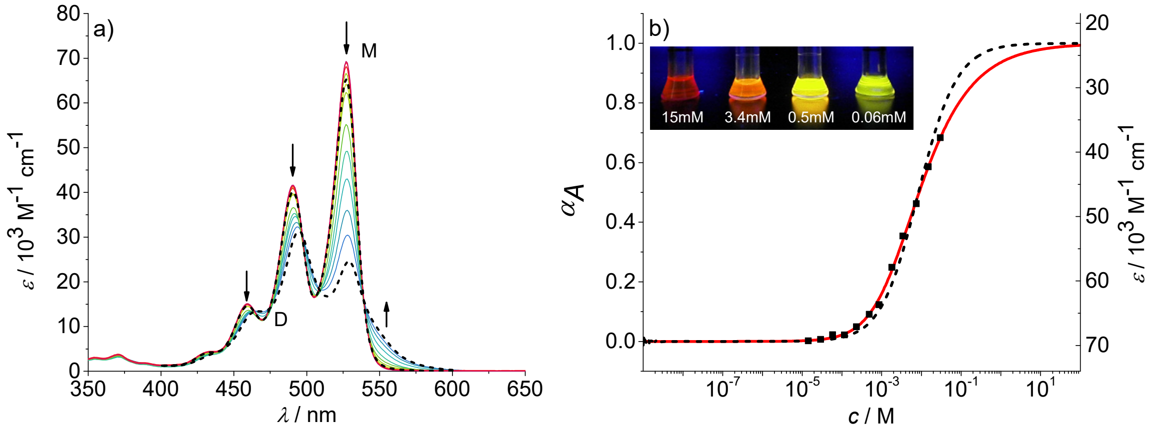

Figure 37: a) Concentration-dependent UV/Vis absorption spectra of PBI **8** in chloroform ($c = 1.4 \times 10^{-5} - 3.0 \times 10^{-2}$ M) at 293 K. The dotted lines are the calculated monomer (M) and dimer (D) spectra from available data in terms of the dimer model. Arrows indicate the spectral changes upon increasing concentration. b) Analysis of the concentration-dependent data at 527 nm according to the dimer (red line) and isodesmic (black dashed line) aggregation models ($R^2 = 0.998$ for dimer fit). Left and right axes display the degree of aggregation and extinction, respectively, for a direct comparison. Inset: photograph of PBI **8** in chloroform under UV light ($c = 5.8 \times 10^{-5}$, 4.9×10^{-4}, 3.4×10^{-3} and 1.5×10^{-2} M).

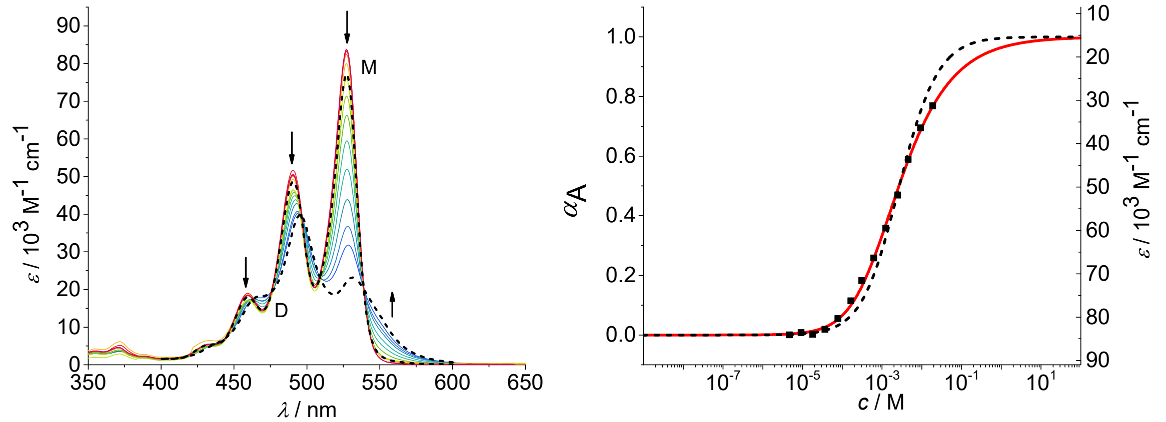

Figure 38: a) Concentration-dependent UV/Vis absorption spectra of PBI **9** in chloroform ($c = 4.7 \times 10^{-6} - 1.9 \times 10^{-2}$ M) at 293 K. The dotted lines are the calculated monomer (M) and dimer (D) spectra from available data in terms of the dimer model. Arrows indicate the spectral changes upon increasing concentration. b) Analysis of the concentration-dependent data at 527 nm according to the dimer (red line) and isodesmic (black dashed line) aggregation models ($R^2 = 0.998$ for dimer fit). Left and right axes display the degree of aggregation and extinction, respectively, for a direct comparison.

Thus, dimerization constants K_2 of 1.1×10^2 M^{-1} for PBI **8** and 3.8×10^2 M^{-1} for PBI **9** could be determined. Although both K_2 values are in the same range, the aggregation tendency of PBI **8** is somewhat reduced due to the larger sterical impact imposed by the branched alkyl substituents. The obtained degrees of aggregation α_A reach the values of 68% and 77%, respectively, which confirm the incomplete aggregation at the highest applicable concentrations.

3.2.6 Comparison and critical evaluation of the aggregation constants of PBIs 5-9

All the studied PBIs **5-9** have structural similarities, i.e. a core-unsubstituted π-scaffold and amide groups at the imide positions, which should lead to similar self-assembly behavior of these PBIs. Undoubtedly, the π-π-interactions are important driving forces for the π-stacking the PBI molecules. But, the limitation of the aggregate size is significantly dependent on the positions and the orientation of the amide substituents. In the case of PBIs **5-9**, the intermolecular hydrogen bonding pattern is realized from the NH amide group to the carbonyl oxygen of the PBI core of the other molecule and not to the carbonyl oxygen atom of the amide group. This feature is decisive for the formation of discrete dimers instead of large aggregates as observed previously for structurally quite similar organogelator.[116]

The obtained dimerization constants (K_2) and the degrees of aggregation (α_A) are summarized in Table 2. The comparison of the data reveals that the highest K_2 value of 1.4 x 10^4 M^{-1} is obtained for PBI **5** bearing didodecyloxyphenyl group and the lowest one of 1.1 x 10^2 M^{-1} for PBI **8** that contains branched long alkyl chains directly at amide nitrogen. The phenyl substituent at amide group contribute accordingly significantly to the self-assembly tendency as the K_2 values for PBI **5-7** are appreciably higher than those for **8** and **9**. Moreover, the included oxygen atoms in the side chains increase the stability of the bimolecular complex of the PBIs. This structural variation has obviously a positive impact on the applicable range of concentration and the related scope of spectroscopically observable species in solution.

Table 2: Dimerization constants (K_2) and degrees of aggregation (α_A) of the PBIs **5-9** in chloroform. The aggregation constants (K) of the PBIs **5-9** determined by the isodesmic model are presented for comparison.

PBI	5	6	7	8	9
K_2 / M^{-1}	1.4 x 10^4	1.3 x 10^3	6.0 x 10^3	1.1 x 10^2	3.8 x 10^2
α_A[a]	6 – 96%	1 – 87%	7 – 93%	1 – 68%	1 – 77%
K[b] / M^{-1}	-	9.8 x 10^2	-	1.2 x 10^2	3.5 x 10^2

[a] α_A value at the lowest concentration and at the highest concentration, respectively.
[b] aggregation constants K derived from isodesmic model.

At this point, it is important to highlight some interesting aspects of the way how the obtained spectroscopic data are processed and which difficulties are encountered. The issue of experimental limitations, which often lead to misinterpretation of the data, has already been addressed in Chapter 2. The application of several spectroscopic methods can circumvent this problem. However, some of the above assigned data are good examples to demonstrate that misunderstanding and wrong evaluation of the data may occur if only UV/Vis absorption spectroscopy is chosen to rely on.

In Section 3.2.5, the procedure for fitting the absorption data has been explained. In the above presented fitting curves only one wavelength was analyzed but also other wavelengths were subjected to the fitting procedure leading to the same results (data not shown). The obtained absorption data at different wavelengths were fitted by the monomer-dimer and isodesmic model revealing that they clearly match with the monomer-dimer model rather than with the isodesmic model in the case of PBIs **5** and **7** (Figure 39a, b). In contrast, for PBIs **6**, **8** and reference **9**, the difference between the two applied mathematical models is not that obvious anymore (Figure 39c, d, e).

In the case of PBIs **5** and **7**, the data points in the low and high concentration region evidently make the difference between the two applied models. The data points of PBIs **6**, **8** and **9** cover mainly the region of low concentrations which hamper the discrimination of the two models. The two last data points at the highest concentrations of PBI **6** (1.9×10^{-2} and 1.2×10^{-2} M, Figure 39c) imply that the dimer model fits better, but surely, the used concentration range is too narrow to draw a safe conclusion.

In Chapter 2, the issue of the indistinguishability of the monomer-dimer and isodesmic model was addressed from the mathematical point of view. As discussed there, these models can not be distinguished when $2K_2 = K$ is valid. During the analysis of the numerous absorption data and the experience made in our group, we realized that in the most cases, where the data could not be distinguished by these two models, very similar aggregation constants were obtained for the same system by different models.[125] This is, indeed, the case for PBIs **6**, **8** and **9** since both models (monomer-dimer and isodesmic) afforded nearly identical aggregation constants of 9.8×10^2 M^{-1} ± 88 M^{-1}, 1.2×10^2 M^{-1} ± 9 M^{-1} and 3.5×10^2 M^{-1} ± 34 M^{-1}, respectively, for these PBIs (see Table 2). The only possibility to estimate which mathematical model fits the best for these three systems is the extension of the study to other techniques such as NMR spectroscopy. Also, global analysis of the absorption spectra might be helpful to overcome this problem which is addressed in the next Chapter.

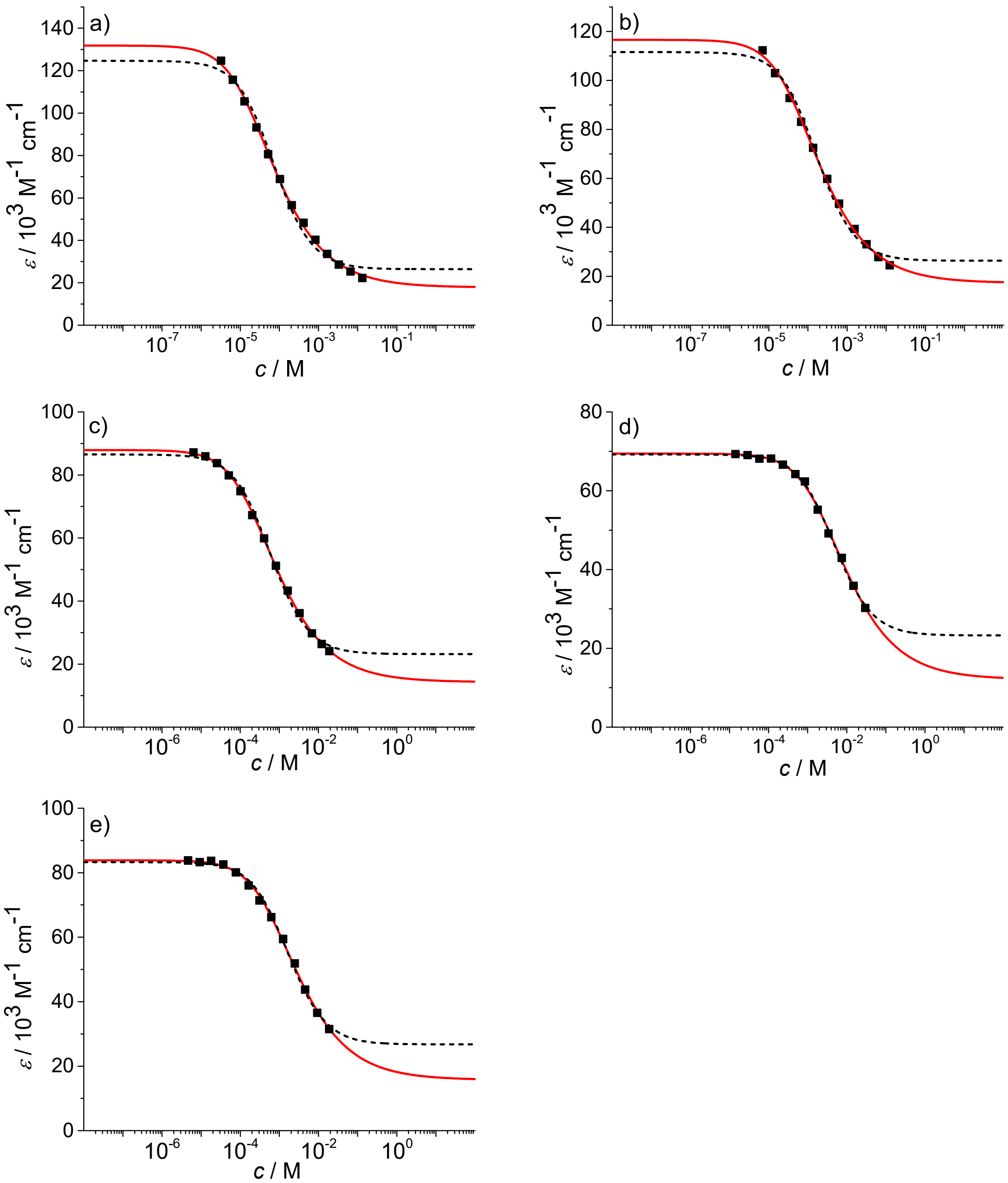

Figure 39: Analysis of the concentration-dependent absorption data of PBI **5** (527 nm), b) PBI **7** (529 nm), c) PBI **6** (528 nm), d) PBI **8** (527 nm) and e) **9** (527 nm) according to the dimer (red line) and the isodesmic aggregation models (black dashed line).

3.2.7 ^{1}H NMR and DOSY NMR studies of PBIs 6-8

Due the structural similarities of PBIs **6-8** with **5**, it is reasonable that the former ones also form dimers in chloroform. To confirm the results obtained by UV/Vis absorption spectroscopy, ^{1}H NMR and DOSY studies for PBI **6** were performed in chloroform whereas for PBIs **7** and **8** only DOSY spectra were recorded. The concentration-dependent ^{1}H NMR spectra of PBI **6** were recorded in the concertation range of 5.2 x 10^{-6} M to 1.1 x 10^{-2} M in chloroform (Figure 40a,b).

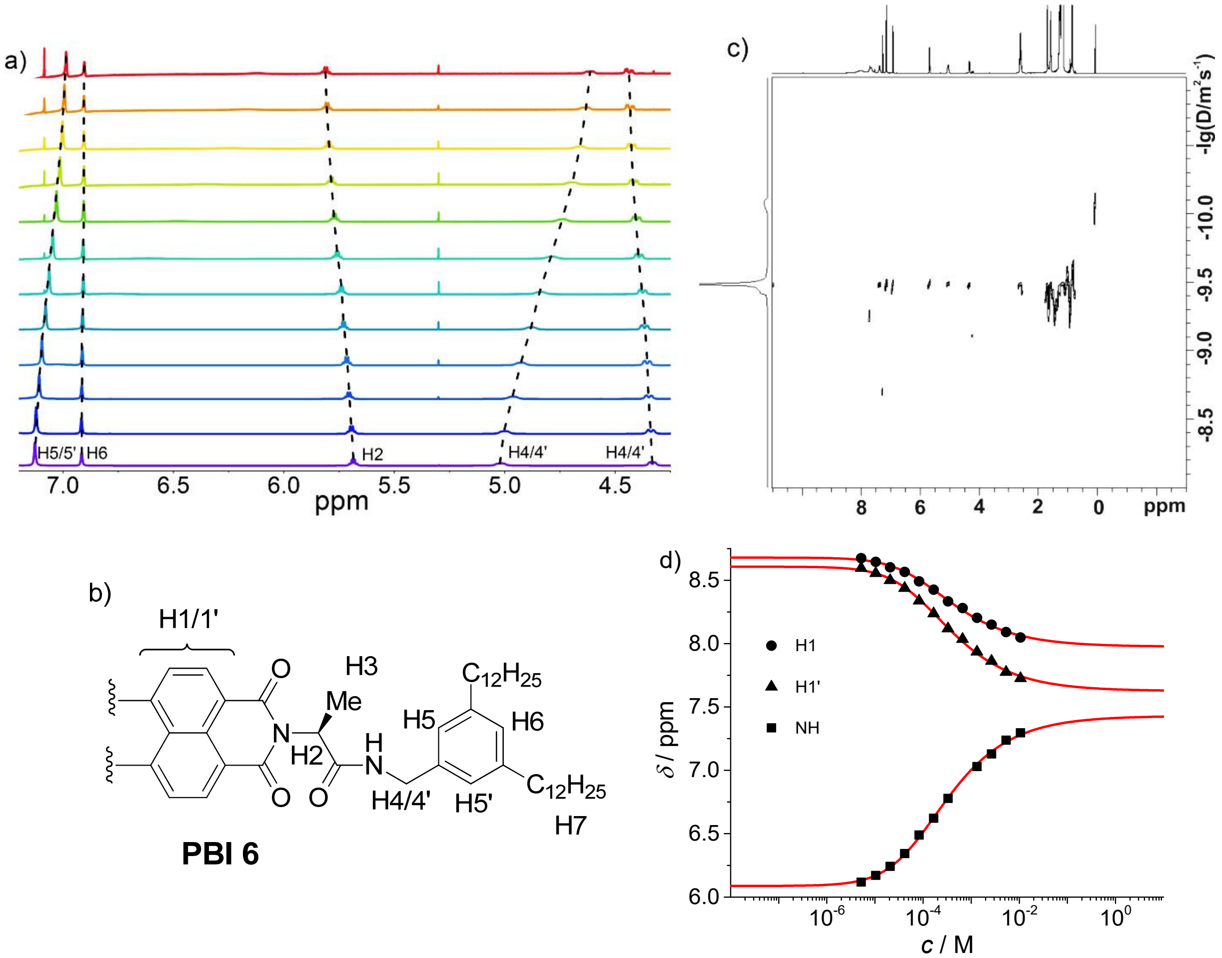

Figure 40: a) Changes of the chemical shifts of PBI **6** protons (H2, H4/4', H5/5' and H6) in concentration-dependent ^{1}H NMR spectra (600 MHz) in $CDCl_3$ at 298 K (1.1 x 10^{-2} M (bottom) – 5.2 x 10^{-6} M (top)). b) Structure of one half of the symmetric PBI **6** with numbering of significant protons. c) DOSY NMR (600 MHz NMR) spectrum of PBI **6** at c = 2.0 x 10^{-2} M in chloroform at 293 K. The diffusion coefficients D [m^2 s^{-1}] are plotted in a logarithmic scale against the chemical shift δ [ppm]. d) Fitting of the concentration-dependent chemical shift (δ) changes of protons H1 and NH to the dimer model by means of nonlinear least-squares analysis as representative examples (correlation coefficient R^2 = 0.999).

As expected, the spectra display almost the same signal patterns as those of PBI **5** (*vide supra*). With increasing concentration, the signals of the perylene protons (H1/1') show a considerable upfield shift from 8.7 and 8.6 ppm to 8.1 and 7.7 ppm, respectively, indicating π-π-interactions between the PBI molecules (black symbols in Figure 40d). [14, 121] On the other hand, the signal of the amide NH proton is displaced to the downfield, from 6.1 to 7.3 ppm, implying the formation of hydrogen bonds (black symbols in Figure 40d). [122] As in the case of PBI **5**, the signals of other protons of **6** exhibit only small changes ($\Delta\delta < 0.4$ ppm, see Figure 40a,b). The downfield shift of H5/5'upon increasing concentration is referred to the weak C-H···O hydrogen bonding to the carbonyl oxygen atom. The similar upfield shift of H2 and H6 protons can be attributed to the aromatic shielding effect by the neighboring PBI dye upon π-π-stacking. Also for PBI **6**, the diastereotopic protons H4 and H4' are separated into two signals.

The nonlinear least-squares analysis of the changes of the proton signals displayed a good fit to the monomer-dimer model nicely corroborating the results of UV/Vis spectroscopic studies as illustrated in Figure 40d for the perylene protons H1/1' and the amide NH proton. Details on the fitting procedure are given in the Experimental Section. The fitting of the chemical shift changes of the protons of PBI **6** indicated in the structure (Figure 40b) afforded an average dimerization constant K_2 of 3 x 10^3 M^{-1} and the degree of aggregation α_A between 1 and 90% (Table 3).

Table 3 Dimerization constants (K_2) and degrees of aggregation (α_A) obtained in the considered concentration range (5.2 x 10^{-6} – 1.1 x 10^{-2} M) from the best fitting of the chemical shift changes of the protons of PBI **6** in chloroform.

Protons	**H1**	**H1'**	**NH**	**H2**	**H3**	**H4**	**H4'**	**H5/5'**
K_2 / 10^3 M^{-1}	2.7 ± 0.1	2.9± 0.1	3.4± 0.1	2.9 ± 0.1	3.5 ± 0.1	3.1 ± 0.1	3.5 ± 0.1	2.9 ± 0.1
α_A[a]	1 – 90%	1 – 90%	2 – 90%	1 – 90%	2 – 92%%	1 – 90%	2 – 92%	1 – 89%

[a] α_A value at the lowest concentration of 5.2 x 10^{-6} M and the highest concentration of 1.1 x 10^{-2} M, respectively.

These values are in the same range as those obtained from UV/Vis absorption studies. Thus, both spectroscopic methods provide congruent results on the aggregation process of PBI **6**. Since the PBIs **7** and **8** possess similar structural features, i.e. bay-unsubstituted PBI core and chiral amide function at the imide positions, we assume that these PBIs will show very similar concentration-dependent ^{1}H NMR spectral changes as observed for PBI **6**. Accordingly, the K_2 and α_A values should reflect those obtained by concentration-dependent UV/Vis absorption studies (Table 1). Therefore, we evade performing concentration-dependent ^{1}H NMR measurements for PBIs **7** and **8**. However, DOSY NMR experiments of these PBIs **7** and **8**, in comparison with PBI **6** (Figure 40c) were performed in chloroform at the concentration of 1.1 x 10^{-2} M 2.8 x 10^{-2} M, respectively, to verify the formation of dimer aggregates (Figure 41). According to the Stokes-Einstein equation (39), a hydrodynamic diameter of 2.4 nm for PBI **6** and 2.1 nm for PBI **7** were calculated. Unfortunately, the DOSY spectrum of PBI **8** is of inferior quality because for some of the significant protons no signal was observed in the spectrum (Figure 41, right). Nevertheless, considering those belonging to the protons of the molecule, a hydrodynamic diameter of 2.6 nm could be calculated. The hydrodynamic diameters for PBIs **6**, **7** and **8** are in the same range as observed previously of the dimer of PBI **5** (2.6 nm), and thus the formation of higher aggregates can be excluded for the former PBIs as well. Interestingly, the mass of the dimeric species of PBI **8** could be detected in the high resolution mass spectrum (Figure 42 in the Appendix) which was not visible in the mass spectra of the related aryl-substituted PBIs **5**-**7**.

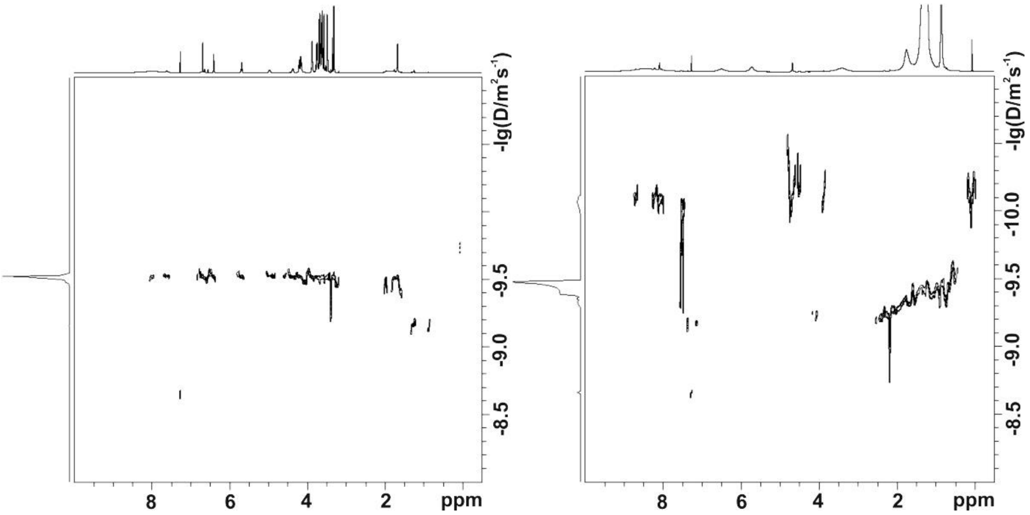

Figure 41: DOSY NMR (600 MHz) spectrum of PBI **7** (left) and **8** (right) at *c* = 1.1 x 10^{-2} M and 2.8 x 10^{-2} M, respectively, in chloroform at 293 K. The diffusion coefficients D [m^2 s^{-1}] are plotted in a logarithmic scale against the chemical shift δ [ppm].

In addition, the reference PBI dye **9** was subjected to concentration-dependent ^{1}H NMR studies, revealing a dimerization constant K_2 of 149 – 345 $M^{-1} \pm 20$ M^{-1} which is in accordance with the value obtained from the UV/Vis absorption studies.[115] A hydrodynamic diameter of 2.1 nm was determined at the highest concentration of 2.5 x 10^{-2} M confirming the formation of small aggregates. Further studies such as 2D NMR and FT-IR spectroscopy, verified the formation of dimers due to π-π-interactions and formation of hydrogen bonds. [115]

3.3 Conclusion

The comprehensive study of the aggregation behavior of PBI **5** showed clearly that introduction of amide substituents at certain positions in the side chains of the PBI dye can direct the self-assembly pathway towards discrete dimers. In particular, the selection of the solvent for the aggregation studies is of high importance because the polarity of the solvent defines the solvation of the molecules. The interplay of π-π interactions and hydrogen bonding of PBI **5** specify the structure of the dimer aggregates in chloroform. Various spectroscopic techniques such as UV/Vis and NMR spectroscopy, and VPO and ITC experiments as well as molecular modelling verified the structure and the size of the PBI **5** dimer. The aggregation behavior of structurally similar PBI dyes **6-8** and reference PBI **9** resemble that of the more extensively studied PBI **5.** The concentration-dependent UV/Vis absorption and the NMR studies clearly showed the formation of dimers caused by π-π-interactions and hydrogen bonds.

The structure-aggregation property relationship of PBIs **5-9** could be elaborated in a comparative manner. The bay-unsubstituted PBI core and the hydrogen bonding amide functions derived from the amino acid L-alanine are responsible for the formation of discrete and highly defined dimers of these PBIs. The combination of π-π-interactions and hydrogen bonding functional groups in the most appropriate positions in the molecule ensures particularly the limitation to the dimer aggregate and exclude further growth.

3.4 Experimental section

3.4.1 Materials and Methods

Solvent and reagents were purchased from commercial sources, unless otherwise stated, and purified and dried according to standard procedures.[126] Reactions were monitored by TLC on silica gel plates (Merck TLC silica gel 60 F254 aluminum sheets). All perylene bisimide derivatives are colored compounds, thus no additional visualization of the spots was necessary. Column chromatography was performed on silica gel (MerckSilica 60, particle size 0.04 – 0.063 mm). Gel permeation chromatography was performed on a Shimadzu Recycling GPC system (LC-20AD prominence pump; SPDMA20A, prominence diode array detector) using three preparative columns (JAIGEL-1H, JAIGEL-2H und JAIGEL-2.5H) from Japan Analytical Industries Co., Ltd. and chloroform as eluent. NMR experiments were conducted on a Bruker Avance 400 or Bruker DMX 600 spectrometer with TMS or residual undeuterated solvent as internal standard. The chemical shifts are reported in ppm relative to TMS or residual undeuterated solvent as internal standard (δ scale). The apparent coupling constants J are given in Hertz (Hz). The following abbreviations are used to describe the signal fine structure: s = singlet, d = doublet, t = triplet, q = quartet, quint = quintet, dd = doublet of doublets, m = multiplet, bs = broad singlet, and bm = broad multiplet. Melting point was measured on a polarization microscope BX41 of Olympus equipped with MGW Lauda RM6 cooling systems and is uncorrected. All FT-IR spectra were measured on a FT/IR-4100 spectrophotometer (Jasco). High-resolution electrospray ionization (ESI) mass spectra were measured on a MicroTOF Focus instrument (Bruker Daltronik GmbH).

The UV/Vis absorption spectra were recorded in conventional quartz cells of appropriate path length on a Perkin Elmer Lambda 35 spectrophotometer equipped with a Peltier system for temperature control. Chloroform of spectroscopic grade were used for the measurements.

The vapor pressure osmometry (VPO) measurements were performed at 303 K on a KNAUER osmometer with a universal temperature measurement unit. Benzil was used as standard to generate calibration curves in terms of R (ohm) vs. molal osmotic concentration in the respective solvent.

Isothermal titration calorimetry (ITC) measurements were recorded on a VP-ITC instrument from MicroCal. Dilution ITC experiments were performed by sequential injections of a concentrated solution of PBI **5** (7.5 x 10^{-3} M) into the stirred calorimeter cell (1.43 mL) which contains at the beginning pure solvent. An injection sequence of 127 x 1.5 µL in 2 min intervals was used. The data were analyzed using MicroCal Origin.

3.4.2 Synthesis of *N*,*N*'-(L-alanyl(3,5-bis(dodecyloxy)benzyl))perylene-3,4:9,10-tetracarboxylic acid bisimide (PBI 5)

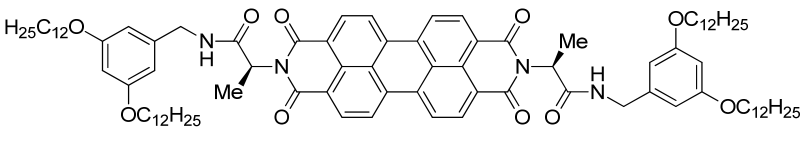

PBI **5**

A suspension of the L-alanine functionalized PBI **4**[117] (112 mg, 0.210 mmol, 1 equiv.), 3,5-bis(dodycyloxy)benzylamine **1**[14] (300 mg, 0.630 mmol, 3 equiv.), *O*-(7-azabenzotriazol-1-yl)-*N*,*N*,*N*',*N*'-tetramethyluronium hexafluorophosphate (HATU) (119 mg, 0.313 mmol, 1.5 equiv.) and catalytic amount of *N*,*N*-diisopropylethylamine (DIPEA) (1.6 mL) was stirred in dichloromethane (20 mL) at room temperature for 16 h. After removal of the solvent in vacuo, the crude product was purified by column chromatography (SiO_2, CH_2Cl_2/MeOH/NEt_3, *v/v/v* = 30:1:0.5) and recycling GPC. Yield: 137 mg (0.095 mmol, 45%) of a red solid; MW ($C_{92}H_{128}N_4O_{10}$) 1450.02 g/mol; m.p.: 88 – 90 °C; ^{1}H NMR (400 MHz, $CDCl_3$): δ = 8.04 (bm, 10H, perylene protons and N*H*), 6.56 (d, ^4J = 2.0 Hz, 4H, Ph-*H*), 6.36 (t, ^4J = 2.4 Hz, 2H, Ph-*H*), 5.69 (q, ^3J = 6.8 Hz, 2H, C*H*), 4.99 (m, 2H, CH_2), 4.38 (dd, ^3J = 4.0 Hz, ^2J = 14.8 Hz, 2H, CH_2), 4.00 (m, 8H, CH_2), 1.78 (quint, ^3J = 6.8 Hz, 8H, CH_2), 1.69 (d, ^3J = 6.8 Hz, 6H, CH_3), 1.45 (m, 8H, CH_2), 1.23 (m, 64H, CH_2), 0.86 (t, ^3J = 6.8 Hz, 12H, CH_3); HRMS (ESI pos.), calculated for ($[M+H]^+$: 1449.97032, found *m/z* = 1449.97386; calculated for ($[M+Na]^+$): 1471.95227, found *m/z* = 1471.95227; elemental analysis calculated (%) for $C_{91}H_{126}N_4O_{10}$: C 76.11, H 8.84, N 3.90; found: C 75.98, H 8.90, N 3.61; λ_{max}($CHCl_3$)/nm 528, 491 and 460 (ε / M^{-1} cm^{-1}134000, 81500 and 29900).

3.4.3 Synthesis of 2-undecyltridecan-1-amine (4)

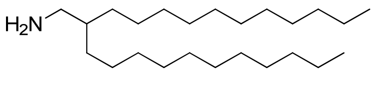

Amine 4

$LiAlH_4$ (315 mg, 6.44 mmol, 3 equiv.) was suspended in 5 mL anhydrous THF and cooled to 0 °C. 2-undecyltridecanenitrile (**16**) (751 mg, 2.15 mmol, 1 equiv.) in 7.5 mL anhydrous THF was added to the mixture within 10 min. After the addition, the reaction mixture was stirred for 1 h at room temperature. The mixture was poured into 30 mL iced water and extracted with ethyl acetate (3 x 30 mL). The combined organic phases were dried over Na_2SO_4. After removal of the solvent in vacuo a colorless oil of amine **4** (758 mg, 2.14 mmol) was obtained in quantitative yield. Yield: 751 mg (2.12 mmol, 99%); MW ($C_{24}H_{51}N$) 353.40 g/mol; ^{1}H NMR (400 MHz, $CDCl_3$): δ = 8.32(bs, 2H, NH_2), 2.88 (m, 1H, C*H*), 1.32 (m, 40H, CH_2), 0.88 (t, ^3J = 6.9 Hz, 6H, CH_3); HRMS (ESI pos.), calculated for ($[M+H]^+$: 354.4094, found *m/z* = 354.4099.

3.4.4 Synthesis of *N*,*N*'-(L-alanyl(3,5-bis(dodecyl)benzyl))perylene-3,4:9,10-tetracarboxylic acid bisimide (PBI 6)

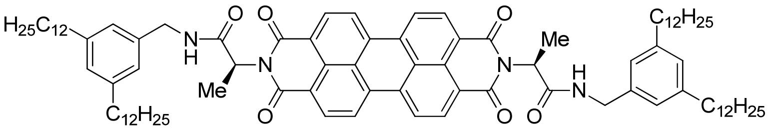

PBI **6**

A suspension of the L-alanine functionalized PBI **4**[117] (116 mg, 0.210 mmol, 1 equiv.), 3,5-bis(dodecyl)benzylamine **2**[118] (289 mg, 0.651 mmol, 3 equiv.), *O*-(7-azabenzotriazol-1-yl)-*N*,*N*,*N*',*N*'-tetramethyluronium hexafluorophosphate (HATU) (200 mg, 0.526 mmol, 2.4 equiv.) and catalytic amount of *N*,*N*-diisopropylethylamine (DIPEA) (1.6 mL) was stirred in anhydrous dichloromethane (20 mL) at room temperature for 3.5 h. After removal of the solvent in vacuo, the crude product was purified by column chromatography (SiO_2, CH_2Cl_2/MeOH/NEt_3, *v/v/v* = 98:1.5:0.5). Yield: 163 mg (0.117 mmol, 54%) of a red solid; MW ($C_{92}H_{128}N_4O_6$) 1386.02 g/mol; m.p.: 80 – 82 °C; ^{1}H NMR (400 MHz, $CDCl_3$): δ = 8.00 (bm, 8H, perylene protons), 7.10 (s, 4H, Ph-*H*), 6.91 (s, 2H, Ph-*H*), 5.71 (q, ^3J = 6.9 Hz, 2H, C*H*), 4.95 (dd, ^3J = 7.1 Hz, ^2J = 15.1 Hz, 2H, CH_2), 4.35 (dd, ^3J = 4.2 Hz, ^2J = 14.7 Hz, 2H, CH_2), 2.59 (m, 8H, CH_2), 1.70 (d, ^3J = 6.4 Hz, 6H, CH_3) 1.23 (m, 80H, CH_2), 0.86 (t, ^3J = 6.8 Hz, 12H, CH_3); HRMS (ESI pos.), calculated for ($[M+Na]^+$: 1408.9727, found *m/z* = 1408.9761; elemental analysis calculated (%) for $C_{92}H_{128}N_4O_6$: C 79.72, H 9.31, N 4.04; found: C 79.40, H 9.31, N 3.97; λ_{max}($CHCl_3$)/nm 528, 491 and 460 (ε / M^{-1} cm^{-1}86900, 52400 and 19300).

3.4.5 Synthesis of *N*,*N*'-(L-alanyl(3,5-bis(2,5,8,11-tetraoxatridecan-13-yloxy)benzyl) perylene-3,4:9,10-tetracarboxylic acid bisimide (PBI 7)

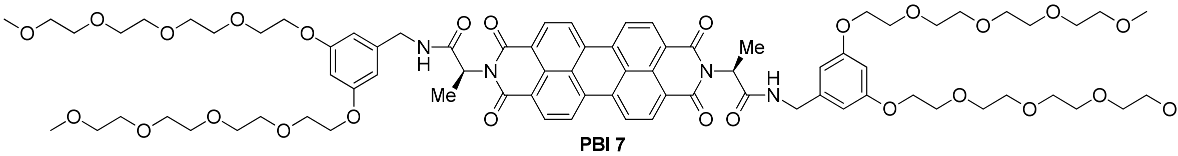

PBI 7

A suspension of the L-alanine functionalized PBI **4**[117] (100 mg, 0.187 mmol, 1 equiv.), 3,5-bis((2,5,8,11-tetraoxatridecan-13-yloxy)phenyl)methanamine **3**[119] (291 mg, 0.561 mmol, 3 equiv.), *O*-(7-azabenzotriazol-1-yl)-*N*,*N*,*N*',*N*'-tetramethyluronium hexafluorophosphate (HA-

TU) (142 mg, 0.374 mmol, 2 equiv.) and catalytic amount of *N*,*N*-diisopropylethylamine (DIPEA) (5.4 mL) was stirred in anhydrous DMF (20 mL) at room temperature for 16 h. After removal of the solvent in vacuo, the crude product was purified by column chromatography (SiO_2, CH_2Cl_2/MeOH *v/v* = 98:5) and recycling GPC. Yield: 179 mg (0.116 mmol, 63%) of a red viscous solid; MW ($C_{80}H_{104}N_4O_{26}$) 1537.69 g/mol; glass transition at 63 °C (DSC analysis); ^1H NMR (400 MHz, MeOD): $\delta = 7.47$ (bs, 4H, perylene protons), 6.90 (bs, 4H, perylene protons), 6.58 (bs, 4H, Ph-*H*), 6.43 (bs 2H, Ph-*H*), 5.50 (bquart., $^3J = 6.6$ Hz, 2H, C*H*), 4.58 (bd, $^2J = 15.3$ Hz, 2H, CH_2), 4.35 (bs, $^2J = 15.3$ Hz, 2H, CH_2), 4.15 (bs, 8H, CH_2), 3.83 (bs, 8H, CH_2), 3.62 (m, 40H, CH_2), 3.48 (m, 8H, CH_2), 3.31 (s, 12H, CH_3) partially covered by the MeOD peak, 1.73 (bd, $^3J = 6.6$ Hz, 6H, CH_3) ppm; ^{13}C NMR (100 MHz, MeOD): $\delta = 171.6$, 163.5, 161.6, 143.2, 133.5, 131.4, 128.4, 124. 6, 123.7, 122.7, 107.0, 101.7, 73.0, 71.8, 71. 6, 71. 4, 70. 9, 68.9, 59.2, 51.9, 44.3, 15.2 ppm; HRMS (ESI, pos.), calculated for $[M+Na]^+$ $m/z = 1559.6831$, found $m/z = 1559.6819$; $\lambda_{max}(CHCl_3)$/nm = 529, 492 and 461 (ε / M^{-1} cm^{-1} 112000, 70500 and 26100); λ_{max} (MeOH)/nm = 523, 488 and 457 (ε / M^{-1} cm^{-1} 138000, 89000 and 33300).

3.4.6 Synthesis of *N*,*N*'-(L-alanyl(2-undecyltridecan-1-amine))perylene-3,4:9,10-tetracarboxylic acid bisimide (PBI 8)

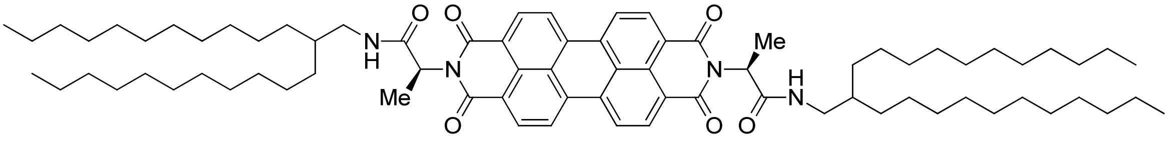

PBI **8**

A suspension of the L-alanine functionalized PBI **4**[117] (133 mg, 0.248 mmol, 1 equiv.), 2-undecyltridecan-1-amine **4** (264 mg, 0.746 mmol, 3 equiv.), *O*-(7-azabenzotriazol-1-yl)-*N*,*N*,*N*',*N*'-tetramethyluronium hexafluorophosphate (HATU) (189 mg, 0.498 mmol, 2 equiv.) and catalytic amount of *N*,*N*-diisopropylethylamine (DIPEA) (1.6 mL) was stirred in anhydrous dichloromethane (20 mL) at room temperature for 4 h. After removal of the solvent in vacuo, the crude product was purified by column chromatography (SiO_2, CH_2Cl_2/MeOH/NEt_3, *v/v/v* = 97:2.5:0.5) and HPLC (CH_2Cl_2/MeOH, *v/v* = 98.2:0.8).

Yield: 110 mg (0.0912 mmol, 37%) of a red solid; MW ($C_{78}H_{116}N_4O_6$) 1205.78 g/mol; m.p.: 69–71 °C; ^1H NMR (400 MHz, $CDCl_3$): $\delta = 8.66$ (bs, 4H, perylene protons), 8.56 (bs, 4H, perylene protons), 5.94 (bs, 2H, C*H*), 5.71 (bq, ^3J = 6.9 Hz, 2H, C*H*), 3.35 (bm, 2H, CH_2), 3.24 (bm, 2H, CH_2), 1.76 (d, ^3J = 6.9 Hz, 6H, CH_3) 1.25 (m, 80H, CH_2), 0.86 (t, ^3J = 6.8 Hz, 12H, CH_3); HRMS (ESI pos.), calculated for ([*M*+*Na*]$^+$: 1227.8788, found *m/z* = 1227.8771; calculated for ([*M*+*K*]$^+$: 1243.8527, found *m/z* = 1243.8516; elemental analysis calculated (%) for $C_{78}H_{116}N_4O_6$: 77.70, H 9.70, N 4.56; found: C 76.96, H 10.00, N 4.56; λ_{max}($CHCl_3$)/nm 527, 490 and 459 (ε / M^{-1} cm^{-1} 69000, 41600 and 14900).

3.4.7 Application of the monomer-dimer model[6] on ^{1}H NMR data

The mathematical description of the equilibrium between monomer (M) and dimer (D) in solution can be written as $M + M \rightleftharpoons D$, and the equilibrium constant K_2 can be expressed as:

$$K_2 = [M_2\ ]/\ [M]^2 = [c_D\ ]/c_M^2 \qquad \text{(E1)}$$

where $[M] = c_M$ is the concentration of the monomers and $[M_2] = c_D$ the concentration of the dimers.

The fraction of monomers α_M (eqn (E2)) and the fraction of aggregated species α_A (eqn (E3)) can be calculated as follows:

$$\alpha_M = c_M\ /c \qquad \text{(E2)}$$

$$\alpha_A = 1 - \alpha_M \qquad \text{(E3)}$$

where c denotes the total concentration.

Considering $c = 2c_D + c_M$ the following equations for c_M, α_M and α_A as functions of K_2 and c can be derived:

$$c_M = \frac{\sqrt{8K_2c+1}-1}{4K_2} \qquad \text{(E4)}$$

$$\alpha_M = \frac{\sqrt{8K_2c+1}-1}{4K_2c} \qquad \text{(E5)}$$

$$\alpha_A = \frac{4K_2c+1-\sqrt{8K_2c+1}}{4K_2c} \qquad \text{(E6)}$$

Using eqn (E5) and (E6) to describe the change of the chemical shifts with concentration, the dimer model can be fitted to the NMR data of PBI **5** in chloroform in the concentration range 6.5 x 10^{-6} M – 1.3 x 10^{-2} M yielding the results presented in the main text (Figure 27 and Table 1).

3.5 Appendix

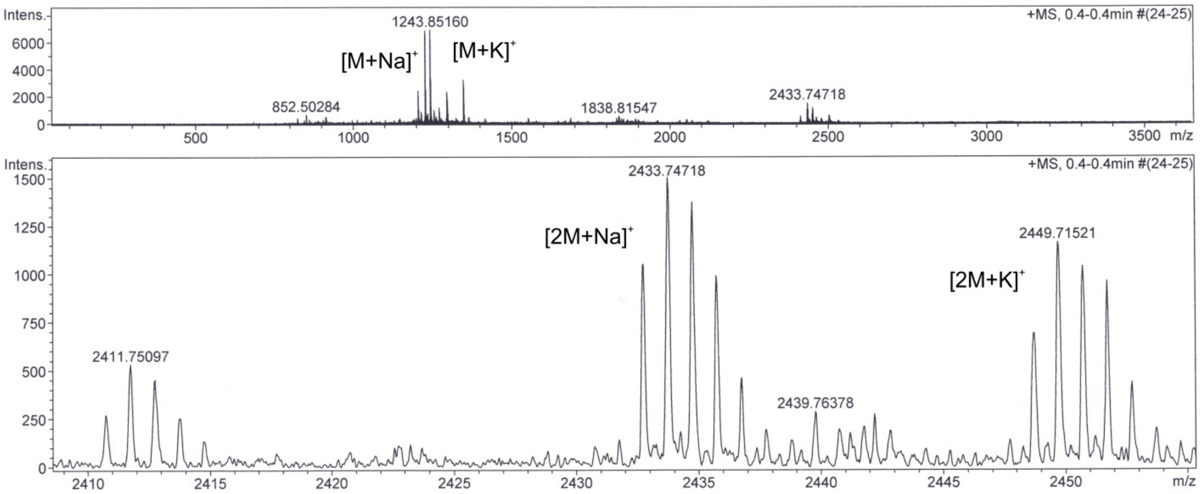

Figure 42: HRMS spectrum of PBI **8**.

Chapter 4

Anti-cooperative supramolecular polymerization: a new K_2-K model applied to the self-assembly of perylene bisimide dye proceeding via well-defined hydrogen-bonded dimers *

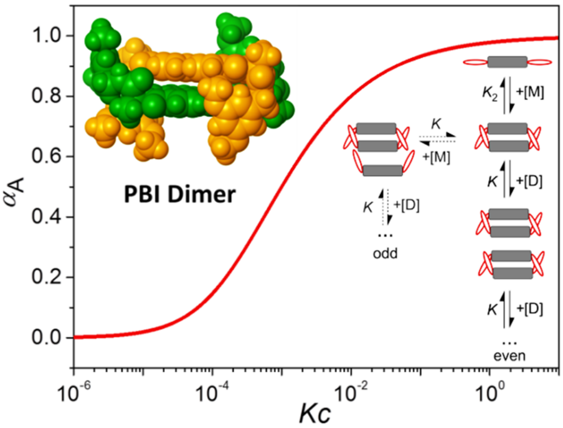

Abstract: A perylene bisimide dye bearing amide functionalities at the imide positions derived from amino acid L-alanine and a dialkoxy-substituted benzyl amine self-assembles into tightly bound dimers by π-π-stacking and hydrogen bonding in chloroform. In less polar or unpolar solvents like toluene and methylcyclohexane, and in their mixtures, these dimers further self-assemble into extended oligomeric aggregates in an anti-cooperative process in which even numbered aggregates are highly favoured. The stepwise transition from dimers into oligomers can not be properly described by conventional K_2-K model, and thus a new K_2-K aggregation model has been developed, which interprets the present anti-cooperative supramolecular polymerization more appropriately. The newly developed K_2-K model will be useful to describe self-assembly processes of a plethora of other π-conjugated molecules that are characterized by a favored dimer species.

---

*This chapter was published by Jana Gershberg, Franziska Fennel, Thomas H. Rehm, Stefan Lochbrunner, Frank Würthner, *Chem. Sci.* **2016**, *7*, 1729-1737. The new mathematical model was developed by Franziska Fennel. Reproduced and adopted with permission from the Royal Society of Chemistry.

4.1 Introduction

Supramolecular polymers of $(A)_n$-type are formed by molecules with two self-complementary binding sites when the concentration range is reached at which the interaction enthalpy between the receptor groups can overcome the entropic penalty associated with self-association. [6, 95] As π-conjugated aromatic molecules have two faces that may act as self-complementary binding sites for self-assembly by dispersion and electrostatic forces, it is thus no surprise that the majority of supramolecular polymers of such systems consist of columnar π-stacks (scheme Figure 43). Interestingly, for many decades the so-called isodesmic or equal *K* model ($K = K_2$, violet curve in Figure 43a and c) was preferably applied to analyze concentration- and temperature-dependent supramolecular polymerizations through π-π-stacking[127] for all kinds of dye aggregates, for instance, phthalocyanines,[99e] hexabenzocoronenes,[128] conjugated oligomers,[129] and perylene bisimides.[13, 101a, 101b, 123] Only about a decade ago, the generality of isodesmic growth was questioned and experimental proof was provided that numerous isodesmic aggregation processes, including many of those reported previously, follow indeed a cooperative nucleation-elongation growth model in which the formation of smaller aggregates is considerably less favoured than the further elongation into extended aggregates (blue curves in Figure 43a and d).[6, 8, 95-96, 116a, 130] While the mathematical models to evaluate cooperative self-assembly processes are obviously more complicated than those applicable to isodesmic self-assembly,[94e, 104c, 131] it is at least experimentally quite easy to distinguish between isodesmic and cooperative systems because the latter are characterized by a critical temperature or concentration at which monomers self-assemble directly into larger oligomers, see Figure 43a, d).

The most simple nucleation-elongation self-assembly process where dimerization affords a dimer nucleus (characterized by the dimerization constant K_2), followed by more favorable further aggregation (characterized by elongation constant *K,* Figure 43), the so-called K_2-K model (eqn (42)) can be applied to concentration-dependent studies.

$$Kc = (1-\sigma)Kc_M + \frac{\sigma K c_M}{(1-Kc_M)^2} \qquad \text{with} \quad \alpha_A = 1 - \frac{Kc_M}{Kc} \qquad (42)$$

Here, c is the total concentration, c_M the monomer concentration and $\sigma = K_2/K$ the cooperativity factor (see the section K_2-K model in Experimental Section for details).[102-103] The main physical variable which describes cooperative growth is the cooperativity factor σ. In order to allow a comparison between different systems the degree of aggregation is often plotted in dependence of the concentration c normalized with the elongation constant K, as this result in a degree of aggregation α_A which only depends on the cooperativity factor σ and is independent on the aggregation constants.

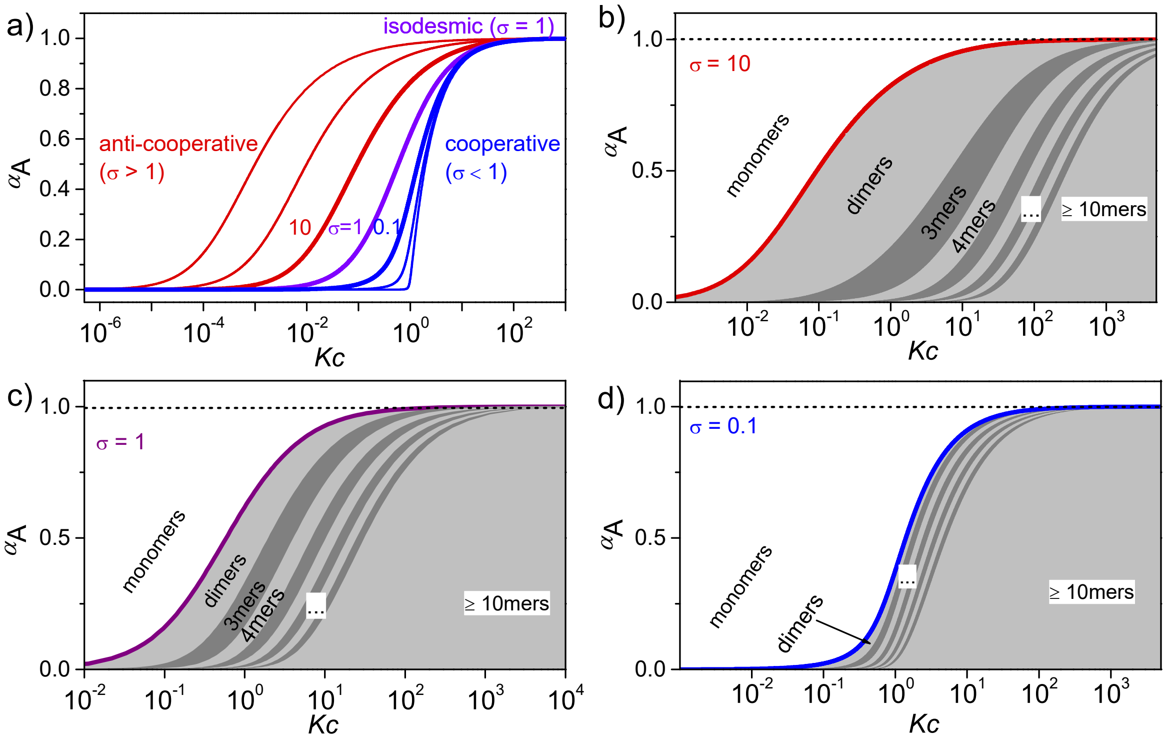

Figure 43: a) Schematic illustration of a K_2-K aggregation process. Plot of the fraction of aggregated molecules α_A as a function of the normalized concentration Kc with different σ values according to eqn (42). For the curves from left to right $\sigma = 10^3$, 10^2, 10, 1, 10^{-1}, 10^{-2}, and 10^{-4} were applied.[6] b), c) and d) Oligomer size distribution for representative σ values for anti-cooperative (b, σ = 10), isodesmic (c, σ = 1), and cooperative (c, $\sigma = 0.1$) aggregation with a nucleus size of s = 2. In the anti-cooperative case a strong prevalence of the dimer is observed for a large concentration regime, whereas in the cooperative case long oligomers are formed as soon as the critical concentration $Kc = 1$ is reached. In the isodesmic case a continuous size distribution can be observed.

For a compound with known aggregation constants K_2 and K, the concentration of molecules in aggregates with a size of n, c_n can then be calculated by

$$c_n = nK_2K^{n-2}c_M^n \tag{43}$$

Thus, the plot of the degree of aggregation $\alpha_n = c_n/c$ against the concentration leads to a continuous distribution of aggregate sizes (see Figure 43b, c and d). As exemplified for $\sigma = 0.1$ and $\sigma = 10$ in Figure 43b and d there is either an accumulation of dimers in the intermediate concentration range (Figure 43) or an instantaneous formation of extended aggregates (Figure 43d).

Remarkably, while a broad variety of cooperative self-assembly processes ($\sigma < 1$) have meanwhile been characterized in great detail, work demonstrating the opposite case of anti-cooperative growth ($\sigma > 1$) is scarce.[8, 105, 131a, 132] This is even more surprising because a large number of molecules are known to self-assemble into dimers for instance by hydrogen bonding,[133] or electrostatically driven π-stacking of dipolar dyes.[99a, 134]

Accordingly, the situation of anti-cooperative growth with preferential dimerization (see area marked as dimer in Figure 43b) and subsequent less favorable growth into larger aggregates (denoted as grey areas) should be more prevalent than known to date. During our investigations of such an anti-cooperative aggregation process we became aware of some problems inherent in the common K_2-K model for the case of anti-cooperative growth. For instance, for anti-cooperative aggregation with a nucleus size of two a dominance of aggregates consisting of an even number of monomers should be prevail due to the stacking of dimers. This circumstance is not covered at all by eqn (42) and (43) because these equations do not distinguish between even and odd numbered aggregates. Therefore, the development of a more elaborate model for the proper analysis of anti-cooperative K_2-K self-assembly processes is necessary.

Perylene bisimide (PBI) dyes appear as good choice to derive a suitable model system for the elucidation of anti-cooperative self-assembly for many reasons. First, PBIs exhibit a pronounced aggregation strength enabling aggregate formation in dilute solutions.[11a, 135] Second, their self-assembly by π-π-stacking can be easily monitored by concentration- or temperature-dependent changes in UV/Vis absorption spectra. And third, PBI derivatives show a variable aggregation behavior in dependence on the substituents. For instance, there are several PBI derivatives such as **2** (for structure see Scheme 6) whose aggregation has been proven to be isodesmic, i.e. showing equal binding constants K for the stepwise growth of the aggregate,[13, 101a, 101b, 123] whereas some more sophisticated structures were shown to self-assemble into dimers.[14, 87, 99d, 100a, 114] Such PBI dimers were realized, for example, by the introduction of sterically highly demanded substituents,[14, 99d] embedding of PBI dimer aggregates into the minor groove of DNA[87, 114] to prohibit further growth, and by strengthening of the dimerization by metal ion-crown ether[100a] or hydrogen-bonding interactions.[100b] Accordingly, towards our envisioned goal, and inspired by the hydrogen-bonded example of Syamakumari et al.,[100b] we have designed PBI **5** (Scheme 6) for which the dimerization should be privileged with regard to further aggregation by additional intermolecular hydrogen bonds between two π-stacked PBI molecules.

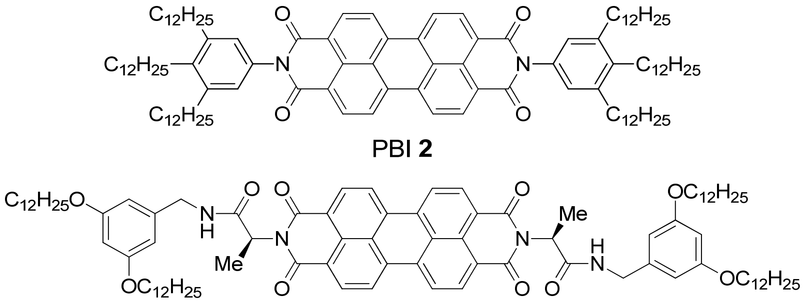

PBI **2**

PBI **5**

Scheme 6: Structure of PBI **2** that showed isodesmic self-assembly,[13, 101a, 101b, 123] and newly designed PBI **5**.

4.2 Results and discussion

4.2.1 Self-assembly in toluene

In the previous concentration-dependent UV/Vis spectroscopic studies in chloroform only dimers of PBI **5** could be observed within the explored concentration range (see Chapter 2). This can be rationalized by the fact that all available amide NH units are involved in the formation of the dimer, hence further aggregate growth is not supported anymore by hydrogen bonding, and/or even hindered by the orientation of the didodecyloxyphenyl substituents in the bimolecular complex (see Figure 32, Chapter 2). Our previous work on the aggregation of PBI dyes by only π-π-stacking interactions suggested that the binding strength can be considerably increased by reducing the solvent polarity. For instance, aggregation constants of $K < 20\ \mathrm{M}^{-1}$ in chloroform, $K = 590\ \mathrm{M}^{-1}$ in toluene, and $K = 9.7 \times 10^4\ \mathrm{M}^{-1}$ in methylcyclohexane were determined for the non-hydrogen bonding PBI **2**.[13] Thus, a rational choice of solvent would provide the possibility to tune the aggregation properties and disclose the transition from discrete dimers to oligomers, and finally to extended aggregates. Therefore, we performed aggregation studies of PBI **5** in less polar toluene by concentration-dependent ($c = 2.0 \times 10^{-7} - 1.3 \times 10^{-2}$ M) UV/Vis spectroscopy. Similar to chloroform, the spectra in toluene at low concentrations showed the vibronic features of the monomeric dye **5** with maxima at 529, 493 and 460 nm (see Figure 44a). Likewise, the spectra also experienced a broadening and hypsochromic shift of the absorption maximum to 499 nm upon increasing the concentration to 1.3×10^{-2} M, indicating the formation of H-type aggregates. In contrast to the absorption spectra in chloroform, however, the spectra in toluene do not show isosbestic points over the whole concentration range. Moreover, at concentrations above 2.1 x 10^{-4} M a pronounced decrease of absorption strength (hypochromism) was observed. The disappearance of the isosbestic points with increasing concentration suggests the presence of an equilibrium between more than two species.

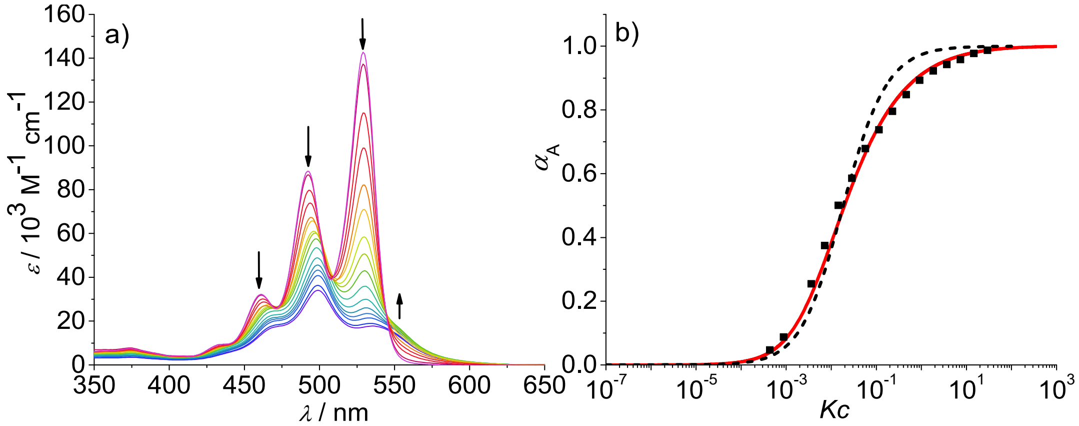

Figure 44: a) Concentration-dependent UV/Vis absorption spectra of PBI **5** in toluene (c = 2.0 x 10^{-7} – 1.3 x 10^{-2} M) at 293 K. Arrows indicate the spectral changes upon increasing the concentration. b) Analysis according to isodesmic (dashed black line) and K_2-K (red line) aggregation models.

The simplest explanation for this observation might be that the dimerization constant K_2 differs from K values for further growth into larger aggregates.[6, 95b] By plotting α_A values obtained from the monomer absorption maximum at 529 nm as a function of Kc with the nucleus size of s = 2, σ value of 50 and K = 2.20 x 10^3 M^{-1}, a good fit with the common K_2-K model[102-103] can be deduced (see Figure 44b). From $\sigma = K_2/K$, a dimerization constant K_2 of 1.10 x 10^5 M^{-1} is obtained. The high σ value indicates that the aggregation process is of anti-cooperative character, meaning that dimers are more easily formed than larger aggregates. The aggregation constant K of 2.2 x 10^3 M^{-1} is in the range of known values for PBI π-stacking in toluene,[13] while the high dimerization constant obviously originates from the formation of hydrogen bonds which was further confirmed by FT-IR spectroscopy (see Figure 51 in the Appendix of this Chapter).

In toluene, the size of the aggregates is still small as observed by DOSY NMR experiments. At the PBI **5** concentration of 1.3 x 10^{-2} M, a translational diffusion coefficient D of 2.76 x 10^{-10} m^2 s^{-1} and a hydrodynamic diameter of 2.8 nm are obtained (see Figure 52, left, in the Appendix of this Chapter). The small diameter indicates that even at the highest concentration of 1.3 x 10^{-2} M the aggregates are still of small size. This implies that mainly dimers are formed, which could be further confirmed by VPO measurements (see Figure 53 in the Appendix of this Chapter).

Based on our so far acquired understanding, dimers are the prevailing species. In more concentrated solutions or aggregation supporting solvents, the further growth should favor even numbered aggregates. Unfortunately, such a process cannot properly be described by the conventional K_2-K model (eqn (42) and (43)), because this model does not consider the differentiation between the even and odd numbered aggregates. Therefore, the development of a new model that considers such differentiation is in demand.

4.2.2 Self-assembly in methylcyclohexane and mixtures of methylcyclohexane and toluene

To promote the growth of larger aggregates, we performed aggregation studies in nonpolar methylcyclohexane and mixtures of methylcyclohexane and toluene. Absorption studies were first conducted in methylcyclohexane in the concentration range of 1.1 x 10^{-6} to 1.3 x 10^{-2} M (see Figure 45a). At the highest concentration (1.3 x 10^{-2} M), a broad spectrum with a maximum at 499 nm is observed. Upon decreasing the concentration, the spectral features remain unchanged but experience a slight hypsochromic shift to 495 nm and a hyperchromic effect (increase of absorbance for smaller aggregates). Even at low concentrations, no transition to the spectrum of PBI **5** monomers is observed. This indicates that a large amount of hydrogen-bonded dimers (structure is probably similar to that shown in Figure 32, Chapter 2 but with didodecyloxyphenyl groups oriented outwards) seems to exist even at the lowest concentration. These dimers then grow into larger (even numbered) aggregates upon increasing concentration.[136] One option to characterize this aggregation behavior is to assume a complete dimerization and to describe the further aggregation by an isodesmic growth with the dimer as the smallest repeat unit. Based on these assumptions, the absorption data at 530 nm in methylcyclohexane could be fitted according to isodesmic model (see Figure 45b). The degree of aggregation increases with increasing concentration from 1% to 93%, and a binding constant K of 1030 $M^{-1} \pm 60$ M^{-1} is obtained for the π-π-stacking of the PBI H-dimers into larger aggregates. It is noteworthy that such analysis anticipates that all larger oligomers are composed of dimeric units, hence the aggregates are of even numbered size. However, the analysis of the absorption data at some other wavelengths revealed a plateau for the extinction coefficients in the concentration range from 1 x 10^{-5} to 5 x 10^{-5} M (for representative example see Figure 54a).

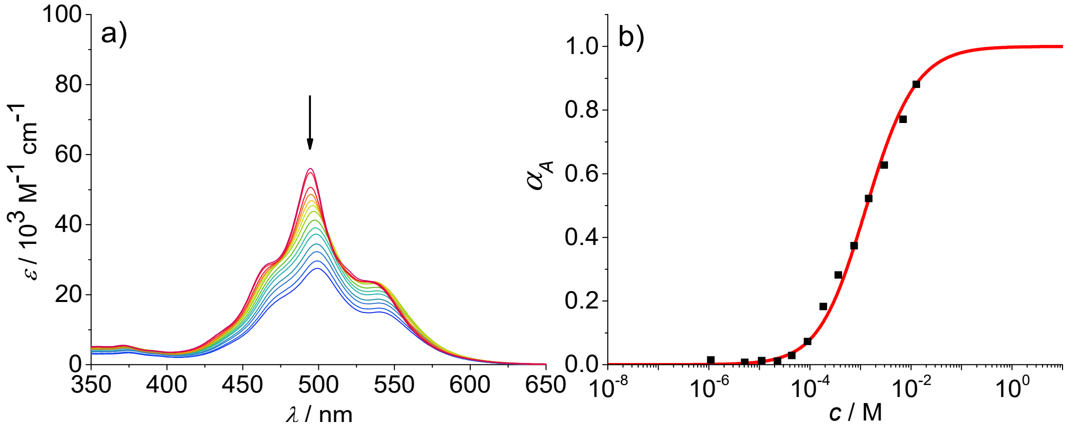

Figure 45: a) Concentration-dependent UV/Vis absorption spectra of PBI **5** in methylcyclohexane ($c = 1.1 \times 10^{-6} - 1.3 \times 10^{-2}$ M) at 293 K. Arrows indicate the spectral changes upon increasing concentration. b) Analysis of the absorption data according to isodesmic model at 530 nm ($R^2 = 0.995$).

Such a plateau is indicative for more complex aggregation behavior and shows that the assumption of a complete dimerization at low concentration is wrong and therefore the description with the isodesmic model fails (see Figure 54a in the Appendix of this Chapter). Consequently, we tried to analyze the data with a successive description by the dimer model for low concentrations (Figure 54b in the Appendix of this Chapter) and the isodesmic model for higher concentrations, where the dimer is considered to be the smallest repeat unit (Figure 54c in the Appendix of this Chapter). This fitting procedures lead to a dimerization constant K_2 of 8.3×10^5 M^{-1} ± 7×10^4 M^{-1} and to an elongation constant K of 890 M^{-1} ± 50 M^{-1}. This kind of successive analysis is obviously prone to significant errors, because the concentration regimes for dimerization and elongation are not always sufficiently separated. Especially, for the sub-step of dimerization the analysis is crude since a small dynamic dimerization range from 23% – 85% is covered. Desirable for a proper modelling is an environment where the whole dynamic range from monomers to long aggregates is observable.

As an ideal solvent to cover the entire range of species from monomers to extended aggregates, a particular mixture of toluene and methylcyclohexane should be most appropriate. Therefore, the absorption spectra of PBI **5** in various mixtures of methylcyclohexane and toluene at a concentration of 1.6×10^{-6} M were analyzed, which displayed the expected transition from the monomeric PBI in pure toluene to the aggregated species for 90% methylcyclohexane content (see Figure 55 in the Appendix of this Chapter). A 30:70 mixture of methylcyclohexane/toluene proved to be the best suitable solvent for further investigations. At the lowest concentration of 2.7×10^{-7} M in this solvent mixture, the spectrum displayed the characteristic vibronic structure of the monomeric species ($A^{0\rightarrow0}/A^{0\rightarrow1} = 1.5$) with three prominent bands at 528, 491 and 460 nm (see Figure 46a and Figure 57, top panel, in the Appendix of this Chapter). With increasing concentration up to 1.3×10^{-2} M, the spectrum of the aggregated species appears with the hypsochromically shifted maximum at 498 nm. The analysis of the absorption data at distinct wavelengths again showed a plateau region at intermediate concentrations similar to the observations made in pure methylcyclohexane (for representative example see inset in Figure 46a). By the separate fitting of the data for the two regimes, i.e. by the monomer-dimer model for the formation of dimers and the isodesmic model for the aggregation of the dimers to larger assemblies, a value for K_2 of 1.13×10^6 $M^{-1} \pm 2.3 \times 10^4$ M^{-1} and for K of 1.80×10^4 $M^{-1} \pm 600$ M^{-1} were determined (see Figure 56 in the Appendix of this Chapter).

4.2.3 K_2-K model for anti-cooperative supramolecular polymerization

Clearly, as mentioned before, this method of analysis is of un-satisfactory accuracy and is completely useless if the two processes are not sufficiently separated as it is the case for weak anti-cooperativity. Moreover, as already pointed out, the conventional K_2-K model is also not suitable because it does not distinguish between more favoured even and less favoured odd aggregate species. Thus, to evaluate anti-cooperative supramolecular polymerization processes via the most common dimer intermediates and subsequent growth into even numbered aggregates, an appropriate mathematical model had to be derived. For this purpose, we elaborated a model which is based on the K_2-K model but distinguishes between even and odd numbered aggregates (for details see Experimental Section).

Dimers are formed by the assembly of two monomers M with a dimerization constant K_2:

$$M + M \rightleftharpoons D; \qquad [M_2] = K_2[M]^2 \tag{44}$$

where $[M] = c_M$ is the monomer and $[M_2] = c_D$ the dimer con-centration. The π-surfaces of the dimers are shielded by the substituents, and hence leading to a less favorable aggregation with an elongation constant K. The dimer can be extended either with another monomer, leading to trimers with a trimer concentration $[M_3]$ of:

$$D + M \rightleftharpoons M_3; \qquad [M_3] = K\,[M_2]\,[M] \tag{45}$$

or with another dimer, leading to tetramers with a concentration $[M_4]$ of:

$$D + D \rightleftharpoons M_4; \qquad [M_4] = K[M_2]^2 \tag{46}$$

Further association leads to

$$[M_n] = K_2^{\frac{n-1}{2}} K^{\frac{n-1}{2}} [M]^n \tag{47}$$

or odd numbered aggregates and to

$$[M_n] = K_2^{\frac{n}{2}} K^{\frac{n-2}{2}} [M]^n \tag{48}$$

for even numbered aggregates. These equations indicate that as soon as an aggregation degree is reached where dimers dominate with respect to monomers the formation of even numbered aggregates is favoured.

If the sum over all odd, as well as for all even n is performed, the resulting concentration of molecules in odd aggregates is given by

$$c_A^{odd} = \frac{K\ [\mathrm{M}][M_2]\ (3-K\ [M_2])}{(1-K\ [M_2])^2} \tag{49}$$

and for molecules in even aggregates (including dimers) by

$$c_A^{even} = \frac{2[M_2]}{(1-K\ [M_2])^2} \tag{50}$$

The total concentration of molecules is then given by

$$c = c_M + c_A^{odd} + c_A^{even} \tag{51}$$

This model is fitted globally to the absorption data of PBI **5** in the solvent mixture methylcyclohexane/toluene 30:70 and thereby the aggregation constants K_2 and K as well as the absorption spectra of monomer, dimer and oligomer are extracted. Details on the fitting procedure are given in the Experimental Section.

By using this modified K_2-K model for anti-cooperative supra-molecular polymerization, the whole data set at 476 nm (see inset in Figure 46a) as well as for all other wavelengths (Figure 57, bottom panel, in the Appendix of this Chapter) can be fitted perfectly, covering the complete curve formed by the experimental data points. Additionally, the entire absorption spectra at each concentration are in very good agreement with the spectra calculated by the newly derived model (Figure 46a, black dashed lines; for complete data set see Figure 57, top panel, in the Appendix of this Chapter). It has to be noted that the calculation of α_A from the spectra by means of eqn (41), Chapter 3, is not possible in this case due to the fact that three different species (monomers, dimers, larger aggregates) with significant different extinction contribute to the spectra.

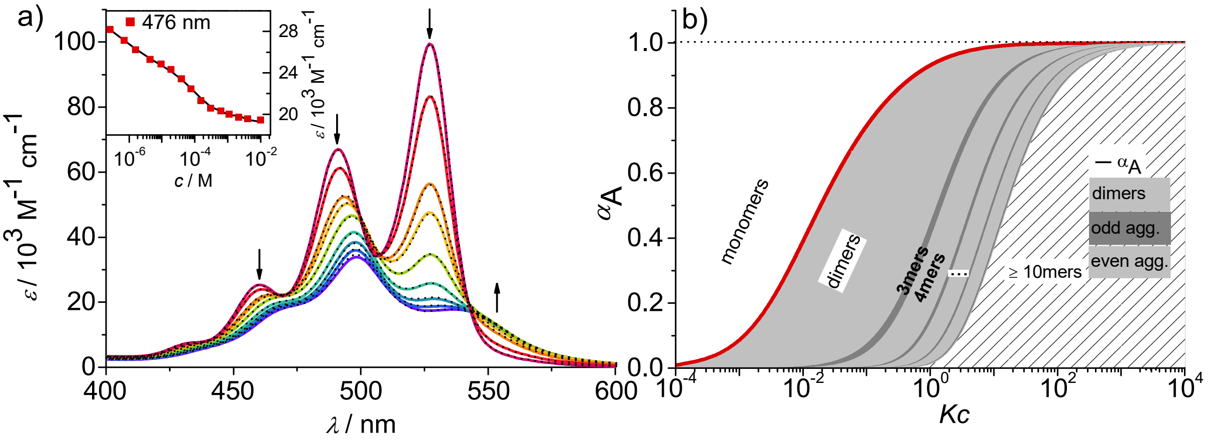

Figure 46: a) Concentration-dependent UV/Vis absorption spectra (colored lines) and the spectra reconstructed by the new K_2-K model for anti-cooperative supramolecular polymerization (black dashed lines) of PBI **5** in a methylcyclohexane/toluene (30:70) mixture ($c = 2.7 \times 10^{-7} - 1.0 \times 10^{-2}$ M) at 293 K, the complete data set is shown in the Appendix. Arrows indicate the spectral changes upon increasing concentration. Inset: Comparison between fit (black line) and the concentration dependent extinction at the wavelength of 476 nm (red symbols) for stepwise aggregation of PBI **5**. b) Degree of aggregation α_A (red line) and the size distribution of n-mer aggregates of PBI **5** (light grey for even numbered aggregates and dark grey for add numbered aggregates) calculated according to the new anti-cooperative K_2-K model (eqn (47) and (48)). Even numbered aggregates dominate in the sample as expected.

The calculated dimerization constant K_2 of 4.5×10^5 M^{-1} and the elongation constant K of 1.1×10^4 M^{-1} are in the same range as the ones obtained before by separating of the 476 nm data into two ranges, but now describe the aggregation process in total. Furthermore, the calculated amount of odd numbered aggregates at the highest concentration of 1.0×10^{-2} M is about 16% (eqn (E18)) and even numbered aggregates accordingly indeed prevail (~ 84%) as expected.

From the plot of α_n as a function of Kc the distribution of the distinct species in methylcyclohexane/toluene mixture can be obtained (Figure 46b and Figure 58). Starting from the lowest concentration, the amount of monomers decreases to zero while the amount of the favoured dimer species accumulates at intermediate concentrations up to > 60%. At higher concentrations, the growth into larger aggregates starts, leading most likely to a columnar π-stack. In such stack each dye molecule has a more close (supported by hydrogen bonding and π-π-stacking) and a distant neighbor (just π-π-stacking). Figure 47 illustrates the proposed aggregation pathway and the prevalence of even numbered aggregates. Due to the accumulation of dimers, the formed oligomers consist mainly of an even number of molecules resulting in an alternating distribution of even and odd numbered aggregates (see light and dark grey areas in Figure 46b and the histogram in Figure 58 in the Appendix of this Chapter). The newly developed K_2-K model for anti-cooperative supramolecular polymerization is capable to describe the prevalence of even numbered aggregates which is obviously not possible by the conventional K_2-K model which exhibits a continuous size distribution for anti-cooperative aggregation (see Figure 43b).

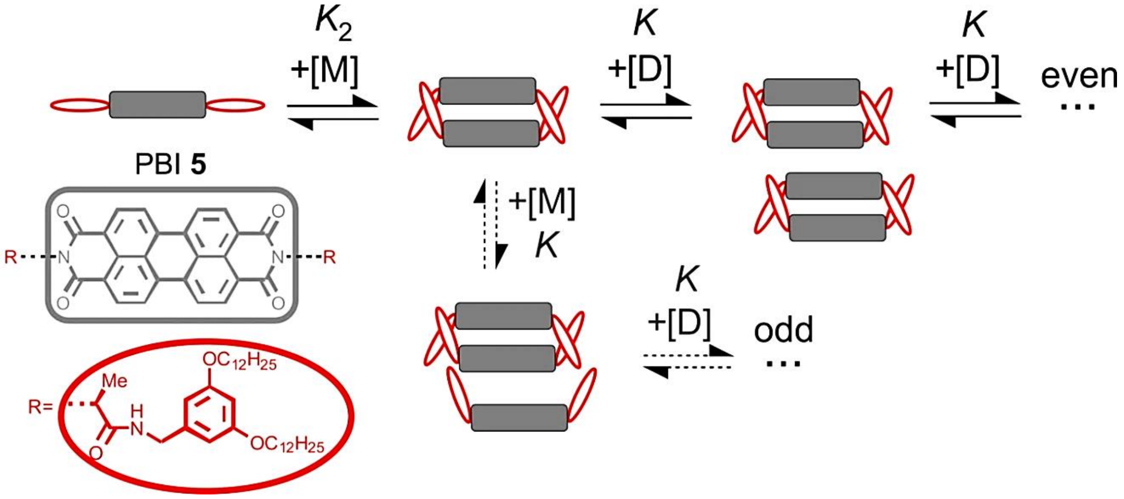

Figure 47: Schematic illustration of the new model for supramolecular polymerization which describes the aggregation pathway of PBI **5**.

At the highest concentration of our study (1.0 x 10^{-2} M), a broad distribution of dominantly even numbered oligomers exists and only < 20% of the molecules are found in small stacks composed of less than 10 units (see shaded area in Figure 46b). Additionally, the global analysis of the experimental spectra with the anti-cooperative aggregation model gives the distinct spectra of monomer, dimer and aggregate (see Figure 48). The spectrum of the monomer shows the characteristic vibronic structure, while the ones of the dimer and longer aggregates display significant differences. The dimer spectrum still exhibits significant vibronic structure, which seems to vanish in the aggregate spectrum. This is an important finding and may be rationalized by less defined contacts between the respective dimers, i.e. a broader distribution of translational and rotational displacements for the non-hydrogen-bonded contacts (i.e. disorder) compared to the structurally more homogeneous hydrogen-bonded dimers.

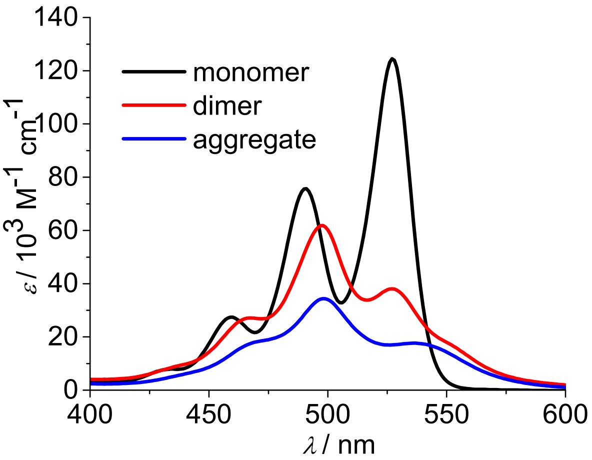

Figure 48: Calculated monomer, dimer and aggregate spectra of PBI **5** according to the new anti-cooperative K_2-K model.

Moreover, the extinction coefficient of dimers per chromophore is obviously higher than the one of the larger aggregate species, which is in accordance with the theory of hypochromism that was derived to explain this effect for π-stacked oligonucleotides in DNA already half a century ago.[58] With the new K_2-K model for anti-cooperative supramolecular polymerization, we can now also analyze the concentration-dependent absorption spectra obtained in pure toluene. Even though the analysis of the data with the simple K_2-K model (as used for cooperative supramolecular polymerization) provided a quite good fit, the resulting distribution with equal amounts of odd and even numbered species left us unsatisfied (see above). In this regard, the outcome of our analysis employing the new K_2-K model is quite pleasing because the obtained dimerization constant K_2 of 9.8 x 10^4 M^{-1} and elongation constant K of 1.9 x 10^3 M^{-1} are indeed quite similar to those determined by the conventional K_2-K model, but the amount of odd numbered aggregates is below 14% over the whole investigated concentration range in toluene according to our advanced analysis. The calculated distribution of species in toluene shows that small aggregates up to hexamers prevail in the investigated concentration range up to 1.3 x 10^{-2} M (data not shown).

Our studies have shown that the newly designed PBI molecule is properly suited for a complete analysis of the self-assembly process in various solvents. The new K_2-K model provides a comprehensive description of the anti-cooperative stepwise association pathway of this PBI dye. Thus, this new model may be applied to other π-conjugated systems.

4.2.4 Macroscopic studies of PBI 5 in toluene and methylcyclohexane

The morphologies of the aggregates of PBI **5** were studied by AFM in both toluene and methylcyclohexane. In both solvents, images were recorded at three different concentrations on HOPG surface. At the highest concentration of $c = 1.4 \times 10^{-2}$ M, the AFM images displayed an area covering film consisting of nanoparticles of 9 to 10 ± 1 nm (Figure 59 and Figure 60 in the Appendix of this Chapter).

In methylcyclohexane, the size of nanoparticles didn't change with decreasing concentration to 2.3×10^{-3} M and 6.8×10^{-5} M. However, at the lowest concentration the particles could be well resolved. The height of the agglomerated globular subjects is 2.7 to 2.8 ± 0.2 nm (Figure 49 and Figure 61 in the Appendix of this Chapter). Taking into account the tip broadening effect,[137] the values are in accordance with the value obtained from DOSY experiments of PBI **5** in methylcyclohexane (see Figure 52 in the Appendix of this Chapter).

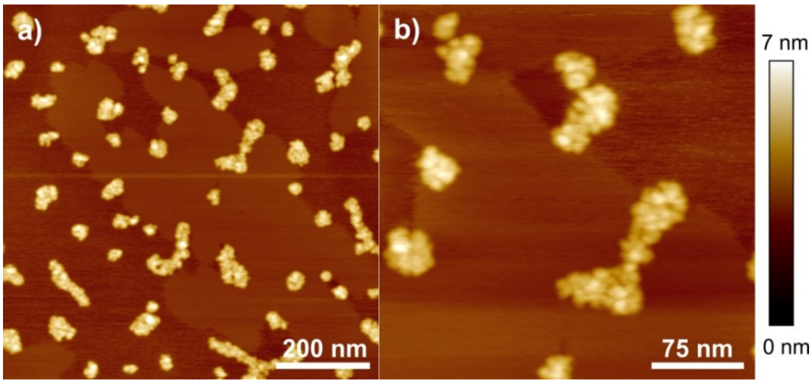

Figure 49: AFM height images of spin-coated samples of PBI **5** (5.000 rpm, $c = 6.8 \times 10^{-5}$ M, methylcyclohexane) onto HOPG.

In comparison to the nanoparticles in methylcyclohexane, which had the same size at the three measured concentrations, in toluene the size decreased with decreasing concentration. At the concentration of 1.3×10^{-3} M, nanoparticles of two different diameters of 9 ± 2 nm and 4.5 ± 1.0 nm were monitored (Figure 50). The average height of the particles was 1.4 to 1.5 nm.

At the tenfold lower concentration (1.3×10^{-4} M), only monolayers on the HOPG surface were visible. The lamella-form like structures exhibit periodicity of 4.2 ± 0.2 nm and the height of 0.55 nm of the ordered and disordered domains (see Figure 62 in the Appendix of this Chapter).

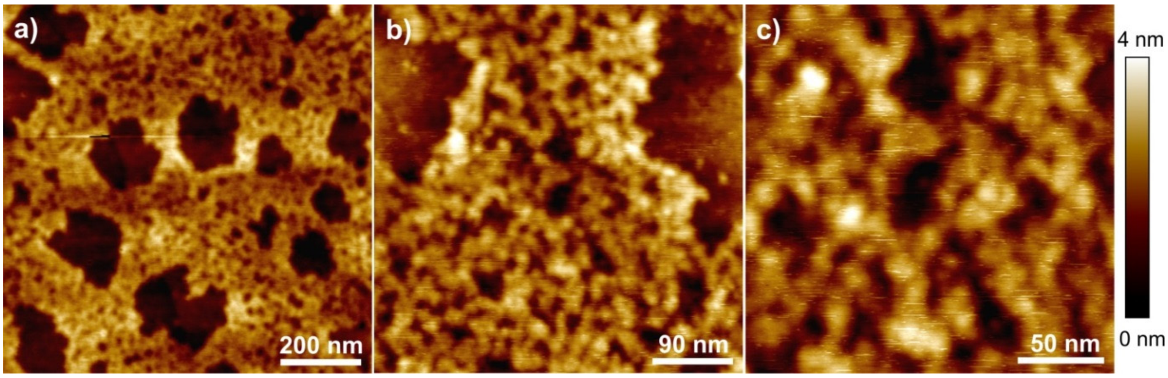

Figure 50: AFM height images of spin-coated samples of PBI **5** (10.000 rpm, c = 1.3 x 10^{-3} M, toluene) onto HOPG.

A comparison of the aggregates of PBI **5** in solution and on the surface is questionable because of the different measurement techniques. Nevertheless, some assumptions can be considered. In methylcyclohexane as well as toluene, neither in solution nor on the surface long aggregates of PBI **5** could be observed suggesting that similar aggregate structures could be formed in/on both media which have to be of oligomeric size. In methylcyclohexane, the particle size does not change over the whole concentration range. Similar behavior was observed in the UV/Vis absorption studies indicating, additionally, the similarity of the formed oligomers. Furthermore, the nanoparticle sizes, spin-coated from the concentrated samples in methylcyclohexane and toluene, are the same which could mean that the formed structures are of similar size and shape in solutions as well. Finally, the reduction of the aggregate size in toluene was noticed in solution as well as on the surface confirming the similarities of the formed aggregate structures.

4.3 Conclusion

In this chapter, an anti-cooperative supramolecular polymerization process is elucidated for the first time in detail from both the experimental and theoretical point of view. For this purpose, a new perylene bisimide dye (PBI **5**) was designed and synthesized, which shows a strong preference for the formation of dimers by the assistance of hydrogen bonds from the alanine driven amide function at the imide position to the carbonyl groups which was elucidated in detail in Chapter 2.

For this PBI dye, the aggregation process from monomers via dimers to larger oligomers was characterized by various spectroscopic techniques which also disclosed the responsible driving forces for the formation of aggregates, i.e. π-π-stacking interactions and hydrogen bonds. The stepwise aggregation process with increasing concentration via dimers, tetramers, hexamers, etc. is confirmed and elucidated in detail by a newly derived K_2-K model for anti-cooperative supramolecular polymerization. This new model should also be the choice for the analysis of other anti-cooperative self-assembly processes. The oligomeric aggregates could be visualized on the surface and their morphology was investigated by AFM. The obtained images showed agglomerated nanoparticles of relatively small size which mostly confirmed the observations in solution.

4.4 Experimental section

4.4.1 Materials and Methods

NMR experiments were conducted on a Bruker Avance 400 or Bruker DMX 600 spectrometer with TMS or residual undeuterated solvent as internal standard. The chemical shifts are reported in ppm relative to TMS or residual undeuterated solvent as internal standard (δ scale). The apparent coupling constants J are given in Hertz (Hz). The following abbreviations are used to describe the signal fine structure: s = singlet, d = doublet, t = triplet, q = quartet, quint = quintet, dd = doublet of doublets, m = multiplet, and bm = broad multiplet. All FT-IR spectra were measured on a FT/IR-4100 spectrophotometer (Jasco). The UV/Vis absorption spectra were recorded in conventional quartz cells of appropriate path length on a Perkin Elmer Lambda 35 spectrophotometer equipped with a Peltier system for temperature control. Chloroform, toluene and methylcyclohexane of spectroscopic grade were used for the measurements.

The vapor pressure osmometry (VPO) measurements were performed at 303 K on a KNAUER osmometer with a universal temperature measurement unit. Benzil was used as standard to generate calibration curves in terms of R (ohm) vs. molal osmotic concentration in the respective solvent.

The AFM measurements were performed on MultiMode$^{\text{TM}}$ 8 AFM-system operating in tapping mode. Silicon cantilevers (Olympus, Japan) with a resonance frequency of ~ 300 kHz and a spring rate of 40 Nm^{-1} were used. The solutions of PBI **5** were spin-coated (5.000 or 10.000 rpm) on highly oriented pyrolytic graphite (HOPG, NanoTechnology Instruments, Netherlands).

4.4.2 Conventional K_2-K model[6, 95a]

Taking into account that the equilibrium constant of the dimerization differs from the elongation constant, the isodesmic model has to be modified. With the nucleus of s = 2, the equilibrium is described as follows:

$$M + M \overset{K_2}{\rightleftharpoons} M_2$$

$$M_2 + M \overset{K_3}{\rightleftharpoons} M_3$$

$$M_{n-1} + M \overset{K_n}{\rightleftharpoons} M_n$$

$$K_2 \neq K_3 = \ldots K_n = K \qquad \text{(E7)}$$

By defining $\sigma = K_2/K$, the concentration of n-mer c_n and the total concentration c can be obtained with the following equations:

$$c_n = K_2 K^{n-2} c_M^n = \sigma K^{n-1} c_M^n \qquad \text{(E8)}$$

$$c = c_M + \sum_{n=2}^{\infty} n\sigma K^{-1}(Kc_M)^n = (1-\sigma)c_M + \frac{\sigma c_M}{(1-Kc_M)^2} \qquad \text{(E9)}$$

By multiplying eqn (E3) with K, eqn (42) shown in the main text is obtained.

4.4.3 K_2-K-model for anti-cooperative supramolecular polymerization

The K_2-K model for anti-cooperative supramolecular polymerization describes an aggregation behavior where the formation of dimers is favoured by a strong interaction between the involved molecules, e.g. by the formation of H-bonds. As the dimerization leads to a saturation of the bond donating unit, further elongation is disadvantaged due to a much weaker stacking force. Therefore, the elongation constant K is considerably smaller compared to the dimerization constant K_2. Such an aggregation behavior favors the formation of even numbered aggregates. In the following, the equations that describe the aggregation behavior are derived.

Even numbered aggregates:

Monomers grow into dimers with the dimerization constant K_2. The stacking of dimers into even numbered aggregates continues with the elongation constant K.

$$M + M \rightleftharpoons D \qquad [M_2] = K_2 c_M^2 \qquad \text{(dimer)} \qquad \text{(E10)}$$

$D + D \rightleftharpoons D_2$ $[M_4] = K[M_2]^2$ (tetramer) (E11)

$D_2 + D \rightleftharpoons D_3$ $[M_6] = K[M_2][M_4] = K^2[M_2]^3$ (hexamer) (E12)

$D_{n-1} + D \rightleftharpoons D_n$ $[M_{2n}] = K[M_2]^{n-1}[M_2] = K^{n-1}[M_2]^n$ ((2n)-mer) (E13)

where $[M_{2n}]$ is the concentration of aggregates which contain *2n* monomers. To obtain the number of monomers in an aggregate with a size of *2n* monomers, eqn (E13) has to be multiplied by $2n$.

The concentration of molecules in even numbered aggregates is calculated by performing the sum over all possible *n* starting at *n* = 1 (dimer) up to infinity:

$$c_A^{even} = 2 * [M_2] + 2 * 2[M_4] + 2 * 3[M_6] + \cdots + 2n * [M_{2n}] = 2 * \sum_{n=1}^{\infty} n\,[M_{2n}] = 2 * \sum_{n=1}^{\infty} nK^{n-1}[M_2]^n = \frac{2}{K}\sum_{n=1}^{\infty} nK^n[M_2]^n \qquad \text{(E14)}$$

The sum is evaluated making use of the geometric power series

$$\sum_{n=0}^{\infty} nq^n = \frac{q}{(1-q)^2} \qquad \text{with } q = K[M_2] <. \qquad \text{(E15)}$$

Consequently, the concentration of molecules in an even numbered aggregate is given by:

$$c_A^{even} = \frac{2}{K}\frac{K[M_2]}{(1-K[M_2])^2} = 2\frac{K_2 c_M{}^2}{(1-KK_2c_M^2)^2} \qquad \text{with } K[M_2] < 1 \qquad \text{(E16)}$$

Odd numbered aggregates:

Odd numbered aggregates are constructed either by the elongation of an even numbered aggregate with a monomer or of an odd numbered aggregate with a dimer. In both cases the aggregation process is quantified by the elongation constant *K* describing the weaker interaction.

$D + M \rightleftharpoons M_3$ $[M_3] = K[M_1][M_2] = KK_2c_M^3$ (trimer) (E17)

$D_2 + M \rightleftharpoons M_5$ $[M_5] = K[M_1][M_4] = K[M_2][M_3] = K^2K_2^2c_M^5$ (pentamer) (E18)

$D_n + M \rightleftharpoons M_{2n+1}$ $[M_{2n+1}] = K_2^{n-1}K^{n-1}c_M^{2n-1} = c_MK^n[M_2]^n$ ((2n+1)-mer) (E19)

The concentration of molecules in odd numbered aggregates (with a size of at least 3 monomers) can be calculated with the help of eqn (E15) by:

$$c_A^{odd} = 3 * [M_3] + 5 * [M_5] + \cdots + (2n+1) * [M_2]^n K^n c_M = \sum_{n=1}^{\infty}(2n+1) * [M_2]^n K^n c_M = 2c_M * \sum_{n=0}^{\infty} n * ([M_2]K)^n + c_1 * \sum_{n=0}^{\infty}([M_2]K)^n - c_M = c_M \frac{[M_2]K+1}{(1-[M_2]K)^2} - c_M = \frac{[M_2]Kc_M(3-[M_2]K)}{(1-[M_2]K)^2} = \frac{KK_2{c_M}^3(3-KK_2{c_M}^2)}{(1-KK_2{c_M}^2)^2} \quad \text{with } KK_2{c_M}^2 < 1 \qquad \text{(E20)}$$

The term $-c_M$ has to be added in order to change the lower limit of the summation index *n* from 1 to 0.

The total concentration *c* in the system can be calculated in dependence of the monomer concentration c_M by:

$$c = c_M + \underbrace{\frac{2K_2{c_M}^2}{(1-K_2{c_M}^2K)^2}}_{even} + \underbrace{\frac{KK_2{c_M}^3(3-KK_2{c_M}^2)}{(1-KK_2{c_M}^2)^2}}_{odd} \qquad \text{(E21)}$$

The ratio between even and odd numbered aggregates is given by:

$$\frac{c_A^{odd}}{c_A^{even}} = \frac{Kc_M[M_2](3-[M_2]K)}{(1-[M_2]K)^2}\frac{(1-[M_2]K)^2}{2[M_2]} = \frac{Kc_M(3-[M_2]K)}{2} \qquad \text{(E22)}$$

For simplification, the abbreviation $K[M_2] = a$ is used. This leads to an expression for the monomer concentration of $c_M = \sqrt{\frac{a}{K_2K}}$. Insertion of the latter term into eqn (E22) and reformulation leads to:

$$\frac{c_A^{odd}}{c_A^{even}} = \sqrt{\frac{K}{K_D}}\ \frac{\sqrt{a}}{2}(3-a) \qquad \text{(E23)}$$

The term $\frac{\sqrt{a}}{2}(3-a) < 1$ for all $a < 1$. Therefore, the maximal fraction of molecules in odd numbered aggregates is always smaller than the square root of the aggregation constants:

$$\frac{c_A^{odd}}{c_A^{even}} < \sqrt{\frac{K}{K_2}} \qquad \text{(E24)}$$

4.4.4 Fit algorithm to analyze the anti-cooperative supramolecular polymerization

The K_2-K model for anti-cooperative supramolecular polymerization is fitted to the data by varying the aggregation constants K_2 and K. Additionally, the extinctions of the three distinct species, monomer, dimer and oligomer are optimized. The fitting routine is implemented in Labview and optimizes the model parameters globally in order to describe the two dimensional, experimental data set of concentration-and wavelength-dependent extinction $\boldsymbol{data}(\lambda, c)$. The fit algorithm is comparable to our previously reported procedure,[131b] the basic steps are:

0. The start values of the aggregation constants K_2 and K are chosen manually.
1. An array of size N for the monomer concentration c_M is constructed by following way: The minimum value of the monomer concentration is chosen to be $c_{M,min} = 1 \times 10^{-7}$ M and the maximum monomer concentration for anti-cooperative supramolecular polymerization is given by the aggregation constants $c_{M,max} = \sqrt{\frac{1}{K_2 K}}$. The maximum monomer concentration is reached asymptotically for high dye concentrations and a small variation of the monomer concentration for a large interval of the total concentration is inherent for anti-cooperative supramolecular polymerization. Therefore, a non-equidistant grid is used for the monomer concentration with large intervals for low dye concentrations, i.e. the first N/2 steps and small steps for high dye concentrations in the second half of the c_M - axis.

$$n = 1 \ldots \frac{N}{2}: c_{M,n} = c_{M,min} * \left(\frac{c_{M,max}}{c_{M,min}}\right)^{n-1 \Big/ \frac{N}{2}} \qquad \text{(E25)}$$

$$n = \frac{N}{2} + 1 \ldots N: c_{M,n} = c_{M,N/2} + \frac{c_{M,max} - c_{M,N/2}}{N/2} * \left(n - \frac{N}{2}\right) \qquad \text{(E26)}$$

2. The concentration of molecules in dimers and in aggregates is calculated in dependence of the monomer concentration $c_{M,n}$. The concentration of molecules in dimers is given by

$$c_D = 2\, K_2 c_M^2 \qquad \text{(E27)}$$

The concentration of molecules in aggregates is the sum of molecules in odd (eqn E20)) and even (eqn (E18)) numbered aggregates minus the concentration of molecules in dimers:

$$c_A = c_A^{odd} + c_A^{even} - c_D \tag{E28}$$

The total concentration is calculated with eqn (E21).

3. The fraction of molecules in a distinct species is calculated by $\alpha_{M,D,A} = \frac{c_{M,D,A}}{c_T}$ and the total concentration *c* is interpolated to the measured concentrations for comparison.
4. The extinction of each species (monomer, dimer and aggregate) is calculated for the given set of aggregation constants by $\boldsymbol{\varepsilon}_{\boldsymbol{M,D,A}}(\lambda) = \boldsymbol{data}(\lambda, c)\boldsymbol{\alpha}(c)[\boldsymbol{\alpha}^T(c)\boldsymbol{\alpha}(c)]^{-1}$with $\boldsymbol{\alpha}(c) = [\alpha_M\ \alpha_D\ \alpha_A]$.
5. The aggregation constants *K*2 and *K* are optimized and step 1 to 5 are repeated until the error between the fitted and measured extinction is minimized.

4.5 Appendix

4.5.1 FT-IR measurements in toluene

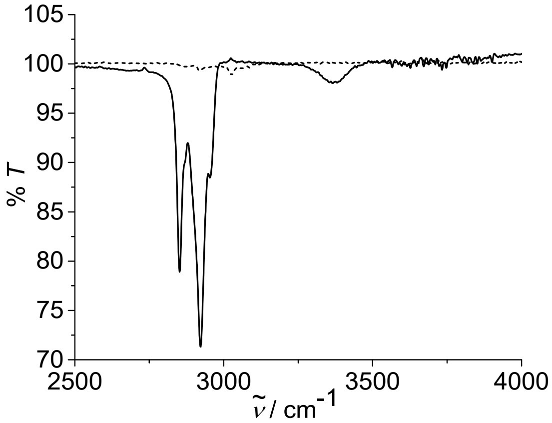

Figure 51: FT-IR spectra of PBI **5** at the concentrations of 1.3 x 10^{-2} M (solid line) and 4.1 x 10^{-4} M (dotted line) in toluene (right) at 293 K. The spectra of PBI **5** show two sets of signals. The prominent signals at 2853 and 2922 cm^{-1} are assigned to the CH stretching vibrations. The small broad band at 3367 cm^{-1} in toluene is attributed to the hydrogen bonded NH stretching vibration. The stretching vibrations of free NH groups which can usually be found in the region between 3500 and 3600 cm^{-1} could not be detected, which means that all NH groups are involved in hydrogen bonds.[100b]

4.5.2 DOSY NMR experiments toluene

The hydrodynamic radius *R* of PBI **5** is determined from the diffusion coefficient *D* using the Stokes-Einstein equation (eqn (A1)):

$$D = \frac{k_B T}{6\pi\eta R} \tag{A1}$$

where k_B is the Boltzmann constant, T the temperature, and η the viscosity of the solvent. The diffusion constant in turn results from DOSY NMR measurements.

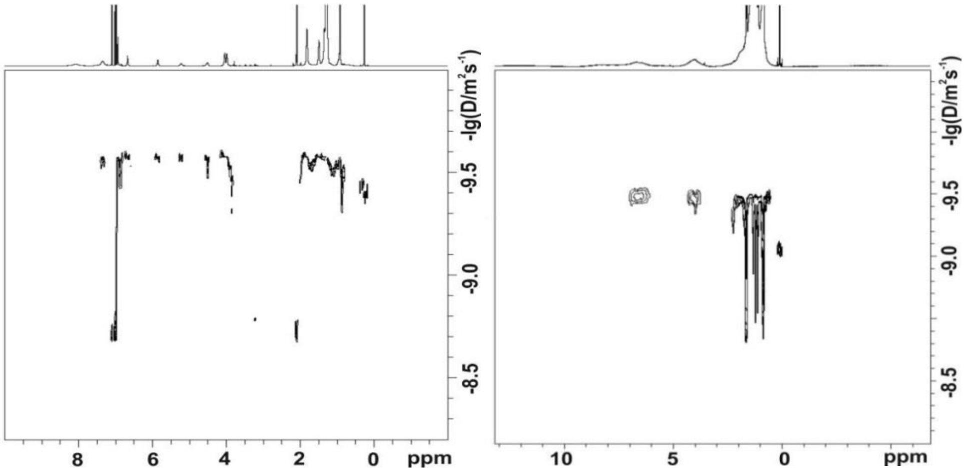

Figure 52: DOSY NMR spectrum of PBI **5** at $c = 1.3 \times 10^{-2}$ M in toluene (left) and methylcyclohexane (right) recorded at 600 MHz NMR at 293 K. The diffusion coefficients D [$m^2\ s^{-1}$] are plotted in a logarithmic scale against the chemical shift δ [ppm].

4.5.3 VPO measurements in toluene

$$M = {}^{K_{cal}}/_{K_{meas}} = 3068.59\ {}^{g}/_{mol} \tag{A2}$$

$$N = {}^{M}/_{M_{PBI\ \mathbf{5}}} = 2.12N \tag{A3}$$

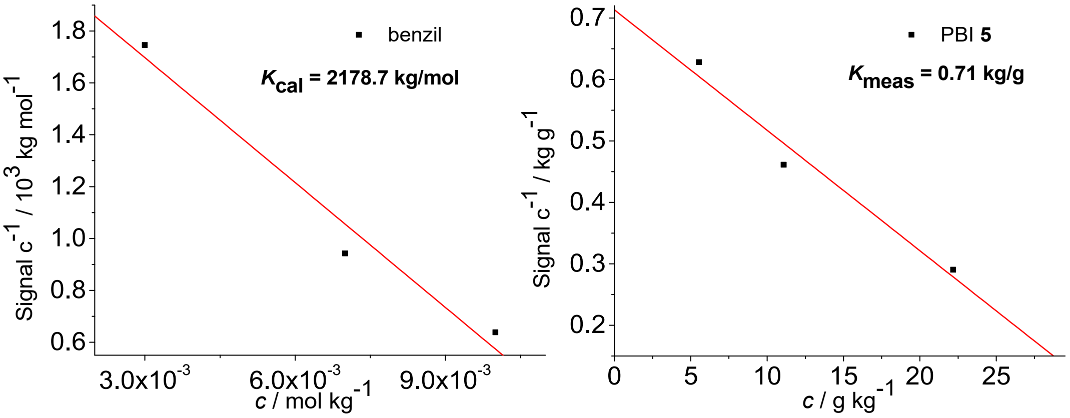

Figure 53: VPO measurements of benzil (calibration curve, left) and PBI **5** in toluene at 303 K (1.3 x 10^{-2} to 1.7 x 10^{-3} M, right). The *K* values are obtained by interpolating the data to x = 0.

4.5.4 Analysis of absorption data of PBI 5 in methylcyclohexane at 502 nm

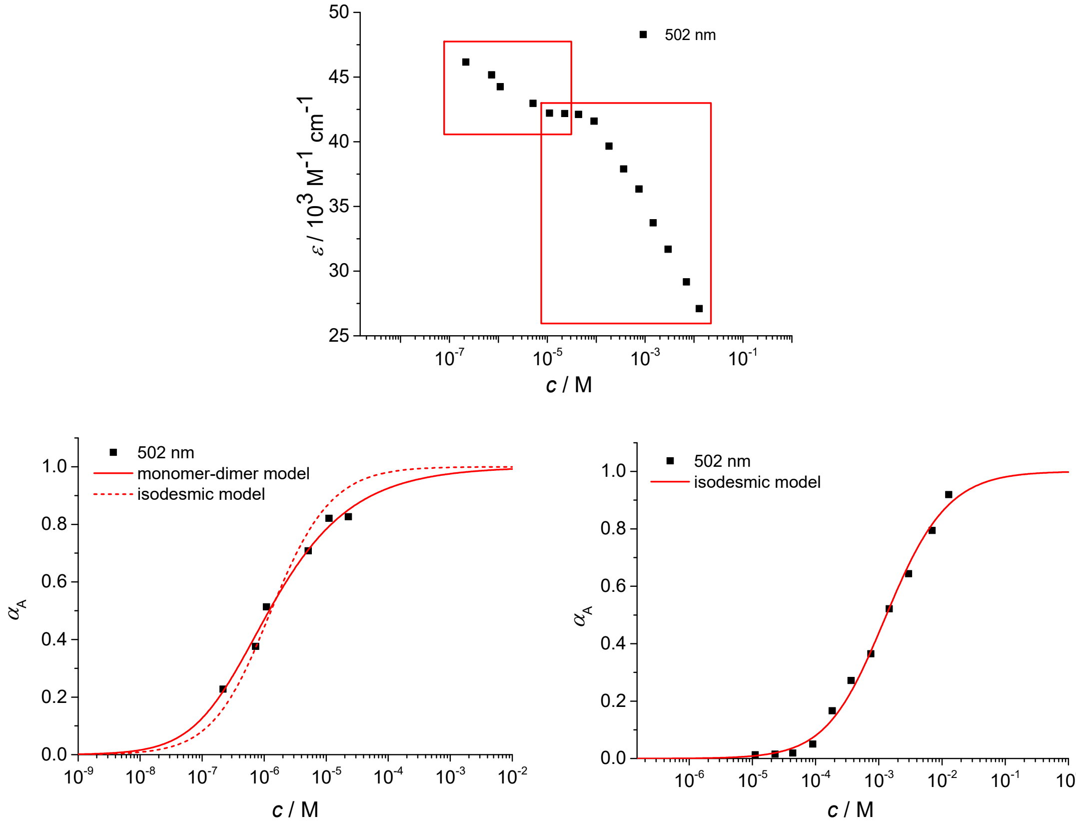

Figure 54: a) Concentration-dependent absorption data of PBI **5** in methylcyclohexane at 502 nm. b) Fit of the data to the monomer-dimer model (*c* = 2.3 x 10^{-5} to 2.2 x 10^{-7} M, R² = 0.978); dashed line: isodesmic model for comparison. c) Fit of the data to the isodesmic model (*c* = 1.3 x 10^{-2} to 1.1 x 10^{-5} M, R² = 0.994).

4.5.5 Absorption spectra of PBI 5 in methylcyclohexane/toluene mixtures

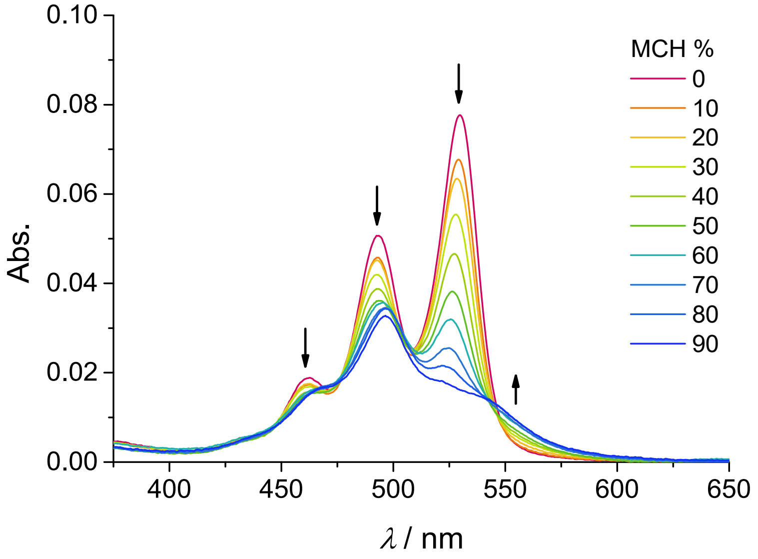

Figure 55: Solvent-dependent UV/Vis absorption spectra of PBI **5** (methylcyclohexane content from 0 to 90%) at the concentration of 1.6 x 10^{-6} M recorded at 293 K. Arrows indicate the spectral changes upon increasing methylcyclohexane content.

4.5.6 Analysis of absorption data of PBI 5 in a methylcyclohexane/toluene (30:70) mixture at 476 nm

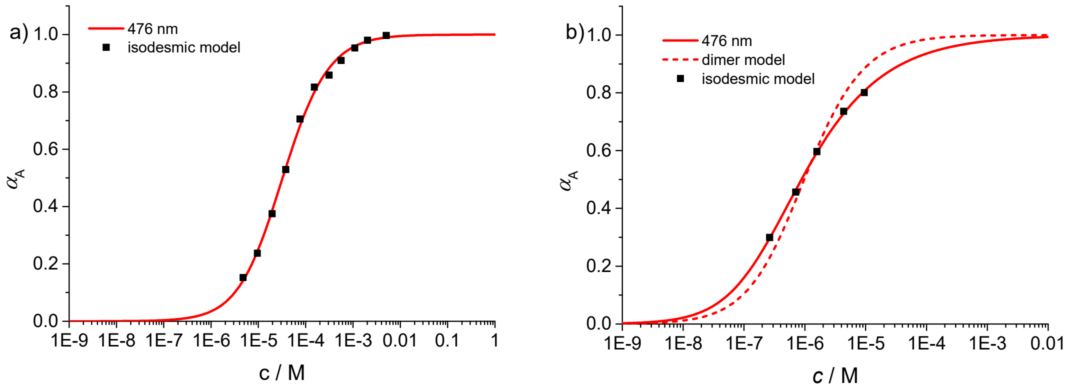

Figure 56: a) Fit of the isodesmic model ($R^2 = 0.998$) to the data obtained at the concentration range $c = 1.0 \times 10^{-2}$ to 9.5×10^{-6} M. b) Fit to the monomer-dimer model ($R^2 = 0.998$) of the data obtained at the concentration range $c = 9.5 \times 10^{-6}$ to 2.7×10^{-7} M. Dashed line: isodesmic model for comparison.

4.5.7 Analysis of the concentration-dependent UV/Vis spectra of PBI 5 in a methylcyclohexane/toluene mixture of 30:70 by the K_2-K model for anti-cooperative supramolecular polymerization

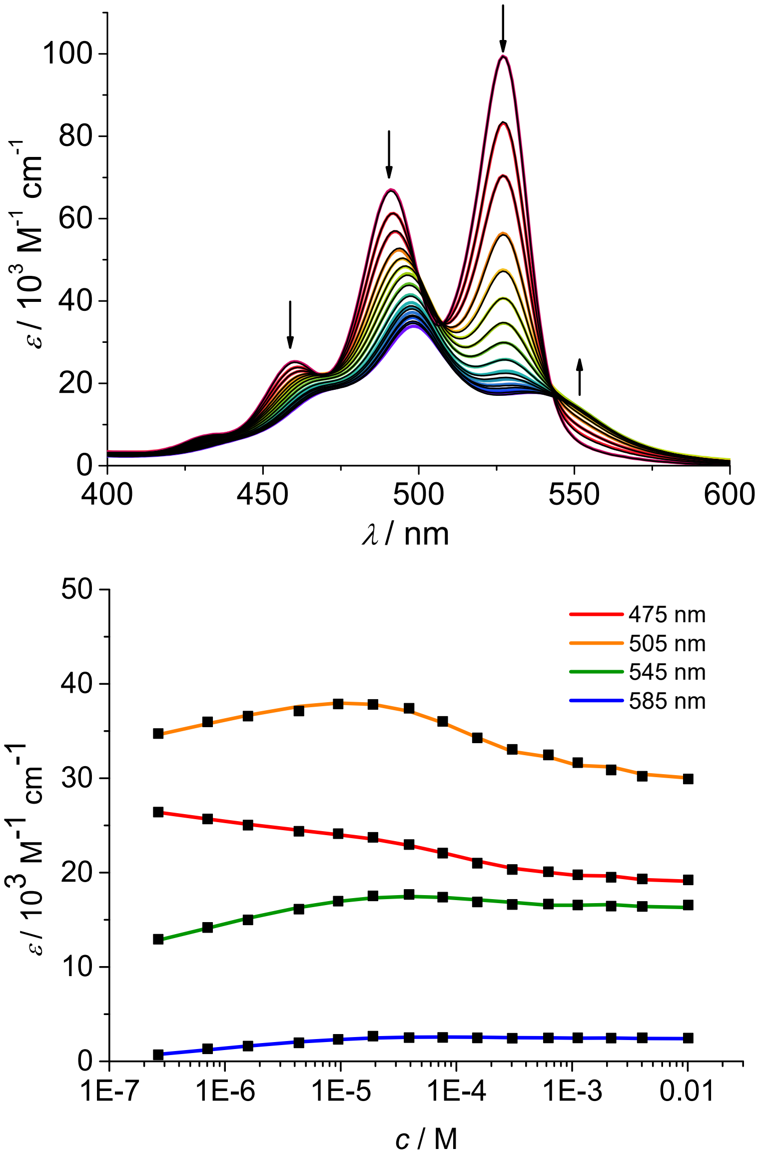

Figure 57: Concentration-dependent UV/Vis absorption spectra (colored lines) and the spectra reconstructed by the new K_2-K model for anti-cooperative supramolecular polymerization (black lines) of PBI **5** in a methylcyclohexane/toluene (30:70) mixture (c = 2.7 x 10^{-7} – 1.0 x 10^{-2} M) at 293 K (top). Arrows indicate the spectral changes upon increasing concentration. Fit of the K_2-K model for anti-cooperative supramolecular polymerization to the concentration-dependent absorption data at various wavelengths (bottom).

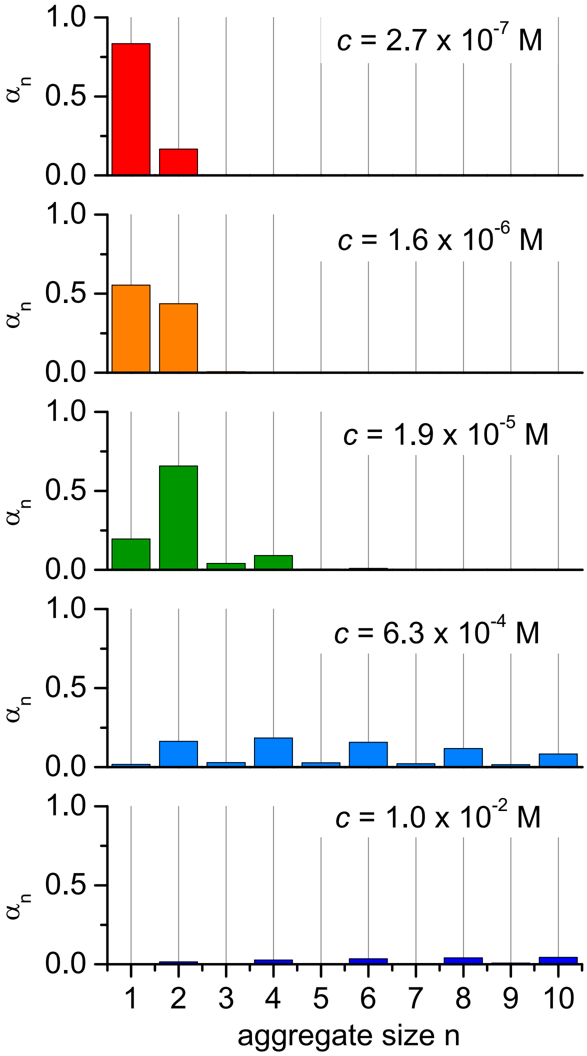

Figure 58: Histograms obtained from eqn (E13) and eqn (E19) for five different concentrations showing the aggregate size distribution up to an aggregate size of ten. A prevalence for even numbered aggregates is observed as soon as the system starts to aggregate.

4.5.8 AFM studies of PBI 5 in toluene and methylcyclohexane

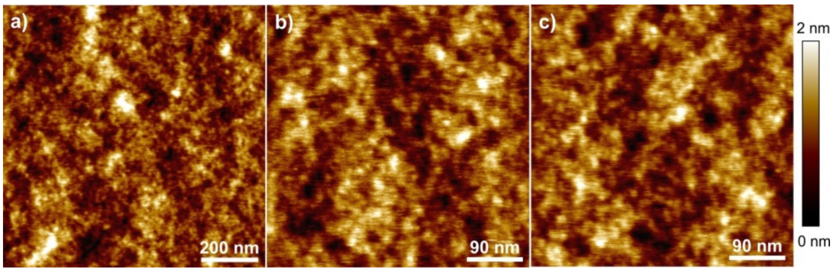

Figure 59: AFM height images of spin-coated samples of PBI **5** (10.000 rpm, *c* = 1.4 x 10^{-2} M, toluene) onto HOPG.

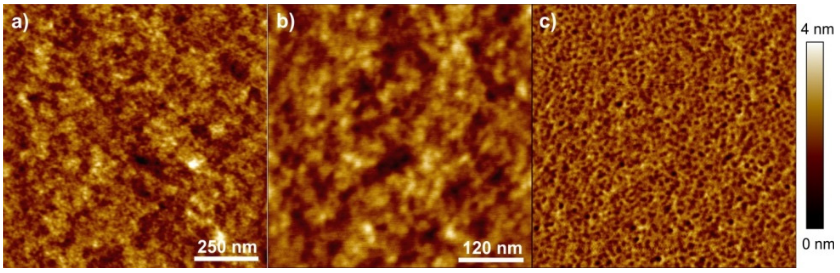

Figure 60: AFM height (a,b) and phase (c) images of spin-coated samples of PBI **5** (10.000 rpm, *c* = 1.4 x 10^{-2} M, methylcyclohexane) onto HOPG.

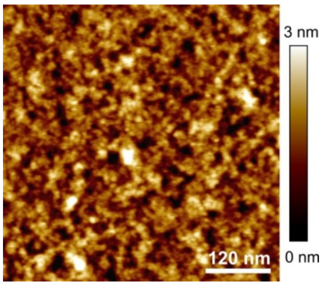

Figure 61: AFM height image of spin-coated sample of PBI **5** (10.000 rpm, *c* = 2.3 x 10^{-3} M, methylcyclohexane) onto HOPG.

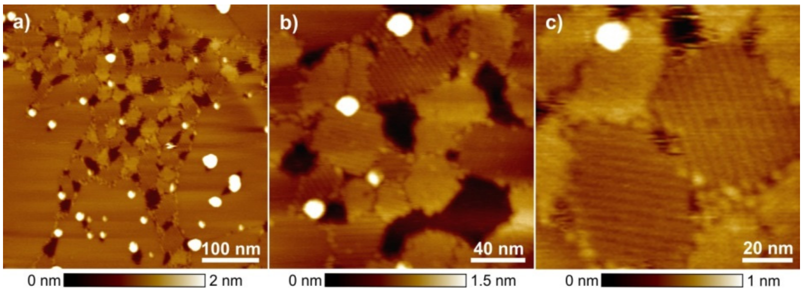

Figure 62: AFM height images of spin-coated samples of PBI **5** (10.000 rpm, *c* = 1.3 x 10^{-4} M, toluene) onto HOPG.

Chapter 5
Sensing of double-stranded DNA/RNA secondary structures by water soluble homochiral perylene bisimide dyes*

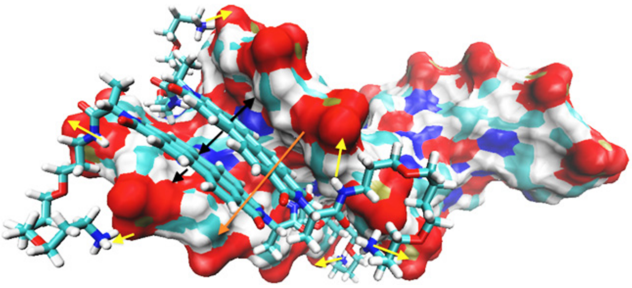

Abstract: A broad series of homochiral perylene bisimide (PBI) dyes were synthesized that are appended with amino acids and cationic side chains at the imide positions. Self-assembly behavior of these ionic PBIs has been studied in aqueous media by UV/Vis spectroscopy, revealing formation of excitonically coupled H-type aggregates. The interactions of these ionic PBIs with different ds-DNA and ds-RNA have been explored by thermal denaturation, fluorimetric titration and circular dichroism (CD) experiments. These PBIs strongly stabilized ds-DNA/RNA against thermal denaturation as revealed by high melting temperatures of the formed PBI/polynucleotide complexes. Fluorimetric titrations showed that these PBIs bind to ds-DNA/RNA with high binding constants depending on the number of the positive charges in the side chains. Thus, spermine-containing PBIs with six positive charges each showed higher binding constants (log $K_s = 9.2 - 9.8$) than their dioxa analogues (log $K_s = 6.5 - 7.9$) having two positive charges each. Induced circular dichroism (ICD) of PBI assemblies created within DNA/RNA grooves was observed. These ICD profiles are strongly dependent on the steric demand of the chiral substituents of the amino acid units and the secondary structure of the DNA or RNA. The observed ICD effects can be explained by non-covalent binding of excitonically coupled PBI dimer aggregates into the minor groove of DNA and major groove of RNA which is further supported by molecular modeling studies.

---

*This chapter was published by: J. Gershberg, M. Radić Stojković, M. Škugor, S. Tomić, T. H. Rehm, S. Rehm, C. R. Saha-Möller, I. Piantanida, F. Würthner, *Chem. Eur. J.* **2015**, *21*, 7886-7895. Reproduced and adopted with permission from John Wiley and Sons (Copyright 2016).
The **(N)**-series PBIs were synthesized by S. Rehm and T. H. Rehm. Studies of interaction of the **(N)**-series PBIs with DNA/RNA were performed by M. Radić Stojković and M. Škugor. Molecular modelling was performed by S. Tomić.

5.1 Introduction

Nucleic acids are most important biomolecules as they code the information of life. Thus, small molecules targeting deoxyribonucleic acid (DNA) and ribonucleic acid (RNA) have attracted significant scientific interest due to medicinal, biochemical and biological implications of such molecular recognition events.[138] For instance, sequence specific detection of double-stranded (ds)-DNA and (ds)-RNA by molecular recognition has become increasingly more valuable as diagnostic tool in molecular biology and medicine.[139] Non-covalent recognition of DNA/RNA by small molecules very often relies on single dominant binding mode such as intercalation, groove binding, or electrostatic sugar-phosphate backbone binding.[140] Only in the last decade small molecules combining two or more dominant non-covalent binding modes have been studied to a larger extent,[140] aiming for new compounds to be able to selectively report on structural differences of DNA and RNA secondary structure. In the recent years, researchers have focused attention on molecules with extended π-cores such as pyrene[141] and perylene[142] derivatives.[143] However, only recently interaction of perylene bisimide (PBI) dyes with DNA and RNA have gained appreciable attention. PBI dyes have been covalently attached to DNA to create DNA conjugates, which self-assemble into duplex and triplex structures by π-π-interactions of PBI molecules.[84a, 84e, 144] Moreover, PBIs have been studied for selective non-covalent interactions with G-quadruplexes.[145] However, only limited information is available on non-covalent interactions of PBIs with other DNA and RNA structures, like triple helices or specific double-stranded structures.[142, 146] Even there studies were often performed as parallel experiments to those with G-quadruplexes.[86, 147] Investigations of PBI-DNA conjugates have shown that stacked PBI molecules within the DNA scaffold give specific induced circular dichroism (ICD) profiles, which are strongly dependent on the freedom of adjustment of PBI molecules in the DNA.[148] This finding suggests that PBI dyes can be used as sensitive probes for the chiral environment of polynucleotides and as non-covalently interacting sensors for various DNA and RNA structures.

In the last decade, Piantanida et al. have been particularly interested in small molecules able to bind efficiently via non-covalent interactions to the most of naturally occurring ds-DNA/RNA as well as to report different signals for each of the most common secondary structures of ds-DNA and RNA by sensitive and biologically applicable methods (e. g. UV/Vis, CD, fluorescence, surface-enhanced Raman spectroscopy).[149] The development of such single-molecule sensors with several properties could replace the necessity of multiple dyes each being specific for one particular DNA or RNA target. The signal selectivity could be achieved by the fine tuning of the interaction of chromophores with secondary structures of polynucleotides which include the introduction of sterically demanding or binding modulating substituents attached to the dye. [149] In this regard, one of the most effective approaches seems to be the variation of selectivity-controlling substituents, which are closely and rigidly attached to the chromophore.

During the last decade, self-assembly of a huge variety of PBI dyes have been investigated and their aggregates have found various applications as (opto-)electronic materials.[11, 112a, 135] As PBI dyes possess a hydrophobic extended π-core, a particular challenge being the exploration of the aggregation properties of PBI dyes in water which is, however, required for the application of these dyes in biological systems.[150] Beside other approaches, including ionic self-assembly,[150d, 150e] the attachment of polyamine chains at the imide positions of PBIs provides the necessary solubility of core-planar PBIs in water which make them interesting for the investigation of interactions with biomacromolecules such as DNA.[18d, 88, 151] Recently, we have communicated the first examples of spermine-functionalized homochiral PBIs with unique properties such as strong thermal stabilization and high binding affinity towards ds-DNA and RNA.[87]

Here we present our comprehensive studies on the interaction of PBI dyes with a broad variety of polynucleotides by applying a broad new series of homochiral PBIs (L)- and (D) PBI **17**, (L)- and (D) PBI **18** and (L)- and (D) PBI **19**. These PBIs are appended with amino acids possessing substituents of varied sterical demand at the chirality centers and incorporate spermine or 4,9-dioxa-1,12-dodecanediamine side chains at the imide positions (Scheme 7). For the purpose of comparison, we have included in this study the achiral reference compound PBI **20** [88] and the previously reported compounds (L)- and **(D)** PBI **16**.[87] We have investigated the spectroscopic response of the PBIs for structurally different double-stranded DNA and RNA under biologically relevant conditions. For these studies, we have chosen synthetic polynucleotides instead of short oligonucleotides because the latter are not suitable for our investigations due to the "capping" binding of PBIs at the exterior side of alternating basepairs which would strongly compete with the few binding sites along the double strands of oligonucleotides.[145, 152] In contrast, polynucleotides consisting of more than 100 basepairs will assure large excess of binding sites along the double helix, thus the "capping" effect should be negligible. Our detailed thermal denaturation experiments, fluorimetric titrations and CD spectroscopic measurements corroborate strong interactions of the homochiral ionic PBIs with the employed polynucleotides and the formation of excitonically coupled dimer aggregates in the grooves of the ds-DNA/RNA. The binding properties of these PBIs with ds-DNA/RNA are found to be dependent on the number of the positive charges, chirality and sterical hindrance of the PBIs. Thus, a structure-property relationship could be established.

5.2 Results and discussion

5.2.1 Synthesis

A series of symmetric, homochiral perylene bisimides (denoted as (L)- and (D) PBI **16**, (L)- and (D) PBI **17**, (L)- and (D) PBI **18** and (L)- and (D) PBI **19** that are appended with *α*-amino acid derivatives as imide substituents, bearing spermine or its dioxa analogue as side chains, were synthesized from commercially available perylene-3,4:9,10-tetracarboxylic bisanhydride (PBA) in three steps according to the route outlined in Scheme 7.

The reaction of PBA with homochiral (L- or D-enantiomer) alanine or phenylalanine in imidazole afforded the corresponding amino acid functionalized symmetrical PBIs (L)-[117] or (D) PBI **10** and (L)- or (D) PBI **11** in excellent yields. The successive amidation of the PBI-appended dicarboxylic acids with threefold Boc-protected spermine **Boc-(N)**[153] using the activation reagents dicyclohexylcarbodimide (DCC) and hydroxylbenzotriazole (HOBt) in DMF led to the spermine-bearing PBI derivatives (L)- or (D) PBI **12** and (L)- or (D) PBI **13** in 29 to 72% yields. Deprotection of the Boc-groups with trifluoroacetic acid (TFA) afforded the desired products (L)- or (D) PBI **16** and (L)- or (D) PBI **17** as trifluoroacetic salts in quantitative yields, which were then lyophilized from water to obtain them in pure form. For the amidation of the dicarboxylic acids with Boc-protected 4,9-dioxa-1,12-dodecanediamine **Boc-(O)**[154], however, the activation reagents *N*,*N*-diisopropylethyl-amine (DIPEA) and *O*-(7-azabenzotriazol-1-yl)-*N*,*N*,*N*',*N*'-tetramethyluroniumhexafluoro-phosphate (HATU), instead of DCC and HOBt were required. The deprotection of Boc-groups in the resulted (L)- or (D) PBI **14** and (L)- or (D) PBI **15** with TFA afforded the products (L)- or (D) PBI **18** and (L)- or (D) PBI **19** in 84 to 97% yields, which were subsequently purified by lyophilization from water.

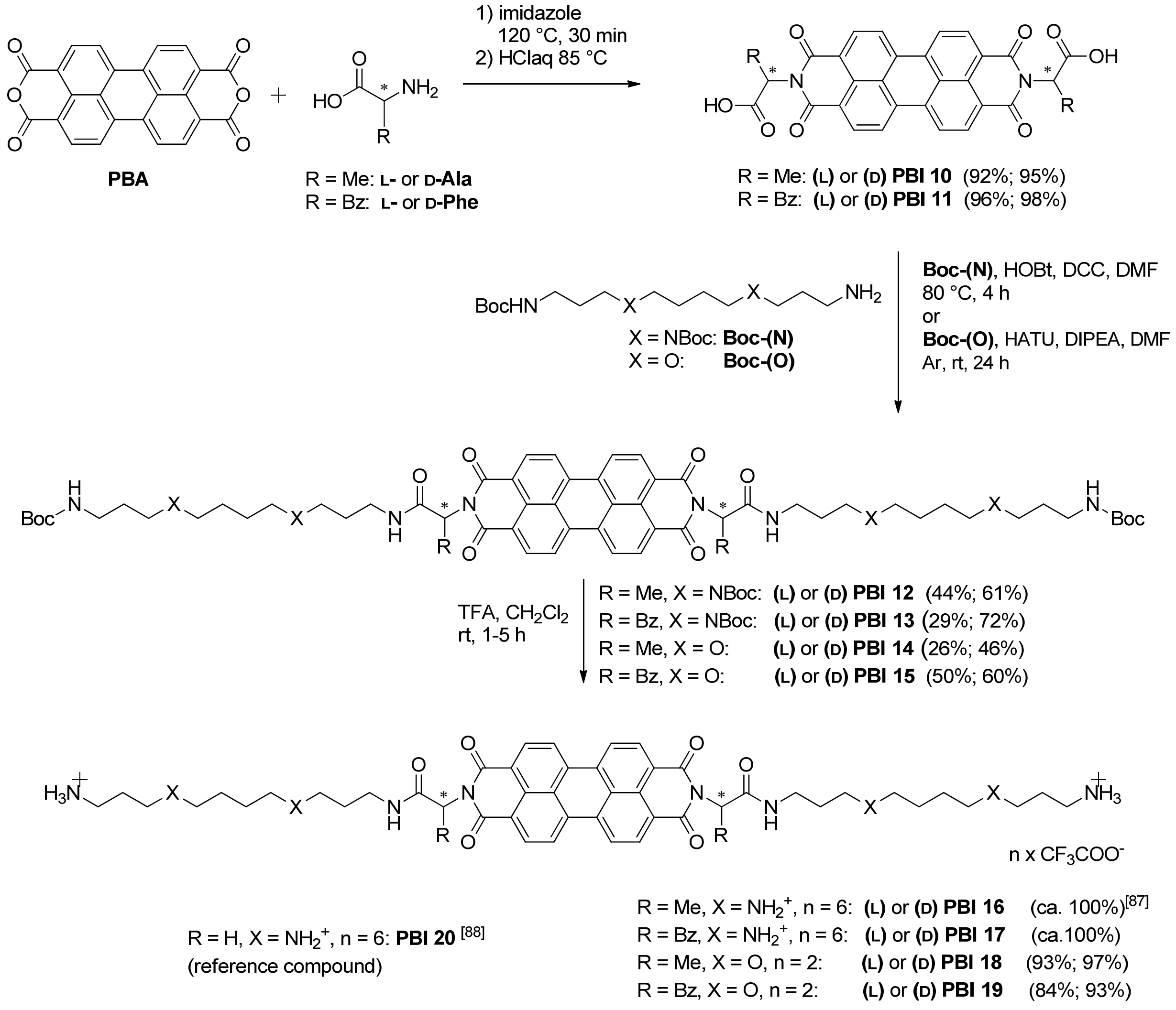

Scheme 7: Synthetic route to amino acid appended homochiral perylene bisimide dyes. Please note that both chirality centers of each of these homochiral PBIs have identical conformation, i.e. either L,L or D,D. For simplicity and easier comparison they are denoted as L- and D-enantiomer.

The alanine-functionalized compounds (L)- and (D) PBI **16** have previously been reported in our communication.[87] The reference achiral compound PBI **20** was prepared according to the literature.[88] All the new compounds were characterized by ^{1}H NMR, high-resolution mass spectroscopy and, where possible, also by elemental analysis. The details of the synthesis and characterization data of the new compounds are given in the Experimental Section.

5.2.2 UV/Vis spectroscopic studies of homochiral PBIs

To ascertain the appropriate conditions for the investigation of interactions of these homochiral PBIs with double-stranded (ds)-polynucleotides by different spectroscopic methods such as UV/Vis, fluorescence and circular dichroism (CD), we have initially performed concentration-dependant UV/Vis studies of these PBIs in water and DMSO (Figure 63 and Figure 70 in the Appendix of this Chapter). As a representative example of the spermine-containing PBIs (denoted as **(N)-**series), the concentration-dependent absorption spectra of (L) PBI **17** in pure water are displayed in Figure 63a. At a low concentration of 5 x 10^{-6} M, this dye exhibits for PBI monomers typical vibronically resolved spectrum with maxima at 537, 500 and 467 nm. With increasing concentration up to 5 x 10^{-3} M the intensities of monomer bands decreased with concomitant appearance of a strongly hypsochromically shifted band at 508 nm and a slightly

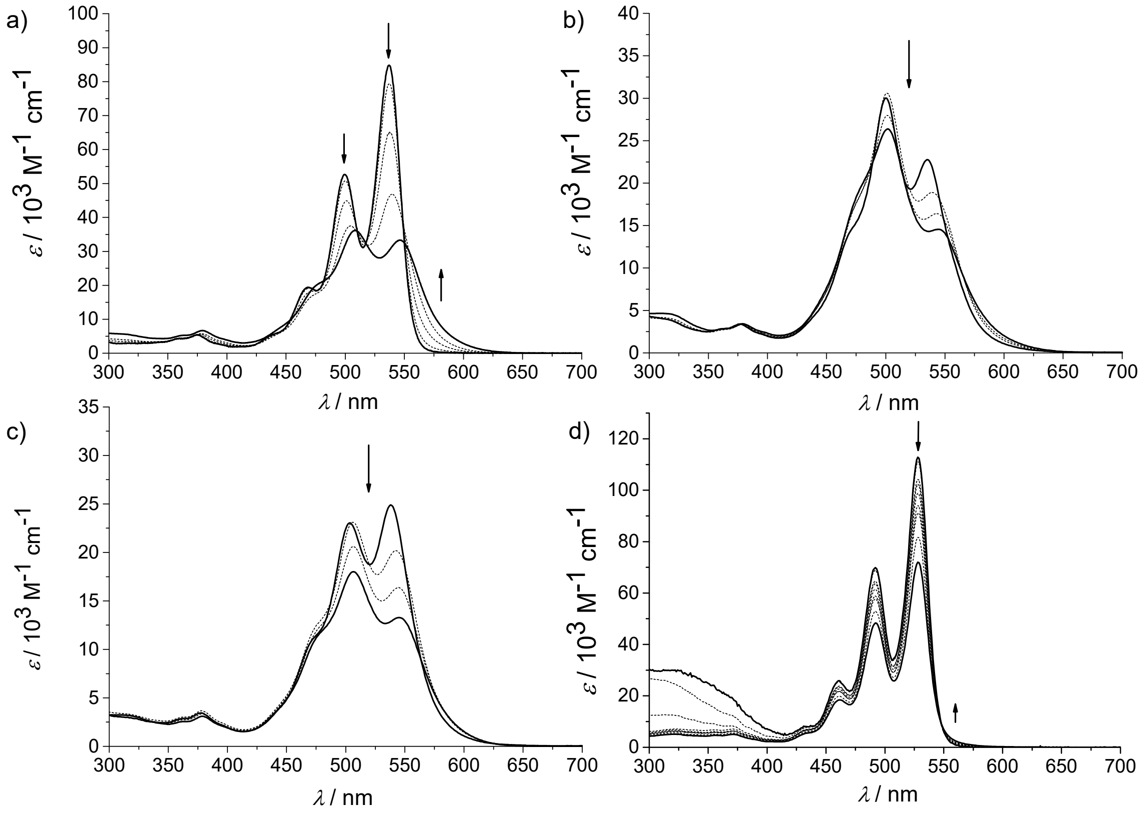

Figure 63: Concentration-dependent UV/Vis spectra (c = 5 x 10^{-6} to 5 x 10^{-3} M) of a) (L) PBI **17**, b) (L) PBI **18**, c) (L) PBI **19** in water and d) (L) PBI **18** in DMSO (c = 8 x 10^{-6} to 2 x 10^{-3} M) as representative example. Arrows indicate the spectral changes upon increasing concentration.

red-shifted band at 546 nm, indicating the formation of aggregates with H-type excitonic coupling.[13] Identical concentration-dependent spectral changes were observed for the corresponding D-enantiomer in water (spectra not shown). The concentration-dependent absorption properties of these phenylalanine-functionalized PBIs resemble those of the alanine analogues (L)- and (D) PBI **16**.[87] Since for the latter dimer formation, and no further growth to extended aggregates due to electrostatic repulsion of positive charges, was confirmed in the given concentration range, similar behavior can be assumed for the phenylalanine derivatives (L)- and (D) PBI **17**. In contrast to spermine-bearing PBIs (the **(N)**-series), the absorption spectra of their dioxa analogues (L)- and (D) PBI **18**, and (L)- and (D) PBI **19** revealed over the whole concentration range from 5 x 10^{-6} to 5 x 10^{-3} M existence of aggregated species in pure water. Upon increasing the concentration, hypochromic shift of the absorption bands at 500 and 535 nm for each of (L)- and (D) PBI **18**, and at 503 and 538 nm for each of (L)- and (D) PBI **19** occurred (Figure 63b,c and Figure 70a,b in the Appendix of this Chapter). In contrast to the PBIs of the **(N)**-series, the dioxa derivatives form more extended aggregates and hence tend slowly to precipitate in pure water due to decrease of positive charges and incorporation of more hydrophobic oxygen atoms in the side chains. However, the positions of the absorption maxima and the spectra shapes suggest that similar H-type aggregates as for the **(N)**-series are formed. On the other hand, the concentration-dependent UV/Vis spectra of the **(O)**-series in DMSO revealed the presence of well dissolved monomeric species over the whole concentration range from 8 x 10^{-6} to 2 x 10^{-3} M (the absorption spectra of (L) PBI **18**are shown as representative example in Figure 63d). Thus, stock solutions of **(O)**-series PBIs were prepared in DMSO for the studies with DNA/RNA (see next Section).

For the investigation with DNA/RNA, it is also of importance to know whether the addition of salts has any influence on the ionic self-assembly behavior of the newly synthesized homochiral PBIs, since such experiments are performed in buffer solutions of defined ionic strength. Thus, aggregation behavior of these PBIs at different salt concentrations has been studied by UV/Vis spectroscopy by adding up to 0.1 M of 1 M $NaCl_{aq}$ solution to the water solution of a particular PBI. Upon addition of increasing amounts of NaCl solution (from 0 to 0.1 M) to the aqueous solution of (L)- ($c = 5 \times 10^{-6}$ M) or (D) PBI **17** (1.25 x 10^{-5} M) the monomeric bands at 537 and 500 nm (for each of the enantiomers) gradually decreased (Figure 71a,b in the Appendix of this Chapter). Similar ionic strength induced aggregation was previously observed for (L)- and (D) PBI **16**.[87] As mentioned above, due to higher aggregation propensity of the less charged dioxa derivatives (L)- and (D) PBI **18** and (L)- and (D) PBI **19**, aggregate bands of these PBIs are evident even at a low concentration of $c = 5 \times 10^{-6}$ M (for each) in water. The addition of NaCl solution (from 0 to 0.1 M) to aqueous solutions of these PBIs at this concentration provoked hypochromic shift and changes in relative intensity for the vibronic excitonically coupled absorption bands, clearly indicating growth of larger PBI aggregates (Figure 71c-f in the Appendix of this Chapter).

5.2.3 Thermal denaturation of ds-DNA in the presence of PBIs

We have explored the interaction of homochiral PBIs (L)- and (D) PBI **16**, (L)- and (D) PBI **17**, and their dioxa analogues (L)- and (D) PBI **18**, and (L)- and (D) PBI **19** with ds-polynucleotides by the commonly used DNA thermal denaturation method. By this method the differences in melting temperatures (ΔT_m) of free ds-polynucleotides and their complexes with ligands (small molecules) are determined by UV/Vis spectroscopy, which provide valuable information on non-covalent interactions between DNA and small molecules.[155] Based on the results of UV/Vis absorption studies discussed before, for the DNA experiments stock solutions of spermine-containing PBI derivatives (**(N)**-series) were prepared in water ($c \sim 10^{-4}$ M, no salt nor buffer added), while those of dioxa analogues (**(O)**-series) in DMSO ($c \sim 10^{-4}$ M). By using DMSO stock solutions, time- and temperature-stable solutions of **(O)**-series PBIs in cacodylate buffer (pH = 7) could be obtained in which the content of DMSO never exceeded 1 vol%. Afterwards, mixtures of a chosen polynucleotide and one of the present PBIs were prepared by adding stock solution of the respective PBI to dissolved polynucleotide in cacodylate buffer (pH = 7) reaching a particular concentration ratio $r = [c\ (\text{PBI})] / [c\ (\text{polynucleotide})]$.

Since in many cases precipitation was observed at $r > 0.1$, thermal denaturation experiments were performed on solutions with $r = 0.025 - 0.1$. The thermal denaturation of poly(dA-dT)$_2$ with (L) PBI **18** is shown as representative example in Figure 64.

All of the present PBIs provoked an enhancement of the melting temperatures of the employed ds-polynucleotides even at these low concentration ratios. At $r = 0.05 - 0.1$, for the complexes of spermine-containing PBI derivatives (L)- and (D) PBI **16** and (L)- and (D) PBI **17** with all of the applied ds-polynucleotides ΔT_m values between 7 and > 35 °C were observed, while the corresponding dioxa analogues showed considerably lower ΔT_m values between 3 and 30 °C (see Table 4).

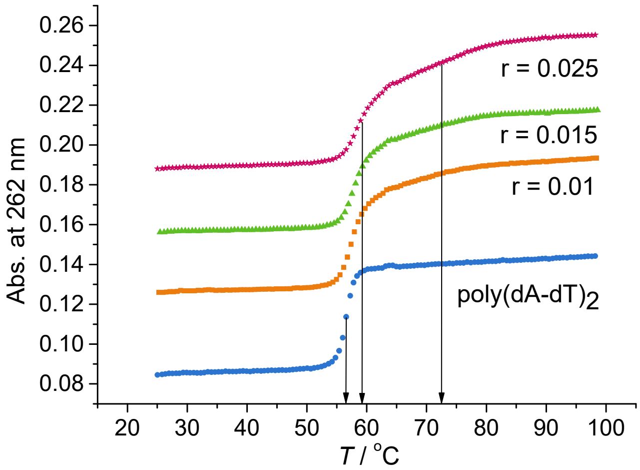

Figure 64: Thermal denaturation of poly(dA-dT)$_2$ upon addition of (L) PBI **18** as a representative example; *r* = [*c* (compound)] / [*c* (polynucleotide)] = 0.01-0.025, at pH 7.0, buffer sodium cacodylate, *I* = 0.05 M.

Obviously, due to larger number of positive charges (six each) the ΔT_m values of the **(N)-**series are higher than those observed for the **(O)**-series (two positive charges each). Notably, at *r* = 0.025 – 0.05 most of the DNA denaturation experiments showed biphasic curves consisting of a transition of the PBI non-bound polynucleotide moiety (T_m similar to that of the respective free DNA/RNA) and a transition at the significantly higher T_m corresponding to the PBI/polynucleotide complex (see Figure 64 for an example).

However, at *r* = 0.05 – 0.1 transitions of the free polynucleotides are either not present or observed in few cases with negligible intensity, which suggest complete saturation of PBI binding sites with the applied DNA and RNA at the ratio of *r* = 0.1. Only (L)- and (D) PBI **18** with *calf thymus* (ct)-DNA and (D) PBI **18** with poly(dA-dT)$_2$ showed biphasic transitions even at *r* = 0.1, which is indicative of mixed binding modes.

Since at *r* = 0.1 most of the denaturation curves are monophasic, and thus reveal the transition of the respective PBI/polynucleotide complex, a comparison of the melting temperature difference (ΔT_m) at this *r* value is most insightful. Spermine-containing achiral reference PBI **20** showed with ds-DNA (ct-DNA, poly dA-poly dT and poly(dA-dT)$_2$) ΔT_m values above 20 °C and a lower ΔT_m value of 16 °C with RNA (poly A-poly U). The chiral spermine-functionalized analogues displayed with all of the used ds-polynucleotides ΔT_m values above 14 °C, in some cases even higher than 35 °C, with the exception of (D) PBI **17**. The latter displayed the weakest enhancement of the T_m value of 8 °C with ct-DNA in comparison to other spermine-substituted derivatives. This is most likely owing to the weak binding of (D) PBI **17** to the GC-basepairs rich sequences of ct-DNA.

Table 4: The ΔT_m[a] values (°C) of polynucleotides upon addition of PBIs to give different ratios r[b] at pH 7.0, buffer sodium cacodylate, $I = 0.05$ M.

		ct-DNA		poly A-poly U		poly dA-poly dT		poly(dA-dT)$_2$	
PBI	r[b] =	0.05	0.1	0.05	0.1	0.05	0.1	0.05	0.1
PBI **20**		17	>20[c]	16[d]	16	26	25	23	23
(L) PBI **16**[e]		>20[c]	>20[c]	15	-	15/>35[c,d]	-	13/25[d]	[c]
(D) PBI **16**[e]		17[c]	>17[c]	13/35[d]	>35[c]	16/>35[c,d]	>35[c]	17	[c]
(L) PBI **17**		16	>20[c]	33	33	17/>28[c,d]	-	1/17[d]	18
(D) PBI **17**		7	8	33	31	15/>29[d]	15/>30[d]	13	14
(L) PBI **18**		4/>14[d]	6/>15[d]	10	10	-	4/10[d]	14	15
(D) PBI **18**		1/10[d]	3/11[d]	10	10	-	3/7[d]	4/10[d]	6/11[d]
(L) PBI **19**		3	5	8	9	-	29	-	5
(D) PBI **19**		3	4	9	10	-	30	7	7

[a] Error in $\Delta T_\mathrm{m} \pm 0.5$ °C. [b] $r =$ [c (compound)] / [c (polynucleotide)]. [c] T_m of complex > 100 °C. [d] Biphasic thermal denaturation transitions. [e] Previous reported data are shown for comparison.[87]

Oxygen bearing PBIs ((L)- and (D) PBI **18**, and (L)- and (D) PBI **19**) exhibited larger variations in ΔT_m values at the ratio of $r = 0.1$ depending on the applied polynucleotides. (L) PBI **18** and (D) PBI **18** showed generally stronger DNA stabilization effect compared with that of the corresponding phenylalanine-substituted PBIs with ΔT_m values of higher than 10 °C. The phenylalanine-substituted PBIs (L)- and (D) PBI **19** revealed smaller ΔT_m values between 4 and 10 °C. This difference between the alanine- and the phenylalanine- substituted PBIs of the **(O)**-series reveals stronger influence of the steric hindrance at the chiral centers of the amino acids on the interaction of these PBIs with DNA compared to that of the **(N)**-series PBIs. The steric impact seems to be more pronounced when the amount of positive charges in the side chains is reduced. For the complexes of homonucleotide poly dA-poly dT with (L)- and (D) PBI **19** exceptionally high values around 30 °C were observed which is remarkable for the quite narrow minor groove of this polynucleotide.[156] In the case of RNA no difference between the alanine- and phenylalanine-substituted PBIs could be observed since for both systems an average ΔT_m value of around 9 °C was determined. Apparently, the wide RNA groove provides sufficient space thus the steric hindrance does not play a significant role.[157] Moreover, several DNA/PBI complexes were submitted to slow cooling to room temperature after thermal denaturation to allow re-annelation of the complexes and again thermally denaturated, whereby excellent reproducibility between the first and second denaturation cycle was observed (representative examples are displayed in Figure 72a,b in the Appendix of this Chapter), indicating the formation of the same type of complex.

5.2.4 Fluorimetric titrations of PBIs with DNA/RNA

We have then determined the binding constants for the complexes of present PBIs with different ds-polynucleotides by fluorimetric titration experiments. To avoid reabsorption, emission intensities were monitored above $\lambda > 590$ nm upon excitation at a wavelength of $\lambda_{ex} = 498$ nm. Processing of the fluorescence titration data by means of non-linear fit to Scatchard equation[38, 63] provided binding constants log K_s for PBI/ds-polynucleotide complexes and pointed at saturation of dominant binding sites at r [c (PBI] / [c (polynucleotide)]) = 0.1. The binding constants obtained for the investigated PBIs with different polynucleotides are summarized in Table 5. The fluorescence titration spectra of the enantiomeric pair (L)- and (D) PBI **17** with poly(dG-dC)$_2$ are shown as representative examples in Figure 73, and those of the oxygen analogues (L)- and (D) PBI **19** with poly(dG-dC)$_2$ and poly(dA-dT)$_2$, respectively, in Figure 74 (see Appendix of this Chapter). The interaction of the ds-polynucleotides with **(N)**-series PBIs led to very high binding constants (log K_s = 9 – 9.8). These values are significantly higher than those reported so far for non-covalently interacting molecules.[158] The addition of the employed polynucleotides to highly charged spermine-functionalized derivatives ((L)- and (D) PBI **16**, (L)- and (D) PBI **17**), respectively, completely quenched their fluorescence at the saturation regime (Int. = 0, see Table 5).

This emission quenching can be attributed to the formation of non-fluorescent H-type PBI aggregates [88, 159] and their binding to polynucleotides.[84b, 160] In contrast to **(N)**-series PBIs, the dioxa analogues (L)- and (D) PBI **18**, and (L)- and (D) PBI **19** remained even upon saturation of DNA/RNA binding sites at the end of titration to some extent fluorescent (Int. = 0.07 to 0.46). Analysis of the binding parameters revealed that the dioxa analogues with two positive charges each bind more weakly to polynucleotides (log K_s = 6.5 to 7.9) than the spermine derivatives with six positive charges (log K_s > 9). Moreover, in contrast to the spermine derivatives, for dioxa analogues no trend between binding affinity and fluorescent properties of the formed

PBI/polynucleotide complexes was observed. For example, the binding constants of (L) PBI **19** with poly(dA-dT)$_2$, poly(dG-dC)$_2$ and poly dA-poly dT are within the narrow range of 6.5 – 6.9, but the fluorescence intensities at saturation regime appreciably vary from 0.15 to 0.42 (see Table 5).

Table 5: Binding constants log K_s[a] determined from the fluorescence titration data of PBIs with ds-polynucleotides at pH 7.0, buffer sodium cacodylate, I = 0.05 M.

	poly(dA-dT)$_2$ log K_s / Int.[b]	**poly(dG-dC)$_2$** log K_s / Int.[b]	**poly dA-poly dT** log K_s / Int.[b]	**poly A-poly U** log K_s / Int.[b]
PBI **20**	8-9[d]	8-9[d]	8-9[d]	8-9[d]
(L) PBI **16**[c]	9.7 / 0	>9[e] / 0	9.4 / 0	9.8 / 0
(D) PBI **16**[c]	9.6 / 0	9.5 / 0	9.5 / 0	9.5 / 0
(L) PBI **17**	9.5 / 0	>9[e] / 0	9.7 / 0	9.4 / 0
(D) PBI **17**	9.4 / 0	9.7 / 0	9.6 / 0	9.2 / 0
(L) PBI **18**	7.9 / 0.13	6.9 / 0.07	7.5 / 0.3	6.9 / 0.27
(D) PBI **18**	7.3 / 0.15	7.2 / 0.22	7.6 / 0.3	7.5 / 0.4
(L) PBI **19**	6.8 / 0.15	6.5 / 0.23	6.9 / 0.42	7.6 / 0.39
(D) PBI **19**	6.8 / 0.46	6.8 / 0.25	6.7 / 0.37	7.5 / 0.19

[a] The best Scatchard fit was obtained for ratio n ([bound PBI] / [polynucleotide]) = 0.2 – 0.1, and for easier comparison all binding constants were re-calculated for the fixed ratio n ([bound PBI] / [polynucleotide]) = 0.1. [b] Int. = fluorescence emission intensity at the end of titration. [c] Previously reported data added for comparison.[87] [d] Oscillation of PBI **20** fluorescence during titration with DNA/RNA allowed only estimation of the affinity within the given order of magnitude. [e] Almost linear emission quenching till Int. = 0 (reached at r [c (PBI)] / [c (polynucleotide)] = 0.1), which allowed only an estimation by Scatchard fit.

Possible explanation for this observation could be delivered by fluorescence lifetime experiments. The single exponential fluorescence decay and the fluorescence lifetime of 4.5 ns were recorded for the (L) PBI **18**/ct-DNA complex under the same conditions as applied for fluorimetric titrations (see Figure 75 in the Appendix of this Chapter). This could be explained by an equilibrium between the emissive PBI monomer and the non-emissive PBI aggregate within the ds-polynucleotides binding site. The huge excess of DNA/RNA used allows enough binding space within the grooves to accommodate such dimer-monomer equilibrium. The equilibrium is shifted towards strongly bound PBIs to ds-polynucleotides in the case of the **(N)**-series PBIs caused by additional interactions of the multiple positive charges of the side chains. Accordingly, these PBIs bind more strongly with ds-polynucleotides than their dioxa analogues.

5.2.5 CD spectroscopic studies of PBI/ds-polynucleotides complexes

To gain more insight into the DNA/RNA binding properties of chiral PBIs, we have performed circular dichroism (CD) spectroscopy studies by using a set of polynucleotides that possess specific minor groove features. Since achiral small molecules were reported to entail induced CD spectrum (ICD) upon binding to polynucleotides, providing useful information on DNA-binding modes,[161] we have first investigated the achiral glycine-bridged reference PBI **20**. This inherently CD silent PBI, indeed, showed distinct ICD bands depending on the employed polynucleotide (Figure 65).

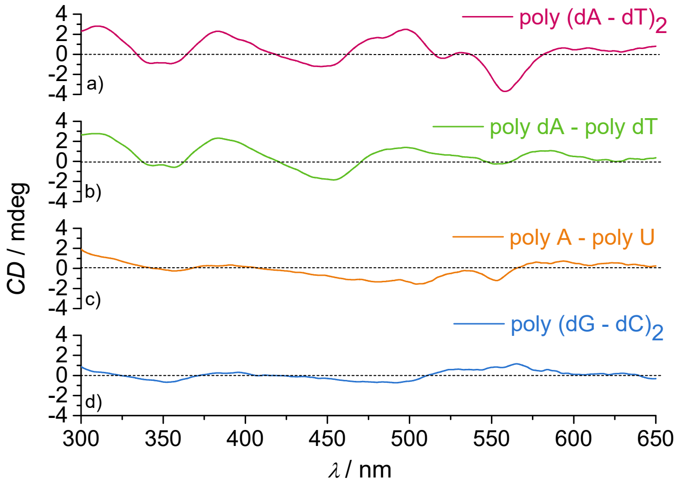

Figure 65: CD spectra of achiral reference PBI **20** upon interaction with a) poly(dA-dT)$_2$, b) poly dA-poly dT, c) poly A-poly U and d) poly(dG-dC)$_2$ at pH 7.0 in sodium cacodylate buffer, $I = 0.05$ M; polynucleotide concentration: 4 x 10^{-5} M; r [c (PBI)] / [c (polynucleotide)] = 0.16.

Addition of poly(dA-dT)$_2$ (4 x 10^{-5} M in sodium cacodylate buffer, pH = 7) to this PBI (r [c (PBI)] / [c (polynucleotide)] = 0.16) provoked clear bisignate Cotton effect in the $S_0 - S_1$ electronic transition region of PBI (> 400 nm) with maxima at 558 nm (-3.65 mdeg) and 498 nm (2.48 mdeg). Such bisignate CD signals are indicative of excitonic coupling of dyes which is only possible for dimers or larger aggregates with helical arrangement. Likewise, for poly(dG-dC)$_2$ bisignate CD bands, but with opposite signs, at 564 nm (1.18 mdeg) and 492vnm (-0.72 mdeg) were observed. The signs of the CD signals with poly(dA-dT)$_2$ are similar to those previously reported for (L) PBI **16** with this polynucleotide,[87] which suggest the preference of the same type of PBI dimer aggregate in the groove of poly(dA-dT)$_2$ also for PBI **20**. The guanine amino groups protruding into the GC-DNA minor groove may restrict the space to accommodate PBI **20** dimer in minor groove of poly(dG-dC)$_2$, and thus less intensive bisignate CD signals are observed with this polynucleotide. The opposite signs of the respective signal with poly(dG-dC)$_2$, compared with those with poly(dA-dT)$_2$, obviously point at a different orientation of the anticipated PBI dimer in the groove. As shown in Figure 65, for the much narrower minor groove of poly dA-poly dT,[162] PBI **20** exhibited similar CD spectral profile with maxima at 583 nm (1.03 mdeg) and 498 nm (1.37 mdeg) as observed for poly(dA-dT)$_2$ but with one significant difference, i.e. the opposite sign of the long-wavelength band (> 550 nm), which might be due to the existence of more than one binding mode. Addition of PBI **20** to A-U RNA resulted only in negative CD bands with maxima at 553 nm (-1.24 mdeg) and 506 nm (-1.58 mdeg). The absence of bisignate CD signals suggests the presence of single intercalated PBI **20** molecule into RNA as a dominant binding mode.[61, 84a] Possible explanation for this might be that PBI **20** does not have any significant steric hindrance due to the absence of a chiral substituent at the imide position, enabling intercalation into the minor groove of RNA that is wider than that of DNA.[163]

Next, we have investigated the CD spectroscopic profiles of chiral PBI derivatives in the presence of different polynucleotides that were also used for the achiral PBI **20**. The CD spectroscopic features of alanine-functionalized derivatives (L)- and (D) PBI **16** with these polynucleotides have been reported previously.[87] Their hitherto unknown dioxa analogues (L)- and (D) PBI **18**, which contain significantly less positive charges (each two) compared with their **(N)**-counterparts (each six), have been investigated in a comparative manner to assess the impact of positive charges on DNA/RNA binding properties that should be evident in CD spectra with different polynucleotides. The CD spectra of **(O)**-series PBIs are shown in Figure 66 and Figure 77 and, for the purpose of comparison, those of (L)- and (D) PBI **16** in Figure 76 (see Appendix of this Chapter).

The decrease of the positive charges in (L)- and (D) PBI **18** resulted in higher aggregation tendency of these oxygen-bearing PBIs, compared to the respective **(N)**-analogues, leading to relatively strong bisignate CD signals at a concentration of 6 x 10^{-6} M in water in the absence of any polynucleotide. These bisignate CD signals originate from excitonic coupling of stacked PBI dyes and demonstrate the influence of the chiral substituents at the imide groups on the helicity of the columnar PBI π-stack.[164] The (L) PBI **18** displayed CD signals at 557 nm (-4.2 mdeg) and 496 nm (5.2 mdeg) and the corresponding D-enantiomer at 558 nm (3.9 mdeg) and 496 nm (-4.6 mdeg).

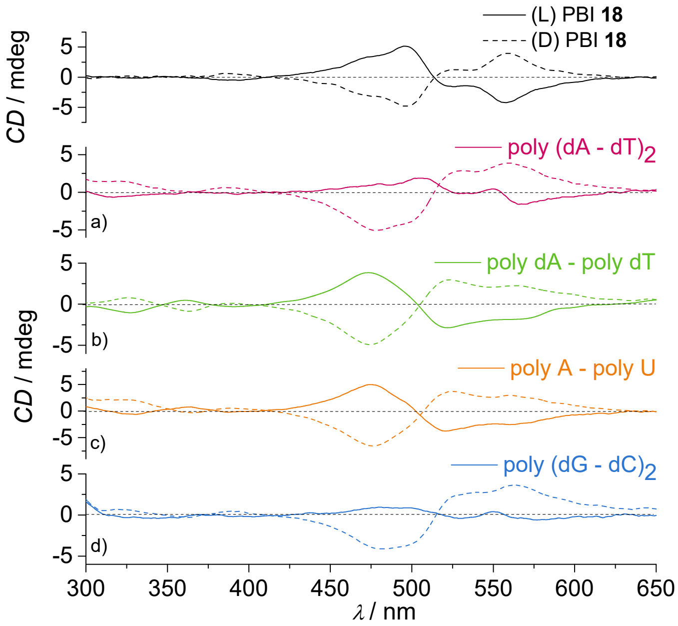

Figure 66: CD spectra of (L)- and (D) PBI **18** (note that CD spectra of (L)- and (D) PBI **18** at 6 x 10^{-6} M in water without polynucleotides are depicted above) upon interaction with a) poly(dA-dT)$_2$, b) poly dA-poly dT, c) poly A-poly U and d) poly(dG-dC)$_2$ at pH 7.0 in sodium cacodylate buffer, I = 0.05 M; polynucleotide concentration: 4 x 10^{-5} M; r [c (PBI)] / [c (polynucleotide)] = 0.15; L-configured PBI (solid line), D-configured PBI (dashed line).

The two enantiomers share one isoelliptic point at 514 nm (Figure 66, top). CD spectra of different polynucleotides (4 x 10^{-5} M in 0.05 M sodium cacodylate buffer at pH 7) measured upon addition of varied amounts of each of these PBIs (r [c (PBI)] / [c (polynucleotide)] upto 0.15) revealed emergence of excitonically coupled CD signals in the $S_0 - S_1$ electronic transition region of PBI (> 400 nm) with the strongest intensities at a ratio of r = 0.15 (see Figure 77 in the Appendix of this Chapter). At this ratio, the CD spectra of the enantiomeric (L)- and (D) PBI **18** showed for the applied polynucleotides distinctive spectral pattern (Figure 66). The CD signals of (D) PBI **18** with the various polynucleotides resemble those of PBI alone in water regarding both intensity and shape, which would mean that the PBI dimers formed in the grooves of DNA are similar to those formed in water in the absence of polynucleotides. The CD signals of the L-enantiomer with all of the applied polynucleotides are of weaker intensity compared to those of the counter enantiomer, and PBI alone in water (Figure 66). Moreover, the CD signals of different shapes are observed for (L) PBI **18**with polynucleotides of diverse minor groove properties, indicating a different arrangement of the anticipated PBI dimers in the groove.

In contrast to (L)- and (D) PBI **18**, phenylalanine derivatives of both **(O)**- and **(N)**-series display negligible CD signals at the concentration of 6 x 10^{-6} M in water in the absence of polynucleotides (Figure 78, Figure 79 in the Appendix of this Chapter and Figure 67, top spectra). This result complies with our earlier finding that the bulky phenylalanine substituents prohibit the aggregation of the PBI dyes and that accordingly monomeric dyes are present at this low concentration (see Figure 63 and Figure 70).

Interestingly, in the presence of polynucleotides these phenylalanine bearing PBIs showed, in most of the cases, CD bands in the region > 400 nm that confirm the interaction between these PBIs and the chiral DNA scaffold. The CD spectral pattern of (L)- and (D) PBI **17** at $r = 0.15$ revealed even bisignate Cotton effects with poly dA-poly dT and poly A-poly U at 570 nm and 490 nm which suggest the incorporation of PBI dimers in the minor grooves.

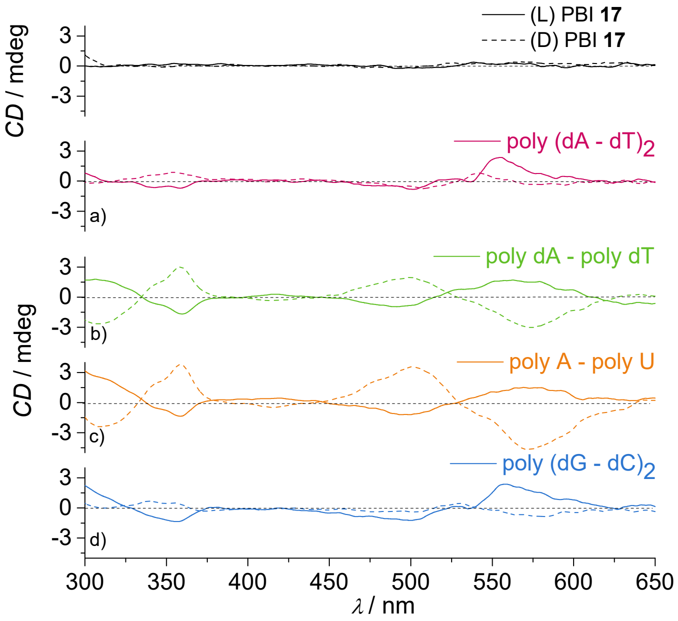

Figure 67: CD spectra of (L)- and (D) PBI **17** upon interaction with a) poly(dA-dT)2, b) poly dA-poly dT, c) poly A-poly U and d) poly(dG-dC)2 at pH 7.0 in sodium cacodylate buffer, $I = 0.05$ M; polynucleotide concentration: 4 x 10^{-5} M; r [c (PBI)] / [c (polynucleotide)] = 0.15; L-configured PBI (solid line), D-configured PBI (dashed line). CD spectra of (L)- and (D) PBI **17** at 6 x 10^{-6} M in water alone are depicted at the top.

The intensities of around 1.5 / -1.0 mdeg for the L-enantiomer and around -4.0 / 2.7 mdeg for the D-enantiomer (Figure 67) are, however, lower compared to those of the respective alanine derivatives (L)- and (D) PBI **17** (Figure 76 in the Appendix of this Chapter). This might be again due to the steric hindrance of the phenylalanine substituent. (D) PBI **17** exhibited rather negligible, small CD signals for poly(dA-dT)2 and poly(dG-dC)2, whereas for the L-enantiomer comparatively strong bisignate CD signals at 550 nm (2.4 mdeg) and 500 nm (-0.98 mdeg) with these polynucleotides were observed. These configuration-dependent CD spectral properties are intriguing as they reveal that relatively small minor grooves of poly(dA-dT)$_2$ and poly(dG-dC)$_2$ can still accommodate dimers of L-configured PBI, and obviously not those of D-configured one. Compared with (L)- and (D) PBI **18**, the phenylalanine derivatives (L)- and (D) PBI **19** showed less pronounced CD signals revealing the impact of the steric hindrance of the benzyl substituent attached at the chiral centers of these PBIs. The CD spectral pattern of (L)- and (D) PBI **19** showed bisignate Cotton effects with poly dA-poly dT and poly A-poly U at 575 nm and 490 nm with intensities of around 1.5 / -1.3 mdeg for the L-enantiomer and around -2.3 / 1.0 mdeg for the D-enantiomer (Figure 68).

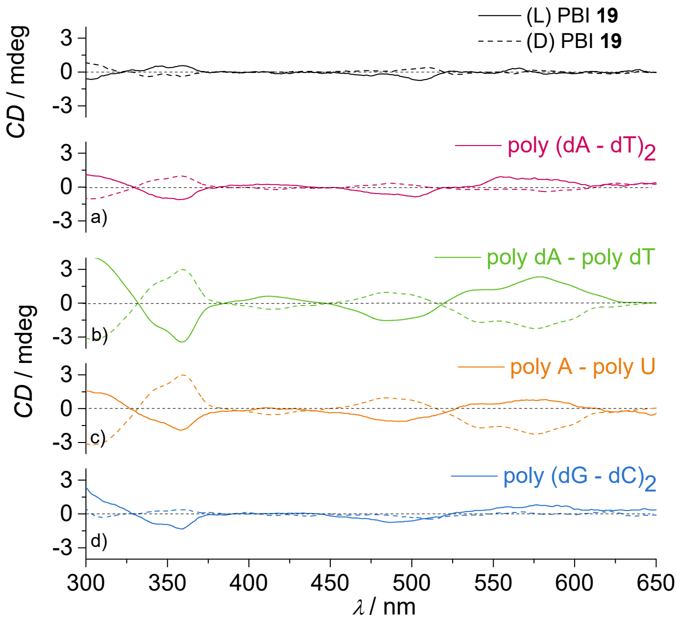

Figure 68: CD spectra of and (L)- and (D) PBI **19** upon interaction with a) poly(dA-dT)$_2$, b) poly dA-poly dT, c) poly A- poly U and d) poly(dG-dC)$_2$ at pH 7.0 in sodium cacodylate buffer, $I = 0.05$ M; polynucleotide concentration: 4×10^{-5} M; r [c (PBI)] / [c (polynucleotide)] = 0.15; L-configured PBI (solid line), D-configured PBI (dashed line). CD spectra of (L)- and (D) PBI **19** alone at a concentration of 6×10^{-6} M in water are depicted at the top.

(L) PBI **19** exhibited with poly(dA-dT)$_2$ and poly(dG-dC)$_2$ CD signals at 560 nm (0.90 mdeg) and 490 nm (0.80 mdeg), while the CD signals of the respective D-enantiomer are nearly negligible. These results indicate again high preference for one enantiomer (in this case L-enantiomer) in the minor groove of these polynucleotides. Moreover, upon thermal denaturation followed by slow cooling, the ICD band pattern was fully reconstituted (a representative example is shown in Figure 79 in the Appendix of this Chapter), pointing at the consistency of the complex formed.

Such enantioselective sensing of polynucleotide secondary structure with small molecules has rarely been reported, thus homochiral PBIs are of high interest for potential application in DNA/RNA sensing.

5.2.6 Molecular modeling

Our spectroscopic results have clearly shown that PBI dimers are formed in the groove of ds-DNA/RNA. For the visualization of the PBI dimer/polynucleotide complexes and to corroborate our spectroscopic results, we have performed molecular modeling studies. For these studies, we have chosen (L) PBI **18** as a representative example for PBI derivatives and ds-polynucleotides poly(dA-dT)$_2$ (Figure 69a) and poly(dG-dC)$_2$ (Figure 69b) with minor grooves of different widths and performed 10 ns molecular modelling simulations.

The positions of positively charged aliphatic substituents are expected to change between various interaction contacts (e.g. with phosphate backbone) in thermodynamic equilibrium due to their own flexibility as well as the dynamic nature of DNA, while the main aim of modelling study is to give insight into the orientation of PBI dimer within the DNA binding site as well as orientation between two PBI molecules within the dimer. This will allow not only visual perception the structure of the complex formed, but also suggest possible inter- and intramolecular interactions of PBI within the binding site (minor groove), which should be instructive for the design of new compounds.

During 10 ns simulations (see Supporting Information for details) of the (L) PBI **18** dimer/poly(dA-dT)$_2$ complex at room temperature, the PBI molecules nicely accommodated into the minor grove of the polynucleotide. In this orientation the (L) PBI **18** dimer aggregate is bound to the poly(dA-dT)$_2$ by four strong hydrogen bonds formed between the terminal protonated amine groups and the phosphate groups of the DNA backbone. This model of the PBI/DNA complex illustrate that, although the PBI dimer aggregate retained in the left-handed (*M*) helical configuration, the mutual position of the two PBI molecules is not perfectly centered as depicted in the molecular model of the free (L) PBI **18** dimer aggregate (Figure 69c). This difference in molecular structure of free PBI dimer and PBI/DNA complex explains the differences in the CD signal patterns observed for the complex of (L) PBI **18** with polynucleotides and free (L) PBI **18** in water (see Figure 66). During the 6 ns simulations of the (L) PBI **18** dimer/poly(dG-dC)$_2$ complex the PBI dimer was not inserted deeply into the polynucleotide minor groove, as in the case of poly(dA-dT)2. This is apparently due to the steric hindrance of guanine amino groups in poly(dG-dC)2. Nevertheless, the complex was stabilized by the hydrophobic interactions, two hydrogen bonds between the terminal protonated amine groups and the phosphate groups of the polynucleotide as well as one additional NH phosphate hydrogen bond (Figure 69b).

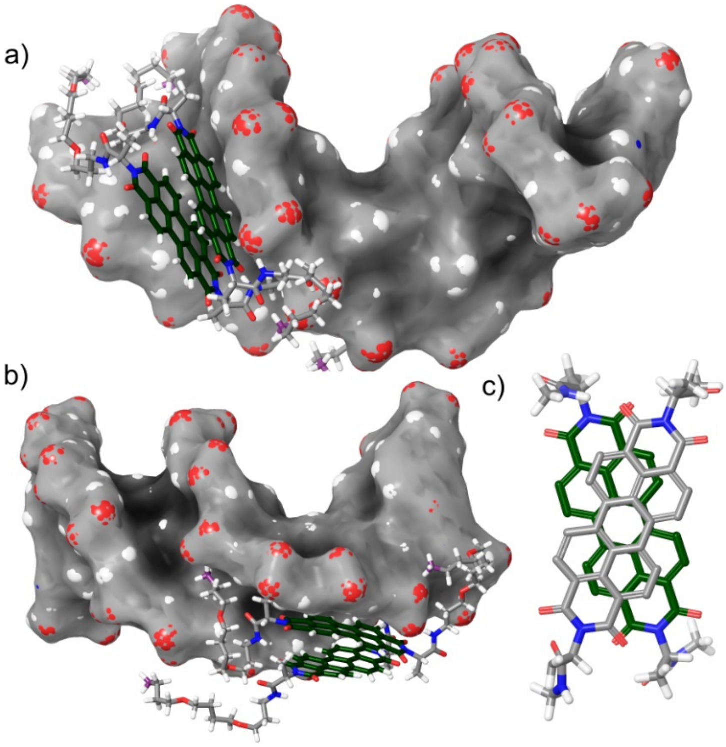

Figure 69: Modeled structure of the a) (L) PBI **18** dimer/poly(dA-dT)$_2$ complex and b) (L) PBI **18** dimer/poly(dG-dC)$_2$ complex obtained after 10 ns simulations in water at room temperature, reflecting the orientation and the arrangement of the PBI dimer aggregate within the minor groove of the ds-polynucleotide. c) Modeled structure of the free (L) PBI **18** dimer with left-handed (*M*-configuration) helicity in water (*OPLS 2001**).

Consequently, the dimer aggregate of (L) PBI **18** is more exposed to the aqueous environment outside the DNA and is less penetrated into the minor groove. Thus, the PBI dimer gains orientation freedom along the DNA helical axis which enables various possible arrangements, leading to much weaker CD signals with respect to those of the (L) PBI **18** dimer/poly(dA-dT)2 complex. The outcome of molecular modeling studies strongly supports our conclusion made on the basis of the results of UV/Vis, fluorescence and CD spectroscopic investigations that PBI dimer aggregates with pronounced excitonic coupling are formed in the minor groove of the ds-DNA.

5.3 Conclusion

In summary, we have synthesized three new enantiomeric pairs of amino acid functionalized amphiphilic perylene bisimide dyes. Our in-depth studies with this broad series of homochiral ionic PBIs possessing varying number of positive charges, steric hindrance and the chiral information revealed convincing structure-property relationships for the interaction of PBI dyes with ds-polynucleotides. Thermal denaturation experiments, fluorimetric titrations and CD measurements confirmed the formation of stable PBI/polynucleotide complexes for the investigated PBIs. The spermine-containing PBIs having six positive charges each exhibited stronger DNA stabilization effect and higher binding constants compared with their dioxa analogues having only two positive charges each, thereby the latter PBIs showed more specific differences depending on their structural features. The CD spectroscopic studies revealed marked differences in ds-DNA/RNA binding properties of PBIs depending on the steric hindrance of the amino acids attached at the imide positions of the PBIs and their configuration, on the one hand, and groove properties of the employed ds-DNA/RNA, on the other hand. The formation of the excitonically coupled PBI dimer aggregates in the minor groove of ds-DNA and the major groove of ds-RNA can be implied from the spectroscopic results, and the structures of PBI/polynucleotide complexes obtained from molecular modeling reinforce the spectroscopic results. Based on our highly interesting findings, we can conclude that the present homochiral PBI dyes should be relevant for the enantioselective sensing of DNA/RNA secondary structures.

5.4 Experimental section

5.4.1 General methods and materials

Solvent and reagents were purchased from commercial sources, unless otherwise stated, and purified and dried according to standard procedures.[126] Polynucleotides poly A-poly U, poly dA-poly dT, poly(dA-dT)$_2$, poly(dG-dC)$_2$ and calf thymus ct-DNA (according to the producer declarations the average length of polynucleotides used is > 500 in base pairs), and perylene bisanhydride (PBA) was obtained from commercial suppliers. Reactions were monitored by TLC on silica gel plates (Merck TLC silica gel 60 F254 aluminium sheets). All perylene bisimide derivatives are colored compounds, thus no additional visualization of the spots was necessary. Amines were visualized by spraying the TLC plate with ninhydrine solution.[165] Column chromatography was performed on silica gel (MerckSilica 60, particle size 0.04 – 0.063 mm). Semipreparative HPLC was performed on a Jasco system (PU 2080 PLUS) with a UV/Vis detector (UV2077 PLUS) using a semipreparative NUCLEOSIL 100–5 NO_2 column (Macherey & Nagel). NMR experiments were conducted on a Bruker Avance 400 spectrometer with TMS or residual deuterated solvent as internal standard. The chemical shifts are reported in ppm relative to TMS or residual deuterated solvent as internal standard (δ scale). The apparent coupling constants J are given in Hertz (Hz). The following abbreviations are used to describe the signal fine structure: s = singlet, br s = broad singlet, br d =vbroad doublet, d = doublet, t = triplet, q = quartet, quint = quintet, dt = doublet of triplets, tt = triplet of triplets, and m = multiplet. Melting points were measured on a polarization microscope equipped with mgw Lauda RM6 cooling systems and are uncorrected. IR spectra of the solid compounds were measured on a FT/IR-4100 Type A spectrophotometer. High-resolution electrospray ionization (ESI) mass spectra were measured on a MicroTOF Focus instrument (Bruker Daltronik GmbH) and MALDI-TOF measurements were carried out on a Bruker Autoflex II.

5.4.2 DNA melting experiments

Thermal melting curves for DNA/RNA and their complexes with the present PBI compounds were determined with UV/Vis spectroscopy by monitoring the absorption change at 260 nm and 262 nm as a function of temperature.[166] Absorbance of the PBI ligands was subtracted from the respective melting curve and the absorbance scale was normalized. The melting temperature T_m values are the midpoints of the transition curves, determined from the maximum of the first derivative and checked graphically by the tangent method.[166] ΔT_m values were calculated by subtracting T_m of the free nucleic acid from that of the respective complex with ΔT_m values are the average of at least two independent measurements and the error in ΔT_m is ca. ± 0.5 °C.

5.4.3 Spectroscopic measurements

The absorption spectra were obtained on a Varian Cary 100 Bio and Perkin–Elmer Lambda 35 spectrometer. The fluorescence spectra were recorded with a PTI QM-4/2003 instrument. The CD spectra were recorded on a JASCO J815 spectrophotometer. The samples were placed in Hellma precision cells 100-QS (10 mm) made of Quartz SUPRASIL™ of appropriate path length. The spectroscopic studies were performed in aqueous buffer solution (pH 7, sodium cacodylate buffer, $I = 0.05$ M). Polynucleotides were dissolved in sodium cacodylate buffer, *I* = 0.05 M, pH 7. Calf thymus (ct)-DNA was additionally sonicated and filtered through a 0.45 μm filter.[167] Polynucleotide concentration was determined spectroscopically.[167] Spectroscopic titrations were performed by adding portions of polynucleotide solution into the solution of the studied PBIs. Obtained data were corrected for dilution. Titration data were processed by Scatchard equation,[63, 168] and satisfactory correlation coefficients (> 0.999) were obtained for the binding constants (K_s).

5.4.4 Molecular Modeling

Double-stranded DNA poly(dA-dT)$_2$ and poly(dG-dC)$_2$ were created with the program NUCGEN, which is a part of the AMBER11 program suite. Substrate ((L) PBI **18** dimer) was docked manually into the polynucleotide minor groove by using the program Insight II. The obtained complexes were neutralized (Na^+ ions added), solvated (TIP3P water was used), energy minimized, equilibrated (temperature was adjusted to 300 K and the water density to about 1 g/cm^3) and simulated at 300 K for 10 ns (with a step of 1 fs) without any constrains. The simulations were accomplished using Periodic Boundary conditions (PBC). Temperature and pressure were kept constant during the simulation by Langevin dynamics (thermostat) and Berendsen barostat, respectively. The Particle Mesh Ewald (PME) method was used for the calculation of long-range electrostatic interactions.

5.4.5 Synthesis and characterization of PBIs

General procedure for the synthesis of PBIs (L)- or (D) PBI 11: Perylene tetracarboxylic bisanhydride PBA (1.00 mmol, 1 equiv), the appropriate α-amino acid **L-** or **D-Phe** (2 equiv) and imidazole (40 mmol) were mixed and heated to 120 °C for 30 minutes. After cooling down to 85 °C the pH value was adjusted to 3-4 with 1 N hydrochloric acid. The precipitate was collected by suction filtration, washed with water and dried in high vacuum.

N**,*****N*****'-(L-phenylalanyl)perylene-3,4:9,10-tetracarboxylic acid bisimide ((L) PBI 11)**: yield: 824 mg (1.20 mmol, 96%) of a dark red solid; MW ($C_{42}H_{26}N_2O_8$) = 686.66 g/mol; m.p.: > 400 °C; ^{1}H NMR (400 MHz, [D$_6$]DMSO): $\delta = 8.87$ (d, $J = 8.2$ Hz, 4H, perylene protons), 8.51 (d, $J = 7.8$ Hz, 4H, perylene protons), 7.19 (d, $J = 1.3$ Hz, 4H, Ph-H), 7.15 (t, $J = 7.2$ Hz, 4H, Ph-H), 7.04 (t, $J = 7.2$ Hz, 2H, Ph-H), 5.92 (q, $J = 5.3$ Hz, 2H, CH), 3.60 (dd, $J = 14.8$ Hz, $J = 5.9$ Hz, 2H, CH_2), 3.38 (dd, $J = 14.2$ Hz, $J = 9.5$ Hz, 2H, CH_2, partially superimposed by the water peak);

FT-IR: 3027 (w), 2936 (w), 1696 (s), 1655 (s), 1590 (s), 1575 (s), 1495 (m), 1434 (m), 1401 (m), 1363 (s), 1342 (s), 1252 (m), 1196 (m), 1128 (m).

***N,N'*-(D-phenylalanyl)perylene-3,4:9,10-tetracarboxylic acid bisimide ((D) PBI 11)**: yield: 823 mg (1.19 mmol, 98%) of a dark red solid; MW ($C_{42}H_{26}N_2O_8$) = 686.66 g/mol; m.p.: > 400 °C; ^{1}H NMR (400 MHz, [D$_6$]DMSO): $\delta = 8.84$ (d, $J = 8.3$ Hz, 4H, perylene protons), 8.50 (d, $J = 7.6$ Hz, 4H, perylene protons), 7.20 (d, $J = 1.3$ Hz, 4H, Ph-H), 7.15 (t, $J = 7.2$ Hz, 4H, Ph-H), 7.05 (t, $J = 7.2$ Hz, 2H, Ph-H), 5.91 (dd, $J = 5.4$ Hz, 2H, Ph-H), 3.60 (dd, $J = 14.4$ Hz, $J = 5.9$ Hz, 2H, CH_2), 3.40 (dd, $J = 14.0$ Hz, $J = 9.5$ Hz, 2H, CH_2); FT-IR: 3027 (w), 2940 (w), 1731 (m), 1695 (s), 1655 (s), 1591 (s), 1576 (s), 1496 (m), 1434 (m), 1401 (m), 1363 (s), 1341 (s), 1252 (m), 1168 (m), 1128 (m);

Synthesis of Boc-protected amine *t*Boc-4,9-dioxa-1,12-dodecanamine (Boc-(O)) (for the structure see Scheme 7in the main text): 4,9-Dioxa-1,12-dodecanediamine (5 g, 24.5 mmol, 5.23 mL, 2.5 equiv) was dissolved in dichloromethane / methanol (3:2, 250 mL) under argon atmosphere. A solution of di-*t*butyl dicarbonate (2.15 g, 9.85 mmol, 1 equiv) in methanol (10 mL) was added dropwise within 10 minutes. The reaction solution was stirred for additional 48 h under argon atmosphere at room temperature. After removal of the solvent in vacuo, the highly viscous oil was purified by column chromatography (SiO_2, CH_2Cl_2/MeOH: NEt_3 = 10:3:0.5 v/v/v) to obtain the desired product as a light yellow oil in 76% yield (2.27 g, 7.46 mmol). MW ($C_{15}H_{32}N_2O_4$) = 304.43 g/mol; $R_f = 0.8$ (CH_2Cl_2:MeOH:NEt_3 = 10:4:1); ^{1}H NMR ($CDCl_3$): $\delta = 4.93$ (br s, 1H, NH), 3.45 (m, 8H, CH_2), 3.21 (m, 2H, CH_2), 2.82 (t, $J = 6.7$ Hz, 2H, CH_2), 2.26 (br s, 2H, NH_2), 1.73 (quint, $J = 6.2$ Hz, 4H, CH_2), 1.64 (quint, $J = 3.1$ Hz, 4H, CH_2), 1.45 (s, 9H, CH_3); MS (MALDI-TOF, matrix: DHB 2:1 in methanol): $m/z = 305.243$; calcd for $[M+H]^+$: 305.244.

General procedure for the synthesis of PBIs (L) **or** (D) PBI 13: A solution of the respective PBI (0.28 mmol, 1 equiv), threefold *t*Boc-protected spermine **Boc-(N)** (2.1 equiv), DCC (3 equiv), HOBt (0.8 equiv) and Hünig's base (EtN(*i*Pr)$_2$, 0.1 mL) were stirred in DMF (5 mL) at 80 °C for 4 h. After the mixture is being cooled down to room temperature, water (50 mL) and CH_2Cl_2 (50 mL) were added. The phases were separated and the aqueous phase was extracted with CH_2Cl_2 (2 x 50 mL). The combined organic phases were washed with water (200 mL) and concentrated under reduced pressure. The crude product was purified by column chromatography (SiO_2, CH_2Cl_2/MeOH = 99:1 to 97:3) and subsequent HPLC (CH_2Cl_2/MeOH = 97:3).

***N,N'*-(L-phenylalanyl(tri-*t*Boc-spermine))perylene-3,4:9,10-tetracarboxylic acid bisimide ((L) PBI 13)**: Yield: 76 mg (0.46 mmol, 29%) of a pink solid; MW ($C_{92}H_{122}N_{10}O_{18}$) = 1656.01 g/mol; R_f = 0.26 (SiO_2, CH_2Cl_2:MeOH = 97:3); m.p.: 91 – 93 °C; ^1H NMR ($CDCl_3$): δ = 8.51 (d, J = 8.0 Hz, 4H, perylene protons), 8.44 (s, J = 8.3 Hz, 4H, perylene protons), 7.62 (br s, 2H, NH), 7.06 (m, 10H, Ph-H), 6.00 (dd, J = 5.9 Hz, J = 4.6 Hz, 2H, CH), 3.79 – 3.74 (m, 2H, CH_2), 3.57 (m, 2H, CH_2), 3.07 (m, 24H, CH_2), 1.56 (m, 8H CH_2), 1.42 (s, 46H, CH_2, CH_3), 0.80 (s, 16H, CH_2, CH_3); HRMS (ESI pos.): *m/z* = 1677.8836; calcd for $[M+Na]^+$:1677.8831; UV/Vis (CH_2Cl_2, c = 5 x 10^{-5} M): λ_{max} (nm) [ε_{max} ($M^{-1}cm^{-1}$)] = 459 [18400], 491 [50800], 527 [85000].

***N,N'*-(D-phenylalanyl(tri-*t*Boc-spermine))perylene-3,4:9,10-tetracarboxylic acid bisimide ((D) PBI 13)**: Yield: 430 mg (0.26 mmol, 72%) of a pink solid; MW ($C_{92}H_{122}N_{10}O_{18}$) = 1656.01 g/mol; R_f = 0.26 (SiO_2, CH_2Cl_2:MeOH = 97:3); m.p.: 92 – 93 °C; ^1H NMR ($CDCl_3$): δ = 8.57 (d, J = 8.3 Hz, 4H, perylene protons), 8.44 (s, J = 6.6 Hz; 4H, perylene protons), 7.69 (br s, 2H, NH), 7.12 (m, 10H, Ph-H), 6.06 (dd, J = 4.2 Hz, J = 5.0 Hz, 2H, CH), 3.84 (m, 2H, CH_2), 3.65 (m, 2H, CH_2), 3.14 (m, 24H, CH_2), 1.61 (m, 8H, CH_2), 1.42 (s, 46H, CH_2, CH_3), 0.87 (s, 16H, CH_2, CH_3); HRMS (ESI pos.): *m/z* = 1677.8852; calcd for $[M+Na]^+$:1677.8831; UV/Vis (CH_2Cl_2, c = 5 x 10^{-5} M): λ_{max} (nm) [ε_{max} ($M^{-1}cm^{-1}$)] = 459 [18200], 491 [50600], 527 [85000].

General procedure for the synthesis of PBIs (L) or (D) PBI 14 and (L) or (D) PBI 15: A suspension of the respective PBI (0.240 mmol, 1 equiv), Boc-protected amine **Boc-(O)** (3 equiv), *O*-(7-azabenzotriazol-1-yl)-*N,N,N',N'*-tetramethyl-uronium hexafluorophosphate (HATU) (2.2 equiv) and Hünig's base (2 equiv) was stirred in dry DMF (15 mL) at room temperature for 24 h under argon atmosphere. After removal of the solvent in vacuo, water (100 mL) was added and extracted with CH_2Cl_2 (4 x 80 mL).The combined organic phases were dried over $MgSO_4$ and concentrated under reduced pressure. The crude product was purified by column chromatography (SiO_2, CH_2Cl_2/MeOH = 20:1).

***N*,*N*’-(L-alanyl(*t*Boc-4,9-dioxa-1,12-dodecanamine))perylene-3,4:9,10-tetracarboxylic acid bisimide ((L) PBI 14)**: Yield: 121 mg (0.108 mmol, 46%) of a red solid; MW ($C_{60}H_{78}N_6O_{14}$) = 1107.29 g/mol; R_f = 0.16 (SiO_2, CH_2Cl_2:MeOH = 20:1); m.p.: 274 – 276 °C; ^{1}H NMR ($CDCl_3$): δ = 8.60 (d, J = 8.0 Hz, 4H, perylene protons), 8.59 (d, J = 8.1 Hz, 4H, perylene protons), 6.74 (t, J = 5.0 Hz, 2H, NH), 5.71 (q, J = 6.9 Hz, 2H, CH), 4.85 (br s, 2H, NH), 3.57 (t, J = 5.7 Hz, 4H, CH_2), 3.49 (m, 4H, CH_2), 3.41 (t, J = 5.9 Hz, 4H, CH_2), 3.36 (m, 4H, CH_2), 3.17 (m, 4H, CH_2), 1.85 (m, 4H, CH_2), 1.73 (d, J = 7.0 Hz, 6H, CH_3), 1.69 (m, 4H, CH_2), 1.41 (br s, 26 H, CH_2, CH_3); MS (MALDI-TOF, matrix: DCTB 1:3 in chloroform): m/z = 1106.399; calcd for [M]: 1106.560; elemental analysis calcd (%) for $C_{60}H_{78}N_6O_{14}$: C 65.08, H 7.10, N 7.59; found: C 64.46, H: 7.50, N 7.42; UV/Vis (CH_2Cl_2, $c = 5 \times 10^{-5}$ M): λ_{max} (nm) [ε_{max} ($M^{-1}cm^{-1}$)] = 459 [17900], 490 [51700], 526 [85400].

***N*,*N*’-(D-alanyl(*t*Boc-4,9-dioxa-1,12-dodecanamine))perylene-3,4:9,10-tetracarboxylic acid bisimide ((D) PBI 14):** Yield: 65.1 mg (0.059 mmol, 26%) of a red solid; MW ($C_{60}H_{78}N_6O_{14}$) = 1107.29 g/mol; R_f = 0.16 (SiO_2, CH_2Cl_2:MeOH = 20:1); m.p.: 275 – 276 °C; ^{1}H NMR ($CDCl_3$): δ = 8.58 (d, J = 8.0 Hz, 4H, perylene protons), 8.44 (d, J = 8.2 Hz, 4H, perylene protons), 6.78 (t, J = 4.8 Hz, 2H, NH), 5.71 (q, J = 7.0 Hz, 2H, CH), 4.89 (br s, 2H, NH), 3.58 (t, J = 5.8 Hz, 4H, CH_2), 3.49 (m, 4H, CH_2), 3.43 (t, J = 6.0 Hz, 4H, CH_2), 3.37 (m, 4H, CH_2), 3.17 (m, 4H, CH_2), 1.86 (m, 4H, CH_2), 1.73 (d, J = 7.0 Hz, 6H, CH_3), 1.69 (m, 4H, CH_2), 1.42 (br s, 26 H, CH_2, CH_3); MS (MALDI-TOF, matrix: DCTB 1:3 in chloroform): m/z = 1106.308; calcd for [M]: 1106.560; elemental analysis calcd (%) for $C_{60}H_{78}N_6O_{14}$: C 65.08, H 7.10, N 7.59; found: C 64.84, H: 7.27, N 7.44; UV/Vis (CH_2Cl_2, $c = 5 \times 10^{-5}$ M): λ_{max} (nm) [ε_{max} ($M^{-1}cm^{-1}$)] = 459 [17500], 490 [50300], 526 [83700].

***N*,*N*’-(L-phenylalanyl(*t*Boc-4,9-dioxa-1,12-dodecanamine))perylene-3,4:9,10-tetracarboxylic acid bisimide ((L) PBI 15)**: Yield: 144 mg (0.114 mmol, 50%) of a red solid; MW ($C_{72}H_{86}N_6O_{14}$ = 1259.49 g/mol; R_f = 0.17 (SiO_2, CH_2Cl_2:MeOH = 20:1); m.p.: 81 – 83 °C; ^{1}H NMR ($CDCl_3$): δ = 8.46 (d, J = 8.0 Hz, 4H, perylene protons), 8.34 (d, J = 8.2 Hz, 4H, perylene protons), 7.21 (d, J = 8.6 Hz, 4H, Ph-H), 7.11 (t, J = 7.1 Hz, 4H, Ph-H), 7.03 (t, J = 7.3 Hz, 2H, Ph-H), 6.69 (br s, 2H, NH), 6.00 (dd, J = 6.3 Hz, 2H, CH), 4,83 (br s, 2H, NH), 3.62 (m, 4H, CH_2), 3.49 (m, 6H, H4, CH_2), 3.34 (m, 10H, CH_2), 3.29 (m, 4H, CH_2), 3.13 (m, 4H, CH_2), 1.82 (quint, J = 6.1 Hz, 4H, CH_2), 1.65 (quint, 4H, J = 6.1 Hz, CH_2), 1.51 (quint, J = 3.0 Hz, 8H,

CH_2), 1.42 (s, 18H, CH_3); MS (MALDI-TOF, matrix: DCTB 1:3 in chloroform): *m/z* = 1258.429; calcd for [M]: 1258.620; elemental analysis calcd (%) for $C_{72}H_{86}N_6O_{14}$: C 68.66, H 6.88, N 6.67; found: C 68.93, H: 7.24, N 6.48; UV/Vis (CH_2Cl_2, $c = 5 \times 10^{-5}$ M): λ_{max} (nm) [ε_{max} ($M^{-1}cm^{-1}$)] = 459 [18400], 491 [52400], 527 [86400].

***N,N'*-(D-phenylalanyl(*t*Boc-4,9-dioxa-1,12-dodecanamine))perylene-3,4:9,10-tetracarboxylic acid bisimide ((D) PBI 15)**: Yield: 181 mg (0.113 mmol, 60%) of a red solid; MW ($C_{72}H_{86}N_6O_{14}$) = 1259.49 g/mol; $R_f = 0.14$ (SiO_2, CH_2Cl_2:MeOH = 20:1); m.p.: 82 – 84 °C; ^1H NMR ($CDCl_3$): $\delta = 8.55$ (m, 8H, perylene protons), 7.19 (d, $J = 6.8$ Hz, 4H, Ph-H), 7.10 (t, $J = 7.6$ Hz, 4H, Ph-H), 7.03 (t, $J = 7.0$ Hz, 2H, Ph-H), 6.56 (br s, 2H, NH), 6.00 (dd, $J = 6.5$ Hz, 2H, CH), 4,80 (br s, 2H, NH), 3.61 (m, 4H, CH_2), 3.48 (m, 6H, H4, CH_2), 3.32 (m, 10H, CH_2), 3.27 (m, 4H, CH_2), 3.11 (m, 4H, CH_2), 1.77 (quint, $J = 5.3$ Hz, 4H, CH_2), 1.64 (quint, 4H, $J = 6.1$ Hz, CH_2), 1.46 (quint, $J = 3.0$ Hz, 8H, CH_2), 1.40 (s, 18H, CH_3); MS (MALDI-TOF, matrix: DCTB 1:3 in chloroform): *m/z* = 1258.378; calcd for [M]: 1258.620; elemental analysis calcd (%) for $C_{72}H_{86}N_6O_{14}$: C 68.66, H 6.88, N 6.67; found: C 68.66, H: 7.11, N 6.53; UV/Vis (CH_2Cl_2, $c = 5 \times 10^{-5}$ M): λ_{max} (nm) [ε_{max} ($M^{-1}cm^{-1}$)] = 459 [17700], 491 [50300], 527 [82900].

General procedure for the synthesis of PBIs (L)- and (D) PBI 17, (L)- and (D) PBI 18, and (O)- (L)- and (D) PBI 19: A solution of the respective PBI (1 equiv) in trifluoroacetic acid (3 mL) was stirred for 1-5 h at room temperature and subsequently concentrated in vacuo. MilliQ water (5 mL) was added to the residue, yielding a dark red solution, which was then lyophilized twice to obtain pure compound.

***N,N'*-(L-phenylalanyl(spermine))perylene-3,4:9,10-tetracarboxylic acid bisimide ((L) PBI 17)**: Yield: 13.9 mg (8×10^{-6} mol, quantitative) of a red fluffy solid; MW ($C_{74}H_{80}F_{18}N_{10}O_{18}$) = 1739.45 g/mol; m.p.: > 400 °C; ^1H NMR ([D$_6$]DMSO): $\delta = 8.95$ (d, $J = 8.0$ Hz, 4H, perylene protons), 8.72 (br s, 4H, NH), 8.53 (br d, $J = 7.6$ Hz, 6H, perylene protons, NH), 8.22 (t, $J = 6.0$ Hz, 2H, CH), 7.88 (br s, 4H, NH_2), 7.05 (m, 10H, Ph-H), 5.82 (dd, $J = 10.0$ Hz, $J = 5.2$ Hz, 2H, CH_2), 3.65 (dd, $J = 14.0$ Hz, $J = 5.6$ Hz, 2H, CH_2), 3.17 (m, 4H, CH_2), 2.91 (m, 20H, CH_2), 1.89 (quint, $J = 7.2$ Hz, 4H, CH_2), 1.73 (m, 4H, CH_2), 1.66 (br s, 8H, CH_2); HRMS (ESI pos.): *m/z* = 1055.5842; calcd for $[M+H]^+$:1055.5866; UV/Vis (H_2O,

$c = 5 \times 10^{-6}$ M): λ_{max} (nm) [ε_{max} ($M^{-1}cm^{-1}$)] = 469 [19400], 500 [52600], 537 [84900]; fluorescence (H_2O, λ_{ex} = 475 nm): λ_{max} (nm) = 549; Φ_{fl} = 0.79.

***N,N'*-(D-phenylalanyl(spermine))perylene-3,4:9,10-tetracarboxylic acid bisimide ((D) PBI 17)**: Yield: 13.9 mg (8×10^{-6} mol, quantitative) of a red fluffy solid; MW ($C_{74}H_{80}F_{18}N_{10}O_{18}$) = 1739.45 g/mol; m.p.: > 400 °C; ^{1}H NMR ([D$_6$]DMSO): δ = 8.95 (d, J = 8.0 Hz, 4H, perylene protons), 8.78 (br s, 4H, NH), 8.58 (br s, 2H, NH), 8.53 (d, J = 8.0 Hz, 4H, perylene protons), 8.21 (t, J = 6.0 Hz, 2H, CH), 7.91 (br s, 4H, NH_2), 7.06 (m, 10H, Ph-H), 5.82 (dd, J = 10.4 Hz, J = 5.6 Hz, 2H, CH_2), 3.66 (dd, J = 14.4 Hz, J = 5.6 Hz, 2H, CH_2), 3.17 (br s, 4H, CH_2), 2.93 (m, 20H, CH_2), 1.91 (quint, J = 8.0 Hz, 4H CH_2), 1.73 (m, 4H, CH_2), 1.66 (br s, 8H, CH_2); HRMS (ESI pos.): m/z = 1055.5866; calcd for $[M+H]^+$:1055.5866.

***N,N'*-(L-alanyl(4,9-dioxa-1,12-dodecanamine))perylene-3,4:9,10-tetracarboxylic acid bisimide ((L) PBI 18)**: Yield: 115 mg (0.101 mmol, 97%) of a red fluffy solid; MW ($C_{54}H_{64}F_6N_6O_{14}$) = 1135.11 g/mol; m.p.: 103 – 105 °C; ^{1}H NMR ([D$_4$]MeOH): δ = 8.54 (d, J = 8.2 Hz, 4 H, perylene protons), 8.47 (d, J = 8.0 Hz, 4H, perylene protons), 5.67 (q, J = 7.0 Hz, 2H, CH), 3.49 (m, 20H, CH_2), 3.02 (t, J = 7.0 Hz, 4H, CH_2), 1.88 (m, 4H, CH_2), 1.80 (m, 4H, CH_2), 1.78 (d, J = 7.0 Hz, 6H, CH_3), 1.61 (m, 8H, CH_2); HRMS (ESI pos.): m/z = 929.4254; calcd for $[M+Na]^+$: 929.4420; elemental analysis calcd (%) for $C_{54}H_{64}F_6N_6O_{14}$ + 2 H_2O: C 55.38, H 5.85, N 7.18; found: C 55.29, H 5.86, N 7.13; UV/Vis (H_2O, $c = 5 \times 10^{-6}$ M): λ_{max} (nm) [ε_{max} ($M^{-1}cm^{-1}$)] = 500 [30000], 535 [22800], fluorescence (H_2O, λ_{ex} = 480 nm): λ_{max} (nm) = 543, 585;

***N,N'*-(D-alanyl(4,9-dioxa-1,12-dodecanamine))perylene-3,4:9,10-tetracarboxylic acid bisimide ((D) PBI 18)**: Yield: 59.6 mg (0.053 mmol, 93%) of a red fluffy solid; MW ($C_{54}H_{64}F_6N_6O_{14}$) = 1135.11 g/mol; m.p.: 104 – 106 °C; ^{1}H NMR ([D$_4$]MeOH): δ = 8.54 (d, J = 8.1 Hz, 4 H, perylene protons), 8.47 (d, J = 8.0 Hz, 4H, perylene protons), 5.67 (q, J = 7.0 Hz, 2H, CH), 3.50 (m, 20H, CH_2), 3.02 (t, J = 7.0 Hz, 4H, CH_2), 1.90 (m, 4H, CH_2), 1.79 (m, 10H, CH_2, CH_3), 1.62 (m, 8H, CH_2); HRMS (ESI pos.): m/z = 929.4271; calcd for $[M+Na]^+$: 929.4420; elemental analysis calcd. (%) for $C_{54}H_{64}F_6N_6O_{14}$ + 2 H_2O: C 55.38, H 5.85, N 7.18; found: C 55.72, H 6.07, N 7.20; UV/Vis (H_2O, $c = 5 \times 10^{-6}$ M): λ_{max} (nm) [ε_{max} ($M^{-1}cm^{-1}$)] = 500 [33300], 535 [25900], fluorescence (H_2O, λ_{ex} = 480 nm): λ_{max} (nm) = 543, 585.

***N*,*N*'-(L-phenylalanyl(4,9-dioxa-1,12-dodecanamine))perylene-3,4:9,10-tetracarboxylic acid bisimide ((L) PBI 19)**: Yield: 180 mg (0.140 mmol, 93%) of a red fluffy solid; MW ($C_{66}H_{72}F_6N_6O_{14}$) = 1287.30 g/mol; m.p.: 104 – 106 °C; ^{1}H NMR ([D$_4$]MeOH): $\delta = 8.70$ (d, $J = 7.9$ Hz, 4H, perylene protons), 8.49 (d, $J = 7.9$ Hz, 4H, perylene protons), 7.13 (d, $J = 8.0$ Hz, 4H, Ph-H), 7.04 (t, $J = 7.5$ Hz, 4H, Ph-H), 6.97 (t, $J = 7.4$ Hz, 2H, Ph-H), 5.99 (dd, $J = 5.6$ Hz, 2H, CH), 3.63 (m, 4H, CH_2), 3.53 (m, 6H, CH_2), 3.46 (m, 10H, CH_2), 3.38 (m, 4H, CH_2), 3.02 (t, $J = 7.0$ Hz, 4H, CH_2), 1.88 (quint, $J = 6.0$ Hz, 4H, CH_2), 1.78 (quint, $J = 6.5$ Hz, 4H, CH_2), 1.62 (m, 8H, CH_2); HRMS (ESI pos.): $m/z = 1081.5023$; calcd for $[M+Na]^+$: 1081.5046; elemental analysis calcd (%) for $C_{66}H_{72}F_6N_6O_{14} + H_2O$: C 60.73, H 5.71, N 6.44; found: C 60.33, H 5.75, N 6.42; UV/Vis (H_2O, $c = 5 \times 10^{-6}$ M): λ_{max} (nm) [ε_{max} ($M^{-1}cm^{-1}$)] = 503 [23000], 538 [24900], fluorescence (H_2O, $\lambda_{ex} = 480$ nm): λ_{max} (nm) = 545, 588.

***N*,*N*'-(D-phenylalanyl(4,9-dioxa-1,12-dodecanamine))perylene-3,4:9,10-tetracarboxylic acid bis-imide ((D) PBI 19)**: Yield: 180 mg (0.140 mmol, 93%) of a red fluffy solid; MW ($C_{66}H_{72}F_6N_6O_{14}$) = 1287.30 g/mol; m.p.: 101 – 103 °C; ^{1}H NMR ([D$_4$]MeOH): $\delta = 8.65$ (d, $J = 7.9$ Hz, 4H, perylene protons), 8.47 (d, $J = 8.0$ Hz, 4H, perylene protons), 7.14 (d, $J = 7.4$ Hz, 4H, Ph-H), 7.05 (t, $J = 7.1$ Hz, 4H, Ph-H), 6.98 (t, $J = 7.2$ Hz, 2H, Ph-H), 6.00 (dd, $J = 5.5$ Hz, 2H, CH), 3.63 (m, 4H, CH_2), 3.54 (m, 6H, CH_2), 3.47 (m, 10H, CH_2), 3.37 (m, 4H, CH_2), 3.07 (t, $J = 7.0$ Hz, 4H, CH_2), 1.88 (quint, $J = 6.4$ Hz, 4H, CH_2), 1.79 (quint, $J = 6.3$ Hz, 4H, CH_2), 1.60 (m, 8H, CH_2); HRMS (ESI pos.): $m/z = 1081.5023$; calcd for $[M+Na]^+$: 1081.5046; elemental analysis calcd (%) for $C_{66}H_{72}F_6N_6O_{14} + H_2O$: C 60.73, H 5.71, N 6.44; found: C 60.11, H 5.78, N 6.45; UV/Vis (H_2O, $c = 5 \times 10^{-6}$ M): λ_{max} (nm) [ε_{max} ($M^{-1}cm^{-1}$)] = 504 [27500], 538 [28800], fluorescence (H_2O, $\lambda_{ex} = 480$ nm): λ_{max} (nm) = 545, 588.

5.5 Appendix

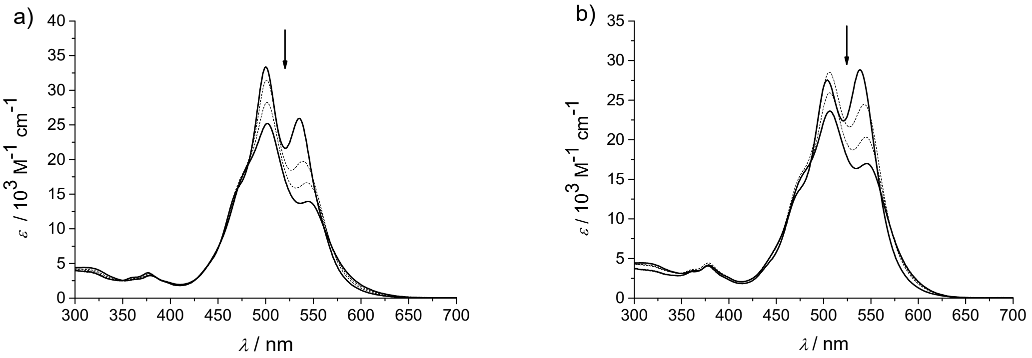

Figure 70: Concentration-dependent UV/Vis spectra of a) (D) PBI **18**and b) (D) PBI **19** in water (c = 5 x 10^{-3} to 5 x 10^{-6} M). Arrows indicate the spectral changes upon increasing concentration.

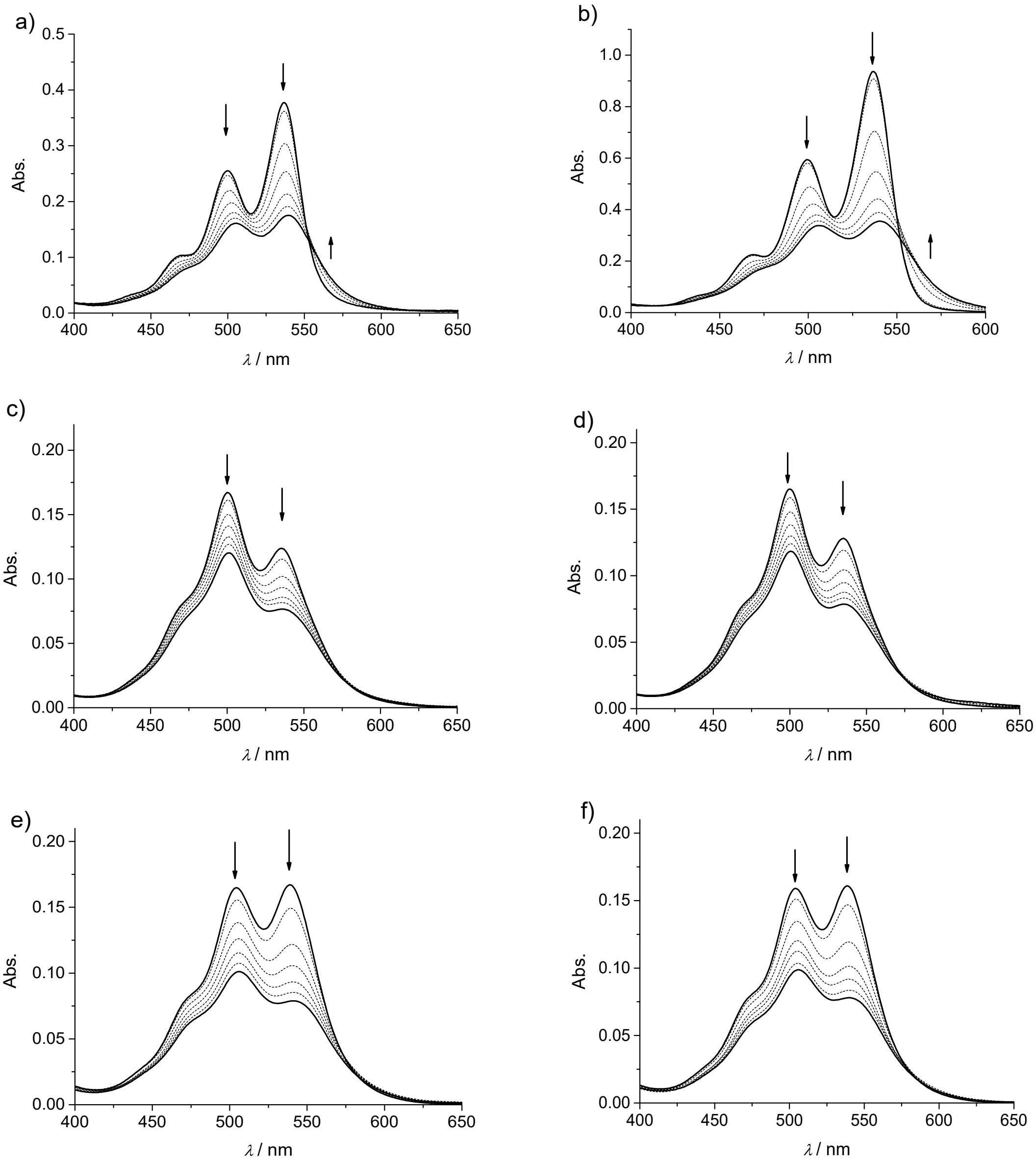

Figure 71: Changes of UV/Vis spectra of PBI a) (L) PBI **17** ($c = 5 \times 10^{-6}$ M), b) (D) PBI **17** ($c = 1.25 \times 10^{-5}$ M), c) (L) PBI **18** ($c = 5 \times 10^{-6}$ M), d) (D) PBI **18** ($c = 5 \times 10^{-6}$ M), e) (L) PBI **19** ($c = 5 \times 10^{-6}$ M) and f) (D) PBI **19** ($c = 5 \times 10^{-6}$ M) in water upon addition of aliquots of 1 M $NaCl_{aq}$ (0 to 0.1 M). Arrows indicate spectral changes upon increasing concentration of NaCl.

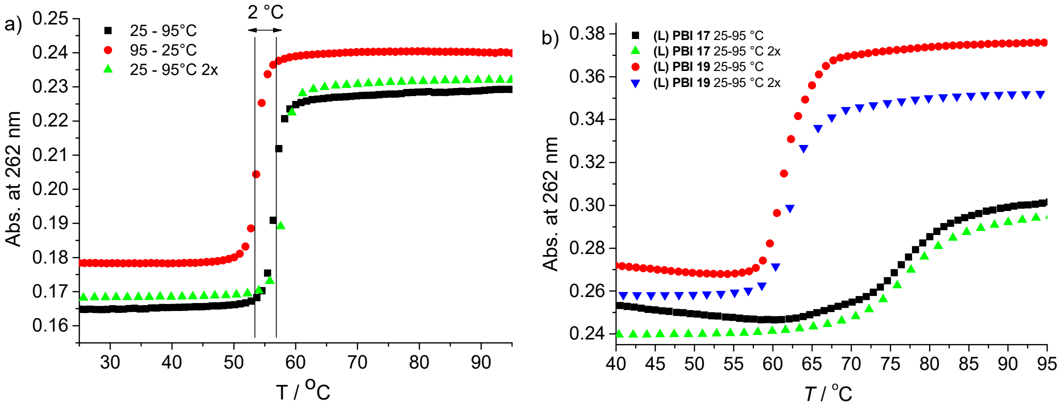

Figure 72: Thermal denaturation of a) the free polynucleotide poly(dA-dT)$_2$ upon heating to 95 °C and reformation of the double stand upon cooling to 25 °C and b) poly(dA-dT)$_2$ upon addition of (L) PBI **17**and (L) PBI **19** , *r* [*c* (PBI)] / [*c* (polynucleotide)] = 0.1, at pH 7.0, buffer sodium cacodylate, *I* = 0.05 M. The small hysteresis of 2 and 1 °C is close to the error of the method (± 0.5 °C). Second heating curve represent the reproducibility of the denaturation experiment.

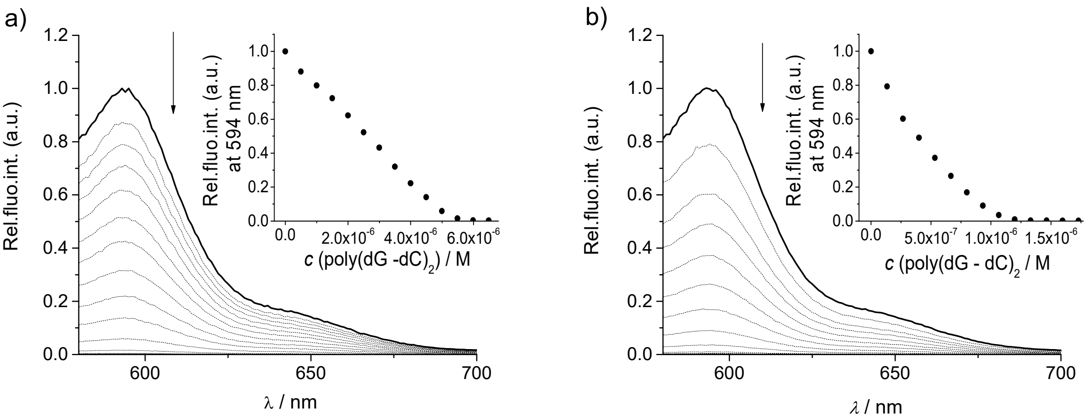

Figure 73: Changes of fluorescence spectra of a) (L) PBI **17** (c = 7.4 x 10^{-7} M) and b) (D) PBI **17** (c = 5.0 x 10^{-7} M) upon addition of poly(dG-dC)$_2$ at pH 7.0, buffer sodium cacodylate, *I* = 0.05 M. Arrows indicate spectral changes with increasing amount of poly(dG-dC)$_2$. Inset: Dependence of fluorescence intensity at λ_{max} = 594 nm on the concentration of poly(dG-dC)$_2$

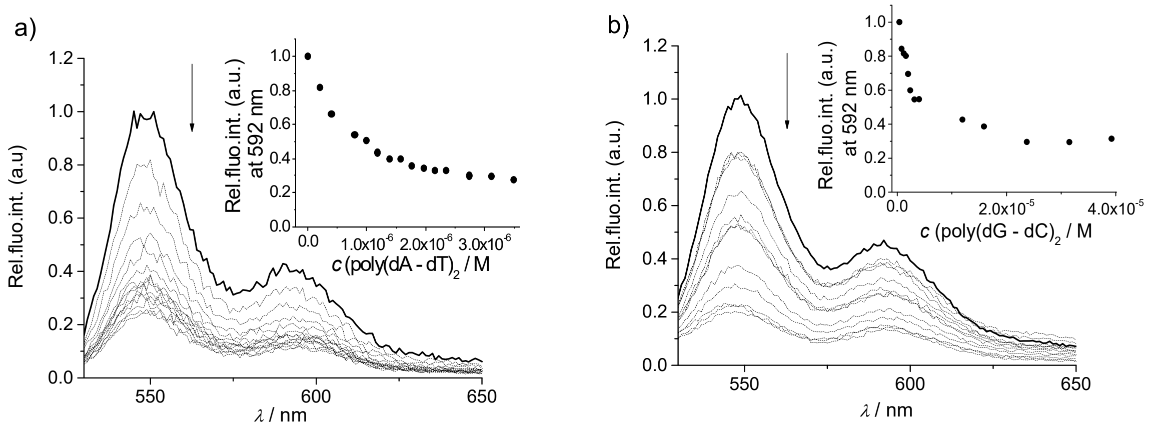

Figure 74: Changes of fluorescence spectra of a) (L) PBI **19** (c = 5.0 x 10^{-8} M) upon addition of poly(dA-dT)$_2$ and b) (D) PBI **19** (c = 5.0 x 10^{-8} M) upon addition of poly(dG-dC)$_2$ at pH 7.0, buffer sodium cacodylate, I = 0.05 M. Arrows indicate spectral changes with increasing amount of poly(dA-dT)$_2$ and poly(dG-dC)$_2$. Inset: Dependence of fluorescence intensity at λ_{max} = 592 nm on the concentration of poly(dA-dT)$_2$ and poly(dG-dC)$_2$.

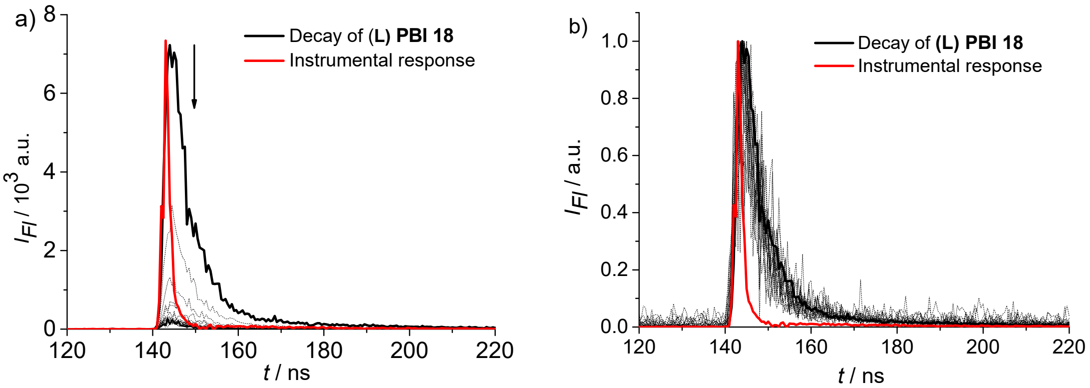

Figure 75: a) Fluorescence intensity decay and b) normalized fluorescence intensity decay (λ_{ex}=490 nm, λ_{det} = 547 nm) of (L) PBI **18** (c = 5.0 x 10^{-8} M) upon addition of ct-DNA at pH 7.0, buffer sodium cacodylate, I = 0.05 M. Arrows indicate spectral changes with increasing amount of ct-DNA.

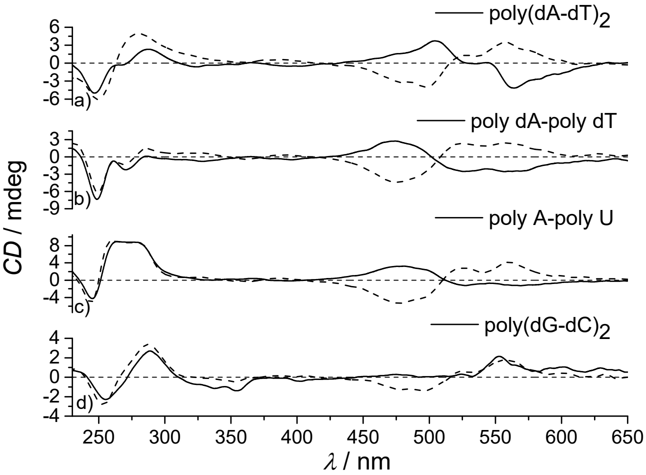

Figure 76: CD spectra of (L)- and (D) PBI **16** upon interaction with a) poly(dA-dT)$_2$, b) poly dA-poly dT, c) poly A-poly U and d) poly(dG-dC)$_2$ at pH 7.0 in sodium cacodylate buffer, $I = 0.05$ M; polynucleotide concentration: 4 x 10^{-5} M; r [c (PBI)] / [c (polynucleotide)] = 0.15; L-configured PBI (solid line), D-configured PBI (dashed line), shown for the purpose of comparison.[87]

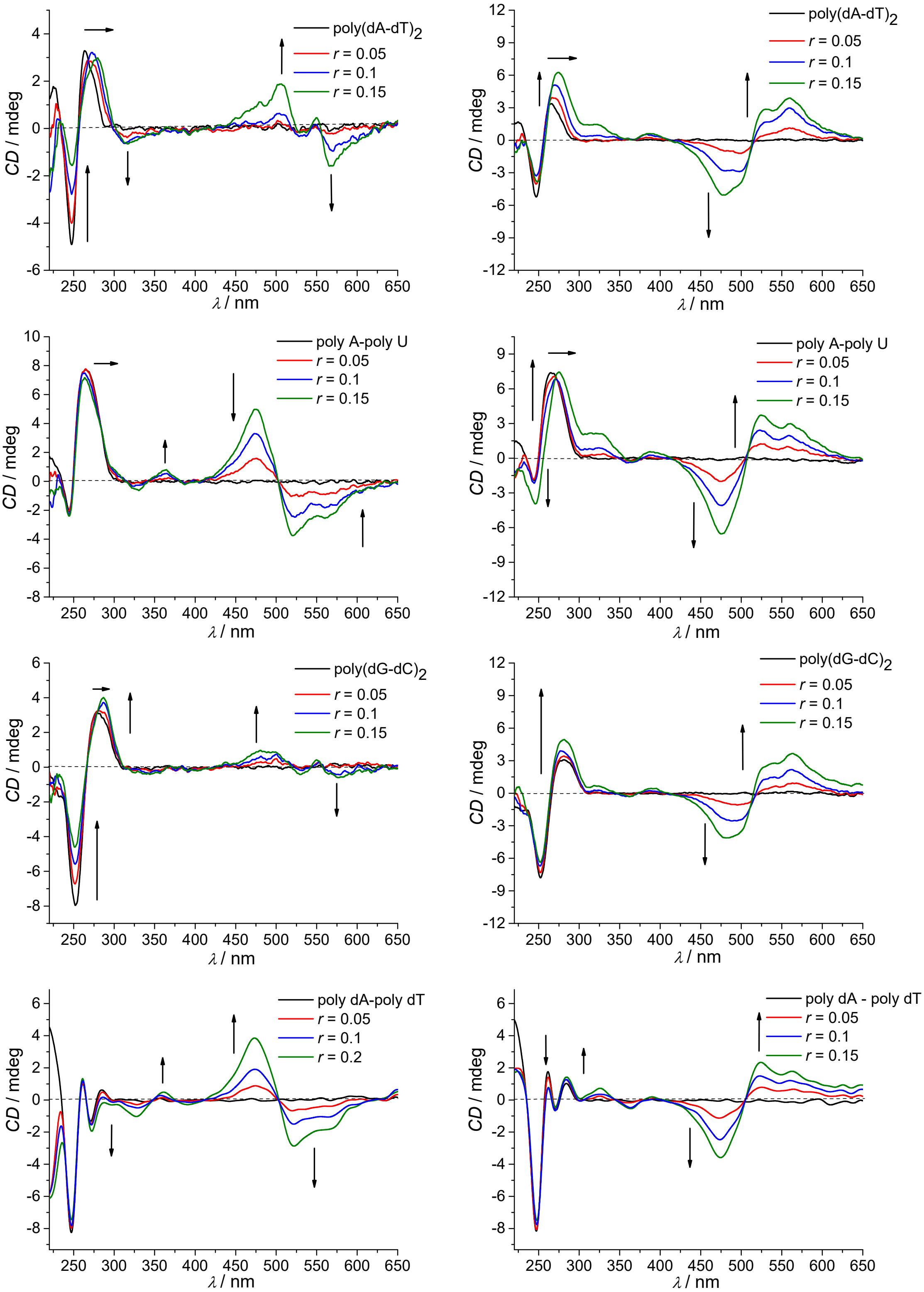

Figure 77: Changes of CD spectra upon addition of increasing amounts of (L) PBI **18** (left) and (D) PBI **18** (right) to various DNA/RNA (c = 4 x 10^{-5} M) at different ratios r; pH 7.0 in sodium cacodylate buffer, I = 0.05 M. Arrows indicate spectral changes upon increasing concentration of (L)- and (D) PBI **18**.

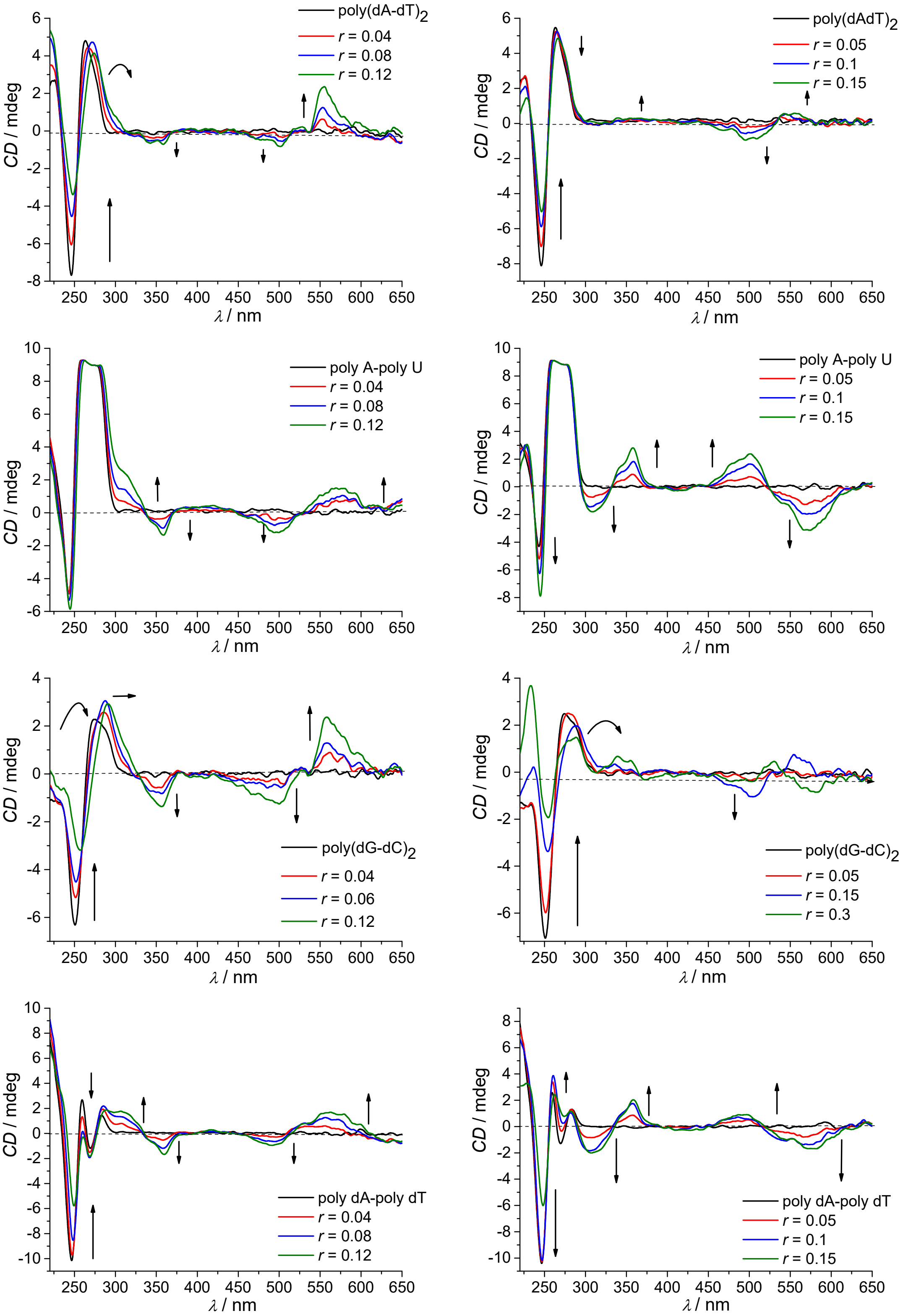

Figure 78: Changes of CD spectra upon addition of increasing amounts of (L) PBI **17** (left) and (D) PBI **17** (right) to various DNA/RNA (c = 4 x 10^{-5} M) at different ratios r; pH 7.0 in sodium cacodylate buffer, I = 0.05 M. Arrows indicate spectral changes upon increasing concentration of (L)- and (D) PBI **17**.

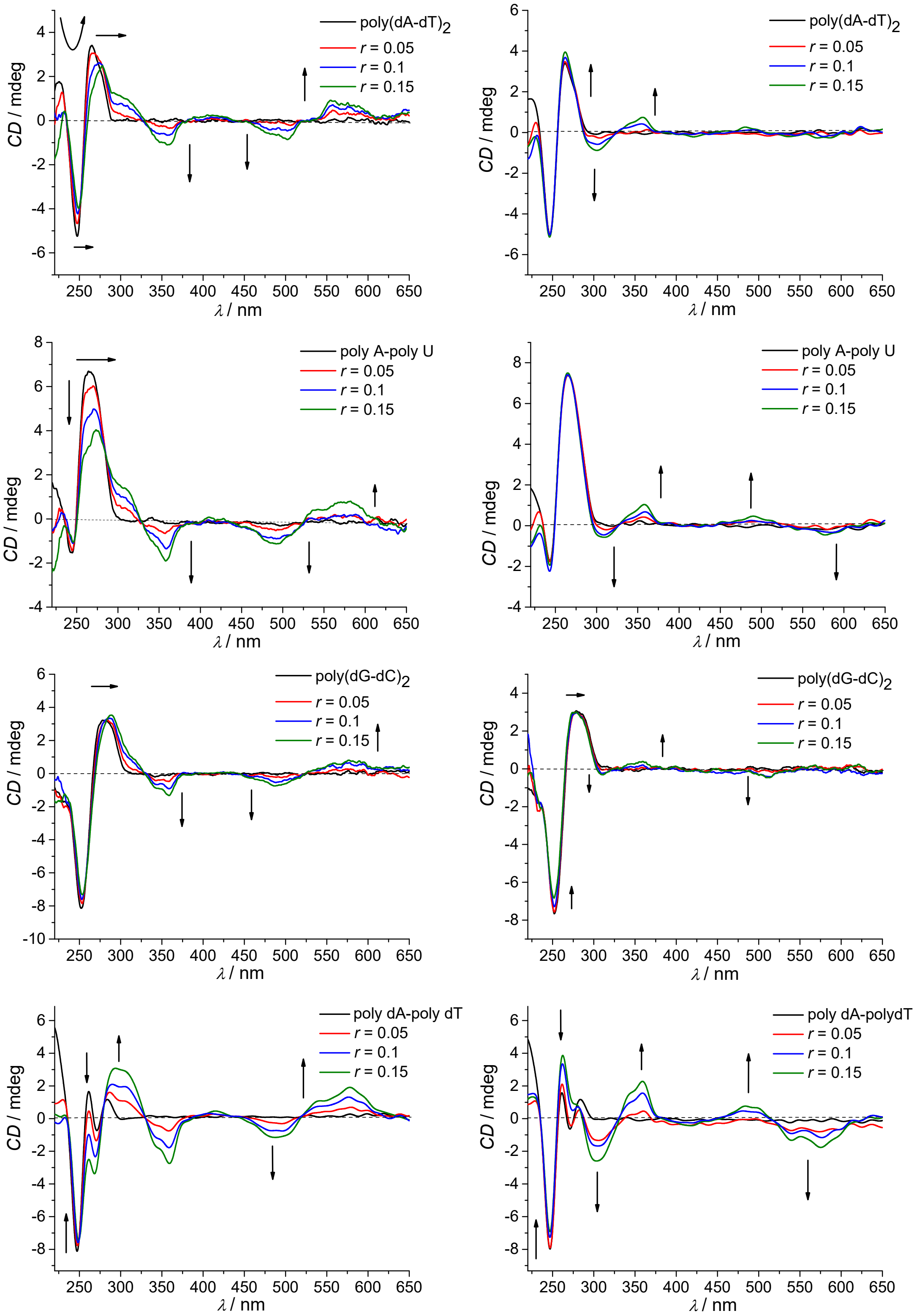

Figure 79: Changes of CD spectra upon addition of increasing amounts of(L) PBI **19** (left) and (D) PBI **19** (right) to various DNA/RNA (c = 4 x 10^{-5} M) at different ratios r; pH 7.0 in sodium cacodylate buffer, I = 0.05 M. Arrows indicate spectral changes upon increasing concentration of (L)- and (D) PBI **19**.

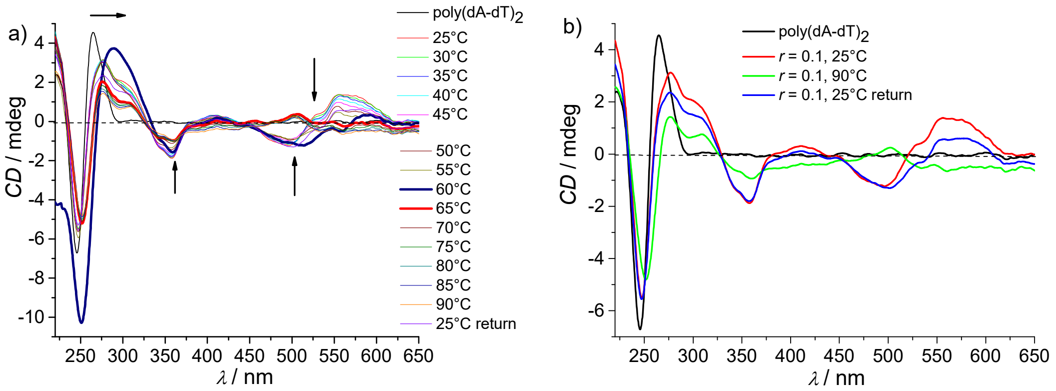

Figure 80: a) Changes of CD spectra of (L) PBI **19** / poly (dA-dT)$_2$ complex (c (poly (dA-dT)$_2$) = 4 x 10^{-5} M; r = [compound] / [polynucleotide] = 0.1) with increase of temperature; pH 7.0 in sodium cacodylate buffer, I = 0.05 M. Arrows indicate spectral changes with increase of temperature from 25 – 90 °C; b) CD spectra at 25 °C (start and return temperature) and 90 °C.

Chapter 6
Summary

The self-assembly of molecules based on π-π-interactions and hydrogen bonding is of significant importance in nature. These processes enable the formation of complex supramolecular structures with diverse functions. For the transfer of the concepts from nature to artificial supramolecular structures, a basic understanding of those processes is needed. For this purpose, π-conjugated aromatic molecules with an easy synthetic access are suitable as their functionalities can be changed effortless. Perylene bisimide (PBIs) dyes are attractive candidates since they fulfill these requirements owing to their tendency to self-assemble in solution due to their large aromatic π-surfaces. Furthermore, the changes of the optical properties (for instance absorption, emission or circular dichroism) of PBI dyes, caused by their self-assembly, are easy to study experimentally. Structural variations of PBI dyes including additional non-covalent interactions, such as hydrogen bonding, enable to direct their self-assembly process. Thus, the formation of interesting supramolecular structures of PBI dyes could be realized, although, often of undefined size. The aim of this thesis was to develop strategies to restrict the aggregate size of PBI dyes. Therefore, defined structural features of PBI molecules were combined and a variation of external influences such as solvent and concentration included. Furthermore, DNA was utilized as a template for the limitation of the aggregate size of PBI dyes.

Chapters 1 and 2 provide general information and describe examples from literature which are necessary to understand the following experimental work. The first chapter is based on the interactions of various molecules with DNA. Therefore, DNA is considered as a supramolecular biomacromolecule containing specific structural and functional features to interact with small molecules. Afterwards, the main interaction modes of small molecules with DNA such as electrostatic interaction, intercalation and groove binding with corresponding examples are discussed. Among all techniques applied to study the interaction of ligands with DNA, UV/Vis absorption, fluorescence and circular dichroism spectroscopy were described in detail. At the end of this chapter, examples of already pre-associated systems showing interactions with DNA are presented.

The second chapter is focused on the determination and mathematic evaluation of the self-assembly processes. The simplest models such as monomer-dimer and isodesmic model are described and supplemented by examples. Furthermore, the simplest modification of the isodesmic model, the K_2-K model, is presented. Additionally, experimental problems, which may arise during the investigations of the self-assembly processes, are addressed. For the description of the entire self-assembly process, a sufficiently large concentration range and an appropriate measurement method that is sensitive in this concentration range is necessary. Furthermore, the full transition from the monomeric to the aggregated species has to be spectroscopically ascertainable. This enables an accurate mathematic evaluation of the self-assembly process and provides meaningful binding constants. The self-assembly pathway can be controlled by the variation of solvent, concentration or temperature. However, this pathway can also be directed by a rational design of the molecular structure of the considered system. For example, a specific interplay of π-π-interactions and hydrogen bonding may promote isodesmic as well as cooperative growth into large structures.

The main focus of this thesis is to develop strategies to control the aggregate size of PBI dyes (Chapter 3). For this purpose, a PBI scaffold was designed which contains hydrogen bonding amide functions at the imide positions derived from the amino acid L-alanine and solubilizing side groups in the periphery (Figure 81). The variations of the residues R/R' range from di-dodecyloxyphenyl, didodecylphenyl, dioligo(ethylene glycol)phenyl to branched and linear alkyl chains.

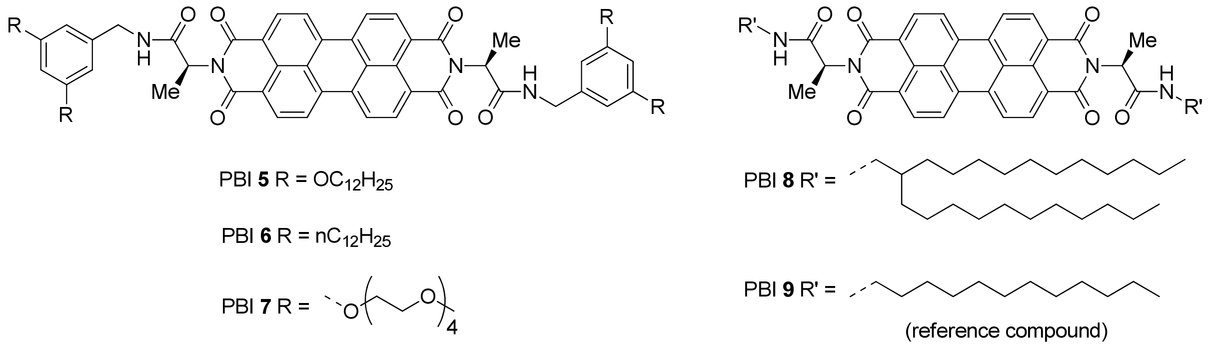

Figure 81: Structures of PBIs **5**-**9**.

The most extensive study of the aggregation behavior was performed for the PBI dye **5**. Concentration-dependent ^{1}H NMR and UV/Vis absorption measurements clearly revealed the formation of dimers in chloroform. Further investigations by means of 2D NMR, VPO and ITC confirmed the exclusive presence of dimer aggregates of PBI **5** in the investigated concentration range. Molecular modelling studies, supported by NMR and FT-IR experiments, provided structural reasons for the absence of further growth into larger aggregates. The specific combination of π-π interactions and hydrogen bonds between the NH groups of the amide groups and the carbonyl oxygen atoms of the PBI core are decisive for the formation of the discrete dimer stack (see Figure 82). The investigations of the aggregation behavior of PBIs **6-9** were less extensive but consistent with the results obtained for PBI **5**. However, the determined binding constants vary over a considerable range of 1.1×10^2 M^{-1} (PBI **8**) to 1.4×10^4 M^{-1} (PBI **5**). These differences could be attributed to structural variations of the dyes. The electron-rich phenyl substituent promoted the aggregation tendency of PBIs **5-7** compared with **8** and **9** that carry only alkyl side chains. Thus, the π-π interactions of bay-unsubstituted PBI cores in combination with hydrogen bonding of the amide functions control the formation of discrete dimers of these PBI dyes.

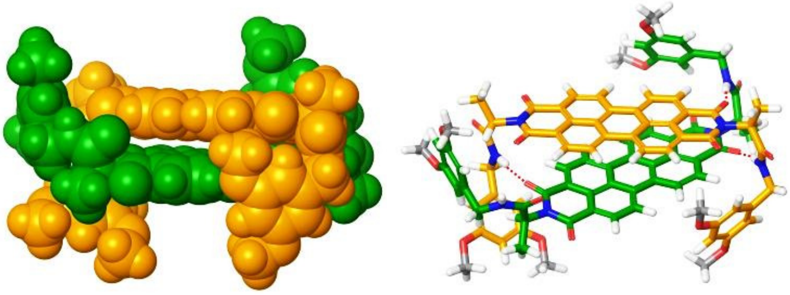

Figure 82: *OPLS2001** (MacroModel) geometry-optimized structure of self-assembled PBI **5** dimer with dodecyloxy chains replaced by methoxy groups.

The variation of conditions, such as solvent, change the aggregation behavior of PBI dyes. In the solvents toluene and/or methylcyclohexane, anti-cooperative growth into larger aggregates of PBI **5** was observed (Chapter 4). The important feature of this self-assembly process is the absence of isosbestic points over the whole concentration range in the UV/Vis absorption measurements. The preference for the dimeric species of PBI **5** remained in both solvents as well as in mixtures of them, but upon increasing the concentration these dimers self-assemble into larger aggregates. An important feature of the self-assembly process is the preferred formation of even-numbered aggregates compared to the odd-numbered ones (see Figure 83). Although, the conventional K_2-K model provides plausible binding constants, it is not capable to describe the aggregation behavior adequately, since it considers a continuous size distribution. The gradual aggregation process over dimers, tetramers, hexamers, etc. was therefore analyzed with a newly developed K_2-K model for anti-cooperative supramolecular polymerization. By the global analysis of the UV/Vis absorption spectra a very good agreement between the experimental and simulated spectra, which were based on the new K_2-K model, was obtained. Furthermore, the calculated UV/Vis absorption spectra of a dimer and an aggregate highlighted the most important structural differences. The absorption spectrum of the dimer still has a pronounced vibronic structure which gets lost in the spectrum of the aggregate.

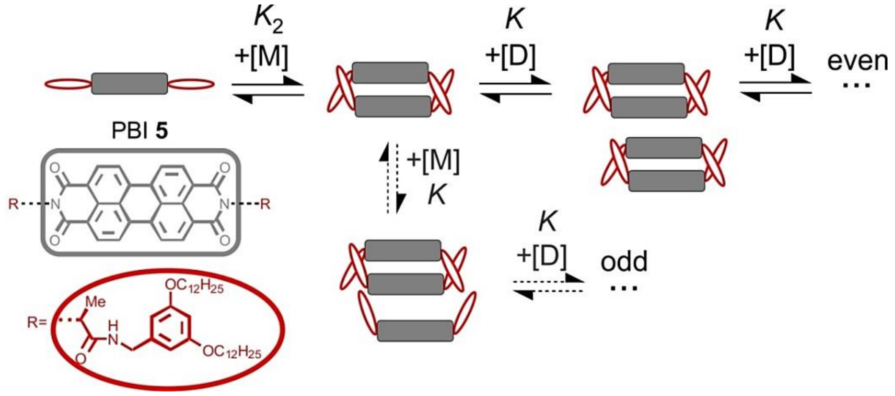

Figure 83: Schematic illustration of the new model for supramolecular polymerization which describes the aggregation pathway of PBI **5**.

In another part of this work, a series of water soluble PBI dyes were described which contain similar PBI scaffolds as PBIs **5-8** (Chapter 5). These PBI dyes self-assemble into similar dimer aggregates in water due to their positively charged side chains causing electrostatic repulsion between the molecules (see Figure 84). Here, however, the self-assembly behavior has not been studied thoroughly in water due to the similarities of already reported PBI dyes.

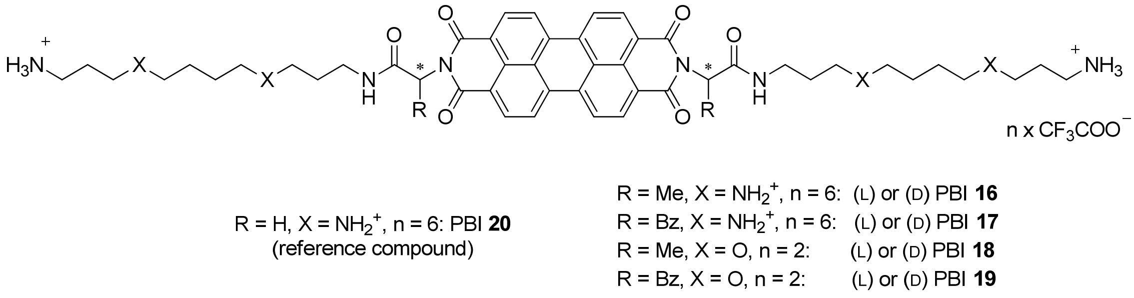

Figure 84: Structures of water soluble PBIs **20**, (L)- and (D) PBI **16**, (L)- and (D) PBI **17**, (L)- and (D) PBI **18**, und (L)- and (D) PBI **19**.

Instead, the focus here is on the characterization of the interactions of these dyes with DNA/RNA. The comprehensive studies using thermal denaturation experiments showed the high stability of these PBI/polynucleotide complexes. The spermine-functionalized PBI dyes having six positive charges showed strong interactions with DNA/RNA which was expressed in a significant increase of the melting temperatures of DNA/RNA (ΔT_m values between 7 and > 35 ° C). The dioxa analogues containing only two positive charges had lower enhancement of the melting temperature of DNA/RNA (ΔT_m values between 3 and 30 ° C). A similar trend has been observed in the fluorimetric titrations. The spermine-functionalized PBI dyes showed high binding constants ($\log K_s = 9.2 - 9.8$), independently of the used polynucleotides. In contrast, the dioxa analogues displayed smaller binding constants ($\log K_s = 6.5 - 7.9$) without any correlation between binding affinity and binding strength of the PBI dyes and the applied polynucleotides. The CD-spectroscopic measurements revealed significant differences in the binding properties of the dyes with DNA/RNA. They were dependent on the steric hindrance of the amino acid residues at the imide position and their configuration on one side and the grooves properties of ds-DNA/RNA on the other side. The spectroscopic results confirmed the formation of excitonically coupled PBI dimers in the minor groove of ds-DNA and the major groove of ds-RNA. Depending on the sequence, the grooves of the polynucleotides provide different amount of space for embedding molecules. The guanine amino groups protrude into the minor groove of the polynucleotide poly(dG-dC)$_2$ increasing the steric hindrance, which is not the case for poly(dA-dT)$_2$. Molecular modeling studies showed that the PBI dimers penetrate deeper into the groove of poly(dA-dT)$_2$ due to the absence of the steric hindrance, in comparison to the groove of poly(dG-dC)$_2$ (see Figure 85).

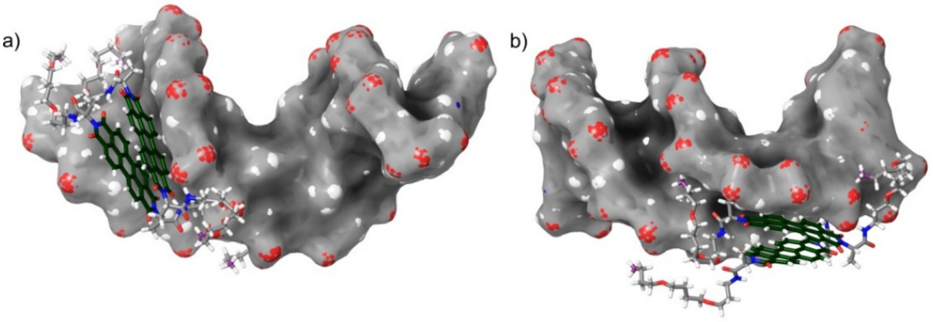

Figure 85: Molecular structures of a) (L) PBI **18** dimer/poly(dA-dT)$_2$ and b) (L) PBI **18** dimer/poly(dG-dC)$_2$ complexes showing the orientation and the arrangement of the PBI dimers in the minor groove of ds-polynucleotides.

Chapter 7
Zusammenfassung

Die Selbstassemblierung von Molekülen, die auf π-π-Wechselwirkungen und Wasenstoffbrückenbindungen basiert, ist von entscheidender Bedeutung in der Natur. Selbstassemblierungsprozesse ermöglichen den Aufbau von komplexen supramolekularen Strukturen mit vielfältigen Funktionen. Um Konzepte aus der Natur für künstliche supramolekulare Systeme nutzen zu können, müssen die wesentlichen Abläufe der Selbstassemblierungsprozesse verstanden werden. Dazu eignen sich π-konjugierte aromatische Moleküle, die einen relativ einfachen synthetischen Zugang bieten und vielfältig funktionalisiert werden können. Perylenbisimid-Farbstoffe (PBI) stellen für diesen Zweck eine attraktive Substanzklasse dar, da sie aufgrund von großen aromatischen π-Flächen zur Selbstassemblierung tendieren. Zusätzlich können durch die Selbstassemblierung einhergehenden Änderungen der optischen Eigenschaften (beispielsweise Absorption, Emission oder Circulardichroismus) von PBI-Farbstoffen einfach experimentell studiert werden. Die vielen strukturellen Variationsmöglichkeiten von PBI-Farbstoffen erlauben das Einbeziehen von weiteren nichtkovalenten Wechselwirkungen zwischen den Molekülen, beispielsweise Wasserstoffbrückenbindungen, sodass der Selbstassemblierungsprozess dirigiert werden kann. Mit diesem Ansatz gelang es bisher interessante supramolekulare Strukturen von PBI-Farbstoffen aufzubauen, allerdings waren diese oft von undefinierter Größe. Daher war das Ziel dieser Arbeit die Entwicklung von Konzepten um die Aggregatgröße von PBI-Farbstoffen zu begrenzen. Hierzu wurden definierte Strukturmerkmale von PBI Molekülen kombiniert, der äußere Einfluss wie Lösungsmittel und Konzentration variiert und DNA als Templat für die größenlimitierte Aggregatstruktur der PBI-Farbstoffe eingesetzt.

Die Kapitel 1 und 2 geben allgemeine Informationen und diskutieren Beispiele aus der Literatur, die nötig sind, um die nachfolgend diskutierten experimentellen Arbeiten zu verstehen. Das erste Kapitel diskutiert die Wechselwirkungen verschiedener Molekülen mit DNA. Hierbei wird DNA als ein supramolekulares Biomakromolekül betrachtet und seine spezifischen strukturellen und funktionalen Eigenschaften beschrieben, die für die Interaktionen mit kleinen Molekülen ausschlaggebend sind. Die wichtigsten Interaktionsformen wie elektrostatische Wechselwirkungen mit dem Phosphatrückgrat, Interkalation durch π-π-Wechselwirkungen mit den Basenpaaren und

Furchenbindung durch Wasserstoffbrückenbindungen und van der Waals-Wechselwirkungen werden anhand ausgewählter Beispiele diskutiert. Von der Vielzahl möglicher Techniken, die angewendet werden, um Wechselwirkungen zwischen Liganden und DNA zu untersuchen, werden UV/Vis-, Fluoreszenz- und Circulardichroismus-Spektroskopie in Detail erläutert. Am Ende des Kapitels werden Beispiele von Wechselwirkungen von bereits prä-assoziierten supramolekularen Systemen mit DNA vorgestellt.

Das zweite Kapitel beschäftigt sich mit der Bestimmung und mathematischen Beschreibung von Selbstassemblierungsprozessen. Die einfachsten Modelle, wie das Monomer-Dimer und das isodesmische Modell, werden beschrieben und mit Beispielen ergänzt. Des Weiteren wird die einfachste Modifikation des isodesmischen Modells, das K_2-K Modell vorgestellt. Anschließend wird auf experimentelle Probleme eingegangen, die bei der Untersuchung von Selbstassemblierungsprozessen auftreten können. Um den Assemblierungsprozess vollständig beschreiben zu können, wird ein ausreichend großer Konzentrationsbereich und eine entsprechende Messtechnik, die für diesen Konzentrationsbereich empfindlich genug ist, benötigt. Des Weiteren sollte der vollständige Übergang vom Monomer zum assemblierten System spektroskopisch erfassbar sein. Dies ermöglicht eine akkurate mathematische Auswertung des Selbstassemblierungsprozesses und liefert sinnvolle Bindungskonstanten. Der Selbstassemblierungspfad kann oft durch Variation des Lösungsmittels, Konzentration und Temperatur kontrolliert werden. Darüber hinaus besteht die Möglichkeit, den Selbstassemblierungspfad mit Hilfe eines spezifischen Designs der molekularen Struktur von dem untersuchten System zu dirigieren. Es konnte gezeigt werden, dass ein besonderes Zusammenspiel von π-π-Wechselwirkungen und Wasserstoffbrückenbindungen sowohl zum isodesmischen als auch kooperativen Wachstum von großen Strukturen führen kann.

Der Hauptfokus dieser Arbeit liegt in der Entwicklung von Strategien für die Kontrolle der Aggregatgröße von PBI Farbstoffen. (Kapitel 3). Um dieses Ziel zu erreichen, wurde ein PBI Gerüst entworfen, das Amidfunktionen in den Imidpositionen für die Ausbildung von Wasserstoffbrückenbindungen enthält, die von der Aminosäure L-Alanin abgeleitet wurden. Zusätzlich wurden in der Peripherie des Farbstoffgerüsts jeweils löslichkeitsfördernde Seitengruppen R/R‘ wie Didodecyloxyphenyl, Didodecylphenyl, Dioligo(ethyleneglykol)phenyl sowie verzweigte oder lineare Alkylketten eingeführt (siehe Abbildung 81). Der PBI-Farbstoff **5** wurde ausführlich im Hinblick auf sein Aggregationsverhalten untersucht. Konzentrationsabhängige ^{1}H NMR- und UV/Vis Absorptionsmessungen haben klar gezeigt, dass im Lösungsmittel Chloroform dimere Strukturen ausgebildet werden.

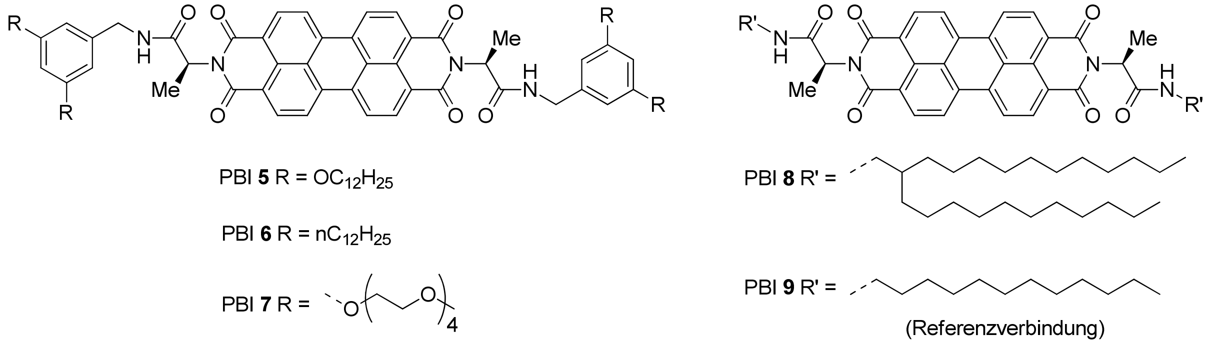

Abbildung 81: Strukturen der PBI-Farbstoffe **5**-**9**.

Begleitende Untersuchungen (2D NMR, VPO und ITC) bestätigten die ausschließliche Präsenz von Dimeren von **5** im experimentell zugänglichen Konzentrationsbereich. Molekulare Modellierungs-Studien, die durch NMR und FT-IR Untersuchungen unterstützt werden, illustrieren sehr gut die Ursachen für das Ausbleiben einer weiteren Aggregation zu größeren Strukturen. Die besondere Kombination aus den π-π-Wechselwirkungen und den Wasserstoffbrückenbindungen zwischen den NH-Gruppen der Amidfunktionen und den Carbonylsauerstoffen des PBI-Kerns sind demzufolge entscheidend für die Bildung des diskreten Dimer-Stapels (siehe Abbildung 82).

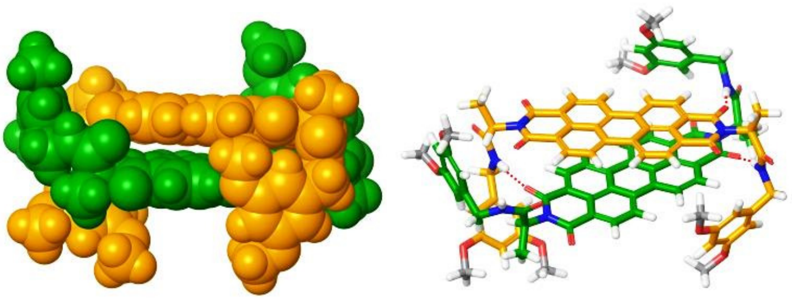

Abbildung 82: OPLS2001* (MacroModel) geometrieoptimierte Struktur des aggregierten PBIs **5**. Die Dodecyloxy-Seitenketten wurden aus Übersichtlichkeitsgründen durch Methoxygruppen ersetzt.

Die Untersuchungen zum Aggregationsverhalten der PBI-Farbstoffe **6**-**9** waren weniger ausführlich, stehen aber im Einklang mit den für PBI **5** gefundenen Ergebnissen. Die ermittelten Bindungskonstanten variieren jedoch über einen beachtlichen Bereich von 1.1 x 10^2 M^{-1} (PBI **8**) bis 1.4 x 10^4 M^{-1} (PBI **5**). Diese Unterschiede konnten auf strukturelle Variationen der Farbstoffe zurückgeführt werden. Der elektronenreiche Phenylsubstituent förderte die Assemblierungstendenz von PBIs **5**-**7** im Vergleich zu **8** und **9**, die nur Alkylseitenkennten tragen. Die π-π-

Wechselwirkungen der in den Buchpositionen unsubstituierten PBI-Kerne in Kombination mit wasserstoffbrückenbildenden Amidfunktionen steuern somit die Ausbildung diskreter Dimere dieser PBI-Farbstoffe.

Durch die Variation der Bedingungen, beispielsweise des Lösungsmittels, ändert sich das Aggregationsverhalten der PBI-Farbstoffe. In den Lösungsmitteln Toluol und/oder Methylcyclohexan wurde für das PBI **5** anti-kooperatives Wachstum zu größeren Aggregaten beobachtet (Kapitel 4). Das entscheidende Merkmal dieses Selbstassemblierungsprozesses ist das Fehlen von isosbestischen Punkten über den kompletten Konzentrationsbereich in den UV/Vis Absorptionsmessungen. Die Bevorzugung der dimeren Struktur von PBI **5** blieb in beiden Lösungsmitteln bzw. deren Mischungen erhalten, allerdings assemblierten diese Dimere durch den Anstieg der Konzentration in größere Aggregate. Ein wichtiger Schritt im Selbstassemblierungsprozesses ist die bevorzugte Bildung von geradzahligen Aggregaten gegenüber den ungeradzahligen Aggregaten (siehe Abbildung 83).

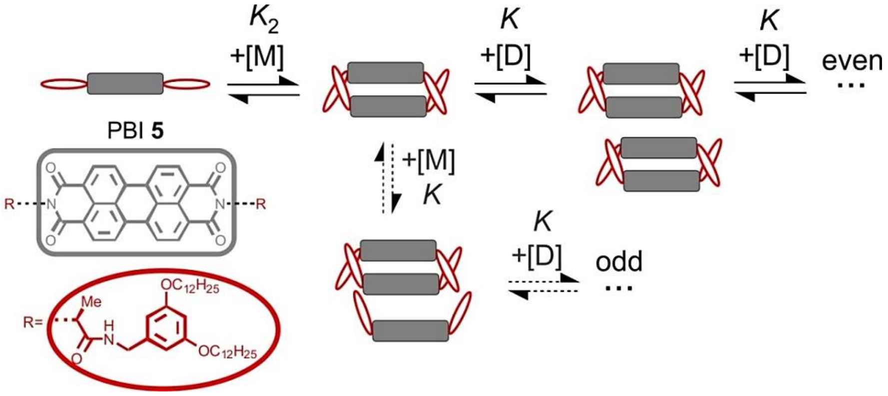

Abbildung 83: Schematische Darstellung des neuen Modells für die supramolekulare Polymerisation, die den Aggregationspfad von PBI **5** beschreibt.

Das konventionelle K_2-K Modell liefert zwar plausible Bindungskonstanten, kann dieses Aggregationsverhalten aber nur ungenügend beschreiben, da hier von kontinuierlicher Größenverteilung ausgegangen wird. Der schrittweise Aggregationsprozess über Dimere, Tetramere, Hexamere usw. wurde daher im Folgenden mit einem neu entwickelten K_2-K-Modell für anti-kooperatives supramolekulares Wachstum analysiert. Durch die globale Analyse von UV/Vis Absorptionsspektren konnte eine sehr gute Übereinstimmung zwischen den experimentellen und den auf das neue K_2-K Modell basierenden, simulierten Spektren erhalten werden. Des Weiteren zeigten berechnete UV/Vis Absorptionsspektren eines Dimer- und Aggregatspektrums die wichtigsten strukturellen Unterschiede. Das Absorptionsspektrum des Dimers weist immer noch eine ausgeprägte vibronische Struktur auf, welche im Spektrum des Aggregats verloren geht.

In einem weiteren Teil dieser Arbeit wird eine Serie von wasserlöslichen PBI-Farbstoffen beschrieben, die ein ähnliches durch Aminosäuren funktionalisiertes PBI-Gerüst wie PBIs **5-8** aufweisen (Kapitel 5). Aufgrund der positiv geladenen Seitenketten, die für die elektrostatische Abstoßung zwischen den Molekülen sorgen, aggregieren diese Farbstoffe in Wasser zu ähnlichen Dimerstrukturen (siehe Abbildung 84). Hier wurde allerdings das Selbstassemblierungsverhalten in Wasser aufgrund der strukturellen Ähnlichkeit zu bereits publizierten PBI-Farbstoffen nicht eingehend untersucht.

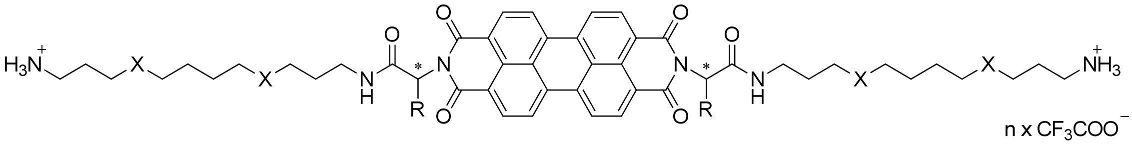

R = H, X = NH_2^+, n = 6: PBI **20**
(Referenzverbindung)

R = Me, X = NH_2^+, n = 6: (L) oder (D) PBI **16**
R = Bz, X = NH_2^+, n = 6: (L) oder (D) PBI **17**
R = Me, X = O, n = 2: (L) oder (D) PBI **18**
R = Bz, X = O, n = 2: (L) oder (D) PBI **19**

Abbildung 84: Strukturen von wasserlöslichen PBI-Farbstoffen PBI **20**, (L)- und (D) PBI **16**, (L)- und (D) PBI **17**, (L)- und (D) PBI **18**, und (L)- und (D) PBI **19**.

Stattdessen lag der Fokus hier auf der Charakterisierung der Wechselwirkungen dieser Farbstoffe mit DNA/RNA. Die umfassenden Studien mit Hilfe von thermischen Denaturierungsstudien zeigten eine hohe Stabilität der PBI/Polynukleotid-Komplexe. Die Spermin-funktionalisierten PBI-Farbstoffe, welche sechs positive Ladungen aufweisen, zeigten starke Wechselwirkungen mit DNA/RNA, was sich durch deutliche Schmelzpunkterhöhung der DNA/RNA (ΔT_m-Werte zwischen 7 und > 35 °C) äußerte. Die analogen Dioxa-Verbindungen mit nur zwei positiven Ladungen wiesen geringere Schmelztemperaturerhöhungen der jeweiligen DNA/RNA (ΔT_m-Werte zwischen 3 und 30 °C) auf. Dieser Trend wurde auch in den fluorimetrischen Titrationsstudien beobachtet. Die Spermin-funktionalisierten PBI-Farbstoffe zeigten hohe Bindungskostanten ($\log K_s = 9.2 - 9.8$), unabhängig von den verwendeten Polynukleotiden. Im Gegensatz dazu wiesen die Dioxa-Analoge kleinere Bindungskonstanten ($\log K_s = 6.5 - 7.9$) auf, wobei kein Zusammenhang zwischen Bindungsaffinität und Bindungsstärke zwischen den PBI-Molekülen und den verwendeten Polynukleotiden hergestellt werden konnte. Die CD-spektroskopischen Messungen verdeutlichten die signifikanten Unterschiede in den Bindungseigenschaften der Farbstoffe mit DNA/RNA. Entscheidend waren die sterische Hinderung der Aminosäurereste in den Imidposition und deren Konfiguration auf der einen Seite und die Furcheneigenschaften von ds-DNA/RNA auf der anderen Seite. Die spektroskopischen Ergebnisse belegten die Bildung von exzitonisch gekoppelten PBI-Dimeren in der kleinen Furche von ds-DNA und der großen Furche von ds-RNA. Die Furchen der Polynukleotide bieten unterschiedlich viel Raum für das Einbetten von Molekülen, was von der jeweiligen Sequenz abhängt. Die Guanin-Aminogruppen ragen in die kleine Furche des Polynukleotids poly(dG-dC)$_2$, wodurch die sterische Hinderung im Vergleich mit dem Polynukleotid poly(dA-dT)$_2$ zunimmt. Molekulare Modellierungsstudien belegten, dass die PBI-Dimere tiefer in die Furche von poly(dA-dT)$_2$, als in die Furche von poly(dG-dC)$_2$ eingeschlossen werden, was auf die eben genannte sterische Hinderung zurückgeführt werden kann (siehe Abbildung 85).

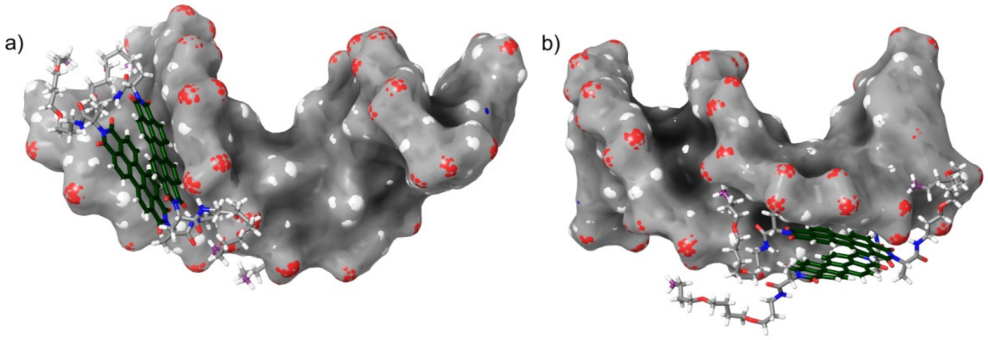

Abbildung 85: Modellierte Strukturen von a) (L) PBI **18** Dimer/poly(dA-dT)$_2$ und b) (L) PBI **18** Dimer/poly(dG-dC)$_2$ Komplexen, die die Orientierung und Anordnung der PBI-Dimere in den kleinen Furchen der ds-Polynukleotide veranschaulichen.

References

[1] G. M. Whitesides, B. Grzybowski, *Science* **2002**, *295*, 2418-2421.

[2] D. Philp, J. F. Stoddart, *Angew. Chem. Int. Ed.* **1996**, *35*, 1154-1196.

[3] E. Busseron, Y. Ruff, E. Moulin, N. Giuseppone, *Nanoscale* **2013**, *5*, 7098-7140.

[4] a) J.-M. Lehn, *Proc. Natl. Acad. Sci. U. S. A.* **2002**, *99*, 4763-4768; b) J. W. Steed, J. L. Atwood, in *Supramol. Chem.*, John Wiley & Sons, Ltd, **2009**, pp. 1-48.

[5] J. S. Lindsey, *New J. Chem.* **1991**, *15*, 153-180.

[6] Z. Chen, A. Lohr, C. R. Saha-Möller, F. Würthner, *Chem. Soc. Rev.* **2009**, *38*, 564-584.

[7] A. S. Mahadevi, G. N. Sastry, *Chem. Rev.* **2016**.

[8] C. Rest, R. Kandanelli, G. Fernández, *Chem. Soc. Rev.* **2015**, *44*, 2543-2572.

[9] J. K. Klosterman, Y. Yamauchi, M. Fujita, *Chem. Soc. Rev.* **2009**, *38*, 1714-1725.

[10] J. A. A. W. Elemans, R. van Hameren, R. J. M. Nolte, A. E. Rowan, *Adv. Mater.* **2006**, *18*, 1251-1266.

[11] a) F. Würthner, *Chem. Commun.* **2004**, 1564-1579; b) F. Würthner, M. Stolte, *Chem. Commun.* **2011**, *47*, 5109-5115.

[12] F. Würthner, C. R. Saha-Möller, B. Fimmel, S. Ogi, P. Leowanawat, D. Schmidt, *Chem. Rev.* **2016**, *116*, 962-1052.

[13] Z. Chen, B. Fimmel, F. Würthner, *Org. Biomol. Chem.* **2012**, *10*, 5845-5855.

[14] C. Shao, M. Grüne, M. Stolte, F. Würthner, *Chem. Eur. J.* **2012**, *18*, 13665-13677.

[15] J. M. Berg, L. Stryer, J. L. Tymoczko, *Biochemie*, 7. ed., Springer Spektrum, Berlin, Heidelberg **2013**.

[16] H. Ihmels, D. Otto, in *Supermolecular Dye Chemistry, Vol. 258* (Ed.: F. Würthner), Springer Berlin Heidelberg, **2005**, pp. 161-204.

[17] a) R. Palchaudhuri, P. J. Hergenrother, *Curr. Opin. Biotechnol.* **2007**, *18*, 497-503; b) X. Cai, P. J. Gray Jr, D. D. Von Hoff, *Cancer Treat. Rev.* **2009**, *35*, 437-450; c) C. J. Suckling, *J. Phys. Org. Chem.* **2008**, *21*, 575-583.

[18] a) X. Peng, T. Wu, J. Fan, J. Wang, S. Zhang, F. Song, S. Sun, *Angew. Chem. Int. Ed.* **2011**, *50*, 4180-4183; b) D. Aigner, R. I. Dmitriev, S. M. Borisov, D. B. Papkovsky, I. Klimant, *J. Mater. Chem. B.* **2014**, *2*, 6792-6801; c) A. Okamoto, *Chem. Rec.* **2010**, *10*, 188-196; d) B.

Roy, T. Noguchi, D. Yoshihara, Y. Tsuchiya, A. Dawn, S. Shinkai, *Org. Biomol. Chem.* **2014**, *12*, 561-565.

[19] a) M. J. Hannon, *Chem. Soc. Rev.* **2007**, *36*, 280-295; b) G. M. Blackburn, M. J. Gait, D. Loakes, D. M. Williams, in *Nucleic Acids in Chemistry and Biology, Vol. 3*, RSC Publishing, Cambridge, **2006**, pp. 341-382; c) B. A. D. Neto, A. A. M. Lapis, *Molecules* **2009**, *14*, 1725-1746.

[20] J. D. Watson, F. H. C. Crick, *Nature* **1953**, *171*, 737-738.

[21] H. R. Drew, R. M. Wing, T. Takano, C. Broka, S. Tanaka, K. Itakura, R. E. Dickerson, *Proc. Natl. Acad. Sci. U. S. A.* **1981**, *78*, 2179-2183.

[22] R. Corradini, S. Sforza, T. Tedeschi, R. Marchelli, *Chirality* **2007**, *19*, 269-294.

[23] a) G. S. Manning, *Q. Rev. Biophys.* **1978**, *11*, 179-246; b) M. T. Record, C. F. Anderson, T. M. Lohman, *Q. Rev. Biophys.* **1978**, *11*, 103-178; c) J. Lipfert, S. Doniach, R. Das, D. Herschlag, *Annu. Rev. Biochem.* **2014**, *83*, 813-841.

[24] A. A. Zinchenko, N. Chen, S. Murata, *J. Synth. Org. Chem. Jpn.* **2006**, *64*, 1122-1131.

[25] Wallace, *Eur. J. Clin. Invest.* **2000**, *30*, 1-3.

[26] A. Rescifina, C. Zagni, M. G. Varrica, V. Pistarà, A. Corsaro, *Eur. J. Med. Chem.* **2014**, *74*, 95-115.

[27] a) L. S. Lerman, *J. Mol. Biol.* **1961**, *3*, 18-IN14; b) L. S. Lerman, *Proc. Natl. Acad. Sci. U. S. A.* **1963**, *49*, 94-102.

[28] S. E. Patterson, J. M. Coxon, L. Strekowski, *Bioorg. Med. Chem.* **1997**, *5*, 277-281.

[29] F. A. Tanious, S. F. Yen, W. D. Wilson, *Biochemistry* **1991**, *30*, 1813-1819.

[30] M. Egli, L. D. Williams, C. A. Frederick, A. Rich, *Biochemistry* **1991**, *30*, 1364-1372.

[31] S. F. Yen, E. J. Gabbay, W. D. Wilson, *Biochemistry* **1982**, *21*, 2070-2076.

[32] H.-K. Liu, P. J. Sadler, *Acc. Chem. Res.* **2011**, *44*, 349-359.

[33] J. B. Chaires, *Arch. Biochem. Biophys.* **2006**, *453*, 26-31.

[34] J. Ren, T. C. Jenkins, J. B. Chaires, *Biochemistry* **2000**, *39*, 8439-8447.

[35] C. K. Smith, G. J. Davies, E. J. Dodson, M. H. Moore, *Biochemistry* **1995**, *34*, 415-425.

[36] A. K. Todd, A. Adams, J. H. Thorpe, W. A. Denny, L. P. G. Wakelin, C. J. Cardin, *J. Med. Chem.* **1999**, *42*, 536-540.

[37] A. Canals, M. Purciolas, J. Aymani, M. Coll, *Acta Crystallogr., Sect. D: Biol. Crystallogr.* **2005**, *61*, 1009-1012.

[38] J. D. McGhee, P. H. von Hippel, *J. Mol. Biol.* **1974**, *86*, 469-489.

[39] A. Sarai, H. Kono, *Annu. Rev. Biophys. Biomol. Struct.* **2005**, *34*, 379-398.

[40] a) N. G. A. Abrescia, A. Thompson, T. Huynh-Dinh, J. A. Subirana, *Proc. Natl. Acad. Sci. U. S. A.* **2002**, *99*, 2806-2811; b) K. Hoogsteen, *Acta Cryst.* **1963**, *16*, 907-916.

[41] N. T. Thuong, C. Hélène, *Angew. Chem. Int. Ed.* **1993**, *32*, 666-690.

[42] a) G. S. Khan, A. Shah, Zia-ur-Rehman, D. Barker, *J. Photochem. Photobiol., B* **2012**, *115*, 105-118; b) M. P. Barrett, C. G. Gemmell, C. J. Suckling, *Pharmacol. Ther.* **2013**, *139*, 12-23.

[43] S. Neidle, *Nat. Prod. Rep.* **2001**, *18*, 291-309.

[44] M. Munde, M. A. Ismail, R. Arafa, P. Peixoto, C. J. Collar, Y. Liu, L. Hu, M.-H. David-Cordonnier, A. Lansiaux, C. Bailly, D. W. Boykin, W. D. Wilson, *J. Am. Chem. Soc.* **2007**, *129*, 13732-13743.

[45] Y. Xie, V. K. Tam, Y. Tor, in *The Chemical Biology of Nucleic Acids*, John Wiley & Sons, Ltd, **2010**, pp. 115-140.

[46] a) P. G. Baraldi, B. Cacciari, A. Guiotto, R. Romagnoli, A. N. Zaid, G. Spalluto, *Il Farmaco* **1999**, *54*, 15-25; b) P. G. Baraldi, A. Bovero, F. Fruttarolo, D. Preti, M. A. Tabrizi, M. G. Pavani, R. Romagnoli, *Med. Res. Rev.* **2004**, *24*, 475-528.

[47] T. A. Larsen, D. S. Goodsell, D. Cascio, K. Grzeskowiak, R. E. Dickerson, *J. Biomol. Struct. Dyn.* **1989**, *7*, 477-491.

[48] P. E. Pjura, K. Grzeskowiak, R. E. Dickerson, *J. Mol. Biol.* **1987**, *197*, 257-271.

[49] a) D. Suh, J. B. Chaires, *Bioorg. Med. Chem.* **1995**, *3*, 723-728; b) D. Suh, Y.-K. Oh, J. B. Chaires, *Process Biochem. (Amsterdam, Neth.)* **2001**, *37*, 521-525.

[50] Y. Chai, M. Munde, A. Kumar, L. Mickelson, S. Lin, N. H. Campbell, M. Banerjee, S. Akay, Z. Liu, A. A. Farahat, R. Nhili, S. Depauw, M.-H. David-Cordonnier, S. Neidle, W. D. Wilson, D. W. Boykin, *ChemBioChem* **2014**, *15*, 68-79.

[51] a) W. C. Tse, D. L. Boger, *Acc. Chem. Res.* **2004**, *37*, 61-69; b) T. Jenkins, in *Drug-DNA Interaction Protocols, Vol. 90* (Ed.: K. Fox), Springer New York, **1997**, pp. 195-218.

[52] a) Q. Feng, N.-Q. Li, Y.-Y. Jiang, *Anal. Chim. Acta* **1997**, *344*, 97-104; b) M. Sirajuddin, S. Ali, A. Haider, N. A. Shah, A. Shah, M. R. Khan, *Polyhedron* **2012**, *40*, 19-31; c) M. M. Aleksić, V. Kapetanović, *An Overview of the Optical and Electrochemical Methods for Detection of DNA – Drug Interactions, Vol. 61*, **2014**; d) S. S. Kalanur, U. Katrahalli, J. Seetharamappa, *J. Electroanal. Chem.* **2009**, *636*, 93-100; e) S. Rauf, J. J. Gooding, K. Akhtar, M. A. Ghauri, M. Rahman, M. A. Anwar, A. M. Khalid, *J. Pharm. Biomed. Anal.* **2005**, *37*, 205-217.

[53] a) J. B. Chaires, *Ann. Rev. Biophys.* **2008**, *37*, 135-151; b) R. J. Falconer, A. Penkova, I. Jelesarov, B. M. Collins, *J. Mol. Recognit.* **2010**, *23*, 395-413.

[54] J. Ren, J. B. Chaires, *Biochemistry* **1999**, *38*, 16067-16075.

[55] J. A. Bordelon, K. J. Feierabend, S. A. Siddiqui, L. L. Wright, J. T. Petty, *J. Phys. Chem. B* **2002**, *106*, 4838-4843.

[56] M. Sirajuddin, S. Ali, A. Badshah, *J. Photochem. Photobiol., B* **2013**, *124*, 1-19.

[57] G. M. Blackburn, M. J. Gait, D. Loakes, D. M. Williams, in *Nucleic Acids in Chemistry and Biology, Vol. 3*, RSC Publishing, Cambridge, **2006**, pp. 427-458.

[58] a) I. Tinoco, *J. Am. Chem. Soc.* **1960**, *82*, 4785-4790; b) N. L. Vekshin, *J. Biol. Phys.* **1999**, *25*, 339-354.

[59] A. I. O. Víctor González-Ruiz, M. Antonia Martín, Pascual Ribelles, M. Teresa Ramos and J. Carlos Menéndez, i. M. A. , S. O.-J. E. Komorowska, Biomedical Engineering, Trends,, Research and Technologies. In Tech, pp. 65–90., *An Overview of Analytical Techniques Employed to Evidence Drug-DNA Interactions. Applications to the Design of Genosensors, Biomedical Engineering, Trends, Research and Technologies*, **2011**.

[60] M. Sirajuddin, S. Ali, N. A. Shah, M. R. Khan, M. N. Tahir, *Spectrochim. Acta, Part A* **2012**, *94*, 134-142.

[61] T. Biver, *Appl. Spectrosc. Rev.* **2012**, *47*, 272-325.

[62] a) F. Arjmand, A. Jamsheera, *Spectrochim. Acta, Part A* **2011**, *78*, 45-51; b) G. Pratviel, J. Bernadou, B. Meunier, in *Adv. Inorg. Chem., Vol. Volume 45* (Ed.: A. G. Sykes), Academic Press, **1998**, pp. 251-312; c) N. Shahabadi, S. Kashanian, M. Khosravi, M. Mahdavi, *Transition Met. Chem. (London)* **2010**, *35*, 699-705.

[63] G. Scatchard, *Ann. N. Y. Acad. Sci.* **1949**, *51*, 660-672.

[64] H. A. Benesi, J. H. Hildebrand, *J. Am. Chem. Soc.* **1949**, *71*, 2703-2707.

[65] a) P. Thordarson, *Chem. Soc. Rev.* **2011**, *40*, 1305-1323; b) O. V. Tsodikov, J. A. Holbrook, I. A. Shkel, M. T. Record Jr, *Biophys. J.* **2001**, *81*, 1960-1969; c) F. H. Stootman, D. M. Fisher, A. Rodger, J. R. Aldrich-Wright, *Analyst* **2006**, *131*, 1145-1151; d) M. S. Rocha, *Integr. Biol.* **2015**, *7*, 967-986.

[66] a) G. Cohen, H. Eisenberg, *Biopolymers* **1969**, *8*, 45-55; b) K. R. Fox, N. L. Harrison, M. J. Waring, *FEBS Lett.* **1981**, *133*, 305-310.

[67] M. M. Murr, M. T. Harting, V. Guelev, J. Ren, J. B. Chaires, B. L. Iverson, *Bioorg. Med. Chem.* **2001**, *9*, 1141-1148.

[68] F. Cui, R. Huo, G. Hui, X. Lv, J. Jin, G. Zhang, W. Xing, *J. Mol. Struct.* **2011**, *1001*, 104-110.

[69] J. R. Lakowicz, *Principles of fluorescence spectroscopy*, 3nd ed., Kluwer Academic/Plenum, New York, **2006**.

[70] P. E. Schipper, B. Nordén, F. Tjerneld, *Chem. Phys. Lett.* **1980**, *70*, 17-21.

[71] M. Eriksson, B. Nordén, in *Methods Enzymol., Vol. Volume 340* (Ed.: M. J. W. Jonathan B. Chaires), Academic Press, **2001**, pp. 68-98.

[72] M. Coll, C. A. Frederick, A. H. J. Wang, A. Rich, *Proc. Natl. Acad. Sci. U. S. A.* **1987**, *84*, 8385-8389.

[73] a) J. G. Pelton, D. E. Wemmer, *Proc. Natl. Acad. Sci. U. S. A.* **1989**, *86*, 5723-5727; b) J. G. Pelton, D. E. Wemmer, *J. Am. Chem. Soc.* **1990**, *112*, 1393-1399.

[74] S. N. Mitra, M. C. Wahl, M. Sundaralingam, *Acta Crystallogr., Sect. D: Biol. Crystallogr.* **1999**, *55*, 602-609.

[75] a) W. S. Wade, M. Mrksich, P. B. Dervan, *J. Am. Chem. Soc.* **1992**, *114*, 8783-8794; b) M. Mrksich, P. B. Dervan, *J. Am. Chem. Soc.* **1993**, *115*, 9892-9899.

[76] a) C. L. Kielkopf, S. White, J. W. Szewczyk, J. M. Turner, E. E. Baird, P. B. Dervan, D. C. Rees, *Science* **1998**, *282*, 111-115; b) C. L. Kielkopf, R. E. Bremer, S. White, J. W. Szewczyk, J. M. Turner, E. E. Baird, P. B. Dervan, D. C. Rees, *J. Mol. Biol.* **2000**, *295*, 557-567.

[77] a) W. Zhang, Y. Dai, U. Schmitz, T. W. Bruice, *FEBS Lett.* **2001**, *509*, 85-89; b) L. Wang, A. Kumar, D. W. Boykin, C. Bailly, W. D. Wilson, *J. Mol. Biol.* **2002**, *317*, 361-374; c) M. Munde, A. Kumar, R. Nhili, S. Depauw, M.-H. David-Cordonnier, M. A. Ismail, C. E. Stephens, A. A. Farahat, A. Batista-Parra, D. W. Boykin, W. D. Wilson, *J. Mol. Biol.* **2010**, *402*, 847-864; d) S. Laughlin, S. Wang, A. Kumar, A. A. Farahat, D. W. Boykin, W. D. Wilson, *Chem. Eur. J.* **2015**, *21*, 5528-5539.

[78] a) Y. Kawabe, S. Kato, *Dyes Pigm.* **2012**, *95*, 614-618; b) M. J. Ruedas-Rama, A. Orte, M. C. Martin-Domingo, F. Castello, E. M. Talavera, J. M. Alvarez-Pez, *J. Phys. Chem. B* **2014**, *118*, 6098-6106; c) S. Kaloyanova, V. M. Trusova, G. P. Gorbenko, T. Deligeorgiev, *J. Photochem. Photobiol., A* **2011**, *217*, 147-156.

[79] a) A. L. Mikheikin, A. L. Zhuze, A. S. Zasedatelev, *J. Biomol. Struct. Dyn.* **2000**, *18*, 59-72; b) M. Eriksson, H. J. Karlsson, G. Westman, B. Åkerman, *Nucleic Acids Res.* **2003**, *31*, 6235-6242; c) H. J. Karlsson, M. Eriksson, E. Perzon, B. Åkerman, P. Lincoln, G. Westman, *Nucleic Acids Res.* **2003**, *31*, 6227-6234.

[80] K. M. Sovenyhazy, J. A. Bordelon, J. T. Petty, *Nucleic Acids Res.* **2003**, *31*, 2561-2569.

[81] J. L. Seifert, R. E. Connor, S. A. Kushon, M. Wang, B. A. Armitage, *J. Am. Chem. Soc.* **1999**, *121*, 2987-2995.

[82] K. C. Hannah, B. A. Armitage, *Acc. Chem. Res.* **2004**, *37*, 845-853.

[83] a) B. A. Armitage, in *DNA Binders and Related Subjects, Vol. 253* (Eds.: M. Waring, J. Chaires), Springer Berlin Heidelberg, **2005**, pp. 55-76; b) B. Armitage, in *Heterocyclic Polymethine Dyes, Vol. 14* (Ed.: L. Strekowski), Springer Berlin Heidelberg, **2008**, pp. 11-29; c) G. Y. Guralchuk, A. V. Sorokin, I. K. Katrunov, S. L. Yefimova, A. N. Lebedenko, Y. V. Malyukin, S. M. Yarmoluk, *J. Fluoresc.* **2007**, *17*, 370-376.

[84] a) C. Wagner, H.-A. Wagenknecht, *Org. Lett.* **2006**, *8*, 4191-4194; b) D. Baumstark, H.-A. Wagenknecht, *Angew. Chem. Int. Ed.* **2008**, *47*, 2612-2614; c) F. D. Lewis, L. Zhang, R. F. Kelley, D. McCamant, M. R. Wasielewski, *Tetrahedron* **2007**, *63*, 3457-3464; d) R. Carmieli, T. A. Zeidan, R. F. Kelley, Q. Mi, F. D. Lewis, M. R. Wasielewski, *J. Phys. Chem. A* **2009**, *113*, 4691-4700; e) M. Hariharan, Y. Zheng, H. Long, T. A. Zeidan, G. C. Schatz, J. Vura-Weis, M. R. Wasielewski, X. B. Zuo, D. M. Tiede, F. D. Lewis, *J. Am. Chem. Soc.* **2009**, *131*, 5920-5929; f) P. P. Neelakandan, T. A. Zeidan, M. McCullagh, G. C. Schatz, J. Vura-Weis, C. H. Kim, M. R. Wasielewski, F. D. Lewis, *Chem. Sci.* **2014**, *5*, 973-981.

[85] a) M. Franceschin, C. M. Lombardo, E. Pascucci, D. D'Ambrosio, E. Micheli, A. Bianco, G. Ortaggi, M. Savino, *Bioorg. Med. Chem.* **2008**, *16*, 2292-2304; b) M. Franceschin, E. Pascucci, A. Alvino, D. D'Ambrosio, A. Bianco, G. Ortaggi, M. Savino, *Bioorg. Med. Chem. Lett.* **2007**, *17*, 2515-2522.

[86] E. Micheli, C. M. Lombardo, D. D'Ambrosio, M. Franceschin, S. Neidle, M. Savino, *Bioorg. Med. Chem. Lett.* **2009**, *19*, 3903-3908.

[87] T. H. Rehm, M. Radić Stojković, S. Rehm, M. Škugor, I. Piantanida, F. Würthner, *Chem. Sci.* **2012**, *3*, 3393-3397.

[88] S. Rehm, V. Stepanenko, X. Zhang, T. H. Rehm, F. Würthner, *Chem. Eur. J.* **2010**, *16*, 3372-3382.

[89] a) C. A. E. Hauser, S. Maurer-Stroh, I. C. Martins, *Chem. Soc. Rev.* **2014**, *43*, 5326-5345; b) C. Gonçalves, P. Pereira, M. Gama, *Materials* **2010**, *3*, 1420.

[90] A. Klug, *Phil. Trans. R. Soc. Lond. B* **1999**, *354*, 531-535.

[91] a) S. Svenson, *Curr. Opin. Colloid Interface Sci.* **2004**, *9*, 201-212; b) V. T. John, B. Simmons, G. L. McPherson, A. Bose, *Curr. Opin. Colloid Interface Sci.* **2002**, *7*, 288-295.

[92] a) S. S. Babu, S. Prasanthkumar, A. Ajayaghosh, *Angew. Chem. Int. Ed.* **2012**, *51*, 1766-1776; b) C. Wang, H. Dong, W. Hu, Y. Liu, D. Zhu, *Chem. Rev.* **2012**, *112*, 2208-2267.

[93] a) D. Wang, G. Tong, R. Dong, Y. Zhou, J. Shen, X. Zhu, *Chem. Commun.* **2014**, *50*, 11994-12017; b) A. Kaeser, A. P. H. J. Schenning, *Adv. Mater.* **2010**, *22*, 2985-2997.

[94] a) L. Brunsveld, B. J. B. Folmer, E. W. Meijer, R. P. Sijbesma, *Chem. Rev.* **2001**, *101*, 4071-4097; b) F. J. M. Hoeben, P. Jonkheijm, E. W. Meijer, A. P. H. J. Schenning, *Chem. Rev.* **2005**, *105*, 1491-1546; c) T. Rehm, C. Schmuck, *Chem. Commun.* **2008**, 801-813; d) Y. Liu, Z. Wang, X. Zhang, *Chem. Soc. Rev.* **2012**, *41*, 5922-5932; e) C. Kulkarni, S. Balasubramanian, S. J. George, *ChemPhysChem* **2013**, *14*, 661-673.

[95] a) R. B. Martin, *Chem. Rev.* **1996**, *96*, 3043-3064; b) T. F. A. De Greef, M. M. J. Smulders, M. Wolffs, A. P. H. J. Schenning, R. P. Sijbesma, E. W. Meijer, *Chem. Rev.* **2009**, *109*, 5687-5754.

[96] C. A. Hunter, H. L. Anderson, *Angew. Chem. Int. Ed.* **2009**, *48*, 7488-7499.

[97] a) P. A. Korevaar, S. J. George, A. J. Markvoort, M. M. J. Smulders, P. A. J. Hilbers, A. P. H. J. Schenning, T. F. A. De Greef, E. W. Meijer, *Nature* **2012**, *481*, 492-496; b) P. A. Korevaar, T. F. A. de Greef, E. W. Meijer, *Chem. Mater.* **2014**, *26*, 576-586; c) P. A. Korevaar, C. Schaefer, T. F. A. de Greef, E. W. Meijer, *J. Am. Chem. Soc.* **2012**, *134*, 13482-13491.

[98] P. Thordarson, in *Supramolecular Chemistry: From Molecules to Nanomaterials, Vol. 2: Techniques* (Eds.: P. A. Gale, J. W. Steed), Wiley-Blackwell, Oxford, **2012**.

[99] a) F. Würthner, S. Yao, T. Debaerdemaeker, R. Wortmann, *J. Am. Chem. Soc.* **2002**, *124*, 9431-9447; b) W. West, S. Pearce, *J. Phys. Chem.* **1965**, *69*, 1894-1903; c) M. M. Safont-Sempere, P. Osswald, K. Radacki, F. Würthner, *Chem. Eur. J.* **2010**, *16*, 7380-7384; d) Z. Chen, U. Baumeister, C. Tschierske, F. Würthner, *Chem. Eur. J.* **2007**, *13*, 450-465; e) A. W. Snow, in *The Porphyrin Handbook* (Eds.: R. Guilard, K. M. Kadish, K. M. Smith), Academic Press, Amsterdam, **2003**, pp. 129-176.

[100] a) A. Weißenstein, F. Würthner, *Chem. Commun.* **2015**, *51*, 3415-3418; b) A. Syamakumari, A. P. H. J. Schenning, E. W. Meijer, *Chem. Eur. J.* **2002**, *8*, 3353-3361.

[101] a) F. Würthner, C. Thalacker, S. Diele, C. Tschierske, *Chem. Eur. J.* **2001**, *7*, 2245-2253; b) Z. Chen, V. Stepanenko, V. Dehm, P. Prins, L. D. A. Siebbeles, J. Seibt, P. Marquetand, V. Engel, F. Würthner, *Chem. Eur. J.* **2007**, *13*, 436-449; c) F. Würthner, C. R. Saha-Möller, B. Fimmel, S. Ogi, P. Leowanawat, D. Schmidt, *Chem. Rev.* **2015**.

[102] R. F. Goldstein, L. Stryer, *Biophys. J.* **1986**, *50*, 583-599.

[103] T. E. Kaiser, V. Stepanenko, F. Würthner, *J. Am. Chem. Soc.* **2009**, *131*, 6719-6732.

[104] a) P. Jonkheijm, P. van der Schoot, A. P. H. J. Schenning, E. W. Meijer, *Science* **2006**, *313*, 80-83; b) M. M. J. Smulders, A. P. H. J. Schenning, E. W. Meijer, *J. Am. Chem. Soc.* **2008**, *130*, 606-611; c) M. M. J. Smulders, M. M. L. Nieuwenhuizen, T. F. A. de Greef, P. van der Schoot, A. P. H. J. Schenning, E. W. Meijer, *Chem. Eur. J.* **2010**, *16*, 362-367.

[105] R. van der Weegen, P. A. Korevaar, P. Voudouris, I. K. Voets, T. F. A. de Greef, J. A. J. M. Vekemans, E. W. Meijer, *Chem. Commun.* **2013**, *49*, 5532-5534.

[106] M. P. Evstigneev, A. S. Buchelnikov, V. V. Kostjukov, I. S. Pashkova, V. P. Evstigneev, *Supramol. Chem.* **2013**, *25*, 199-203.

[107] T. Metzroth, A. Hoffmann, R. Martin-Rapun, M. M. J. Smulders, K. Pieterse, A. R. A. Palmans, J. A. J. M. Vekemans, E. W. Meijer, H. W. Spiess, J. Gauss, *Chem. Sci.* **2011**, *2*, 69-76.

[108] L. J. Prins, D. N. Reinhoudt, P. Timmerman, *Angew. Chem. Int. Ed.* **2001**, *40*, 2382-2426.

[109] a) C. A. Hunter, K. R. Lawson, J. Perkins, C. J. Urch, *J. Chem. Soc., Perkin Trans. 2* **2001**, 651-669; b) C. A. Hunter, J. K. M. Sanders, *J. Am. Chem. Soc.* **1990**, *112*, 5525-5534; c) C. R. Martinez, B. L. Iverson, *Chem. Sci.* **2012**, *3*, 2191-2201; d) S. Grimme, *Angew. Chem. Int. Ed.* **2008**, *47*, 3430-3434.

[110] a) M. L. Waters, *Biopolymers* **2004**, *76*, 435-445; b) K. E. Riley, P. Hobza, *Acc. Chem. Res.* **2013**, *46*, 927-936.

[111] a) F. J. M. Hoeben, P. Jonkheijm, E. W. Meijer, A. P. H. J. Schenning, *Chem. Rev.* **2005**, *105*, 1491-1546; b) F. Aparicio, L. Sánchez, *Chem. Eur. J.* **2013**, *19*, 10482-10486; c) D. González-Rodríguez, A. P. H. J. Schenning, *Chem. Mater.* **2010**, *23*, 310-325.

[112] a) X. Zhan, A. Facchetti, S. Barlow, T. J. Marks, M. A. Ratner, M. R. Wasielewski, S. R. Marder, *Adv. Mater.* **2011**, *23*, 268-284; b) A. Mishra, P. Bäuerle, *Angew. Chem. Int. Ed.* **2012**, *51*, 2020-2067.

[113] a) F. Schlosser, M. Moos, C. Lambert, F. Würthner, *Adv. Mater.* **2013**, *25*, 410-414; b) J. Kumar, H. Tsumatori, J. Yuasa, T. Kawai, T. Nakashima, *Angew. Chem. Int. Ed.* **2015**, *54*, 5943-5947; c) A. Issac, R. Hildner, D. Ernst, C. Hippius, F. Würthner, J. Köhler, *Phys. Chem. Chem. Phys.* **2012**, *14*, 10789-10798; d) H. Yoo, J. Yang, A. Yousef, M. R. Wasielewski, D. Kim, *J. Am. Chem. Soc.* **2010**, *132*, 3939-3944; e) D. Veldman, S. M. A. Chopin, S. C. J. Meskers, M. M. Groeneveld, R. M. Williams, R. A. J. Janssen, *J. Phys. Chem. A* **2008**, *112*, 5846-5857; f) C. Hippius, I. H. M. van Stokkum, E. Zangrando, R. M. Williams, M. Wykes, D. Beljonne, F. Würthner, *J. Phys. Chem. C* **2008**, *112*, 14626-14638; g) J. J. Han, A. D. Shaller, W. Wang, A. D.

Q. Li, *J. Am. Chem. Soc.* **2008**, *130*, 6974-6982; h) T. Kawai, K. Kawamura, H. Tsumatori, M. Ishikawa, M. Naito, M. Fujiki, T. Nakashima, *ChemPhysChem* **2007**, *8*, 1465-1468; i) W. Wang, L. Wang, B. J. Palmer, G. J. Exarhos, A. D. Q. Li, *J. Am. Chem. Soc.* **2006**, *128*, 11150-11159; j) H. Langhals, A. Hofer, S. Bernhard, J. S. Siegel, P. Mayer, *J. Org. Chem.* **2011**, *76*, 990-992; k) H. Langhals, J. Gold, *Liebigs Ann./Recl.* **1997**, *1997*, 1151-1153; l) J. Kumar, T. Nakashima, T. Kawai, *Langmuir* **2014**, *30*, 6030-6037; m) J. M. Giaimo, J. V. Lockard, L. E. Sinks, A. M. Scott, T. M. Wilson, M. R. Wasielewski, *J. Phys. Chem. A* **2008**, *112*, 2322-2330; n) A. D. Shaller, W. Wang, H. Gan, A. D. Q. Li, *Angew. Chem. Int. Ed.* **2008**, *47*, 7705-7709; o) F. Schlosser, V. Stepanenko, F. Würthner, *Chem. Commun.* **2010**, *46*, 8350-8352.

[114] J. Gershberg, M. Radić Stojković, M. Škugor, S. Tomić, T. H. Rehm, S. Rehm, C. R. Saha-Möller, I. Piantanida, F. Würthner, *Chem. Eur. J.* **2015**, *21*, 7886-7895.

[115] T. H. Rehm, *Unpublished work* **2011**.

[116] a) S. Ogi, V. Stepanenko, K. Sugiyasu, M. Takeuchi, F. Würthner, *J. Am. Chem. Soc.* **2015**, *137*, 3300-3307; b) R. Marty, R. Nigon, D. Leite, H. Frauenrath, *J. Am. Chem. Soc.* **2014**, *136*, 3919-3927; c) K. Sugiyasu, N. Fujita, S. Shinkai, *Angew. Chem. Int. Ed.* **2004**, *43*, 1229-1233; d) S. S. Babu, V. K. Praveen, A. Ajayaghosh, *Chem. Rev.* **2014**, *114*, 1973-2129; e) S. Ogi, V. Stepanenko, J. Thein, F. Würthner, *J. Am. Chem. Soc.* **2016**, *138*, 670-678.

[117] Y. J. Xu, S. W. Leng, C. M. Xue, R. K. Sun, J. Pan, J. Ford, S. Jin, *Angew. Chem. Int. Ed.* **2007**, *46*, 3896-3899.

[118] A. Bothe, in *Bachelorthesis "Synthese molekularer Pinzetten auf Basis von Perylenbisimidfarbstoffen"*, Würzburg, **2015**.

[119] a) D. K. Smith, *J. Chem. Soc., Perkin Trans. 2* **1999**, 1563-1566; b) Y. Rio, J.-F. Nicoud, J.-L. Rehspringer, J.-F. Nierengarten, *Tetrahedron Lett.* **2000**, *41*, 10207-10210; c) H. Stephan, S. Juran, K. Born, P. Comba, G. Geipel, U. Hahn, N. Werner, F. Vogtle, *New J. Chem.* **2008**, *32*, 2016-2022; d) U. Hahn, S. Engmann, C. Oelsner, C. Ehli, D. M. Guldi, T. Torres, *J. Am. Chem. Soc.* **2010**, *132*, 6392-6401; e) X. Yin, F. Meng, L. Wang, *J. Mater. Chem. C.* **2013**, *1*, 6767-6773; f) M. Ouchi, Y. Inoue, Y. Liu, S. Nagamune, S. Nakamura, K. Wada, T. Hakushi, *Bull. Chem. Soc. Jpn.* **1990**, *63*, 1260-1262; g) D. H. Tang, Q. H. Fan, *J. Chem. Research (S)* **2003**, 698-699; h) S. Zhang, H.-J. Sun, A. D. Hughes, B. Draghici, J. Lejnieks, P. Leowanawat, A. Bertin, L. Otero De Leon, O. V. Kulikov, Y. Chen, D. J. Pochan, P. A. Heiney, V. Percec, *ACS Nano* **2014**, *8*, 1554-1565.

[120] a) J. Duschmale, S. Kohrt, H. Wennemers, *Chem. Commun.* **2014**, *50*, 8109-8112; b) J. Heyes, M. Wood, A. Martin, *Vol. WO 2013/126803 A1*, Canada, **2013**.

[121] a) J. S. Wu, A. Fechtenkötter, J. Gauss, M. D. Watson, M. Kastler, C. Fechtenkötter, M. Wagner, K. Müllen, *J. Am. Chem. Soc.* **2004**, *126*, 11311-11321; b) D. H. Zhao, J. S. Moore, *J. Org. Chem.* **2002**, *67*, 3548-3554.

[122] a) F. H. Beijer, H. Kooijman, A. L. Spek, R. P. Sijbesma, E. W. Meijer, *Angew. Chem. Int. Ed.* **1998**, *37*, 75-78; b) C. Rether, E. Verheggen, C. Schmuck, *Chem. Commun.* **2011**, *47*, 9078-9079; c) R. Wyler, J. de Mendoza, J. Rebek, *Angew. Chem. Int. Ed.* **1993**, *32*, 1699-1701.

[123] X. Zhang, D. Görl, V. Stepanenko, F. Würthner, *Angew. Chem. Int. Ed.* **2014**, *53*, 1270-1274.

[124] a) A. D. Q. Li, W. Wang, L. Q. Wang, *Chem. Eur. J.* **2003**, *9*, 4594-4601; b) V. Dehm, M. Büchner, J. Seibt, V. Engel, F. Würthner, *Chem. Sci.* **2011**, *2*, 2094-2100.

[125] D. Görl, doctoral thesis, Julius-Maximilians Universität Würzburg **2015**.

[126] D. D. Perrin, W. L. F. Armarego, D. R. Perrin, *Purification of laboratory chemicals*, 2d ed., Pergamon Press, Oxford ; New York, **1980**.

[127] C. A. Hunter, *Chem. Soc. Rev.* **1994**, *23*, 101-109.

[128] M. Kastler, W. Pisula, D. Wasserfallen, T. Pakula, K. Müllen, *J. Am. Chem. Soc.* **2005**, *127*, 4286-4296.

[129] A. P. H. J. Schenning, A. F. M. Kilbinger, F. Biscarini, M. Cavallini, H. J. Cooper, P. J. Derrick, W. J. Feast, R. Lazzaroni, P. Leclere, L. A. McDonell, E. W. Meijer, S. C. J. Meskers, *J. Am. Chem. Soc.* **2002**, *124*, 1269-1275.

[130] a) D. Zhao, J. S. Moore, *Org. Biomol. Chem.* **2003**, *1*, 3471-3491; b) D. van der Zwaag, T. F. A. de Greef, E. W. Meijer, *Angew. Chem. Int. Ed.* **2015**, *54*, 8334-8336.

[131] a) G. Fernández, M. Stolte, V. Stepanenko, F. Würthner, *Chem. Eur. J.* **2013**, *19*, 206-217; b) F. Fennel, S. Wolter, Z. Xie, P.-A. Plötz, O. Kühn, F. Würthner, S. Lochbrunner, *J. Am. Chem. Soc.* **2013**, *135*, 18722-18725.

[132] M. J. Mayoral, C. Rest, V. Stepanenko, J. Schellheimer, R. Q. Albuquerque, G. Fernández, *J. Am. Chem. Soc.* **2013**, *135*, 2148-2151.

[133] a) Y. Kobuke, H. Miyaji, *J. Am. Chem. Soc.* **1994**, *116*, 4111-4112; b) K. D. Shimizu, J. Rebek, *Proc. Natl. Acad. Sci. U. S. A.* **1995**, *92*, 12403-12407; c) H. Q. Zeng, X. W. Yang, A. L. Brown, S. Martinovic, R. D. Smith, B. Gong, *Chem. Commun.* **2003**, 1556-1557.

[134] F. Würthner, S. Yao, *Angew. Chem. Int. Ed.* **2000**, *39*, 1978-1981.

[135] T. Seki, X. Lin, S. Yagai, *Asian J. Org. Chem.* **2013**, *2*, 708-724.

[136] *It is to note that DOSY NMR experiments of PBI* **5** *in methylcyclohexane (1.3 x 10^{-2} M) revealed a hydrodynamic diameter of 3.12 nm which is significantly larger than those in chloroform and toluene but could not be related to a particular size of the PBI aggregate (Figure 52, right).*

[137] a) P. Samorí, V. Francke, T. Mangel, K. Müllen, J. P. Rabe, *Opt. Mater.* **1998**, *9*, 390-393; b) R. V. Gainutdinov, P. A. Arutyunov, *Russian Microelectronics* **2001**, *30*, 219-224; c) I. Kvien, B. S. Tanem, K. Oksman, *Biomacromolecules* **2005**, *6*, 3160-3165.

[138] R. B. Silverman, *The organic chemistry of drug design and drug action*, 2nd ed., Elsevier Academic Press, Amsterdam ; Boston, **2004**.

[139] E. Trinquet, G. Mathis, *Mol. BioSyst.* **2006**, *2*, 380-387.

[140] M. Demeunynck, C. Bailly, W. D. Wilson, *Small molecule DNA and RNA binders : from synthesis to nucleic acid complexes*, Wiley-VCH, Weinheim, **2003**.

[141] B. Willis, D. P. Arya, *Biochemistry* **2010**, *49*, 452-469.

[142] L. Xue, N. Ranjan, D. P. Arya, *Biochemistry* **2011**, *50*, 2838-2849.

[143] A. Ruiz-Carretero, P. G. A. Janssen, A. Kaeser, A. P. H. J. Schenning, *Chem. Commun.* **2011**, *47*, 4340-4347.

[144] S. M. Biner, D. Kummer, V. L. Malinovskii, R. Häner, *Org. Biomol. Chem.* **2011**, *9*, 2628-2633.

[145] M. Franceschin, *Eur. J. Org. Chem.* **2009**, 2225-2238.

[146] L. Rossetti, G. D'Isa, C. Mauriello, M. Varra, P. De Santis, L. Mayol, M. Savino, *Biophys. Chem.* **2007**, *129*, 70-81.

[147] a) J. T. Kern, P. W. Thomas, S. M. Kerwin, *Biochemistry* **2002**, *41*, 11379-11389; b) W. Tuntiwechapikul, T. Taka, M. Béthencourt, L. Makonkawkeyoon, T. Randall Lee, *Bioorg. Med. Chem. Lett.* **2006**, *16*, 4120-4126.

[148] D. Baumstark, H. A. Wagenknecht, *Chem. Eur. J.* **2008**, *14*, 6640-6645.

[149] a) L.-M. Tumir, I. Crnolatac, T. Deligeorgiev, A. Vasilev, S. Kaloyanova, M. Grabar Branilović, S. Tomić, I. Piantanida, *Chem. Eur. J.* **2012**, *18*, 3859-3864; b) K. Klemm, M. Radić Stojković, G. Horvat, V. Tomišić, I. Piantanida, C. Schmuck, *Chem. Eur. J.* **2012**, *18*, 1352-1363; c) M. Radić Stojković, S. Miljanić, K. Mišković, L. Glavaš-Obrovac, I. Piantanida, *Mol. BioSyst.* **2011**, *7*, 1753-1765.

[150] a) C. D. Schmidt, C. Böttcher, A. Hirsch, *Eur. J. Org. Chem.* **2007**, *2007*, 5497-5505; b) C. D. Schmidt, C. Böttcher, A. Hirsch, *Eur. J. Org. Chem.* **2009**, *2009*, 5337-5349; c) E. Krieg, E. Shirman, H. Weissman, E. Shimoni, S. G. Wolf, I. Pinkas, B. Rybtchinski, *J. Am. Chem. Soc.* **2009**, *131*, 14365-14373; d) D. Franke, M. Vos, M. Antonietti, N. A. J. M. Sommerdijk, C. F. J. Faul, *Chem. Mater.* **2006**, *18*, 1839-1847; e) Y. Huang, Y. Yan, B. M. Smarsly, Z. Wei, C. F. J. Faul, *J. Mater. Chem.* **2009**, *19*, 2356-2362; f) D. Görl, X. Zhang, F. Würthner, *Angew. Chem. Int. Ed.* **2012**, *51*, 6328-6348.

[151] M. Franceschin, A. Rizzo, V. Casagrande, E. Salvati, A. Alvino, A. Altieri, A. Ciammaichella, S. Iachettini, C. Leonetti, G. Ortaggi, M. Porru, A. Bianco, A. Biroccio, *ChemMedChem* **2012**, *7*, 2144-2154.

[152] V. Casagrande, A. Alvino, A. Bianco, G. Ortaggi, M. Franceschin, *J. Mass Spectrom.* **2009**, *44*, 530-540.

[153] A. J. Geall, I. S. Blagbrough, *Tetrahedron* **2000**, *56*, 2449-2460.

[154] a) S. Fixon-Owoo, F. Levasseur, K. Williams, T. N. Sabado, M. Lowe, M. Klose, A. Joffre Mercier, P. Fields, J. Atkinson, *Phytochemistry* **2003**, *63*, 315-334; b) P. Wellendorph, J. W. Jaroszewski, S. H. Hansen, H. Franzyk, *Eur. J. Med. Chem.* **2003**, *38*, 117-122.

[155] M. Nakamura, Y. Shimomura, Y. Ohtoshi, K. Sasa, H. Hayashi, H. Nakano, K. Yamana, *Org. Biomol. Chem.* **2007**, *5*, 1945-1951.

[156] C. R. Cantor, P. R. Schimmel, *The behavior of biological macromolecules*, W. H. Freeman, San Francisco, **1980**.

[157] S. Neidle, in *Principles of Nucleic Acid Structure* (Ed.: S. Neidle), Academic Press, New York, **2008**, pp. 204-248.

[158] L. Strekowski, B. Wilson, *Mutat. Res., Fund. Mol. Mech. M.* **2007**, *623*, 3-13.

[159] T. Heek, C. Fasting, C. Rest, X. Zhang, F. Würthner, R. Haag, *Chem. Commun.* **2010**, *46*, 1884-1886.

[160] a) N. Rahe, C. Rinn, T. Carell, *Chem. Commun.* **2003**, 2120-2121; b) P. P. Neelakandan, Z. Pan, M. Hariharan, Y. Zheng, H. Weissman, B. Rybtchinski, F. D. Lewis, *J. Am. Chem. Soc.* **2010**, *132*, 15808-15813; c) R. Varghese, H.-A. Wagenknecht, *Chem. Commun.* **2009**, 2615-2624.

[161] a) A. Rodger, B. Nordén, *Circular dichroism and linear dichroism*, Oxford University Press, Oxford ; New York, **1997**; b) N. Harada, K. Nakanishi, *Acc. Chem. Res.* **1972**, *5*, 257-263.

[162] W. D. Wilson, Y. H. Wang, C. R. Krishnamoorthy, J. C. Smith, *Biochemistry* **1985**, *24*, 3991-3999.

[163] W. D. Wilson, L. Ratmeyer, M. Zhao, L. Strekowski, D. Boykin, *Biochemistry* **1993**, *32*, 4098-4104.

[164] V. Dehm, Z. Chen, U. Baumeister, P. Prins, L. D. A. Siebbeles, F. Würthner, *Org. Lett.* **2007**, *9*, 1085-1088.

[165] J. Leonard, B. Lygo, J. Procter, *Praxis der Organischen Chemie*, Wiley-VCH, Weinheim, **1996**.

[166] J. L. Mergny, L. Lacroix, *Oligonucleotides* **2003**, *13*, 515-537.

[167] I. Piantanida, B. S. Palm, P. Čudić, M. Žinić, H.-J. Schneider, *Tetrahedron* **2004**, *60*, 6225-6231.

[168] J. D. McGhee, P. H. v. Hippel, *J. Mol. Biol.* **1976**, *103*, 679.

Publication list

V. Stepanenko, X.-Q. Li, J. Gershberg, F. Würthner, *Chem. Eur. J.* **2013**, *19*, 4176-4183.

J. Gershberg, M. Radić Stojković, M. Škugor, S. Tomić, T. H. Rehm, S. Rehm, C. R. Saha-Möller, I. Piantanida, F. Würthner, *Chem. Eur. J.* **2015**, *21*, 7886-7895.

J. Gershberg, F. Fennel, T. H. Rehm, S. Lochbrunner, F. Würthner, *Chem. Sci.* **2016**, *7*, 1729-1737.

Molecular structures of the synthesized dyes

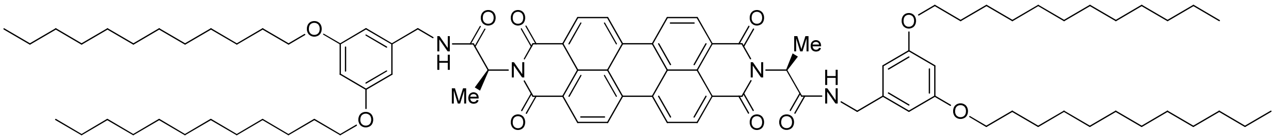

PBI 5

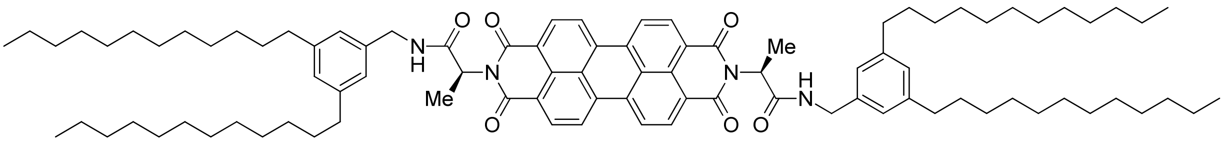

PBI 6

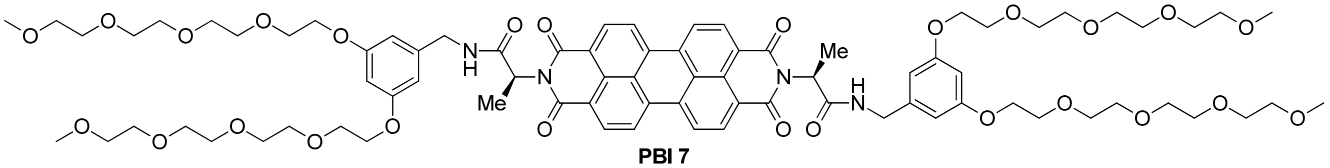

PBI 7

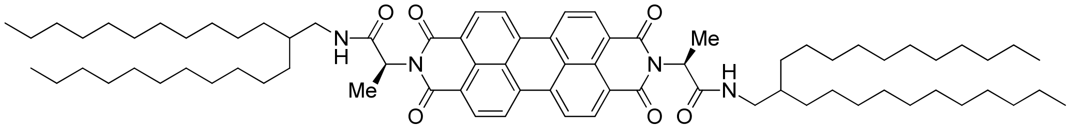

PBI 8

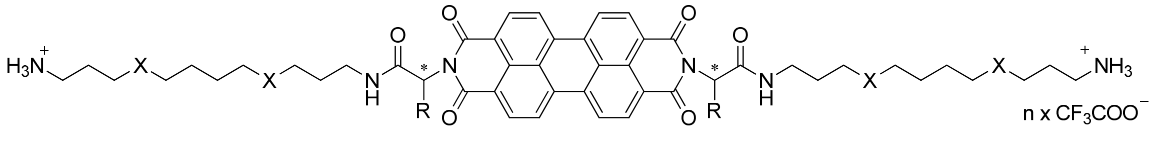

R = Me, X = O, n = 2: (L) or (D) PBI **18**
R = Bz, X = O, n = 2: (L) or (D) PBI **19**